Coventry University
Centre for Future Transport and Cities

Efficiency Enhancement of Class A Foams by Means of Nanoparticles to Fight Wildfires

Ioannis Papagiannis

Director of Studies: Dr Mauro S. Innocente

Co-Supervisors: Dr Evangelos Gkanas, Prof. Guillermo Rein

A thesis submitted in partial fulfilment of the University's requirements for the degree of Doctor of Philosophy

August 4, 2024

Acknowledgement

I would like to express my deepest gratitude to my thesis supervisors Mauro S. Innocente, Evangelos I. Gkanas and Guillermo Rein for their guidance, support, and patience throughout my research journey. Their expertise, insight, and constant encouragement have been invaluable to me. I am also grateful to the members of my thesis committee, for their insightful feedback and suggestions that have helped me shape my research. Heartfelt thanks to my parents and my sister for their unconditional love, support, and encouragement throughout my life. Finally, I would like to thank my friends and colleagues, Ilias Ntoukas, Petros Filippatos, Vaggelis Apostolopoulos, Konstantina Papadopoulou, Louiza Mavrovounioti, Paolo Grasso, Daizy Rajput, Jun Jet Tai and Mohammad Tavakol Sadrabadi for their unwavering support and encouragement during my academic journey. Their belief in me has kept me motivated and inspired. Without them, this achievement would not have been possible.

Abstract

Forest fire statistics are progressing dramatically in the world and humankind is called to address these natural disasters more effectively. Class A foams are firefighting foams aimed at materials prone to catch fire easily, such as wood, and may therefore be used in forest fires. Firefighting foams often face rapid degradation due to gravity-induced drainage and bubble collapse. This thesis is aimed at enhancing the fire suppression performance of Class A foams by incorporating nanoparticles (NPs) under different conditions. In the course of this investigation, nanoparticles (NPs) with specific sizes, shapes, and morphologies are synthesised using the hydrothermal and reflux methods seeking to optimise their integration in the foam structure to improve its stability and fire suppression performance. Iron oxide nanostructures with silica (IONPs)/SiO_2 are also produced through the already synthesised iron oxide nanoparticles (IONPs) and commercial SiO_2. These are used to compare fire suppression performances. Characterisation techniques, including Scanning Electron Microscopy (SEM), X-ray Diffraction (XRD), Fourier Transform Infrared Spectroscopy (FTIR), and Thermogravimetric Analysis (TGA) are used to validate the desired properties of the NPs, such as size uniformity, crystallinity, and resistance to degradation at high temperatures.

This thesis also investigates foam stability under drainage, surface tension, particle size distribution, and the evolution of bubble coalescence over time. A series of foam experiments are performed to study foam deterioration. Test results suggest that liquid loss is delayed when NPs are incorporated, thus keeping the foam wetter for longer. Results also indicate that the morphology of the bubbles remains stable over time, which means that bubbles can withstand being bumped, squeezed, and deformed. Surface tension is also reduced when adding IONPs, and the particle size distribution in the liquid solution tends to be larger at higher concentrations.

Small-scale fire experiments to test the enhanced foam on shredded wood wool (Excelsior) fuel suggest enhanced fire suppression performance. Notably, the addition of the synthesised IONPs with controllable size and morphology significantly enhanced the commercial Class A foam. This is evidenced by slower mass loss rate, reduced flame height, decreased rate of spread, and increased residual mass post-burning. This is attributed to the NPs' high thermal stability, large surface area, radical capture capabilities, and the formation of a protective layer acting as a firebreak. Furthermore, the investigation into the foam's performance in small-scale fire experiments elucidates the positive impact that adding NPs has on fire suppression performance. It reveals a notable reduction in average flame surface area and

suggests potential alterations in the combustion surface's molecular structure as well as the sooting properties of the fire. Comparative analysis between wet and dry foam applications highlights unique benefits for enhanced fire control management. This suggests the potential for an ideal firefighting foam that leverages the advantages of both, promising enhanced fire suppression performance.

Overall, this research demonstrates the fire suppression performance enhancement that may be achieved for a Class A foam by adding various types and concentrations of NPs.

Contents

List of Figures

List of Tables

Chapter 1

Introduction

1.1 Background

Foams find extensive applications in mineral flotation, food production, personal care, firefighting, and several other sectors. Nevertheless, they remain unstable and prone to rapid drainage and collapse. This instability mainly results from the Laplace pressure difference, which leads to slow gas diffusion through the bubble walls. Consequently, smaller bubbles shrink faster than larger ones, ultimately leading to their disappearance. The use of surfactants is essential to achieve foam stability by impeding bubble coalescence through steric effects and reducing foam drainage. Furthermore, the inclusion of nanomaterials with surfactants displays optimistic potential for improving foam stability. Nanoparticles can assemble at the gas-liquid interface, forming a layer that defers foam drainage and impedes gas diffusion between bubbles. Recently, iron oxide nanoparticles have received attention for their remarkable flame retardancy and smoke suppression properties, which have led to the introduction of them as potential additives in firefighting foams. However, no research has been reported on the use of iron-based additives in firefighting foams and their possible enhancement mechanisms. In this investigation, our objective is to analyse the impact of incorporating iron oxide nanoparticles along with other types of nanoparticles into a commercial Class A foam on its stability, drainage rate, bubble surface morphology, wetting characteristics, and fire suppression efficiency. Recognising the mechanisms of foam enhancement will greatly affect the ability to enhance the suppression of forest fires.

1.2 Problem Statement

The efficiency and applicability of Class A foams to fight forest fires have been investigated numerous times in the past. However, due to challenges such as their inherent low stability and the need for specialised equipment, significant advancements in their development have been limited. The primary issue resolves around the need to optimise their low

stability to improve the firefighting capabilities, thereby reducing the quantity of product required to suppress fires. Recent developments in nanotechnology indicate that certain types of nanoparticles can increase the stability of firefighting foams, thus making them more effective in suppressing fires.

1.3 Research Questions

The research questions of this project are the following:

1. Does the addition of nanoparticles to Class A foams enhance their overallfire suppression performance?
2. What relevant properties are enhanced by adding nanoparticles?
3. What are the key underlying mechanisms for nanoparticles to enhance desirable properties?
4. How do Class A foams' performances compare when adding different types of nanoparticles?
5. How do concentrations of nanoparticles affect their impact on Class A foams to maximise fire suppression performance?

1.4 Aim and Objectives

Aim: Enhance the fire suppression performance of Class A foams with the addition of nanoparticles.

Objectives:

1. Synthesise nanoparticles with tailored properties that enhance their potential for fire suppression.
2. Identify the optimal concentration of nanoparticles using standard laboratory procedures
3. Produce the enhanced Class A foam with the nanoparticles being uniformly distributed.
4. Test the enhanced Class A foam on the suppression of real fires and record performance metrics.

1.5 Methodology

This study involves synthesising various types of iron oxide nanoparticles (IONPs) and combining them with silicon dioxide to create structured nanoparticles for comparison against

commercial silicon dioxide nanoparticles. The synthesis focuses on controlling the morphology and size distribution of IONPs. Characterisation of these nanoparticles is crucial, employing techniques such as Scanning Electron Microscopy (SEM), X-ray Diffraction (XRD), Fourier Transform Infrared Spectroscopy (FTIR), and Thermogravimetric Analysis (TGA). These methods are selected to provide comprehensive data on the morphological characteristics, crystalline structures, chemical compositions, and thermal stability.

Incorporating these nanoparticles into Class A foam at various concentrations allows for the preparation of multiple foam formulations. Evaluating the physical properties of these formulations, including foam stability and bubble morphology, is essential. Such assessments determine the foam's efficacy in adhering to surfaces and maintaining structural integrity under high temperatures, which are pivotal for fire suppression performance.

For a thorough assessment of the foam's fire suppression performance, controlled small-scale fire experiments using Excelsior (wood wool) as the fuel will be carried out. Excelsior is chosen for its standardised combustion properties, making it suitable for wildfire scenarios. These experiments should measure the efficiency of fire suppression based on time to extinguishment and foam quantity, alongside additional parameters such as mass loss rate, rate of spread, residual mass, and flame surface area. These metrics are fundamental for understanding the enhanced fire suppression performance of the foam during exposure to fire. A flowchart has been created as shown in Figure 1.1. This flowchart graphically visualises the relationships between the various chapters and sections of this thesis.

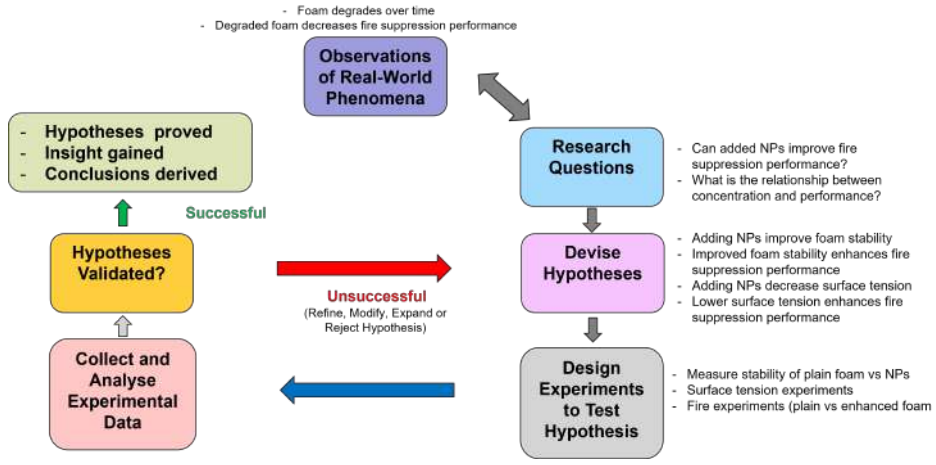

Figure 1.1: *Flowchart of thesis structure.*

1.6 Layout of the Thesis

This thesis is divided into seven chapters. Chapter 1 presents background on foam applications, instability issues and the novel approach using nanoparticles for firefighting foams. Chapter 2 includes a review of previous work on wildfires, firefighting foams and nanopar-

ticles' role in enhancing foam stability and fire suppression. Chapter 3 details the experimental setup used for synthesising and characterising nanoparticles, generating foams and testing their fire suppression performance. Chapter 4 discusses the synthesis methods, characterisation techniques and the effect of various reaction conditions on the development of nanoparticles with unique sizes and morphologies. Chapter 5 investigates the effects of iron oxide nanoparticles on the stability of Class A firefighting foams. Chapter 6 presents the results from fire suppression tests using the enhanced foam with nanoparticles. Mechanisms that cause fire suppression and flame retardancy are also discussed. Chapters 7 summarise the findings, conclusions and recommendations for future research directions.

Chapter 2

Literature Survey

2.1 Wildfires

2.1.1 Introduction

Fires are one of the oldest natural phenomena. Without fire, humankind would have struggled as it has been a vital tool for protection and survival since the early beginning of human history. However, fires can lead to devastating results for humans as they are very hard to control on a large scale. Combating fires can be achieved both from the ground and the air. The most common method of fighting fires is the application of firefighting foams, which separate the burning material, provide cooling effects, and prevent re-ignition. Fires are due to extremely complex physical and chemical processes. The interactions of these processes depend on various parameters, such as weather (atmosphere), topography, fire, and combustible material (vegetation).

2.1.2 Types of Wildland Fires

Forest fires, or large-scale fires, can be categorised into three types: surface fires, crown fires, and ground fires [11]. Surface fires are the most common type, burning slowly through the forest and causing damage to vegetation and other living organisms. As illustrated in Figure 2.1, surface fires can spread with a flaming front and burn various fuels at ground level such as fallen branches, leaf litter and other combustible materials.

Crown fires, on the other hand, are the most intense and dangerous type of fire, burning trees throughout their length and causing the disintegration and fragmentation of the trees [12]. Ground fires manifest themselves in deep accumulations of peat and other dead vegetation that are dry enough to burn [13]. While these types of fires move at a slow pace, they can be extremely difficult to extinguish or fully destroy. In some cases, ground fires may smoulder underground all winter and then resurface in spring. Figure 2.2 shows that crown fires will mainly burn through the top layer of foliage on a tree, known as the canopy.

Figure 2.1: *Illustration of a surface fire. [1]*

Figure 2.2: *Illustration of a crown fire.[1]*

Finally, ground fires usually occur in deep accumulations of peat, and similar dead vegetation that dry out enough to burn. These fires have a very slow pace and can be very difficult to fully extinguish or suppress. Figure 2.3, illustrates that such fires can burn organic matter in the soil beneath the surface and are sustained by glowing combustion [14].

Figure 2.3: *Illustration of a Ground fire. [1]*

Fires usually occur between April and October, with the highest levels of activity occurring between mid-May and August [15]. Particularly devastating fires often occur during long droughts or strong winds. Fires can be categorised as either natural or anthropogenic [16]. In recent years, human activity has been responsible for about 75% of all fires [17]. These fires are due to unprotected flames, combustible debris, equipment malfunctions, carelessly discarded cigarettes, and deliberate acts of arson. In contrast, naturally occurring fires are often the result of lightning-ignition and are more likely to occur in remote areas where properties, timber values, and human lives are not at risk. In these cases, fire suppression can be limited, allowing it to fulfil its natural role within the ecosystem.

2.1.3 Combustion

Fire is essentially an uncontrolled combustion [18]. Combustion is an exothermic reaction, meaning it releases heat, but sometimes the reaction progresses slowly enough that the temperature change is insignificant [19]. The chemical processes that take place in the flame are very complex and usually involve a large number of chemical reactions and intermediate species, most of which are radicals. [9, 20, 21]. Fragments of molecules or atoms can be such radicals and have a high reactivity. The single-step chemical reaction of methane-air combustion is represented by the equation 2.1 below:

$$CH_{4(g)} + 2O_{2(g)} \rightarrow CO_{2(g)} + 2H_2O_{(g)} \tag{2.1}$$

This chemical process of fuel oxidation eventually produces carbon dioxide and water, simultaneously releasing heat. The chemical reaction cannot be fully described by a single equation, as it involves many elemental reactions. During the combustion process of methane,

the chain reaction gradually slows down due to the increased rate of consumption of newly formed free radicals as well as the reduction of the growth rate of free radicals [22].

The term chain reaction in the context of methane-air combustion refers to a series of reactions where reactive intermediates, often free radicals, propagate the combustion process [23]. This process includes several stages [24]:

- Initiation:

  The reaction starts with the formation of highly reactive radicals. For methane (CH_4), this involves breaking the methane and oxygen (O_2) molecules into radicals, as shown in Equation 2.2:

  $$CH_4(g) + O_2(g) \rightarrow \cdot CH_3(g) + \cdot OH(g) \tag{2.2}$$

- Propagation:

  These radicals react with other molecules to form new radicals, propagating the reaction as shown in Equation 2.3:

  $$\cdot CH_3(g) + O_2(g) \rightarrow \cdot CH_3O_2(g) \tag{2.3}$$

  $$\cdot CH_3O_2(g) \rightarrow \cdot CH_2O(g) + \cdot OH(g) \tag{2.4}$$

- Branching:

  Some reactions produce multiple new radicals, exponentially increasing the number of reactive species as shown in Equation 2.5:

  $$\cdot OH(g) + CH_4(g) \rightarrow \cdot CH_3(g) + H_2O(g) \tag{2.5}$$

- Inhibition:

  The reaction slows as radicals are consumed or recombine to form stable molecules, thus reducing the number of reactive intermediates as shown in Equation 2.6:

  $$\cdot CH_3(g) + \cdot OH(g) \rightarrow CH_3OH(g) \tag{2.6}$$

However, methane is a simple hydrocarbon with a consistent molecular structure compared to a forest fuel. Wood-based fuels do not burn efficiently and cleanly like methane, because primarily wood is composed of a complex mixture of compounds, including cellulose, hemicellulose and lignin. Additionally, it can have a variable moisture content, which can significantly impact its combustion characteristics. The following equation 2.7 is an empirical formula based on the ultimate chemical analysis of poplar wood [25].

$$C_{4.3}H_{6.3}O_{2.59(s)} + 4.58\left(O_{2(g)} + 3.76N_{2(g)}\right) \rightarrow 4.30CO_{2(g)} + 3.15H_2O_{(g)} + 4.58(3.76N_{2(g)}) \tag{2.7}$$

To extinguish a fire, one of the three basic elements of the fire triangle must be eliminated. The three elements essential to ignite a fire are fuel, heat, and oxygen. Flammable materials such as wood, fabric, or plastic serve as fuel. Heat ignites the flammable vapours present in the fuel to start the fire, and oxygen acts as an oxidising agent in the chemical reaction. At least 16% oxygen is required for fire ignition regarding natural plant-based materials [26]. Fire blankets and fire extinguishers are designed specifically to remove one of the three elements of fire, usually heat or oxygen, to cool the fire and stop its spread. The successful elimination of one of those three elements can significantly reduce the incidence of fires and the catastrophic damage they can cause.

Combustion Models:

Kung [27] studied a partially pyrolysed element of wood which is regarded to be a partially residual char and partly unpyrolysed active material. As the element pyrolyses the active material is continuously converted into fuel volatiles and residual char. In that case, ρ_a is the time-dependent density of the active material. Initially, the active material density is equal to the virgin wood density, ρ_w. As the pyrolysis proceeds this active material gradually disappears leaving only the char of final density, ρ_f. At any given moment, t, the total density ρ is assumed to be:

$$\rho(t) = \left(1 - \frac{\rho_f}{\rho_w}\right)\rho_a(t) + \rho_f \quad \left(\mathrm{kg\,m^{-3}}\right) \tag{2.8}$$

For simplicity, a single Arrhenius decomposition reaction is considered, that is:

$$\frac{\partial \rho}{\partial t} = -a_\rho \rho_a \exp\left(-\frac{E_\rho}{RT}\right) \quad \left(\mathrm{kg\,m^{-3}\,s^{-1}}\right) \tag{2.9}$$

Where a_ρ is the pre-exponential factor, R is the universal gas constant, and E_ρ is the activation energy.

Combining equation (2.8) and equation (2.9) :

$$\frac{\partial \rho}{\partial t} = -a_\rho \frac{(\rho - \rho_f)\exp\left(-\frac{E_\rho}{RT}\right)}{\left(1 - \frac{\rho_f}{\rho_w}\right)} \quad \left(\mathrm{kg\,m^{-3}\,s^{-1}}\right) \tag{2.10}$$

To get more insight in the endothermic energy Q_p which is related to the generation of unit mass of vapours using the ambient reference temperature T_∞ the authors [27] have altered the previous equations with:

$$\rho C_{ps}\frac{\partial T}{\partial t} = \frac{\partial}{\partial x}\left(\frac{k\partial T}{\partial x}\right) + M_g\frac{\partial h_g}{\partial x} + \frac{\partial \rho}{\partial t}\left[Q_p - \frac{\rho_w}{\rho_w - \rho_f}h_a + \frac{\rho_f}{\rho_w - \rho_f}h_c + h_g\right] \tag{2.11}$$

Where C_{ps} is defined as $\rho C_{ps} = \rho_c C_{pc} + \rho_a C_{pa}$. M_g represents the outward mass flux of volatiles within the solid while h_c, h_a and h_g are the char-specific enthalpy, the active wood-specific enthalpy and the gaseous specific enthalpy respectively. The first three terms describe the effects of transient and spatial temperature changes whereas the last group of terms describe the instantaneous local energy absorption associated with the generation of volatiles.

The energy in equation (2.12) represents the effective local heat of vaporisation at temperature T, which is the energy per unit mass of generated volatiles that one would have to supply to a solid element if it were at uniform and constant temperature.

$$L(T) = Q_p - \frac{\rho_w}{\rho_w - \rho_f} h_a + \frac{\rho_f}{\rho_w - \rho_f} h_c + h_g \quad \left(\mathrm{J\,kg^{-1}}\right) \tag{2.12}$$

The term $\frac{\rho_w}{\rho_w - \rho_f}$ is the mass of active material consumed per unit mass of generated volatiles and the $\frac{\rho_f}{\rho_w - \rho_f}$ is the char produced. Overall, this study developed a complex model to simulate the pyrolysis of wood slab, through transient conduction, Arrhenius decomposition, endothermic decomposition and other physical processes.

On the other hand, *Asensio* [28] introduced a 2-D simplified wildland fire model based on conservation laws, taking into account radiation as the dominant thermal transfer mechanism, as well as convection, which represents the effect of the wind and the slope. Since chemical processes in a wildfire are too complex, their goal was to control the amount of unburnt solid fuel through a simplified chemical reaction for two phases (gas and solid) and two species (fuel and oxygen) with a form of 2.13:

$$Fuel + Oxidant -> [r] Products \tag{2.13}$$

The reaction rate constant r was given empirically by the Arrhenius Law in equation 2.14:

$$r = A \exp\left(-\frac{E_A}{RT}\right) \quad \left(\mathrm{mol\,L^{-1}\,s^{-1}}\right) \tag{2.14}$$

Where R is the universal gas constant $(\mathrm{R} = 1.9872, \mathrm{cal/K, mol})$ and T the absolute temperature. E_A represents the activation energy, and A is the pre-exponential factor for the reaction. In the above equation 2.14, E_A is a constant but A may depend weakly on T. Typically, the approximation for the pre-exponential factor is described in equation 2.15 :

$$A = BT^a \tag{2.15}$$

Where B is constant and $\alpha \in (-1, 2]$ is within the experimental error. Moreover, the authors claimed that there are two well-defined phases in wildfire processes: an endothermic phase

that is denoted as the solid or condensed phase, and an exothermic phase that is denoted as the gaseous phase.

Perminov [29] studied the behaviour of a coupled atmosphere/crown model which is based on the conservation of mass, species, energy and momentum. The main achievement of this mathematical model was the ability to determine the total CO and CO_2 emissions into the atmosphere during the propagation of forest fire at different times. The rate of formulation of the gas-dispersed mixture Q is described in equation 2.16 :

$$Q = (1 - a_c) R_1 + R_2 + \frac{M_c}{M_1} R_3 \quad \left(\mathrm{kg\,s^{-1}}\right) \tag{2.16}$$

Where R_1 is the mass rate of chemical reaction (1- dry organic substance) and is described by:

$$R_1 = k_1 \rho_1 \varphi_1 \exp\left(-\frac{E_1}{RT_s}\right) \quad \left(\mathrm{kg\,s^{-1}}\right) \tag{2.17}$$

R_2 (see Equation2.18) is the mass rate of chemical reaction (2- moisture), k is the coefficient of radiation attenuation, φ_2 is the volume fraction of condensed phase, T_s is the temperature of the solid phase and E_2 is the activation energy.

$$R_2 = k_2 \rho_2 \varphi_2 Y T^{-0.5} \exp\left(-\frac{E_2}{RT_s}\right) \quad \left(\mathrm{kg\,s^{-1}}\right) \tag{2.18}$$

R_3 is the mass rate of chemical reaction (3- condensed pyrolysis products) and is described by equation 2.19:

$$R_3 = k_3 \rho \varphi_3 s_f c_1 \exp\left(-\frac{E_3}{RT_s}\right) \quad \left(\mathrm{kg\,s^{-1}}\right) \tag{2.19}$$

Where c_1 is the mass concentration of the density of oxygen and s_f is the specific surface of the forest fuel.

Morvan [30] described the physical behaviour and the propagation of a small-scale surface fire in a pine needles litter. Flames exhibit three-dimensional behaviour, but their study is often limited to a two-dimensional configuration because the width of many propagating fires in nature is more critical than their depth. This study uses a model based on a detailed physical approach, considering the conservation equations (mass, energy, and momentum) of the system formed by the litter and the surrounding gas mixture.

The authors refer to the mathematical formulation in the solid phase where the reaction rate of water (combustion) is described in equation 2.20:

$$\dot{\omega}_{\mathrm{H_2O}} = \frac{k_{\mathrm{H_2O}}}{\sqrt{T_s}} \rho_s a_s Y^s_{\mathrm{H_2O}} \exp\left(-\frac{E_{\mathrm{H_2O}}}{RT_s}\right) \quad \left(\mathrm{kg\,m^{-3}\,s^{-1}}\right) \tag{2.20}$$

Where $Y^s_{\mathrm{H_2O}}$ is the mass fraction of moisture content, ρ_s is the density of the solid phase, a_s is the volume fraction of the solid phase, T_s is the temperature of the solid particles and $E_{\mathrm{H_2O}}$ is the activation energy. The study reveals that the propagation of a surface fire is predominantly governed by radiative heat transfer and that the increased flow of fresh air can accelerate the propagation velocity of a smaller fire.

Porterie, *Morvan* and *Larini* [30, 31, 32], presented a 2D multi-phase radiative and reactive model of line fire propagation of thermally thin cellulose particles which takes into account the hydrodynamic aspects of the flow and the basic physic-chemical procedures of thermal degradation such as heating, drying, pyrolysis and combustion using first-order Arrhenius kinetics.

Under the assumption that the fuel particles are thermally thin, i.e., the temperature throughout any solid particle is uniform while it is being heated, the solid-phase heat conduction equation reduces to 2.21:

$$a_k \rho_k C_{p,k} \frac{\partial T}{\partial t} = -\dot{m}^{pyr} L^{pyr} - \dot{m}^{\mathrm{char}} L^{\mathrm{char}} - \dot{m}^{\mathrm{H_2O}} L^{\mathrm{H_2O}} + [Q_{\mathrm{cond}}] + [Q_{\mathrm{rad}}] + [Q_{\mathrm{flame}}]_{\mathrm{lgf}} \tag{2.21}$$

Where $C_{p,k}$ is the specific heat of solid phase k and the subscript Igf refers to the interface of gas fuel bed, $[Q_{\mathrm{cond}}$ refers to the conductive-convective energy flux between the gas and the solid phase k, Q_{rad} represents the radiative heat flux between particles of the same phase k and Q_{flame} refers to the radiative energy flux from the flame to the particles at the top of the fuel bed. Finally, a two-dimensional multi-phase radiative and reactive model for line fire propagation was developed, addressing hydrodynamic flow aspects and basic physico-chemical processes like heating, pyrolysis, drying and combustion by employing first-order Arrhenius kinetics.

Grishin [33] suggested that the mass rates due to drying, pyrolysis and char combustion can be extracted from the following Arrhenius-type laws:

$$\dot{m}^{H20} = 6 * 10^5 T^{-0.5} \rho_k^{\mathrm{H_2O}} a_k \rho_k \exp\left(-\frac{6000}{T_k}\right)$$

$$\dot{m}^{pyr} = 3.63 * 10^4 T^{-0.5} \rho_k^{pyr} a_k \rho_k \exp\left(-\frac{9400}{T_k}\right)$$

$$\dot{m}^{char} = \frac{1}{s_1} 430 A_k \rho_{o_2} \exp\left(-\frac{9000}{T_k}\right)$$

Where ρ_k^{pyr} and $\rho_k^{H_2O}$ are the initial percentage of pyrolysis products and the moisture content of particles of solid phase k and s_1 is the stoichiometric ratio of the heterogeneous reaction which is assumed to be in $s_1 = 8/3$ because char is considered as pure carbon. The study's numerical solution indicates a minimum wind velocity threshold in the forest canopy below which a fire does not propagate. Moisture content plays a significant role, revealing that in ventilated forest fuels, radiative heat transfer from an upstream fire front is significantly less than convective heat transfer.

The Prasad model is notable for its ability to address fire suppression using water mist. This model is particularly significant because it represents a major advancement in fire suppression modelling by incorporating water mist as a key factor. *Prasad* and his co-workers [34] presented a two-continuum formulation in which the gas phase and the water mist are both described by equations of the Eulerian form. In their model, they adopted a sectional water mist model in which the entire droplet size domain is divided into discrete sections, and track only one integral quantity within each section. They considered a two-continuum formulation, wherein the gas properties and the droplet properties are each described by equations in the Eulerian form. This Eulerian-Eulerian form is useful when resolution is desired only on a scale larger than the average distance between the droplets.

In this approach, the droplet properties are treated as if they were continuous in the domain of the gaseous properties. The droplet property at a point in space and time represents the average value over many droplets in the neighbourhood of that point. The size distribution of the spray droplets can be described by the concentration of discrete droplets of various sizes per unit volume of fluid n (x, y, t) as a function of spatial coordinates x, y and of time t where i = 1,2,... The magnitude of the integer i represents the total number of discrete droplet sizes. The vaporisation process can be described by a set of coupled differential equations for the concentration of the discrete droplet sizes (see Equation2.22):

$$\frac{\partial n_i}{\partial t} + u_{l,i}\frac{\partial n_i}{\partial x} + v_{l,i}\frac{\partial n_i}{\partial y} = -E_i n_i + E_{i+1} n_{i+1}, \quad i = 1,2,\ldots \tag{2.22}$$

where $u_{l,i}$ and $v_{l,i}$ are the x and y components of the velocity vector of the i^{th} droplet size and E_i is the frequency of the molecule evaporation.

Since the total number of droplet sizes needed to simulate actual water mist sprays can be immense, sectional conservation equations have been developed. This method is based on dividing the droplet size domain into sections and dealing only with one integral quantity in each section. This sectional representation has the advantage that the integral quantity is conserved within the computational domain and the number of conservation equations is substantially reduced to equal the number of sections. They divided the entire droplet size domain into M arbitrary sections, and defined Q_j to be an integral quantity of the spray with the j^{th} section. Thus the quantity of the spray is described in equation 2.23

$$Q_j = \int_{v_{j-1}}^{v_j} vndv, \quad j = 1,2,\ldots,M \tag{2.23}$$

where n(v,t) is the number concentration function and v_{j-1} and v_j denote the volumes of the smallest and largest droplets, respectively, in section j.

The governing equations are rewritten in terms of finite-volume approximations on an Eulerian mesh and solved numerically for specific boundary and initial conditions. A complete solution to these governing equations requires solving the terms for each of the individual processes, as well as accounting for the interaction among the processes.

Lee and his co-workers [35] examined the effects of water addition on the fundamental combustion characteristics of a counter-flow flame. The authors showed that with water addition the yellow luminous zone of a non-premixed flame is reduced instead of the blue zone that is extended. The term blue zone describes the zone that has the maximum flame temperature and therefore primary combustion occurs instead of the yellow zone where soot precursors are formed. This observation is supported by the fact that with more enhanced water addition (H_2O), OH radicals attack and oxidise soot precursors like acetylene. However, they had some discrepancies between the computation and experimental results of the maximum flame temperature due to the conductive and convective heat losses. Therefore, they considered only the radiation heat losses for their experiment.

2.2 Firefighting Foams

2.2.1 Introduction

Firefighting foam is perfectly suitable for suppressing fires. It consists of a premix solution (a ratio of water and concentrated foam) mixed with air. It forms a stable layer of foam that spreads over the fuel and adheres to burning surfaces. Some types of foam, form a blanket over the surface of the fuel and seal the vapors. Firefighting foam can prevent the fuel's contact with oxygen, resulting in fire suppression. It also has a high cooling effect and will prevent re-ignition of the burning material.

Types of Foams:

Firefighting foams can be divided into two very large categories: These categories correspond to the types of fuels for which the foams have been designed.

2.2.2 Class A Foams

Class A foams were developed in the mid-1980s specifically for combating wildfires [36]. They consist of a biodegradable mixture of foaming agents and wetting agent and do not contain fluorinated chemicals, making them environmentally sustainable and non-toxic. Class A foam is 99 % water. The foam increases the efficiency and effectiveness of water as a

fire extinguishing agent [36]. The mechanism by which Class A foams extinguish fire, primarily involves the absorption of heat energy, thus facilitating the phase transition of water molecules to steam. This is the same process that makes water a promising extinguishing agent. However, the introduction of foam enhances the surface area relative to mass, which may allow the liquid to convert to steam more rapidly [36]. Class A foams act as insulating blankets on class A fuels, which help to form a vapour barrier between the burning fuels and oxygen [37]. Class A fuels are materials that involve ordinary combustibles such as wood, paper, cloth, rubber, and some plastics. These materials are commonly found in most environments and require water-based extinguishing agents like foams for effective suppression [37].

Class A foams have physical characteristics that vary depending on the method of generation. These characteristics are influenced by a range of variables such as the concentration of the foam solution, the type of foam concentrate used, hose length, nozzle design and aeration technique. Typically they are classified into three broad categories based on their physical state: wet foam, fluid foam and dry foam [10, 36].

Wet foam is defined by its smaller bubble size and lower expansion ratio, due to the reduced incorporation of air, leading to fast drain time. These kinds of foams are good for initial fire suppression, overhaul and penetrating deeply embedded fires [10, 36, 38] . It can range from an expansion ratio of 1:1 (no expansion) to 5 $\leq$: 1 [39].

Fluid foam features medium to smaller bubbles and moderate drainage times. It is good for direct attack of the fire as well as protection against exposure, and mop-up operations [10, 36]. The range of the expansion ratio of this foam is 5:1 to 10:1 [39]. Fluid foam can also release the liquid solution more rapidly than dry foam but holds its shape and adheres better than wet foam. In that case, fluid foam has the potential to be better at cooling and wetting than dry foam [8].

Finally, dry foam, characterised by a high expansion ratio, resembles shaving or whipped cream. These foams are different due to their slow drainage times and their capacity to maintain structural integrity for longer periods. This provides good exposure protection and the ability to cling to vertical surfaces over extended periods [10, 36, 38]. The range of this foam is 10:1 or greater [39]. This form of foam is suitable for class B fire scenarios. On the other hand, its opposite structure which is the wet foam, exhibits lower expansion ratios and shorter drainage times, with its increased water content which may result in more effective fire suppression [39].

When mixed in the right proportions with water, Class A foam will mainly alter two properties of the liquid. First, it increases its wetting efficiency, allowing for greater penetration into Class ”A” fuels. Second, it imparts a foaming ability to water, allowing it to adhere to both vertical and horizontal surfaces without ”beading up” [36]. Thus, water can absorb more heat.

In recent years, there has been increased research interest in Class A foams due to the challenges in evaluating the potential effects of fluorinated firefighting foams on human health

and the environment [40, 41, 42, 43, 44].

2.2.3 Class B Foams

Class B foams are designed for extinguishing fires involving flammable liquids (classified as Class B fires) and are categorised as fluorinated or fluorine-free [45]. Fluorinated foams, such as aqueous film-forming foams (AFFF), contain various amounts of Per- and Polyfluorinated Substances (PFAS) and have raised concerns about their potential long-term negative effects on human health and the environment [43, 46]. As a result, there has been an increasing effort to identify alternative foams that are safer to use. In comparison to Class A foams, Class B foams have a high biochemical oxygen demand (BOD), meaning they require large amounts of oxygen to biodegrade. When these foams enter aquatic environments, they can lead to reduced oxygen levels and asphyxiation of organisms [47]. Understanding the biodegradability and toxicity of firefighting foams is of vital importance, as their composition plays a significant role in their environmental impacts. However, this information is usually proprietary and available from the manufacturer.

Main difference between Class A and Class B Foams:

The main difference between Class A and Class B foams is their intended use and the types of fires for which they are designed [36]. Class A foam concentrates typically range in percentages between 0.1% and 1.0%, whereas Class B foam concentrates are in higher percentages ranging from 3% to 6%. For example, using 0.3%, 1,000 gallons of Class A foam can be produced with just 3 gallons of Class A foam concentrate and 997 gallons of water [36]. In contrast, an equivalent amount of Class B foam at 3% would require 30 gallons of Class B foam concentrate and 970 gallons of water, resulting in a higher production cost. Thus, Class A foams provide a more economical solution while maintaining high performance.

The fundamental difference between a Class A foam and a Class B foam lies in the way that they interact with the burning fuel. A Class B foam is designed to repel carbon and form a film over the liquid, which suppresses the vapours that are burning [48]. In contrast, a Class A foam penetrates the fuel and combats the fire by cooling the surface, displacing oxygen, and separating the fuel from the heat source. Class A foams are designed for extinguishing fires involving common fuels such as wood, paper, fabric, and other solid materials [36]. One of their main characteristics is that they reduce the surface tension of the water, allowing it to penetrate and cool the combustible material [36]. Also, foam creates a layer that contributes to the extinguishing of the fire due to the suppression of oxygen. Class A foams are typically used in structural firefighting, wildland firefighting, and some industrial applications [43, 49].

Class B foams, on the other hand, are designed for extinguishing fires involving flammable or combustible liquids, such as gasoline, diesel fuel, and oil [46]. This type of foam also forms a white foam blanket that floats on top of the fuel and suppresses the release of flammable vapours, thus preventing the re-ignition of the fire. Class B foams are typically used in industrial and petrochemical firefighting, in aviation firefighting, and in other applications where flammable liquids are stored or transported.

2.2.4 Expansion of Foams

Firefighting foams are classified into three categories based on their expansion ratio. These are low, medium, and high expansion foams [2].

Low expansion foam (see Figure 2.4) is typically used for large hydrocarbon fires, for example in storage tanks and retention basins. This type of foam has a higher density allowing the use of long-range nozzles with hoses or monitors. Regardless of weather conditions, low-expansion foam is the least sensitive to atmospheric conditions. It is stable and provides strong coverage of the burning fuel. Also, it possesses low viscosity and high water content ensuring significant additional cooling [50].

Figure 2.4: *Low Expansion Firefighting Foam [2].*

Medium expansion foam (see Figure 2.5) is used for smaller surfaces, such as solvent storages and cellars, typically in enclosed or semi-enclosed spaces where the spreading is limited. Medium expansion foam can be sprayed to a height of about ten meters. This foam is sensitive to wind and adverse weather conditions due to its low density [51].

High expansion foam (see Figure 2.6) is preferably used for fires of dry products or in spaces where there are mixed hazards, such as stores and warehouses. This type of foam is typically applied in large, enclosed spaces where strong winds will not affect the foam's utility and where internal positions are hard to access [52].

The expansion ratio of the foam represents the ratio of the foam's volume to the volume of the foam solution used to create it. [53]. Equation 2.24 depicts the expansion ratio of the foam.

Figure 2.5: *Medium Expansion Firefighting Foam.*

Figure 2.6: *High Expansion Firefighting Foam.*

$$\text{Expansion Ratio} = \frac{\text{Volume of Foam Produced}}{\text{Volume of Foam Solution Used}} \tag{2.24}$$

Foams can be mainly classified as either dry or wet according to liquid content as illustrated in Figure 2.7, which may be represented by liquid volume fraction ϕ [54]. The expansion ratio is related to the volume fraction by ϕ^{-1}. The gas volume fraction is represented by the equation 2.25, while the liquid volume fraction is represented by equation 2.26:

$$\phi_{\text{gas}} = \frac{\text{vol}_{\text{gas}}}{\text{vol}_{\text{foam}}} \tag{2.25}$$

$$\phi_{\text{liquid}} = \frac{\text{vol.liquid}}{\text{vol.foam}} = 1 - \phi_{\text{gas}} \tag{2.26}$$

Engineers define the $1 - \phi_{\text{gas}}$ as the foam quality. When $\phi_{\text{gas}} \sim 0.65$ then the foam is characterised as wet whereas when $\phi_{\text{gas}} \sim 0.99$ the foam is characterised as dry [3]. The critical value of ϕ_{gas} where bubbles begin to deform is around 0.72.

Table 2.1 lists the foam types that can be made by altering the amount of air and/or foam concentrate to produce the final foam.

Type of Foam	**Appearance**	**Bubble Size**	**Texture**	**Drain Times**
Foam Solution	Clear to milky fluid	Lacks bubble structure	Mostly water	-
Wet Foam	Watery	Large to small bubbles	Lacks body	Fast
Fluid Foam	Similar to watery shaving cream	Medium to small bubbles	Flows easily	Moderate
Dry foam	Like a shaving cream	Medium to small bubbles	Mostly air	Slow

Table 2.1: *Characteristics of foam solutions [10].*

All foam types may be effectively used for both active and passive suppression of fire [55]. The type of foam generated for wildfire applications depends on the intended use. More specifically, its consistency or appearance is usually referred to as being either ”wet” or ”dry” foam. These two terms have less to do with the actual water content in the foam and more to do with how they visually appear when discharged [56].

A ”wet” foam looks runny and does not hold much of its shape. This kind of foam is just the opposite of dry foam, but the greater water content may result in better fire extinguishment [39]. On the other hand, a ”dry” foam holds its shape and has a thicker-looking consistency more like a shaving cream. Dry foams are often used to build a firebreak. National Fire

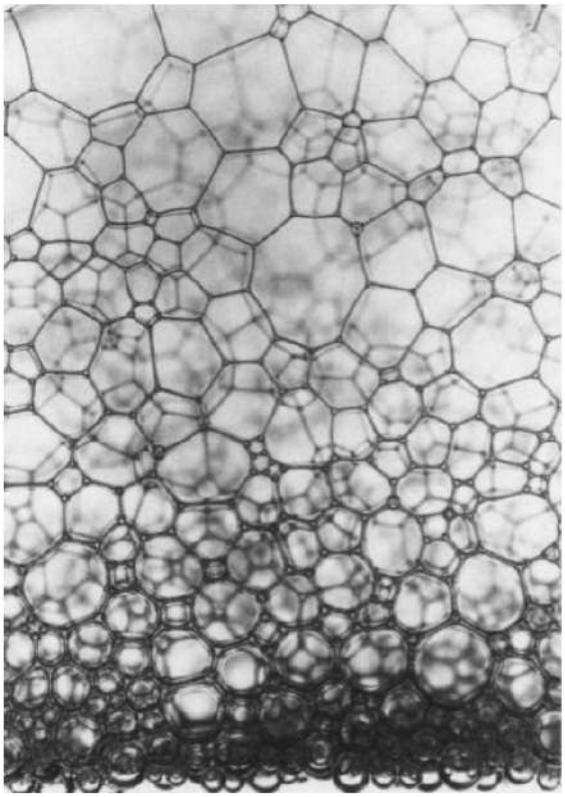

Figure 2.7: *Picture of the foam that persists 2 h after shaking an aqueous solution containing 5% sodium dodecyl sulfate. The bubble shapes are more polyhedral near the top, where the foam is dry, and more spherical near the bottom, where the foam is wet. The average bubble size is ∼2 mm. [3]*

Protection Association (NFPA 1145) [39] suggests that to tackle a fire-ground scenario, a wet type of foam should be applied to wet the material and follow up with dry foam to blanket the exposure.

2.2.5 Foams vs Plain Water

Plain water has limitations in effectively cooling and penetrating burning fuels due to its high surface tension of 72 mN/m [57]. This property causes water to form into droplets, which can roll off the surface of fuels, reducing its ability to absorb heat.

Compared to standard hydrocarbon fuels, water is heavier and when applied directly to them, will submerge and have little or no quenching or vapour suppression effect [58]. Additionally, if the fuel temperature exceeds 100 ºC, the water will boil and potentially spread the fire by expelling it out of the container [59].

However, controlling a fire can be achieved by reducing or eliminating one of the three components required by the combustion process (see Subsection 2.5.2). Water can help achieve this by reducing the available oxygen to the fire when it turns to steam and dilutes the air [60]. Nonetheless, using excessive amounts of water on fuel can create more problems, especially when fuels with lower density than water float to the top and continue to burn.

In this study [61] Class A foam was found to be faster than plain water in fire suppression and extinguishment. Direct and indirect attack was used to evaluate the effectiveness of compressed air Foam systems (CAFs), Class A foams and water. The direct attack is the most widely common technique where water is used at the base of the fire to suffocate it. On the other hand, an indirect attack on a fire involves applying suppression tactics that take place away from the burning edge of the fire [62].

Firefighting foams, unlike water, can extinguish a wildland fire by combining cooling and suffocation mechanisms (see Subsection 2.5.2) while separating the ignition source from the fire's surface. Finished foam alters the properties of water, creating a lighter extinguishing agent than flammable or combustible liquids. By forming a foam blanket, bubbles adhere better to fuels and gradually release water, thus wetting fuels for a longer period than water alone [8, 63]. Thus, foam can both affect the oxygen from the fire triangle (see Figure 2.12) as well as the heat compared to plain water where it only focuses on removing the excess heat of the burning material. This change in physical properties gives firefighters an advantage in controlling fires by creating a barrier on top of the fuel.

However, it is still the water that makes the foam perform better in extinguishing fires. Every fire has a critical application rate which means that in each scenario there is a minimum amount of water that must be applied to extinguish the fire. This applies to the foam as well. Figure 2.8 suggests that both water and foam become more effective in reducing the time for fire extinguishment as more of the product is applied.

Firefighting foams can save water [64, 65] through their ability to spread more easily over the surface of the fuels creating a barrier that cools the fire and achieves better performance

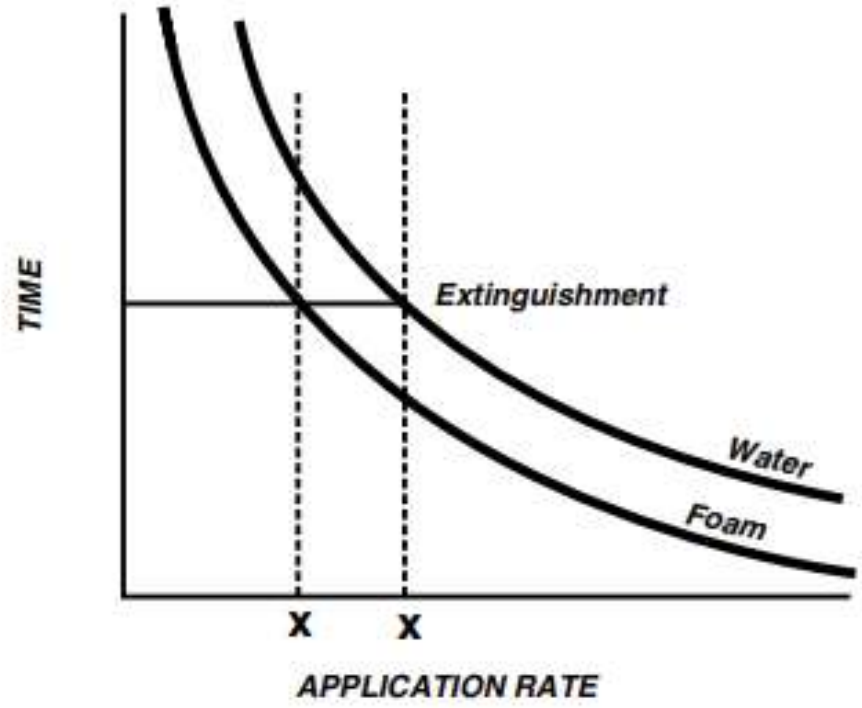

Figure 2.8: *Critical application rate. [4]*

with less water.

2.3 Foam Destabilisation Mechanisms

2.3.1 Introduction

Firefighting foams are a critical tool for suppressing fires due to their stable structure that covers the fire and prevents the vapour release of the burning material. However, the foam can be easily destabilised by certain conditions, thus decreasing its fire suppression capabilities.

The foam is destabilised by three major mechanisms [5, 66]:

- Foam drainage
- Bubble coalescence
- Bubble coarsening

The three destabilisation mechanisms are very interdependent and can accelerate one another.

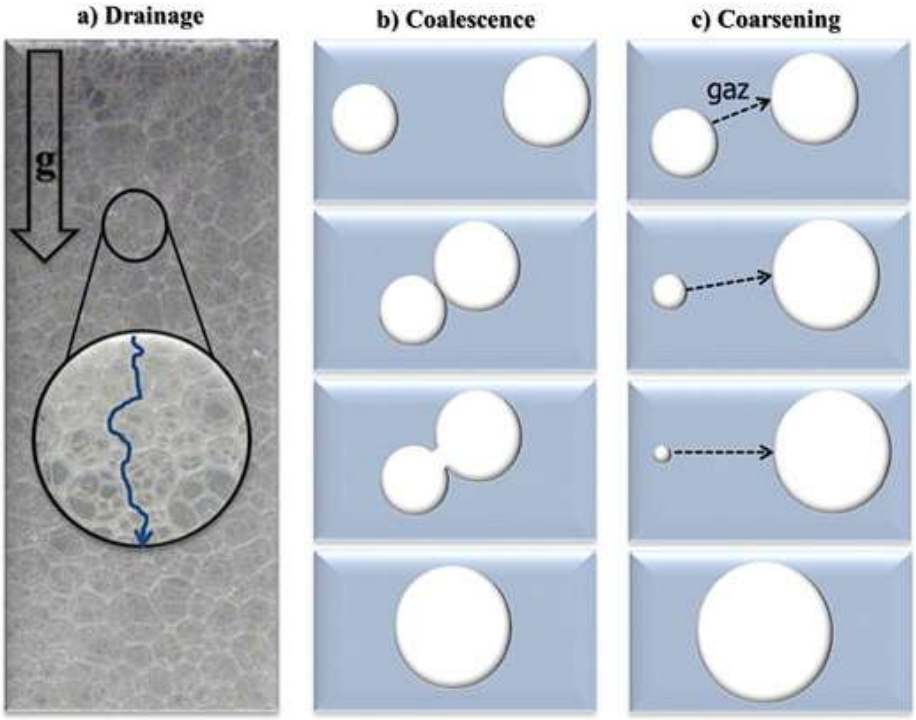

Figure 2.9: *Foam destabilisation mechanisms. (a) liquid drainage due to gravity, (b) coalescence between two bubbles and (c) coarsening of the bubbles due to Laplace pressure [5]*

2.3.2 Foam Drainage

Foams are inherently thermodynamically unstable due to their high interfacial free energy [67], resulting in liquid drainage and bubble coalescence over time (see Section 2.3). The stability of foam is commonly characterised by the time required to lose either 50% of the liquid or 50% of the volume from the foam [68].

Foam drainage is the process of gas and liquid separation by which the liquid within the foam structure drains out due to forces induced by gravity [69, 70]. Foams, (see subsection 2.2.1) consist of gas bubbles that form a white-rich blanket to cover a spill or a fire. As time passes, the foam blanket begins to degrade [71]. The drainage rate is based on how long it takes for the liquid to be drained out out of that foam blanket. During foam drainage, the foam quality decreases with time, and has an impact on foam's rheology [69, 72, 73]. However, drainage does not make all the liquid drain out of the foam [74]. This phenomenon is explained by the equilibrium state that is already obtained, implying that there is a liquid layer that is kept at the bottom of the foam. The length of that layer is represented by equation 2.27:

$$\zeta = \frac{\gamma}{\rho g D} \quad \text{(m)} \tag{2.27}$$

where ζ is the length over which the liquid fraction (see Equation 2.26) varies from 0.36 to 0.18 (ρ is the surfactant solution density and γ is the surface tension [74].

Moreover, foam drainage is closely related to the dynamics of foams [75, 76]. A short drainage time tends to indicate a more vulnerable foam as it loses its water content quickly and renders it unsuitable to high-temperature flame and hot surfaces [77]. Foams with long drainage times, are referred to as being of good quality thus suppressing fires more effectively [78]. The mechanism of the foam decay depends on the liquid volume fraction, the types of surfactant and the foam films separating the foam cells [79]. Foam drainage is the main factor that affects foam stability, as liquid flows down from the top to the bottom of the foam due to gravity, leading to a thinner and less stable foam as its films have a higher chance to break and coarsening occurs at a faster rate.

2.3.3 Bubble Coalescence

Bubble coalescence refers to the process where the films separating bubbles, progressively thin and eventually rupture as foam drainage takes place [80]. *Langevin* and his colleagues [80] observed that coalescence in foams occurs when certain critical values such as liquid fraction, bubble sizes and applied pressure are reached. However, it is challenging to differentiate those mechanisms due to their interconnected nature and constant changes over time due to drainage. The progressive thinning of the foam, results in the breaking of smaller unstable bubbles to form larger ones (see Figure2.9b) [5, 7]. The coalescence of the gas bubbles leads to foam destabilisation, as larger gas bubbles tend to be less stable than their smaller counterparts [81].

Bubble coalescence can also be induced by external factors such as evaporation or applied pressure, which aids in overcoming the disjoining pressure barrier. In the case of foams, evaporation plays a significant role as it causes film thinning and reduces the liquid content within the foam, thereby increasing capillary pressure [82]. In foams, there is a maximum capillary pressure $p_c^{\max}$ at which liquid film ruptures [83]. As this value becomes high, the film is more stable. Capillary pressure is the difference in pressures between two distinct phases, that arises from the surface or interfacial tension [84]. This is typically described by the Young-Laplace equation and is given by:

$$P = \frac{2\gamma}{R} \quad \text{(Pa)} \tag{2.28}$$

Where:

- P is the capillary pressure,
- γ is the surface tension of the liquid,
- R is the radius of curvature of the bubble interface.

Hinnant and his team [71], observed bubble coalescence in the context of foam degradation with fuels like n-heptane. The bubbles underwent sudden rupture of the lamella separating them, leading to coalescence into larger bubbles. They also noted that bubbles farther away from the interface of the foam grew larger but at a much slower rate than those close to the interface. Finally, they found that as the temperature of the fuel was raised, it led to increased coalescence by forming larger bubbles, which in turn enhanced liquid drainage in the foam.

In a recent study, *Qiu* and his co-workers [85] explored the dynamics of bubble coalescence in firefighting foams, particularly focusing on the interaction between aqueous foams and the presence of hydrocarbons. The fire extinguishing performance of foams with different interfacial states was evaluated in pool fire tests, depicting that liquid foams with mobile films spread faster over the burning fuel, whereas those with rigid films were better at suppressing fuel combustion.

Ultimately, coalescence within foams represents a detrimental process, typically occurring at a specific liquid fraction. This process is further influenced by factors such as surfactant concentration and environmental conditions.

2.3.4 Bubble Coarsening

Bubble coarsening in foams, often referred to as Ostwald ripening [86], happens when small gas bubbles merge into larger ones, which are less stable due to thinner film [81]. Coarsening can lead to an increase in the average bubble size over time (see Figure 2.9c)). This phenomenon occurs because smaller bubbles have higher internal pressure due to their curvature (Young-Laplace equation), thus leading to a higher stability of the gas inside the bubbles. As a result, gas diffuses from smaller to larger bubbles through the liquid film.

The type and concentration of surfactants used to generate the foam as well as the temperature, and the presence of various additives can significantly affect bubble coarsening. Surfactants are used to slow down this process by reducing the surface tension and thus the pressure in the bubbles.

Ping et al. [87] focused on the effect of temperature on the stability and film thinning behaviour of class B foams (aqueous film-forming foam) (AFFF). Their study shows that as temperature increases, there is a significant difference in foam morphology over time. More specifically, there is a transition from a three-dimensional elliptical shape to a two-dimensional polygonal structure, which occurs faster at higher temperatures. This indicates that bubble coarsening is accelerated at higher temperatures, thus reducing foam lifetime.

At lower temperatures, coarsening is driven by Laplace pressure [88]. However, at higher temperatures, coarsening is not only driven by the Laplace pressure but also by bubble film breaking under high temperatures [88].

2.4 Foam Stability

2.4.1 Introduction

Foam stability refers to the ability of a firefighting foam to maintain its structure and remain effective over an extended period. In other words, the foam bubbles can maintain their integrity and properties over a specific amount of time. For a firefighting foam to be effective, it must maintain its initial structure long enough to create a barrier between the burning fuel and the air, thus smothering the fire and preventing it from re-ignition. Foam stability is often tested in the laboratory under controlled conditions, where the foam's resistance to breaking down, shrinking, or dissolving over time is measured.

2.4.2 Foam Film Stabilisation

Surfactants are essential for foam film formation and stabilisation. Based on the hydrophilic part of the molecule, surfactants can be *non-ionic, cat-ionic, anionic or zwitter-ionic* [89]. Their purpose is to lower the surface tension of the liquid, allowing bubbles to form more easily [90]. Surface tension gradients can stabilise films through the Marangoni effect. This phenomenon involves the flow of liquid from areas of low to high surface tension, which can reinforce thinning areas of foam films. Figure 2.10 shows the foam lamella where the polar head groups of the surfactant are oriented in the interior of the film, while the non-polar tails head toward the gas phase. If the area of the liquid film is expanded, the surfactant concentration will decrease in the expanded area as shown in Figure 2.10. This expansion causes a rise in local surface tension that provides resistance to further expansions thereby initiating surface contraction. As a result, this contraction prompts fluid movement towards areas where the film is thinner, counteracting film weakening. This is called the Gibbs-Marangoni effect.

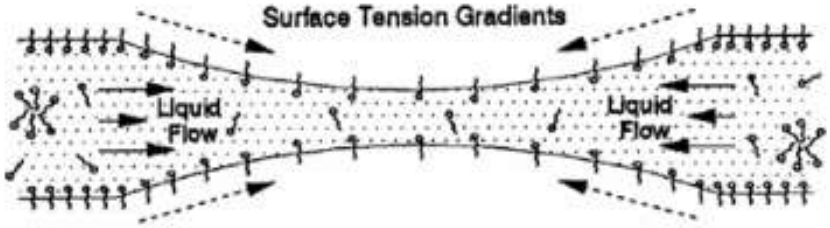

Figure 2.10: *Foam film [6]*

.

Ping et al. [87] describe the Marangoni effect as a phenomenon linked to marginal regeneration. This marginal regeneration facilitates the movement of liquid between thicker and thinner areas at the film boundaries. This movement helps to make the film thickness equal and mitigates thinning, effectively stabilising the foam film.

Yu et al. [91] linked the fire extinguishing performance to the foam film stability. Fluorinated foams, with more stable films, exhibited better fire-extinguishing capabilities and burn-back performance. The fluorocarbon surfactants reduce the surface tension of the foam system, thus slowing down liquid drainage and reducing the rate of bubble coarsening. This leads to the formation of more stable foam films. Foams that have high stability, can resist bubble coalescence and collapse, thus prolonging the foam half-life [68].

2.4.3 Bubble Size Distribution

Bubble size distribution is closely related to foam stability, as the foam has the trend to self-organise into different structures, principally to minimise the surface area [5]. Smaller and more uniform bubbles increase the foam's surface area [92, 93], thus enhancing its ability to create oxygen barriers and cool down the fire area, leading to more efficient fire suppression. However, larger or unevenly sized bubbles can reduce foam stability and effectiveness due to their inherent instability [94]. Those large-sized bubbles tend to coalesce and burst more rapidly than smaller ones, leading to a shorter lifespan of the foam structure.

Magrabi et al. [95] focused on characterising the bubble size distribution in aqueous foams generated by compressed-air foam generators (CAFs). They observed that the initial bubble size distribution in a freshly generated foam with varying liquid fractions, changes as the foam aged with time. The study found that foam with smaller bubbles exhibited enhanced foam stability due to reduced drainage.

Bisprenik et al. [96] explored the relationship between bubble size distribution and various foam characteristics. Their study revealed that smaller and more uniform bubbles contribute to increased foam stability, primarily due to reduced gas diffusion and decreased drainage.

In the study by *Yekeen et al.* [7], the influence of nanoparticles on foam stability was exten-

sively investigated at both bulk and bubble scales. They explored the effects of silicon oxide SiO_2 and aluminum oxide Al_2O_3 nanoparticles on the stability of sodium dodecyl sulfate (SDS) foams. Their findings indicated that the addition of nanoparticles at a concentration of 1 wt% significantly improved foam stability. Specifically, the presence of nanoparticles led to smaller and more numerous bubbles, indicating a reduction in bubble coarsening and coalescence. This improvement was attributed to the adsorption and aggregation of nanoparticles at the foam lamellae, which increased the film thickness and enhanced the foam's dilational viscoelasticity. In the absence of nanoparticles the bubbles were larger and fewer (see Figure 2.11), indicating a high rate of bubble coarsening and coalescence.

The enhanced foam stability was observed to be dependent on the hydrophobicity of the nanoparticles, with modified silica nanoparticles demonstrating superior performance compared to hydrophilic silica and aluminum oxide nanoparticles. This was evidenced by the increased half-life of foams and the finer, more stable bubble structures observed in the presence of nanoparticles.

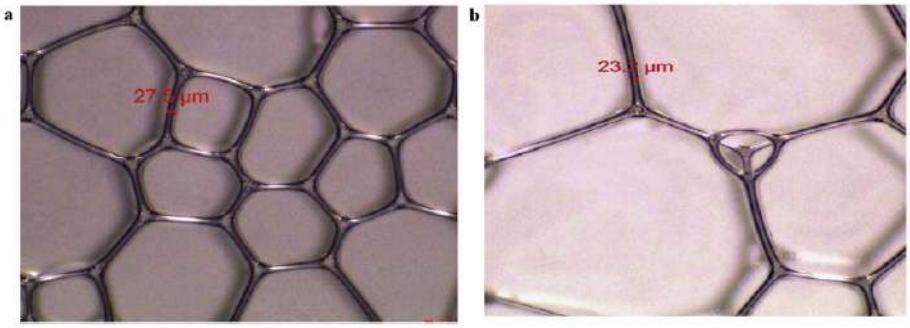

Figure 2.11: *Foam images of SDS-stabilized foam (without NPs) (a) immediately after generation and (b) 60 min after generation [7]*

.

The histograms of bubble size distribution further confirmed these observations, depicting a clear difference in bubble size and quantity in the absence of the NPs.

Politova et al. [97] found that the properties of the surfactant solutions in foams, such as viscosity and surface modulus, play a significant role in determining the bubble size distribution. Higher viscosity and surface modulus lead to smaller bubble sizes. Moreover, the shear rate during the mixing process influences both the rate of foam generation and the size of bubbles formed.

2.5 Mechanisms of Foam Action in Fire Suppression

2.5.1 Introduction

Fire suppression mechanisms refer to the various physical and chemical processes that are involved in extinguishing fires. There are several mechanisms by which foam can be used to

suppress fires, including cooling, smothering, and chemical inhibition.

2.5.2 Cooling

The cooling mechanism is a primary method of fire suppression that involves reducing the temperature of the fuel below its ignition point. By lowering the temperature of the fuel, the combustion process is slowed or stopped, and the fire is eventually extinguished.

Cooling can be achieved through a variety of methods, including the application of water, foam, or other coolants to the surface of the fire [57]. The cooling effect is achieved by absorbing the heat released by the fire, which causes the temperature of the fuel to decrease. The amount of heat required to raise the temperature of a fuel can vary depending on the fuel's specific heat capacity, which is the amount of heat required to raise the temperature of one unit of mass by one degree Celsius.

Water is one of the most commonly used coolants in firefighting, due to its high heat capacity and availability [98, 99]. When water is applied to a fire, it absorbs the heat released by the fire, which causes it to evaporate into steam. This process removes heat from the fuel and cools it, which can slow or stop the combustion process. In addition to its cooling effect, water can also help to dilute the fuel and reduce its concentration, which can make it less flammable [100].

Firefighting foam can also be used to cool fires. As mentioned in Section 2.2, foam is a mixture of air, water, and a foaming agent, and is often used in combination with water to enhance its cooling and extinguishing properties [101]. When foam is applied to a fire, it creates a stable layer of bubbles that cover the surface of the fuel [36, 102]. These bubbles help to insulate the fuel from the heat of the fire, while also absorbing and dissipating heat. The foam also provides a barrier between the fuel and the oxygen needed for combustion, which can prevent the fire from spreading.

This ultimately leads to the cessation of the fire as shown in Figure 2.12.

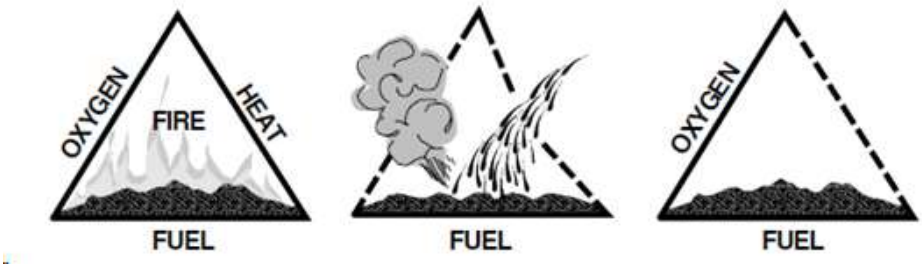

Figure 2.12: *Foam's action on the fire triangle. [8]*

2.5.3 Smothering

Smothering is another commonly used mechanism for suppressing fires. It involves the use of a physical barrier to separate the fuel from the oxygen needed for combustion [75, 102]. Firefighting foams are often used to create a thick layer of bubbles that can smother the fire and prevent it from spreading. The foam can also provide a cooling effect by absorbing heat from the fire. Another example of smothering is the use of dry chemical powders, which can extinguish the fire by forming a layer of fine particles that separates the fuel from the oxygen [103].

The effectiveness of the smothering mechanism depends on several factors, including the type and concentration of the smothering agent, the size and intensity of the fire, and the duration of the smothering application [104, 105, 106, 107]. In general, the more complete the separation of fuel from oxygen, the greater the smothering effect, and the more effective the fire suppression will be.

2.5.4 Chemical Inhibition

The chemical inhibition mechanism is a method of fire suppression that involves the use of chemicals to interrupt or prevent the combustion process. This mechanism works by disrupting one or more of the three elements required for fire which are heat, fuel, and oxygen.

One commonly used chemical inhibition agent is dry chemical powder [20]. Dry chemical powders work by interrupting the chemical chain reaction that occurs during combustion. They do this by creating a barrier between the fuel and the oxygen, which can prevent the combustion process from continuing. Dry chemical powders can be effective on a variety of fuels, including flammable liquids, gases, and solids.

Another chemical inhibition agent is halon, which is a gaseous fire suppressant that works by disrupting the chemical reaction that occurs during combustion [108]. Halon extinguishes fires by interfering with the free radicals that are involved in the combustion process. Halon is effective on a wide range of fires, including Class A, B, and C fires.

Foam can also act as a chemical inhibition agent by adding a film-forming agent, such as a fluorinated surfactant [63, 91], to the foam solution. The film-forming agent forms a protective layer on the surface of the fuel, which can prevent the fuel from vaporizing and releasing flammable gases [109, 110]. This can help to reduce the fuel's concentration and prevent the fire from spreading. However, it has been observed that fluorinated (or polyfluorinated) surfactants exhibit detrimental environmental effects due to their persistence, potential for bio-accumulation, and toxicity [46, 111].

2.6 Mechanisms of NPs in Fire Suppression

2.6.1 Introduction

Nanoparticles (NPs) are materials with overall dimensions in the nanoscale, under 100 nm. Incorporating NPs into foams, clothes, and many other materials, can transform them to become more resistant to fires, thus creating a safer environment. Several different mechanisms by which NPs affect fire suppression or fire containment have been highlighted by researchers in the field.

2.6.2 Heat Absorption

The physical mechanism involves heat absorption during the thermal decomposition of the material, thus reducing the flame temperature [112]. Upon exposure to fire, high heat absorption can occur that reduces the temperature in the outer layer of the material, providing active protection from burning [113, 114]. *Rabajczyk et al.* [113] mention in their study that nanotechnology-based solutions, particularly the use of inorganic NPs like silica and metal oxides, are increasingly being incorporated into firefighting tools and extinguishing agents to enhance their efficiency. These innovations can lead to faster fire extinguishing, greater efficiency and lower heat transmission. However, this depends on the selection of NPs and their effect on the firefighting foams as well as their impact on the environment and human health.

NPs have a high surface area-to-volume ratio, which allows them to better interact with the flame [112]. This increased surface area, allows more material to interact with surrounding substances and react at much faster rates because additional surfaces are available to react [115, 116, 117, 118]. The surface-to-volume ratio is an essential aspect of reactivity, which is defined as the rate at which a chemical reaction will proceed. When incorporated as additives to a material they can absorb heat from the flame and reduce its overall temperature. Latent heat is defined as the amount of heat that a substance absorbs or releases during a phase change under constant temperature and pressure conditions [119]. *Han et al* [119] claim that the addition of nano-additives can alter the original latent heat of the phase change material, probably because nano-additives take up space in the new composite solution. Consequently, the heat required for the material to change its state depends on the combined properties of the solution and the nano-additives. This change in composition alters how the material absorbs heat during phase transition.

Jebasingh and *Arasu* [120], observed that the latent heat in phase change materials with added NPs (NPs) changes depending on how much concentration of NPs is used. They mainly found that two key factors play an important role in this process. Firstly, the way that NPs and the material interact at a molecular level, and secondly, the heat properties of the NPs that do not involve melting. For composites that have less than 1 % concentration of NPs, the molecular interactions are what mainly influence the latent heat. However, for composites with more than 1 % concentration of NPs, the heat properties of the NPs them-

selves have a bigger impact. Delaying the onset of combustion or reducing the burning rate can be possible through that mechanism.

This view is supported by *Zhou et al.* [121] who showed that functional NPs such as silica could significantly enhance the thermal stability of a firefighting foam due to the absorption of the external heat radiation. Insulation performance was found to be improved with higher NP concentrations, which adsorbed the liquid film between bubbles and increased the scattering of the external heat radiation. This heat absorption can cool the flame front line and surrounding areas of the fuel, making the fire less intense and slowing its propagation.

2.6.3 Free Radical Trapping

Free radicals are fundamental to the combustion process. When a material heats up, its molecules begin to vibrate from side to side. During these oscillations, some molecules may break away from the main body of the material. These detached molecules are known as free radicals. The chemical mechanism primarily focuses on scavenging flame-free radicals (FFR) such as $H\cdot\ OH\cdot\ O\cdot$, which are responsible for the branching of radical chain flame reactions [112, 122].

The fire is an exothermic oxidation reaction, characterised by a sequence of gaseous free radical reactions as described below:

$$H\cdot + O_2 \rightarrow HO\cdot + O\cdot \tag{2.29}$$

$$O\cdot + H_2 \rightarrow HO\cdot + H\cdot \tag{2.30}$$

$$HO\cdot + CO \rightarrow H\cdot + CO_2 \tag{2.31}$$

The key radicals responsible for maintaining the combustion chain reaction in the fire are the hydroxyl $(OH\cdot)$ and hydrogen $(H\cdot)$ [112].

The flammability of a given material strongly depends on the concentration of radicals [123]. Radical trapping effectively eliminates the material's ability to burn [124].

Jiang et al. [20] showed that particles at the nano-scale with high specific surface area can absorb a large number of free radicals needed for combustion to quench. More specifically, the metal iron ion could efficiently capture burning free radicals, thus interrupting the chain reaction and leading to fire extinguishing. In another study [125], the simulation results that decreased burning speed for the flame was attributed to the smaller hydrogen radical pool that iron could remove. Particles in the nanoscale can act as fire suppressants by scavenging radicals in combustion reactions [9, 126]. In the study by *Sai et al.* [127], the free radical trapping mechanism effectively reduced the peak heat release rate (PHRR) and mass loss

rate in the resultant polymeric nanocomposites. This indicates that NPs, through their interaction at a molecular level, can capture and neutralise the free radicals that are crucial in fire propagation, thereby reducing the overall flammability of the material.

However, few studies have been published on the suppression characteristics of sub-micron or nano-sized suppressants in the literature [126, 128, 129].

2.6.4 Formation of a Protective Layer

During combustion, the material is exposed to extreme heat and undergoes a process known as pyrolysis, where it decomposes into solid residue (char) and volatile gases [130]. When NPs are used as additives, they can change this char formation and improve the protective layer that acts as thermal insulation and a barrier between oxygen and fuel [131, 132].

Spencer Umfreville Pickering was a pioneering researcher who in 1907 [133], proposed that small solid particles could stabilise emulsions. The emulsions stabilised by the small particles have been termed as 'Pickering emulsions.' The solid particles can adsorb onto the surface of the liquid they are mixed with and create a rigid barrier around the droplets.

In the case of NPs, their adsorption on the interface of the liquids is irreversible [66, 68, 134, 135]. This makes the NPs difficult to detach from the interface due to high adhesion energy, thus providing solid properties to the bubble interface [136].

The energy, E, required for detaching a particle from the interface is related to both the contact angle, θ, and the interfacial tension, $\gamma_{\alpha\beta}$ [135, 136, 137]. Provided that the particle is sufficiently small, typically with a diameter less than a few micrometres, such that gravitational effects can be neglected, the adhesion energy E can be expressed as:

$$E = \pi r^2 \gamma_{\alpha\beta} (1 \pm \cos\theta)^2 \quad \text{(J)} \tag{2.32}$$

The very high adhesion energy between NPs and the gas-liquid interface hinders particles' desorption and deformation of bubbles [138, 139].

It is important to note that while NPs exhibit a significant energy barrier to detachment due to the aforementioned relationship, surfactants tend to detach more readily from the bubble surface under conditions of elevated temperature [140, 141], such as those encountered in fire suppression scenarios.

Lowden and *Hull* [142] showed that iron oxide along with other types of NPs could improve the flame retardancy of wood by forming a protective layer that induced a ceramic structure on the material. This can act as a physical barrier that limits the availability of the surrounding oxygen to the burning material. Without sufficient oxygen, the combustion process is slowed or even comes to an end. Zhao and his co-workers [68] showed that surfactant-NPs assemble at the bubble surfaces and act as a solid barrier to prevent mass transfer between

bubbles. Their research utilised coalescence time, the duration until bubbles fully merge, as a crucial metric for assessing bubble dynamics.

Zhang et al. [143] showed in their study that the fire retardancy effect of the surface layer increases as the pyrolysis process progresses because the depth of the surface layer increases as more NPs are accumulated on the surface. Another study [144] indicated that NPs form a layer that works to create an impenetrable barrier against fire and block the access of oxygen to the organic components of wood.

Furthermore, most NPs tend to aggregate once they are hydrated [145]. The NPs aggregate easily because they have a large ratio of surface area to volume (due to the small particle size); therefore, possess high surface energies and consequently create an aggregate form to minimise these surface energies [146]. This aggregation form can ultimately lead to the form of a close protective layer so that the thermal stability is increased [147, 148]. *Tang et al.* suggested that under thermal radiation, there is a dense protective layer that is provided by NPs on the surface of the alcohol-resistant foam that improves its anti-burning capability.

2.6.5 Enhanced Foam Stability

Many studies have indicated that NPs (NPs) can improve the foam stability of foam solutions [149, 150, 151, 152]. Foam stability is the most important parameter of firefighting foams, as it can directly affect the fire extinguishing efficiency. The aspect of foam stability is extensively discussed in section 2.4, which highlights the concept of foam stability and various factors influencing it. One of the main characteristics of NPs is that they improve foam stability by their adsorption and aggregation at the foam lamella to increase film thickness and dilational viscoelasticity [7]. According to a similar study [153], NPs can improve foam stability, owing to their accumulation at the foam lamella and plateau boundaries.

NPs can also improve the longevity and structural integrity of firefighting foams which correlates with foam stability [88, 147, 121] . In this way, the foam can maintain a stable and consistent barrier between the fire and the fuel source.

Enhanced foam stability is essential in firefighting since foams collapse rapidly and fail to maintain the necessary barrier to extinguish fires [47, 121]. NPs can inhibit foam drainage and prevent gas diffusion between bubbles, thus enhancing the stability of foams [66, 70, 135, 154]. *Sheng et al.* [155], studied the enhancement mechanism of NPs on the foam stability of a mixture with surfactants. They found that with increasing NP concentration, the foam stability was enhanced but the foaming properties were weakened. In conclusion, NPs can have a great influence on the properties of foams. This enhanced foam stability can be crucial for fire suppression, showing that NPs can enhance firefighting methods, making them more efficient.

2.6.6 Surface Tension Reduction

NPs can modify the surface properties of foams by reducing their surface tension [7, 70]. Generally, a lower surface tension, means that the foam can spread more effectively over surfaces, ensuring a better and more uniform coverage. This is particularly important in penetrating narrow spaces which is essential in firefighting to cover as much area as possible. The surface tension affects foam in two obvious ways, though they are the same thing [156].

- The energy needed to increase the surface area A is $\gamma \frac{\delta A}{\delta t}$ so a low γ means more foam for less energy.
- The pressure inside a foam of radius R that leads to its eventual collapse is $\frac{2\gamma}{R}$

Consequently, a foam with the lowest surface tension achieved is going to create a more enduring foam.

Both the contact angle of particles and the interfacial or surface tension are factors that influence the equation for the adhesion energy 2.32 [149, 157].

Foam stability is increased as the contact angle is decreased to 0°. The contact angle is established by the balance of the adhesive force (the liquid maintaining contact with the solid) and the cohesive force inside the liquid (both the internal cohesive force and the force of surface tension). An increase in adhesive force between the liquid and the solid or a decrease in the cohesive force (surface tension) within the liquid will result in greater wettability and a smaller contact angle [158]. However, based on this study by *Yekeen et al.* [7], NPs will adsorb more surfactant molecules at higher concentrations, thus increasing the surface tension of the foaming solution by reducing the free surfactant available in the bulk aqueous phase. Therefore, foam generation reduces with increasing NP concentration. This indicates a complex interaction between NPs, surfactants and other ingredients about their combined effect on foam properties, highlighting the need for a balanced approach in optimising the concentration of NPs to ultimately optimise the foam's performance.

2.6.7 Smoke Suppression

The smoke released during fire poses severe risks to people as well as the environment [113]. Apart from the improved visibility that smoke suppression can offer, smoke contains also a variety of unburnt, partially burnt and fully pyrolysed materials [159]. Smoke suppression can reduce the quantity of these flammable compounds which can significantly contribute to the growth of the fire [160, 161].

Zhang et al. [162] showed that foam induced with NPs not only reduced the combustion sustain time from 520 sec to 211 sec but also decreased the peak heat release rate from 117 kW/m^2 to 58 kW/m^2 and decreased the peak smoke production rate from 0.084m^2/s to 0.0049m^2/s, indicating good fire retardant properties and smoke suppression.

NPs can decompose to produce non-combustible gases and block the smoke released at high temperatures [163, 164, 165, 166]. *Fu et al.* [166] showed that bamboo wood filled with

NPs inhibited the release of combustible gas and smoke as well as isolating the oxygen from outside. Smoke suppression is not only beneficial for visibility and toxicity concerns but can have a huge impact on the fire's dynamics since smoke can carry combustible materials to new locations and ignite more fires [167].

The exact mechanism has not been yet elucidated, however, a probable explanation seems to be that carbon resulting from fuels' degradation, is deposited on the oxide that is produced by the decomposition of metal hydroxide and then, this is volatilised as carbon dioxide, releasing no smoke [168, 169, 170, 171].

2.7 NPs as Foam Additives

2.7.1 Introduction

NPs, which are known for their unique physico-chemical properties due to their nanoscale dimensions, have emerged as promising additives to improve the performance of firefighting foams. The inclusion of NPs can modify the foam structure and change their interaction with burning materials. The biggest challenge with the use of NPs is that we know very little about the effects on the health of the individuals who come across these materials or generally in the environment. However, as *Paracelsus* (1493-1541) said, 'No substance is a poison by itself. It is the dose that makes a substance a poison' [172]. Exploring the role of NPs as foam additives can broaden our understanding of fire suppression mechanisms and provide new firefighting solutions for the future.

2.7.2 Effect of NPs Size on Foam Properties

The effect of NPs size is a crucial parameter when used as an additive. Small particle size results in a high surface-area-to-volume ratio, which facilitates interactions with various types of chemical species, both aqueous and gaseous [173]. Controlled NP size and compatibility with foam are essential for improving thermal stability and flame-retardant properties. When used either alone or in combination with conventional fire retardants, NPs reduce the ignitability of wood. The high surface area and nano-size of nanomaterials make them more effective at low concentrations than other conventional compounds, providing enormous industrial and economic advantages [174]. As the particle size decreases, more particles can be adsorbed at the gas–liquid interface to make the films more stable [144, 147, 175, 176]. Generally, a lower particle size indicates that NPs may easily collect sufficient oxygen to combust [177]. This happens because the number of surface atoms/molecules increases significantly and that leads to a significant reduction of the activation energy (see Equation 2.14).

The effect of the size of silica NPs on the foaming capability and thermal stability of a foam extinguishing agent has been studied [147], showing that the addition of silica NPs reduced the foaming capability of alcohol-resistant foam but increased the thermal stability of the

foam. Silica provided a dense protective layer on the surface of the foam, improving its anti-burning capability. The smaller silica NPs were readily adsorbed at the gas-liquid interface to make the lamella thicker, increasing the viscosity of the liquid and overall foam stability. When the foam was heated, the adsorbed silica NPs readily aggregated at the surface, increasing the rigidity of the lamella and creating a more stable film with high-temperature tolerance. The silica powders with small sizes had high interfacial energy, readily adsorbing at the bubble surface to reduce interfacial energy, and thus, the surface tension of the bubbles in the foam decreased.

However, to ensure NP stability, the particle size must remain consistent. Aggregation to larger particles affects their mobility and reactivity [178]. NP stability is defined as an even distribution of particles throughout the whole volume and the ability of the particles to stay separated from each other over time. Most NPs tend to aggregate once they are hydrated [179], because of their large surface area-to-volume ratio, which creates high surface energies and leads to the formation of aggregates to minimise these energies [146]. Reactivity, defined as the rate at which a chemical reaction will proceed, is an essential aspect that is influenced by the surface-to-volume ratio. Materials with a high surface-to-volume ratio react at much faster rates because additional surfaces are available for reaction.

2.7.3 NPs interaction with Foams

NPs have been widely used in many different industries to improve materials [180]. They have been added to coatings for fire retardant applications and sunscreens to enhance their efficiency. Foams stabilised by NPs are highly dependent on the shape, size, concentration, and hydrophobicity of the particles [66]. For foam generation, the contact between gas and liquid is the first condition, and some surfactants (foaming agents) should be added to stabilise the foam. Two mechanisms of particle location can be considered: (i) particles present only inside the film but not at its surfaces and (ii) at least part of the particles firmly attached to the film surfaces, i.e., to the vapor-water interface [150, 181]. In the first case, solid particles can form a layered structure inside the thinning film, stabilizing it through the so-called oscillatory structural force. The strength of particle attachment to the liquid interface should also be considered when foam stability is evaluated. The stabilizing mechanisms identified in aqueous emulsion films are likely relevant to aqueous foam films [134]. The insertion of NPs can minimise the total surface energy and lead to foam stabilization by creating a network in the bulk aqueous phase. High surface viscosity may also form a more stable foam.

Yekeen et al. [7] investigated the mechanism of foam stability improvement with NPs by studying the bubbles' morphology, films' strength and thickness, and the rate of liquid drainage from the foam. The foam lamella of hydrophilic surfactant (SDS) in combination with NPs showed little or no sign of liquid drainage. However, appropriate concentrations and hydrophobicity of other NPs for firefighting foam stability are yet to be discovered. The accumulation of NPs can also prevent film thinning and bubble coarsening of the foam by creating an interfacial shield around them, proving that agglomeration of NPs can play a ben-

eficial role. Agglomeration may lead to a faster drainage behaviour due to the extra weight of the particles [147]. Still, it has been stated that it is an alternative way to reduce the overall surface energy and foam stability [66].

Adding NPs to foams may cause different interactions that might lead to possible toxicity. A safer design formulation to reduce the DNA damage potential is presented by *Sotiriou et al.* [182], which involves encapsulating nanostructured materials to diminish the hazards to the environment and human health. Encapsulation can enclose potentially hazardous NPs within a less hazardous material. With the encapsulation strategy, firefighting foams can be mixed with any kind of NPs, as long as there is reliability that the potentially hazardous NPs remain encapsulated during the applicable product life cycle stages where exposure may be a risk.

The hydrophobicity of silica NPs affects their ability to stabilise aqueous foams. For very hydrophilic or very hydrophobic NPs, no foam is formed, but the foamability increases for particles of intermediate hydrophobicity [183]. Particle aggregation due to the incorporation of NPs increases the viscosity of the aqueous phase, leading to slower drainage of foams and increased foam stability. Overall, NPs can improve foam stability, provided that the potential hazards are considered and addressed.

An innovative approach to the use of SiO_2 NPs in firefighting foams has been extensively described by researchers [176], demonstrating an extremely high fire prevention efficiency and complete biodegradation. The silica-based sol-gel foams illustrate almost 50 times higher extinguishing efficiency than typical plain water and 15 times better than the state-of-the-art fire extinguishing agent AFFF. This is an important factor in reducing water consumption, which is often wrongly considered an unlimited source. Extinguishing using gelated foams is also characterised by the complete absence of re-ignition of the treated surface during extended exposure to open flame compared to traditional extinguishing agents.

2.7.4 Iron Oxide NPs (IONPs) in Fire Suppression

Iron ranks fourth as one of the most abundant elements on Earth by weight and it constitutes the majority of the planet's core [184]. Hematite and magnetite are the most common sources of iron. Iron oxide nanoparticles (IONPs) are highly effective catalysts due to their small size and increased surface area. This results in an increased number of atoms located on the surface, enhancing the catalytic activity of IONPs such as hematite and maghemite [173, 185]. In addition, these NPs are biocompatible and non-toxic, making them ideal for use in a range of applications [146, 173, 186]. However, all the catalysts do not act in the same way. Most of them speed up the chemical process, while some impede it. The ones which accelerate the rate of a chemical reaction are referred to as positive catalyst. On the other hand, the catalysts that decelerate the chemical reaction rate are known as negative catalysts or inhibitors [187].

To make use of these materials on a large scale, it is crucial to develop strategies for synthesising particles of the desired size, shape, and surface, as well as to protect them from

oxidation. Iron oxide is also used as a flame retardant, as it can disrupt the free radical mechanism involved in the combustion process [21]. By reacting with highly reactive species, it forms less reactive or inert molecules, gradually weakening the chain reaction of a combustion explosion and causing it to become extinguished. IONPs can also adsorb small organic molecules during a flame, catalysing them into chars and improving the flame retardancy of materials due to their catalytic activity [128]. Wang and his co-workers [188] found that magnetite IONPs (Fe_3O_4) proved to act both as a physical barrier and a catalytic agent when added to thermoplastic polyurethane. This in turn reduced the peak heat release rate and total heat release, indicating suppressed heat release and smoke production rate. The magnetism of IONPs shows significant advantages such as a low cost of production, environmental safety, great stability, and compatibility [173, 189].

Transition metal compounds such as iron have received much attention due to their strong radical-scavenging ability in flame chain reactions [190, 191, 192, 193]. The iron species that have inhibitory effects are FeO, FeOH, and $Fe(OH)_2$ [122, 125, 190]. Although the efficiency of suppression can differ depending on the type of flame, typically higher concentrations do not demonstrate effective flame inhibition [9]. When IONPs are evenly mixed with the complex surfactant solution, they can improve the thermal insulation properties of the foam layer, which in turn affects the efficiency of extinguishing and controlling solid and liquid fires [113, 194].

In previous work by *Linteris et al.* [125], iron can have a huge impact on the reduction of hydrogen-free radicals and assist in flame extinguishment through these equations below:

$$FeOH(g) + H(g) \rightleftharpoons FeO(g) + H_2(g) \tag{2.33}$$

$$FeO(g) + H_2O(g) \rightleftharpoons Fe(OH)_2(g) \tag{2.34}$$

$$Fe(OH)_2(g) + H(g) \rightleftharpoons FeOH(g) + H_2O(g) \tag{2.35}$$

$$(\text{net: } H(g) + H(g) \longrightarrow H_2(g)) \tag{2.36}$$

The simulation results indicated that they reduced the burning velocity of premixed methane flames due to the radical inhibition mechanism (see Subsection 2.6.3).

Figure 2.13 represents a series of redox reactions involving iron (*Fe*) and its various compounds under varying conditions.

Additionally, iron can react with hydrogen to form iron(II) hydroxide $Fe(OH)_2$, which can release water (H_2O) to form iron(II) oxide (FeO). This scheme also depicts the possibility of forming iron (II) hydroxide directly from iron (III) oxide by hydrogen addition, which is

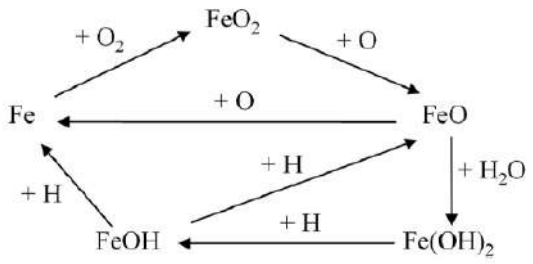

Figure 2.13: *Schematic representation of iron-catalysed radical pathways. [9]*

particularly relevant when considering the catalytic effect and the reactive roles of IONPs in fire suppression applications.

Nanomaterials are very costly to produce as compared to more traditional materials, but when greater quantities are produced, they can become more cost-effective on a per-unit basis as production scales up, hence their price decreases [173, 195].

2.8 Importance of the study

Recent years have seen an increased need to explore the challenging and practically imperative area of fire suppression. This project aimed to enhance the performance of Class A foam by introducing NPs. This was achieved by improving the stability and cooling properties of the foam so that it could have a catalytic effect in suppressing fires. The ultimate goal was to create an efficient tool for suppressing fires, which can quickly limit fire propagation, thus protecting natural habitats and biodiversity. These results provide critical information about the selection of the appropriate size and concentration of NPs for restraining fire expansion.

Chapter 3

Experimental Setup

3.1 Introduction

The experimental procedures used for the synthesis and characterisation of the nanostructures as well as the mixed firefighting foam solution will be discussed in this chapter. The first section concerns the techniques of hydrothermal and reflux synthesis that were followed to synthesise the iron oxide nanoparticles (IONPs). The second section analyses the complementary characterisation techniques used to appraise the acquired nanostructures and the aqueous foam solution prepared with them. However, after a thorough investigation, it was determined that the complexities involved in accurately simulating the foam both by itself and with nanoparticles, were numerous. Appendix A includes the strategies considered to mitigate computational challenges and a discussion on the simulation results.

3.2 Synthetic Procedures

3.2.1 Hydrothermal-Solvothermal Synthesis

The hydrothermal synthesis method involves the crystallisation of the NPs. It usually does so at a high vapour pressure level and using a high-temperature aqueous solution. The process is maintained at a constant temperature difference between the opposing ends of the crystallizing compartment [196]. The end with a higher temperature is wherever the solvent is dissolved. While on the other end, which is comparatively cooler, where the NP growth takes place. The hydrothermal method is versatile and is superior to other methods such as sol-gel, and micro-emulsion because of its advantages in terms of producing NPs of desirable size, shape, high crystallinity, and homogeneous composition.

The reagents used in this study, along with their grades and suppliers, are detailed in Table 3.1. High-purity reagents were selected to ensure the accuracy and reliability of the experimental results. Ethanol, tetraethoxysilane, ammonium hydroxide, acetone, iron(II)

sulfate heptahydrate, N,N-dimethylacetamide, iron(III) chloride hexahydrate, iron(II) chloride tetrahydrate, triethylamine, iron(III) nitrate nonahydrate, and N,N-dimethylformamide were sourced from reputable suppliers such as Fisher Chemical, Thermo Scientific Chemicals, and Alfa Aesar. The grades of these reagents ranged from analytical to extra pure, ensuring the minimisation of impurities and consistency in the experimental procedures.

Reagent	**Grade**	**Supplier**	**Quantity**
Ethanol	Absolute, Extra Pure, SLR	Fisher Chemical	2.5 L
Tetraethoxysilane	99+%	Thermo Scientific Chemicals	500 g
SiO_2	$5-15$ nm	T and Merck Life Science	50 g
Ammonium Hydroxide	25% solution in water, Extra Pure	Thermo Scientific Chemicals	2.5 L
Acetone	99+%, Extra Pure	Thermo Scientific Chemicals	2.5 L
Iron(II) Sulfate Heptahydrate	99.5%, For Analysis	Thermo Scientific Chemicals	250 g
N,N-Dimethylacetamide	99.5%, Extra Pure	Thermo Scientific Chemicals	1 L
Iron(III) Chloride Hexahydrate	97.0-102.0%, ACS	Alfa Aesar	1 kg
Ammonium Hydroxide	28% NH_3	Alfa Aesar	2500 ml
Iron(II) Chloride Tetrahydrate	98%	Alfa Aesar	1000 g
Triethylamine	99+%	Alfa Aesar	1 kg
Iron(III) Nitrate Nonahydrate	98+%, Metals Basis	Alfa Aesar	1 kg
N,N-Dimethylformamide	99%	Alfa Aesar	2500 ml

Table 3.1: *Summary of reagents used in this study including their grades, suppliers and quantities.*

- Pressure autoclave:

The chemical precursor solution was poured into a Teflon liner positioned within the pressure autoclave, as shown in Figure 3.1. The bolts on the cap of the autoclave were tightened to seal the liquid solution within the vessel. The autoclave was inserted into a temperature-controlled furnace at a reaction temperature of 135 °C and placed onto a steel grid to allow uniform heating from all sides. After the reaction time elapsed, the autoclave, once removed from the furnace, was allowed to cool down to room temperature naturally at the fume cup-

Figure 3.1: *Stainless-steel pressure autoclave and a 125 mL Teflon liner used for Hydrothermal Synthesis.*

board.

- Experimental parameters (Series 0,1,2,3):

IONPs were synthesised using the solvothermal technique. More specifically, 0.808 g $Fe(NO_3)_3 \cdot 9H_2O$ and 6 mL triethylamine were dissolved in distilled water (60 mL) to form a homogeneous solution and then the solution was stirred for 25 minutes.

Ultrasonic sonication for about 10 minutes was used as the next step to enhance the dispersibility of the sample and the homogeneity of the mixture. After that, the solution was sealed in a 120 mL Teflon-lined autoclave and the container was maintained at 170 °C for 3,8,12, 24 and 48 hours respectively. The resulting orange products were separated by centrifugation and successively washed with de-ionized water and ethanol at 4000 rpm several times, and finally dried overnight under vacuum at a temperature of 65 °C.

Tables 3.2, 3.3, 3.4, 3.5show the details of the synthesis of IONPs using the hydrothermal technique.

Sample	Precursor	Mass	Solvent	Mass/Volume	Reaction Temperature	Reaction Time
S1	$Fe(NO_3)_3$ $9H_2O$	1mmol (0.404g)	Triethylamine and Water	3mL and 10mL	170 °C	8h
S2	$Fe(NO_3)_3$ $9H_2O$	1mmol (0.404g)	Triethylamine and Water	3mL and 10mL	170 °C	12h

Table 3.2: *Experimental parameters (Series 0)*

- Experimental parameters (Series 4):

Sample	Precursor	Mass	Solvent	Mass/Volume	Reaction Temperature	Reaction Time
S3	$Fe(NO_3)_3\ 9H_2O$	2mmol(0.808g)	Triethylamine and Water	6mL and 20mL	170 °C	3h
S4	$Fe(NO_3)_3\ 9H_2O$	2mmol(0.808g)	Triethylamine and Water	6mL and 20mL	170 °C	6h
S5	$Fe(NO_3)_3\ 9H_2O$	2mmol(0.808g)	Triethylamine and Water	6mL and 20mL	170 °C	8h
S6	$Fe(NO_3)_3\ 9H_2O$	2mmol(0.808g)	Triethylamine and Water	6mL and 20mL	170 °C	12h
S7	$Fe(NO_3)_3\ 9H_2O$	2mmol(0.808g)	Triethylamine and Water	6mL and 20mL	170 °C	16h
S8	$Fe(NO_3)_3\ 9H_2O$	2mmol(0.808g)	Triethylamine and Water	6mL and 20mL	170 °C	18h
S9	$Fe(NO_3)_3\ 9H_2O$	2mmol(0.808g)	Triethylamine and Water	6mL and 20mL	170 °C	24h

Table 3.3: *Experimental parameters (Series 1)*

Sample	Precursor	Mass	Solvent	Mass/Volume	Reaction Temperature	Reaction Time
S10	$Fe(NO_3)_3\ 9H_2O$	3mmol(1.212g)	Triethylamine and Water	6mL and 60mL	170 °C	3h
S11	$Fe(NO_3)_3\ 9H_2O$	3mmol(1.212g)	Triethylamine and Water	6mL and 60mL	170 °C	6h
S12	$Fe(NO_3)_3\ 9H_2O$	3mmol(1.212g)	Triethylamine and Water	6mL and 60mL	170 °C	8h
S13	$Fe(NO_3)_3\ 9H_2O$	3mmol(1.212g)	Triethylamine and Water	6mL and 60mL	170 °C	12h
S14	$Fe(NO_3)_3\ 9H_2O$	3mmol(1.212g)	Triethylamine and Water	6mL and 60mL	170 °C	16h
S15	$Fe(NO_3)_3\ 9H_2O$	3mmol(1.212g)	Triethylamine and Water	6mL and 60mL	170 °C	18h
S16	$Fe(NO_3)_3\ 9H_2O$	3mmol(1.212g)	Triethylamine and Water	6mL and 60mL	170 °C	24h
S17	$Fe(NO_3)_3\ 9H_2O$	4mmol(1.616g)	Triethylamine and Water	12mL and 40mL	170 °C	12h

Table 3.4: *Experimental parameters (Series 2)*

Sample	Precursor	Mass	Solvent	Mass/Volume	Reaction Temperature	Reaction Time
S18	$Fe(NO_3)_3\ 9H_2O$	3mmol(1.212g)	Triethylamine and DMF	6mL and 60mL	170 °C	6h
S19	$Fe(NO_3)_3\ 9H_2O$	3mmol(1.212g)	Triethylamine and DMF	6mL and 60mL	170 °C	8h
S20	$Fe(NO_3)_3\ 9H_2O$	3mmol(1.212g)	Triethylamine and DMF	6mL and 60mL	170 °C	3h
S21	$Fe(NO_3)_3\ 9H_2O$	3mmol(1.212g)	Triethylamine and DMF	6mL and 60mL	170 °C	12h
S22	$Fe(NO_3)_3\ 9H_2O$	3mmol(1.212g)	Triethylamine and DMF	6mL and 60mL	170 °C	16h
S23	$Fe(NO_3)_3\ 9H_2O$	3mmol(1.212g)	Triethylamine and DMF	6mL and 60mL	170 °C	18h
S24	$Fe(NO_3)_3\ 9H_2O$	3mmol(1.212g)	Triethylamine and DMF	6mL and 60mL	170 °C	24h
S25	$Fe(NO_3)_3\ 9H_2O$	3mmol(1.212g)	Triethylamine and DMF	6mL and 60mL	170 °C	48h

Table 3.5: *Experimental parameters (Series 3)*

IONPs were synthesised via a one-step solvothermal process. An amount of 3.796 g ($FeCl_2$ $4H_2O$), and four different variations (5, 10, 20, and 30 mL) of ammonium hydroxide (NH_4OH) and water H_2O (55, 50, 40 and 30 mL) were used for the synthesis. Initially, the $FeCl_2$ $4H_2O$ was dispersed into ultra-pure water to form a homogeneous solution, and then ammonium hydroxide solution was added followed by stirring for 30 minutes and subsequent mixing via ultrasonication. The obtained solution was transferred to a 120 mL Teflon-lined autoclave and sealed. The autoclave was placed in a preheated oven at 135 °C and kept under these conditions for 3h. The resulting black precipitate had magnetic properties and was separated from the solvent by centrifugation and successively washed with 3D water at 4200 rpm at least 3 times, and finally dried overnight under vacuum at 65 °C.

Sample	Precursor	Mass	Solvent	Mass/Volume	Reaction Temperature	Reaction Time
S26	$FeCl_2$ $4H_2O$	21mmol(4.3g)	Ammonium Hydroxide and water	20 mL and 40mL	135 °C	3h
S27	$FeCl_2$ $4H_2O$	21mmol(4.3g)	Ammonium Hydroxide and water	10 mL and 50mL	135 °C	3h
S28	$FeCl_2$ $4H_2O$	21mmol(4.3g)	Ammonium Hydroxide and water	5 mL and 55mL	135 °C	3h
S29	$FeCl_2$ $4H_2O$	21mmol(4.3g)	Ammonium Hydroxide and water	30 mL and 30mL	135 °C	3h

Table 3.6: *Experimental parameters (Series 4)*

Table 3.6 shows the details for the synthesis of IONPs (Series 4) using the hydrothermal technique.

- Experimental parameters (Series 5):

IONPs (series 3) were synthesised via a one-step solvothermal process. An amount of 2.65 g ($FeCl_3$ $6H_2O$) and 0.824g $C_6H_4(CO_2H)_2$ (Terephthalic acid) was mixed either with DMF or DMF and ethanol, in two separate beakers for 30 minutes.

Initially, the $FeCl_3$ $6H_2O$ was dispersed into DMF to form a homogeneous solution which was followed by stirring for 30 minutes and subsequent mixing via ultrasonication. The obtained solution was transferred to a 120 mL Teflon-lined autoclave and sealed. The autoclave was placed in a preheated oven at 135 °C and kept under these conditions for 3h. The resulting black precipitate was separated from the solvent by centrifugation and successively washed with 3D water at 4200 rpm at least 3 times, and finally dried overnight under vacuum at 65 °C.

Sample	Precursor 1	Precursor 2	Mass	Solvent	Mass/Volume	Reaction Temperature	Reaction Time
S30	$C_6H_4(CO_2H)_2$	$FeCl_3$ $6H_2O$	4.95mmol(0.824g) + 9.8mmol(2.65 g)	DMF	60 mL	110 °C	20h
S31	$C_6H_4(CO_2H)_2$	$FeCl_3$ $6H_2O$	4.95mmol(0.824g) + 9.8mmol(2.65 g)	DMF + Ethanol	30 mL and 50 mL	110 °C	20h
S32	$C_6H_4(CO_2H)_2$	$FeCl_3$ $6H_2O$	7.4mmol(1.228g) + 7.4mmol(2g)	DMF	60 mL	110 °C	20h
S33	$C_6H_4(CO_2H)_2$	$FeCl_3$ $6H_2O$	7.4mmol(1.228g) + 7.4mmol(2g)	DMF + Ethanol	30 mL and 50 mL	110 °C	20h

Table 3.7: *Experimental parameters (Series 5)*

Table 3.7 shows the details of the synthesis of IONPs (Series 5) using the hydrothermal technique. During the synthesis of IONPs via a solvothermal process, several safety considerations were taken into account. The use of a Teflon-lined autoclave was handled with care as it can rupture under high pressure or temperature, causing severe injuries or damage

to the laboratory equipment. Therefore, suitable protective clothing, such as heat-resistant gloves and face shields was used. The use of ammonium hydroxide requires careful handling as it is a caustic and toxic substance that can cause severe skin and eye irritation, as well as respiratory problems. Adequate ventilation and protective clothing, including gloves and goggles were used. Moreover, the resulting NPs may pose a risk if not handled properly. Therefore, the NPs were handled in a fume hood and were disposed of properly according to the laboratory's waste management guidelines.

3.2.2 Reflux Synthesis

Reflux involves heating the chemical reaction for a specific amount of time, while continuously cooling the vapour produced back into liquid form, using a condenser [197]. The vapours produced above the reaction continuously undergo condensation, returning to the flask as a condensate (see Figure 3.2). The reflux method is advantageous in terms of lower equipment cost and less labour over hydrothermal synthesis.

Figure 3.2: *Reflux Synthesis of Iron Oxide NPs (IONPs).*

Further adjustment of experimental parameters of reflux synthesis such as lower temperature and longer duration may result in the formation of nanostructures with higher specific surface area.

- Experimental parameters (Series 7):

IONPs were synthesised via a reflux procedure. An amount of 3.796 g ($FeCl_2$ $4H_2O$), and 4 different variations (5, 10, 20, and 30 mL) of ammonium hydroxide (NH_4OH) and water H_2O (55, 50, 40 and 30 mL) were used for the synthesis. Initially, the $FeCl_2$ $4H_2O$ was dispersed into ultra-pure water to form a homogeneous solution, and then ammonium hydroxide solution was added followed by stirring for 30 minutes and subsequent mixing via ultrasonication. The obtained solution was transferred to a 250 mL flask which was sealed by a condenser that contained spirals inside. The flask was placed in a heating mantle at 100 °C and kept under these conditions for 1.5h. The resulting black precipitate was separated from the solvent by centrifugation and successively washed with 3D water at 4200 rpm at least 3 times, and finally dried overnight under vacuum at 65 °C. The black powder had magnetic properties.

Sample	Precursor	Mass	Solvent	Mass/Volume	Reaction Temperature	Reaction Time
S34	$FeCl_2$ $4H_2O$	21mmol(4.3g)	Ammonium Hydroxide and water	20 mL and 40mL	100 °C	1h
S35	$FeCl_2$ $4H_2O$	21mmol(4.3g)	Ammonium Hydroxide and water	10 mL and 50mL	100 °C	1h
S36	$FeCl_2$ $4H_2O$	21mmol(4.3g)	Ammonium Hydroxide and water	5 mL and 55mL	100 °C	1h
S37	$FeCl_2$ $4H_2O$	21mmol(4.3g)	Ammonium Hydroxide and water	30 mL and 30mL	100 °C	1h

Table 3.8: *Experimental parameters (Series 6)*

Table 3.8 shows the details for the synthesis of IONPs (Series 6) using the reflux technique.

- Experimental parameters (series 7-8):

Synthesised IONPs of Fe_3O_4, with a mass of 200 mg, were ultra-sonicated in 300 mL of ethanol at room temperature for 45 minutes to ensure homogeneity. This was followed by the drop-wise addition of 6 mL of ammonium hydroxide, and subsequently, 94 mL of deionised water, both introducing them gradually. After these additions, 1.2 mL of tetra-ethyl orthosilicate (TEOS) was also added drop-wise. The mixture was then stirred continuously for 8 hours at room temperature. When the time elapsed, the NP powder still had magnetic properties coming from the IONPs (series 3.6), and was isolated using a fishing magnet with a metal base, avoiding the typical centrifugation process for separation to save time. That was named as Fe_3O_4/SiO_2 T1 (Technique 1).

For the Fe_3O_4/SiO_2 T2 (Technique 2) initially 225 mg of Fe_3O_4 NPs were dispersed into 80 mL of water via ultra-sonication for 45 minutes to achieve a uniform suspension of the NPs. Following this, 10 mL of ammonium hydroxide was added into the solution drop-wise with a burette. Subsequently, 390 mL of ethanol was added slowly and drop-wise. The final step involved the cautious and gradual addition of 4 mL of tetra-ethyl orthosilicate (TEOS) into the stirring mixture, also performed drop-wise. Ultimately, the new NP powder possessed magnetic properties and was isolated using a fishing magnet with a metal base, avoiding the typical centrifugation process for separation to save time.

Table 3.9 shows the details for the synthesis of IONPs (Series 8-9).

The magnetic properties of Series 3.6, 3.8, can be utilised to improve the precision and effectiveness of firefighting foam by enabling targeted delivery through a drone system [198].

Sample	Precursor 1	Precursor 2	Mass	Solvent	Mass/Volume	Reaction Temperature	Reaction Time
S38	Synthesised Fe_3O_4	Tetraethoxysilane	200 mg	Ammonium hydroxide-Water-Ethanol	6-94-300 mL	25 °C	8h
S39	Synthesised Fe_3O_4	Tetraethoxysilane	225 mg	Ammonium hydroxide-Water-Ethanol	10-80-390 mL	25 °C	8h

Table 3.9: *Experimental parameters (Series 7-8)*

By utilising a magnetic field, the foam containing IONPs as additives can be directed precisely to the desired area, thereby minimising the quantity of foam required and enhancing accuracy.

The use of drones equipped with magnetic field generators to fly over areas affected by surface fires, loaded with a firefighting foam solution mixed with nanoparticles, facilitates targeted delivery. This approach addresses significant challenges, including access to remote locations and the rapid spread of fires.

3.3 Materials Characterisation

3.3.1 NPs Characterisation

X-Ray Diffraction (XRD)

Basic Principles X-ray diffraction (XRD) is a powerful tool for analysing the crystal structure of materials. The technique works by exposing a sample to X-rays and measuring the diffraction pattern of the resulting scattered X-rays. The diffraction pattern provides information about the arrangement of atoms in the sample and can be used to determine the crystal structure and phase composition of the material.

Moreover, it is a non-destructive technique and can be used to analyse a wide range of materials, including powders, thin films, and bulk samples. XRD can be used to determine crystal structure, lattice parameters, phase composition, and crystallite size of the material. XRD is also useful for identifying unknown phases and detecting impurities.

X-ray diffraction occurs when the following equation, also known as Bragg's law is fulfilled:

$$n\lambda = 2d\sin\theta \tag{3.1}$$

In this equation, n stands for the order of diffraction, λ is the wavelength of the incident wave, d represents the distance between the lattice planes, and θ is the angle of incidence that satisfies the condition for diffraction.

XRD analysis involves preparing a sample for analysis, mounting the sample on the XRD instrument, and collecting the diffraction pattern. The data is then processed and analysed using specialised software to obtain information about the crystal structure and composition of the material. Crystalline phase features were identified using X-pert High-Score plus computer software.

The crystalline size, τ, is calculated using the Debye-Scherrer formula Equation 3.2:

$$\tau = \frac{K\lambda}{\beta \cos\theta} \tag{3.2}$$

where:

- τ is the mean size of the ordered (crystalline) domains;
- K is a dimensionless shape factor, with a value close to unity. The shape factor has a typical value of about (0.89¡K¡1), but varies with the actual shape of the crystallite;
- λ is the X-ray wavelength;
- β is the line broadening at half the maximum intensity (FWHM), after subtracting the instrumental line broadening, in radians. This quantity is also sometimes denoted as $\Delta(2\theta)$;
- θ is the Bragg angle.

Scanning Electron Microscopy (SEM)

Basic Principles:

Scanning Electron Microscopy (SEM) is a powerful imaging technique used to visualise the morphology and topography of materials at high magnification. SEM works by focusing a beam of electrons onto the surface of the sample [199], which then interacts with the atoms and produces a range of signals, including secondary electrons and back-scattered electrons. These signals are then detected and used to create an image of the sample surface. SEM can provide high-resolution images with magnifications ranging from 10 to 300,000 times, depending on the instrument and the sample. SEM can also provide information about the elemental composition and distribution of a sample using energy-dispersive X-ray spectroscopy (EDS). In EDS, X-rays are generated when the electron beam interacts with the sample, and the energy and intensity of these X-rays are measured to identify the elements present in the sample [200]. The size distribution can be derived by capturing high-resolution SEM images of the samples, followed by image processing and analysis using specialised software. The software measures the dimensions of individual nanoparticles visible in the SEM images, and these measurements can be used to calculate the size distribution. SEM is widely used in various fields such as materials science, nanotechnology, biology, and geology for the analysis and characterisation of samples. SEM was used to determine the size and the surface morphology of the NPs. The Scanning Electron Microscopy (SEM) micro-graphs were recorded with a ZEISS Gemini SEM 360 microscope.

Fourier Transform Infrared Spectroscopy (FTIR)

Basic Principles:

Fourier Transform infrared spectroscopy (FT-IR) is a powerful analytical technique that provides detailed information about the molecular structure of a sample. This technique uses infrared light to scan the sample and observe bond properties. FT-IR operates in the infrared region of the electromagnetic spectrum, measuring how much light is absorbed by the bonds of vibrating molecules to provide a unique molecular fingerprint. The FT-IR Spectrometer generates an absorbance spectrum in the form of a graph that shows the unique chemical bonds and the molecular structure of the sample material. This absorption spectrum will have peaks representing components present, which indicate functional groups (e.g., alkanes, ketones, acid chlorides). Different types of bonds and functional groups absorb infrared radiation of different wavelengths. The FT-IR spectra were recorded using a Thermo Scientific Nicolet 50 FT-IR spectrometer.

Thermogravimetric Analysis (TGA)

Basic Principles:

Thermogravimetric Analysis (TGA) is a powerful analytical technique used to investigate the thermal stability and decomposition behaviour of materials. In this study, TGA was employed to evaluate the thermal stability of the NPs. The NPs in powder form were subjected to a controlled heating rate under an inert atmosphere, and the weight loss of the sample was measured as a function of temperature. The resulting TGA curves provide information about the thermal degradation profile of the NPs, including onset temperature, rate of degradation, and final residue. The thermal degradation data can be used to assess the potential of the NPs as foam additives. The TGA experiments were performed using a commercial TGA instrument equipped with a high-precision balance and a thermocouple for accurate temperature measurements.

3.3.2 Foam Characterisation

Drop Shape Analysis (DSA)

Basic Principles:

Drop Shape Analysis (DSA) is a technique used to measure the contact angle of a liquid droplet on a solid surface. It is based on the Young-Laplace equation 2.28, which describes the balance of forces at the three-phase contact line between the droplet, the solid surface, and the surrounding atmosphere. DSA can provide information about the wettability and surface tension of the liquid as well as the surface energy of the solid surface. In DSA, a droplet of known volume is placed on the surface of interest and an image of the droplet is taken. The contact angle is then calculated from the shape of the droplet at the three-phase contact line using software analysis. DSA is a non-destructive and non-invasive method that can be used to study a wide range of surfaces and liquids. It is commonly used in materials science, surface chemistry, and biophysics to understand the behaviour of liquids on surfaces.

$$\begin{aligned} \Delta p &= -\gamma \nabla \cdot \hat{n} \\ &= -2\gamma H_f \\ &= -\gamma \left(\frac{1}{R_1} + \frac{1}{R_2} \right) \end{aligned} \tag{3.3}$$

where Δp is the Laplace pressure, the pressure difference across the fluid interface (the exterior pressure minus the interior pressure), γ is the surface tension (or wall tension), $\hat{n}$ is the unit normal pointing out of the surface, H_f is the mean curvature, and R_1 and R_2 are the principal radii of curvature.

Dynamic Light Scattering (DLS)

Dynamic Light Scattering (DLS) is a powerful technique for studying the particle distribution in a suspension and understanding the behaviour of materials containing NPs. In DLS, a laser beam is directed at the sample, and the scattered light is detected at a specific angle. The intensity of the scattered light fluctuates over time due to the Brownian motion of the particles [201]. These fluctuations are analysed using an autocorrelation function to determine the diffusion coefficient, which is then used to calculate the hydrodynamic diameter of the particles through the Stokes-Einstein equation 3.4:

$$D = \frac{kT}{6\pi\eta R_H} \tag{3.4}$$

where k is the Boltzmann constant, T is the temperature in Kelvin, η is the viscosity of the dispersing medium, and R_H is the hydrodynamic radius of the particle. This equation is valid for spherical particles that do not interact among themselves [202].

DLS and SEM provide a comprehensive understanding of nanoparticles size and distribution. SEM offers detailed morphological images of nanoparticles, showing their shape and surface structure. In contrast, DLS provides statistical data on the size distribution of particles in suspension, giving a broader view of particle size and behaviour in solution [203]. Moreover, by combining DLS with zeta potential measurements, the tendency of nanoparticles to agglomerate can be studied over time [204]. Agglomeration of nanostructures results in less surface energy and a more stable system, following thermodynamics [205]. This information is crucial in supporting the research and development of new and enhanced products before they are commercially available.

The samples were prepared by dispersing the nanoparticles in a suitable solvent such as water and foam concentrate, and measurements were conducted to assess their size distribution and stability. This information was critical for understanding the behaviour of the nanoparticles and ensuring the reliability of the experimental results.

Surface Tension

Surface tension is a fundamental physical property that plays a significant role in determining the behaviour of fluids and their interactions with other materials. It is defined as the force per unit length acting perpendicular to an imaginary line drawn on the surface of a liquid, and it arises due to the attractive forces between molecules at the liquid-gas interface. Surface tension affects many aspects of fluid behaviour, such as wetting, spreading, and adhesion. According to thermodynamics, any material or system is stable only in a state with the lowest Gibbs free energy [206]. Thus, reducing surface tension can lower the energy of the foam system and stabilise the foam.

In foam systems, surface tension determines the ability of the liquid to form stable bubbles and influences the bubble size, distribution, and stability. Therefore, measuring and understanding the surface tension of the liquid used in foam generation is crucial for designing effective foam solutions. Various methods are available for measuring surface tension, including the pendant drop technique, the Wilhelmy plate method, and the capillary rise method.

Low surface tension is a crucial factor in firefighting, as it lowers the net force of attraction among molecules, making the foam mixture break down the triangle of a wildfire [207].

A low surface tension γ means more foam for less energy [208]. So, a foam with the lowest surface tension achieved is going to give an easier, long-lasting foam. Finally, lower surface tension allows water to go deeper into the centre of the flame in the burnt materials [209]. Surface tension can be defined as in equation 3.5:

$$\gamma = \frac{F}{2L} \quad \left(\mathrm{N\,m^{-1}}\right) \tag{3.5}$$

where F is the force necessary to increase the surface area per unit length L. In this study, the pendant drop method is used to analyse the surface tension of the foam solution and understand its wettability characteristics along with iron oxide NPs.

The pendant drop technique is preferred for measuring surface tension because it provides a highly accurate and precise measurement of the surface tension of a liquid [210]. This technique allows for the measurement of small changes in the shape of a hanging droplet under the influence of gravity, which in turn provides information about the surface tension of the liquid. Additionally, the pendant drop technique can be used to measure the surface tension of both pure liquids and liquid mixtures, making it a versatile and widely used method in the field of surface science.

Zeta potential

Zeta potential is a useful tool for measuring the degree of aggregation of NPs in a liquid [211, 212, 213]. In the context of foam generation, understanding the extent of NP aggregation in the surface or interior of the foam can be critical to optimizing its fire-extinguishing

properties. The zeta potential of a sample is commonly used as an indicator of its dispersion stability, with larger magnitudes indicating a more electrostatically stable suspension. High absolute values of zeta potential suggest a higher net electric charge on the surface of the particles, leading to greater electrostatic repulsion between them [214]. By indicating the degree of electrostatic repulsion between adjacent, similarly charged particles in a dispersion, the magnitude of the zeta potential can determine the stability of the solution or dispersion and its resistance to aggregation [214, 215].

Bubble Surface Morphology

Bubble surface morphology is an important aspect in the study of foams and bubbles [7, 77, 147, 154]. It refers to the surface features of bubbles, which are a result of the interactions between the surface active agents and the gas-liquid interface. These surface features include the size and shape of the bubbles. The morphology of the bubble surface is influenced by various factors, such as the concentration and type of surfactant, the pH of the solution, the temperature, and the gas flow rate [216]. The study of bubble surface morphology is crucial in understanding the foam stability [217] and the ability of the foam to perform in a more efficient way, such as in the case of fire extinguishing foams.

3.4 Foam Formulation

3.4.1 Preparation of Class A foams

To prepare the Class A foam, a 100 mL mixture of conventional foam concentrate, (0.6 % v/v foam solution as standard in aerial firefighting applications) was prepared for each foam. The foam concentrate used was Forexpan, a commercial concentrate specifically designed for Class A fires and was purchased from Angus Fire UK [218]. The remaining volume was made up of triple distilled water, with various concentrations of IONPs at 0, 0.025 wt%, 0.05 wt%, and 0.1 wt%. The use of triple distilled water aimed at ensuring the highest level of purity and consistency in the experimental conditions.

In the initial phase, the foam was tested under various conditions to determine the optimal mixing parameters [148]. The foam was mixed using an overhead stirrer (see Figure 3.3) at different durations: 5, 10, and 15 minutes, and at varying rotation speeds of 750, 1000, 1250, and 1500 RPM. At the highest speed of 1500 RPM, the stirrer became unstable, causing the foam solution to spill out of the plastic container.

Based on these preliminary results, further experiments were conducted with the foam at rotation speeds of 750 RPM, adjusting the height of the agitator blade inside a Nalgene PP plastic container (250 mL, 8 oz with a 61 mm diameter). The agitator blade, with a width of 36 mm, was positioned at heights of 1 cm, 2 cm, and 3 cm from the bottom of the container.

After evaluating the outcomes of these tests under different conditions, it was decided to proceed with experiments at three rotation speeds (750, 1000, and 1250 RPM) and a single

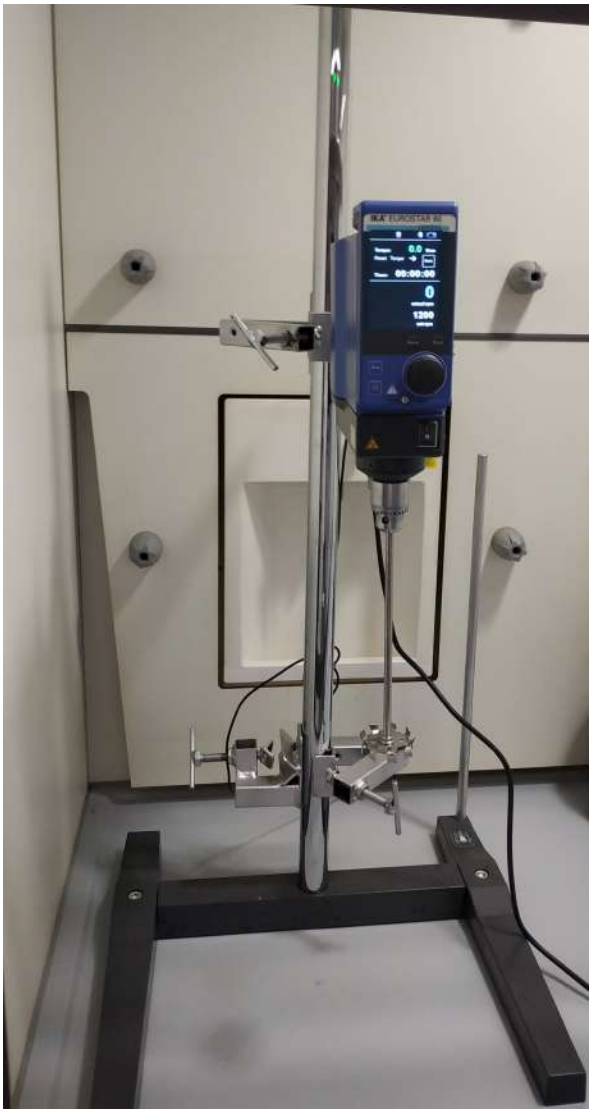

Figure 3.3: *Overhead Stirrer for mixing the NPs with the foam solution.*

agitator blade height of 2 cm from the bottom. The mixing times selected for these trials were 5, 10, and 15 minutes, applying these parameters to foam formulations with varying concentrations of NPs.

3.4.2 Foam Generation

The double syringe technique was used to generate the foam [219]. This technique is presented in Figure 3.4. It consists of 2 syringes with 60 mL volume each, connected by a small plastic tube. The gas bubbles mix with the liquid, and as they move through the mixing chamber, they create foam. For each foam generation trial, the volumes of gas (air) and liquid (foam solution) were 40 and 20 mL respectively. Foam was created by pushing the liquid and gas dispersion repeatedly over 15 times.

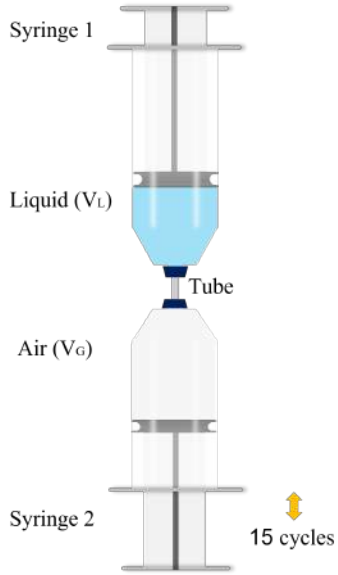

Figure 3.4: *Foam generation through the double syringe technique.*

3.4.3 NPs Integration

After testing with the plain foam solution and water to create foam, the next step involved adding NPs. However, it was essential first to identify an optimal method for dispersing the NPs in the plastic vessel, focusing on rotation speed and sonication time. It is known that when the foam solution from the manufacturer is mixed with water, the surfactants are effective only for a brief period initially, critical for creating the most effective foam.

Thus, the NPs were first dispersed in water and subjected to sonication for two different times: 15 minutes and 30 minutes [112]. It was observed that after 15 minutes of sonication, aggregates were still present in the beaker. However, after 30 minutes, the solution of water and NPs achieved complete homogeneous dispersion as shown in Figure 3.5. Following

this, the foam solution was added at a 0.6% v/v concentration at a fixed rate, with stirring continued for a few more minutes to ensure thorough mixing.

Figure 3.5: *NPs dispersion through a digital ultrasonic cleaner.*

Experiments were conducted with varying NP concentrations, commencing at 0.025% w/v, and progressing through 0.05, 0.1, 0.3, 0.5, 0.7, to 1.0% w/v, utilising both reflux and hydrothermal synthesis methods.

3.5 Setup for Fire Experiments

Fuel: Excelsior (dried shredded wood)

Excelsior (dried shredded wood) was selected to simulate surface fires (see subsection 2.1.2) as the combustion fuel due to its resemblance to loose forest debris in burn behaviour [220]. For instance, in the study on the spread of fires in sloping fuel beds, excelsior was used to model wild-land fuels, demonstrating similar flame spread and heat release characteristics to those observed in natural forest fires [221]. Class A fires involve the combustion of solid materials. These fires include a variety of substances acting as fuel, ranging from vegetation in wildfires to construction materials. Excelsior was first chosen for its ease of implementation, allowing homogeneous bed properties on a wide area. Furthermore, this fuel, composed of fine-sized elements, has a very high consumption ratio ($> 90\%$) and very few materials

remained after the fire spread [222]. Moreover, this choice ensured a controlled and reproducible assessment of the foam application on the surface and the fire suppression efficacy of the fuel. Figure 3.6 displays the excelsior fuel utilised in the fire experiments, provided by Peacock Fibres in the UK [223].

Figure 3.6: *Excelsior fuel.*

This type of fuel is commonly used in laboratory experiments because its combustion occurs easily and without residue. Excelsior was first separated and weighed on a Mettler Toledo scale [224] in two portions totalling 30 g distributed over the dedicated 20 x 60-cm surface area for the foam suppression experiments. The first portion was kept completely dry to initiate ignition with a lighter, allowing the fire to spread to the second portion. The second part, embedded with foam and its additives, was used to assess the efficiency of its new fire-extinguishing characteristics.

Each experiment uses 20 g of Excelsior for pre-wetting as shown in Figure 3.7 and 10 g of Excelsior as the ignition point, which makes a total of 30 g fuel mass.

The procedure followed was first to select the Excelsior and calculate the specific weight using an electronic scale with high accuracy. Then, the bulk density was fixed to be as uniform as possible. Excelsior fuel beds must be carefully constructed to achieve the precise fuel depth, as any variation can drastically alter the bulk density, significantly affecting the rate of spread. The compacted excelsior (fluff) was pulled apart to decrease the bulk density

Figure 3.7: *Excelsior for foam additives.*

so it would burn readily.

Fire Experiments Testing Setup

The surface of the fuel bed is covered with excelsior as shown in Figure 3.8. After igniting the fuel, the sides of the fume hood were lowered to maintain a consistent airflow over the fuel bed. Moreover, the flame front generated after ignition is homogeneous, thus lessening the flame instabilities during the burning.

The fire behaviour in all experiments was recorded with a high-quality Nikon camera, and the mass loss of the excelsior over time was live recorded through a laptop connected to the Mettler Toledo high accuracy scale.

The excelsior fuel was conditioned in a large dehydration oven at a temperature of 35 °C for a minimum of 12 hours to obtain an equilibrium moisture content of approximately 9.125% oven-dry weight, indicative of the specific moisture conditions studied in these experiments. This moisture content is representative of moderate to high wildfire conditions [225].

Foam Delivery Methods

Two methods were employed for foam delivery onto the surface of the excelsior. The first method utilised a commercial airbrush as shown in Figure 3.9, into which the foam concentrate, at a 0.6% concentration in 20 mL of liquid solution with water or water and NPs, was placed in a 20 mL cup and then sprayed over the excelsior surface. The excelsior was placed inside a tray on a high-accuracy scale to record the mass increase following wet foam deposition as shown in Figure 3.10.

In the second approach, foam was produced using a double syringe technique as shown in Figure 3.11, employing the same concentrate solution to create 60 mL of dry foam, which was then applied to the dry excelsior surface as shown in Figure 3.12. This consistent quan-

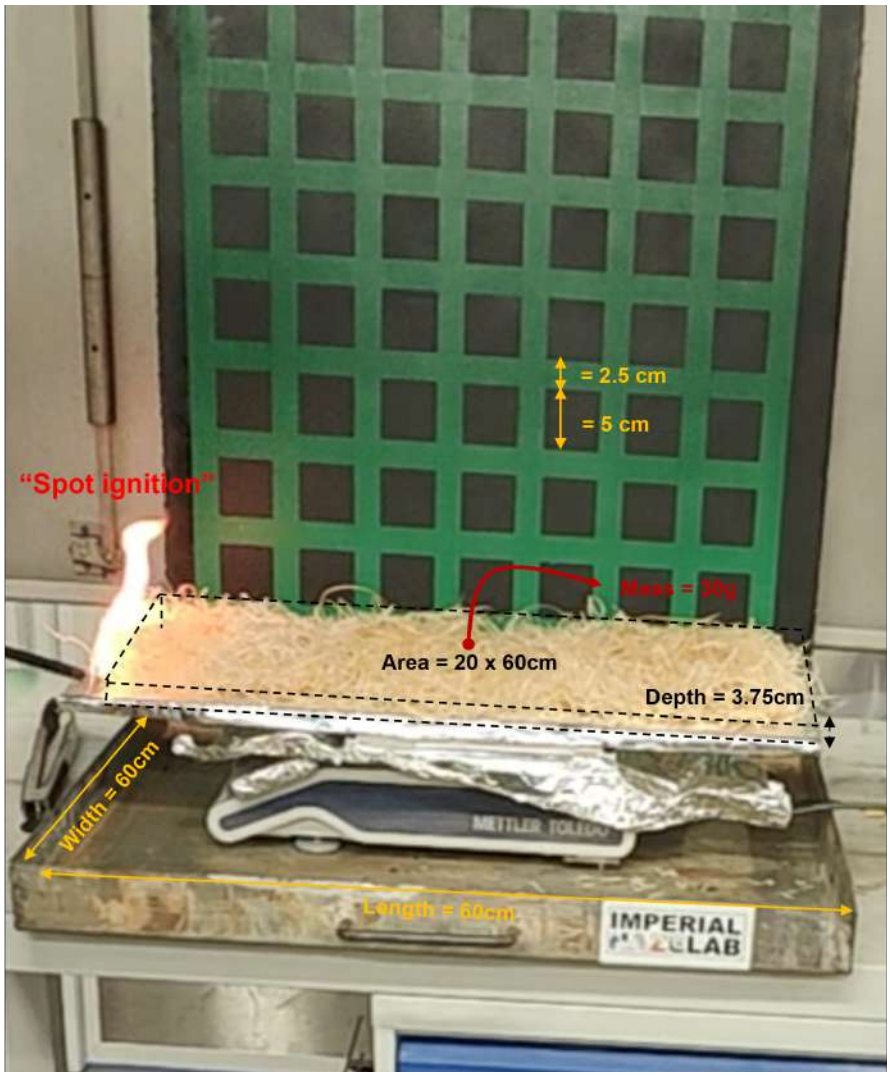

Figure 3.8: *Fuel bed setup.*

tity aimed to evaluate the efficiency of the minimal water and liquid solution needed to delay or even suppress fire spread. This facilitated a comparison between the foams' expansion rates, despite containing identical liquid volumes but generated under varying pressures.

3.6 Summary

In the experimental setup, hydrothermal and reflux synthesis were utilised for the synthesis of IONPs, focusing on their ability to produce NPs with precise morphological characteristics and size.

Several characterisation techniques have been used in this study to analyse the properties of the synthesised NPs and the foam generated. The synthesised NPs were characterised using

Figure 3.9: *Airbrush.*

Figure 3.10: *Airbrush spray on Excelsior fuel.*

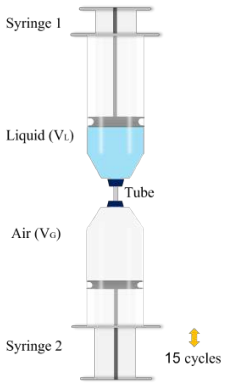

Figure 3.11: *Double syringe technique-dry foam generation.*

Figure 3.12: *Dry foam on Excelsior fuel.*

Scanning Electron Microscopy (SEM), X-ray diffraction (XRD), Fourier Transform Infra-Red Spectroscopy (FT-IR), and Zeta Potential analysis. SEM provided information about the size and morphology of the NPs, while XRD gave insights into their crystal structure. FT-IR helped to identify the functional groups present in the NPs, and Zeta Potential analysis was used to measure their stability in a liquid suspension.

For foam characterisation, the drop shape analysis was used to measure the surface tension and contact angle of the foam solution. Additionally, Dynamic Light Scattering (DLS) and Zeta Potential analysis were used to study the particle distribution and understand the material behaviour with NPs. Moreover, the double syringe technique was used to generate the foam and observe its stability, while the bubble surface morphology was analysed using a digital microscope.

Finally, the foam's fire suppression performance was analysed by conducting small-scale fire tests using a standard procedure. In fire suppression experiments, excelsior was selected as the fuel for its structural similarity to fine shrub fuel and grassland, with careful measurement and setup of fuel beds to ensure repeatability of the results. The efficiency of foam formulations in suppressing fires was evaluated using two delivery methods, an airbrush for wet foam and a double syringe technique for dry foam. The latter aimed to ascertain the minimal water and liquid solution necessary to impede fire spread. The fire behaviour and the excelsior's mass loss were recorded through a high-resolution camera and a precision scale, respectively. Subsequent digital image analysis provided details into flame characteristics. This comprehensive methodology established a foundation for the systematic investigation of NP-enhanced Class A foams aimed at reducing fire spread and ensuring suppression across various fire scenarios.

Table 3.10 summarises the key experiments conducted in this thesis. It outlines the various synthesis methods used for producing iron oxide nanoparticles, the characterisation techniques employed to analyse these nanoparticles, and the procedures for generating and characterising the Class A foams. Finally, it details the small-scale fire experiments performed to evaluate the fire suppression performance of the enhanced foams.

Experiment	Description
Hydrothermal-solvothermal synthesis	Synthesis of iron oxide nanoparticles (IONPs) using hydrothermal and solvothermal methods to control size and morphology.
Reflux synthesis	Reflux method for synthesising IONPs, focusing on different reaction conditions to address scalability.
NPs Characterisation	Characterisation of nanoparticles using SEM, XRD, FTIR, and TGA to determine size, morphology, crystallinity, and thermal stability.
Foam characterisation	Analysis of foam properties including drop shape analysis (DSA), dynamic light scattering (DLS), foam drainage, surface tension, zeta potential, and bubble surface morphology.
Foam generation	Preparation and generation of Class A foams with and without nanoparticle integration, using the double syringe technique and ultrasonic dispersion.
Fire experiments	Small-scale fire experiments using excelsior (dried shredded wood) as fuel to evaluate the fire suppression performance of enhanced foams.

Table 3.10: *Summary of experiments carried out in this thesis.*

Chapter 4

Synthesis and Characterisation of Iron Oxide Nanoparticles

4.1 Introduction

In this chapter, the development of Iron oxide nanostructures using a wide range of hydrothermal synthesis (HS) and reflux synthesis (RS) processing conditions is presented. These are standardised methods presented in Chapter 3. However, a systematic investigation of the effect of synthetic procedures on temperature, solvent and reaction time on the iron oxide nanostructures, morphology crystallinity and molecular structure provides a comprehensive 'protocol outline' for their development and incorporation into firefighting foams. The synthesis of the IONPs by alternating the synthetic parameters allowed precise control over the size, shape and composition of the IONPs.

4.2 Synthetic process conditions

The hydrothermal processing of $Fe(NO_3)_3$ $9H_2O$, $FeCl_2$ $4H_2O$, $FeCl_3$ $6H_2O$ enabled the synthesis of Iron oxide nanoparticles with different morphology and sizes, depending on the reaction temperature, time and solvent. Following the hydrothermal process, reflux synthesis was employed to upscale the quantities of NPs, providing a comparative analysis of the efficiency and yield between hydrothermal and reflux synthesis methods. Finally, the synthesised IONPs were utilised to create Iron oxide/Silica nanostructures using two distinct techniques. The range of experimental conditions investigated is summarised in the methodology chapter (see chapter 3).

4.2.1 Results and Discussions

Effect of reaction time

Iron oxide nanoparticles (IONPs) were synthesised from different precursors and in varying masses, starting from 1 mmol up to 4 mmol for iron nitrate nonahydrate ($Fe(NO_3)_3 \cdot 9H_2O$), 21 mmol for iron chloride tetrahydrate ($FeCl_2 \cdot 4H_2O$), and 7.4 to 9.8 mmol for iron chloride hexahydrate ($FeCl_3 \cdot 6H_2O$). The synthesis explored various reaction times, particularly for iron nitrate nonahydrate, ranging from 3 hours up to 24 hours, and incorporating three different solvents: water, triethylamine, and dimethyl-formamide (DMF).

Scanning electron microscopy (SEM) images reveal the impact of extending reaction times on the gradual growth of IONPs at a consistent temperature of $170°C$ across series 3.3, 3.4 and 3.5. The SEM analysis revealed the morphology of IONPs, highlighting elongated shapes and finely distributed rods as shown in Figure 4.1 . More specifically, the SEM images showed two distinct particle shapes: larger, rhomboid-like crystals measuring several micrometres in length and 1–3 μm in width, alongside smaller, spherical particles. This variation suggests the presence of two phases (goethite and hematite) in the prepared samples from series 3.3. The samples were first ensured to be in a fine powder form. This was critical to maintain uniformity and ease of handling during the SEM imaging process.

Moreover, to reduce charging effects and enhance the quality of the SEM images, a thin layer of gold-palladium alloy (Ag/Pd) was applied to the powdered samples. This coating process helps to increase the conductivity of the samples, which in turn reduces active surface spots that can interfere with image clarity. Once the coating was applied, the samples were carefully placed in the sample holder of the SEM.

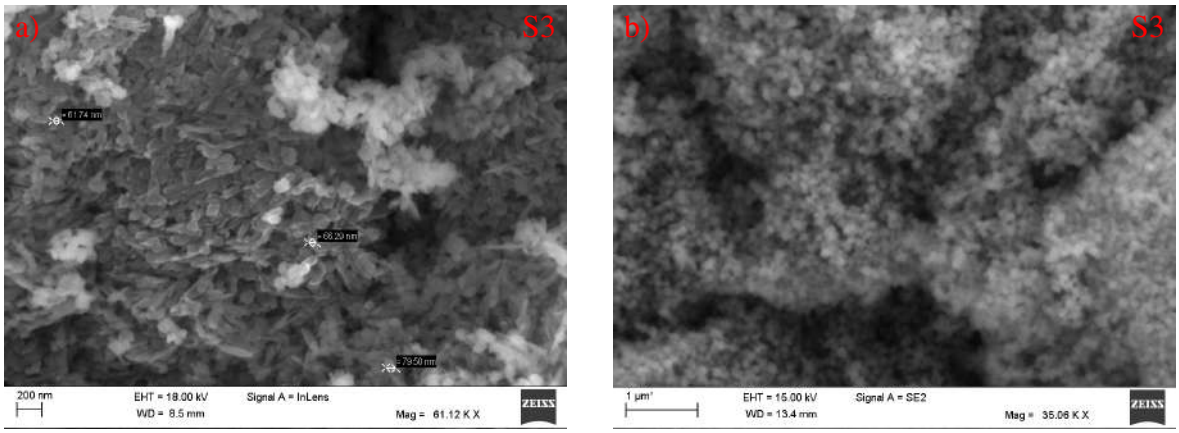

Figure 4.1: *SEM images of the hydrothermal products synthesised at* $170°C$ *with a constant 2mmol of* $Fe(NO_3)_3 \cdot 9H_2O$ *precursor for different reaction times of a) 3 hours b) 24 hours.*

For a higher quantity of the iron precursor at 3 mmol, a noticeable difference in the morphology of the IONPs was observed. At 24 hours, both rod-shaped particles and distorted cubes

were present, while at lower reaction times (3 hours), the majority of the particles were rod-shaped as shown in Figure 4.2. The SEM images in Figures 4.1a) and 4.2a) for the samples S3 and S10 show a mixture of particle shapes and sizes. Specifically, the particles appear as larger, elongated, and rhomboid-like crystals measuring several micrometers in length and $1-3$ µm in width. Alongside these larger particles, there are smaller, spherical particles dispersed throughout the sample. This suggests that at shorter reaction times, the IONPs exhibit a heterogeneous morphology with a combination of larger, well-defined crystals and smaller spherical particles.

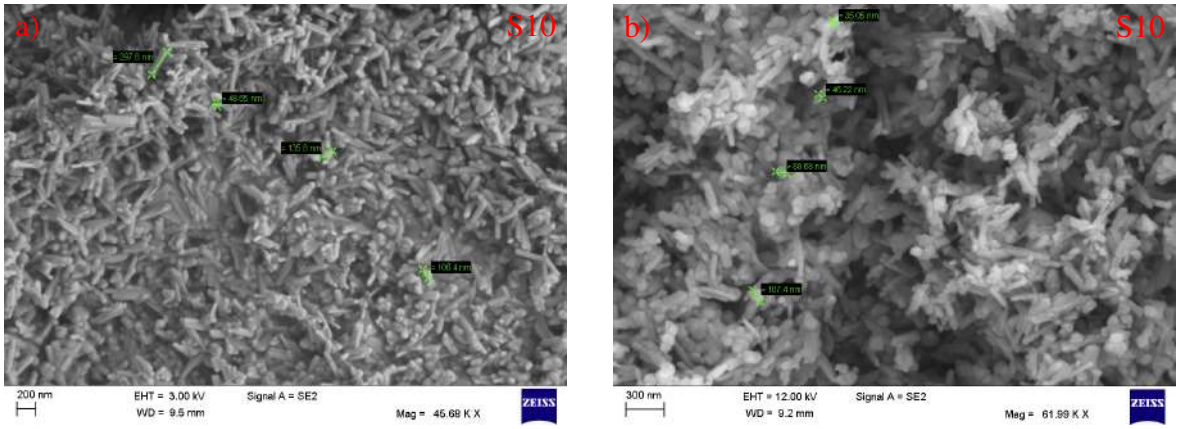

Figure 4.2: *SEM images of the hydrothermal products synthesised at* $170°C$ *with a constant 3mmol of* $Fe(NO_3)_3 \cdot 9H_2O$ *precursor for different reaction times of a) 3 hours b) 24 hours.*

The SEM images in Figures 4.1b) and 4.2b) for the sample S3 and S10 show a notable change in morphology. The particles appear to be more densely packed and finer in distribution compared to samples with less reaction time. There is an indication of a more uniform size and shape, with a significant reduction in the presence of the larger rhomboid-like crystals. The elongated shapes and finely distributed rods are more commonly observed in the sample, suggesting that the extended reaction time leads to a more uniform and refined morphology.

The SEM images of Figure 4.3 illustrate the morphologies of nano-materials grown with different amounts of solvents at a specific temperature (135 °C) for a reaction time of 3 hours from series 3.6. In images a) and b) the particles appear to be relatively uniform in size with some degree of agglomeration. They are spherical and show good mono-dispersity with an average grain size of 60-70 nm. The intermediate stages of higher agglomeration can be visible in c) and d) where the ammonium hydroxide quantity is higher. A higher concentration of ammonium hydroxide can raise the pH level of the solution inside the Teflon autoclave, which can affect the surface charge of the NPs. This indicates that a higher quantity of water shows less agglomeration under hydrothermal conditions. Agglomeration results in larger clustered particles which can be used to improve the stability of foams. Agglomeration of NPs has been considered a mechanism that has been called to explain the high stability of particle-stabilised foams and bubbles. The NPs can accumulate at the gas-water interface

and form a dense protective layer, thus effectively preventing the droplets from getting coalescing or merging. However, while agglomeration can contribute to the higher stability of the foams, excessive agglomeration can lead to several issues.

First of all, it can cause the formation of larger particle clusters that are difficult to diffuse in the foam solution and homogeneously distributed at the gas-water interface. This can lead to uneven distribution of the materials thus making the foam structure even more susceptible to coalescence. Moreover, larger agglomerates may not be efficient in reducing the surface tension of the foam solution thus reducing their surface activity. Finally, a high degree of agglomeration will also reduce the overall high surface area of the NPs, diminishing their potential to interact with more chemical species both aqueous and gaseous of the combustion process.

In Appendix C, SEM images reveal detailed morphologies of the nanoparticles at various concentrations. Although not discussed in the main text, these images provide supplementary visual evidence of the synthesised nanoparticles under different parameters.

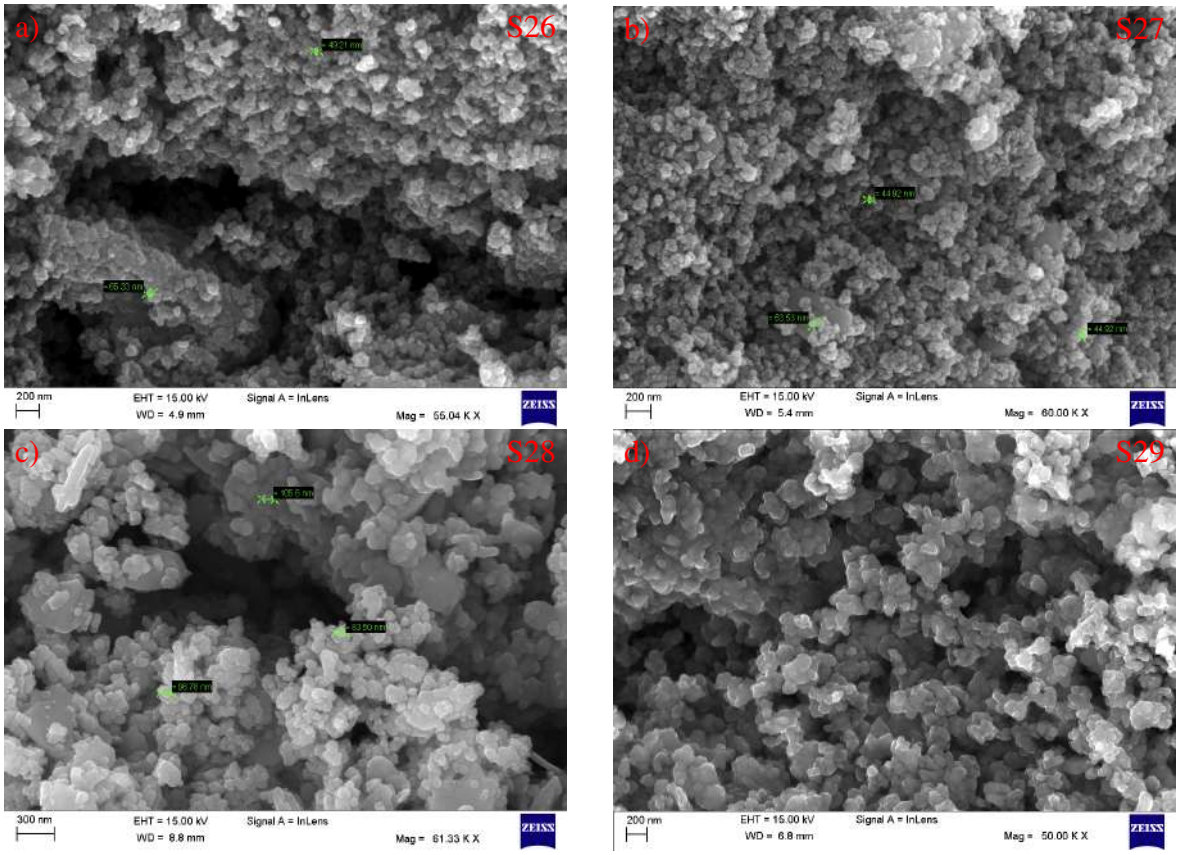

Figure 4.3: *SEM images of the hydrothermal products synthesised for a reaction time of 3 hours at* 135°C. *(a) 20 mL ammonium hydroxide and 40 mL water; (b) 10 mL ammonium hydroxide and 50 mL water; (c) 5 mL ammonium hydroxide and 55 mL water; and (d) 30 mL ammonium hydroxide and 30 mL water.*

The SEM images in Figure 4.4 depict the morphologies of the same product from series 3.6 reproduced under reflux conditions at a steady temperature of 135°*C* over 1 hour from 3.8 as shown in this process (See Figure 3.2).

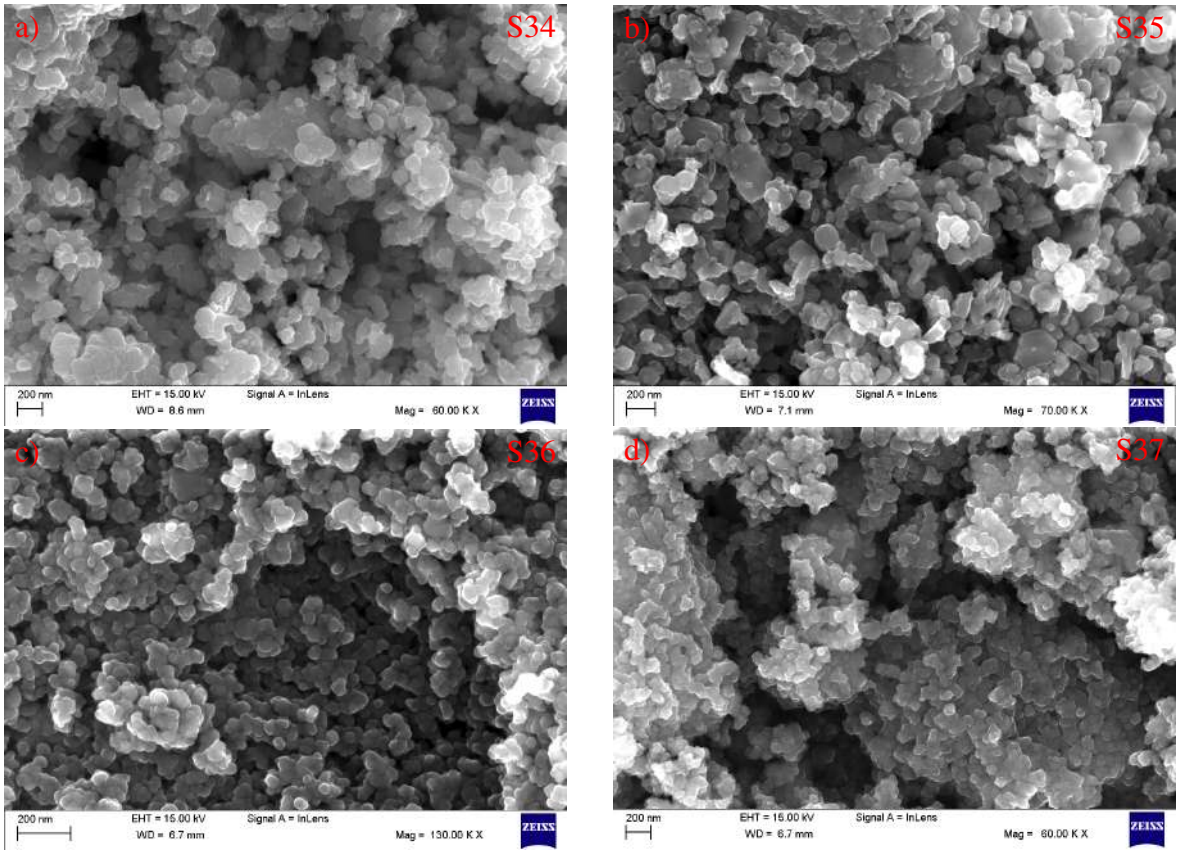

Figure 4.4: *SEM images of the reflux products synthesised for a reaction time of 3 hours at* 135°*C. (a) 20 mL ammonium hydroxide and 40 mL water; (b) 10 mL ammonium hydroxide and 50 mL water; (c) 5 mL ammonium hydroxide and 55 mL water; and (d) 30 mL ammonium hydroxide and 30 mL water.*

The role and mechanism of nanoparticles (NPs) as additives in fire suppression depend on various factors, primarily including their morphology, the presence of functional groups, and their thermal resistance. Nano-additives are usually classified according to their morphology as one-dimensional (including nanotubes, nanowires, and nanofibers), two-dimensional (including nano-sheets and wafers) and three-dimensional (such as spherical nanoparticles, nanoscopes, and nanoclusters) [113]. The morphology and functionalisation of these NPs have significant effects on the thermal properties and fire resistance of the modified materials.

The crystal structure of the as-prepared IONPs R-(Fe_3O_4) and H-(Fe_3O_4) was characterised using XRD. The XRD spectra of both materials are presented in Figure 4.5. Various diffraction peaks appeared, related to the crystalline nature of the samples. In the XRD analysis

of the IONPs, it was observed that the dominant phase present in the sample was magnetite (Fe_3O_4), as evidenced by the characteristic diffraction peaks. However, a closer examination of the XRD pattern revealed the presence of an additional phase, identified as goethite (α-FeOOH), as seen in Figure 4.5b). Figure 4.5c shows the Rietveld refinement of the XRD spectrum for the H-(Fe_3O_4). This secondary phase was discerned through the detection of specific diffraction peaks $2\theta = 21.1381^\circ$ that correspond to the goethite phase, as listed in the standard reference XRD pattern for goethite (ICDD-PDF card # 01-081-0462) [226].

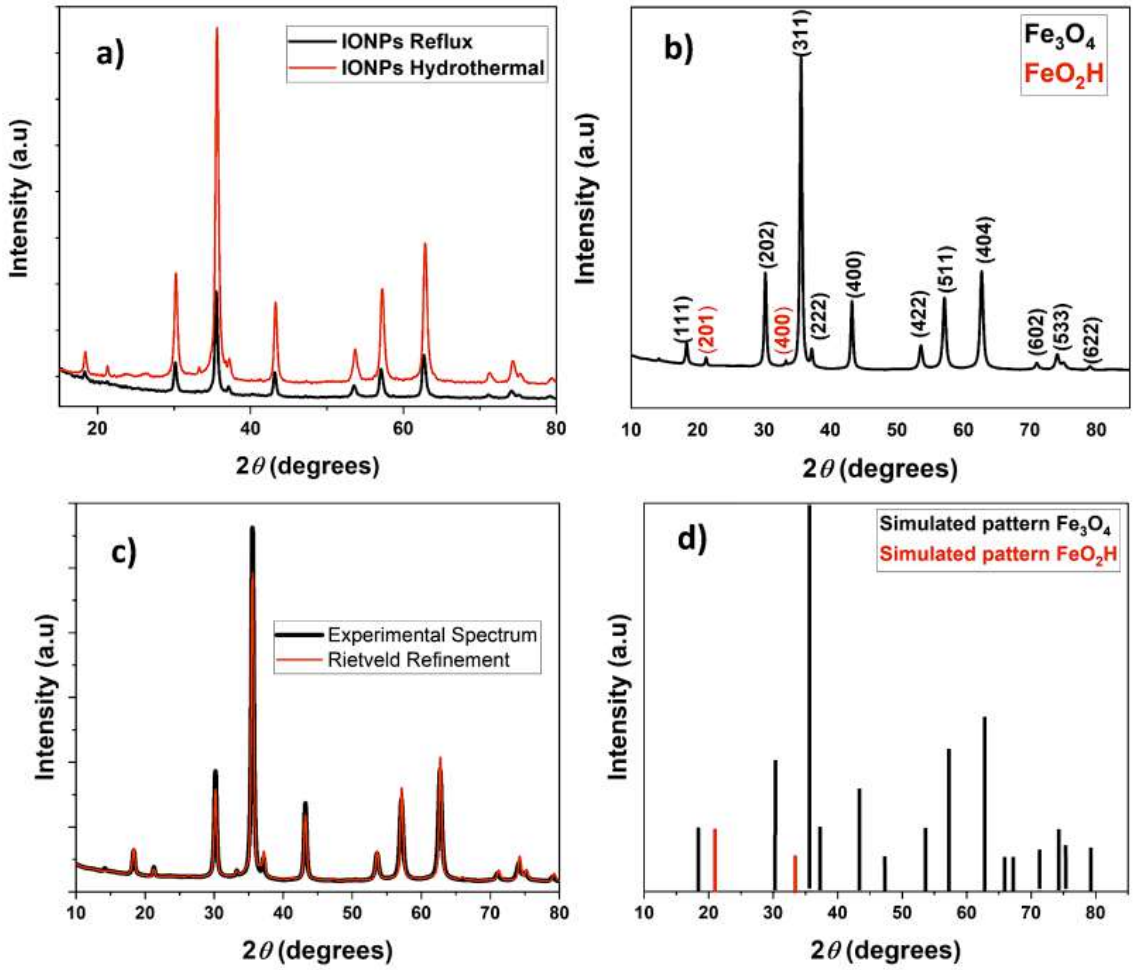

Figure 4.5: *XRD analysis of the synthesised IONPs. Figure 2a shows the XRD spectra for both materials, b) presents the peak identification for the IONPs synthesised with the hydrothermal method, whereas c) shows the Rietveld refinement. Finally, d) presents the simulated patterns for both phases.*

Table 4.1 presents the main peaks for the IONPs synthesised by hydrothermal and reflux processes. From Figure 4.5, it was confirmed that the diffraction peaks belong to magnetite (Fe_3O_4) (ICDD-PDF card # 01-085-1436) phase [227]. The XRD analysis of the magnetite nanoparticles revealed a high degree of crystallinity, as evidenced by the sharp,

well-defined peaks in the diffraction pattern. The XRD patterns obtained for both synthesis techniques exhibit remarkable similarities, strongly suggesting that the resulting materials possess nearly identical crystal structures. Nonetheless, minor variations in peak positions were observed, which could potentially be attributed to differences in crystallite size and the distinct methods of preparation employed. A comparative analysis of the XRD patterns for the reflux-synthesised magnetite nanoparticles R-(Fe_3O_4) and the hydrothermally synthesised magnetite nanoparticles H-(Fe_3O_4) indicates that the application of the reflux technique does not produce any significant impact on the crystal structure of the nanoparticles.

IONPs (Reflux)				IONPs (Hydrothermal)			
Sample	Pos. (2θ)	d-spacing (Å)	hkl	Sample	Pos. (2θ)	d-spacing (Å)	hkl
R-FeO_4	18.3124	4.84481	111	H-FeO_4	18.3243	4.84170	111
R-FeO_4	21.1381	4.20312	110	H-FeO_4	21.2447	4.18226	110
R-FeO_4	30.1029	2.96872	220	H-FeO_4	30.1544	2.96377	220
R-FeO_4	35.4037	2.53544	311	H-FeO_4	35.5022	2.52864	311
R-FeO_4	37.0983	2.42343	222	H-FeO_4	37.1264	2.42166	222
R-FeO_4	43.0912	2.09926	400	H-FeO_4	43.1547	2.09632	400
R-FeO_4	53.4428	1.7152	422	H-FeO_4	53.5285	1.7197	422
R-FeO_4	56.9084	1.61807	511	H-FeO_4	57.0508	1.61436	511
R-FeO_4	62.6069	1.48380	440	H-FeO_4	62.6268	1.48337	440

Table 4.1: *List of the XRD peaks for IONPs synthesised by reflux and hydrothermal process.*

To obtain the average crystallite size of the samples, the diameter, d, is calculated using Debye-Scherrer formula (equation 4.1):

$$d = \frac{K\lambda}{B\cos\theta} \tag{4.1}$$

where K is equal to 0.89 (Scherrer's constant), λ is the wavelength of X-rays, θ_B is the Bragg diffraction angle, and B is the full width at half-maximum (FWHM) of the intense diffraction peaks. The average crystallite size of the IONPs synthesised by hydrothermal and reflux method was found to be $d = 35.56$ nm and $d = 31.57$ nm respectively. These findings are consistent with previous studies on magnetite nanoparticles synthesized using similar methods, which have reported crystallite sizes in the range of 20-30 nm and high phase purity [196, 228].

Table 4.2 lists the parameters for the calculation of crystallite size and phase quantification analysis for the IONPs synthesised by the hydrothermal method.

Product	Reaction time (h)	Temperature($^{\circ}C$)	Phases	Amount (%)	Peak Position (degrees)	FWHM (degrees)	Crystallite size (nm)
S25	3	135	Magnetite/ Goethite	98.4/1.6	35.61	0.381 ± 0.006	22.88
S26	3	135	Magnetite/ Goethite	96.8/3.2	35.53	0.339 ± 0.005	25.71
S27	3	135	Magnetite	100	35.55	0.255 ± 0.004	34.18
S28	3	135	Magnetite/ Goethite	96.8/3.2	35.56	0.443 ± 0.008	19.68

Table 4.2: *Parameters for the calculation of crystallite size and phase quantification analysis.*

The concentration of Ammonium Hydroxide (A.H) affects the crystallite size of the Iron Oxide nanoparticles. More specifically the ratio for S25 was 20 mL (A.H) and 40 mL (H2O). S26 had a ratio of 10 mL (A.H) and 50 mL (H2O). S27 had a ratio of 05 mL (A.H) and 55 mL (H2O). S28 had a ratio of 30 mL (A.H) and 30 mL (H2O) depicting the lowest crystallite size for the highest concentration of (A.H).

Other types of NPs

Silica nanoparticles (SiO_2) are well-known in the literature for their excellent properties at resisting high temperatures and their effectiveness as additives in firefighting foams (see subsec 2.7.3). Consequently, following the synthesis of IONPs, they were combined with tetraethoxysilane as shown in Table 3.9 to create a nanocomposite structure and evaluate the effectiveness of this combination in the modified firefighting foam. On the other hand, commercial silica nanoparticles were obtained for comparison as detailed in Table 3.1. These nanoparticles were of reagent grade, purchased as nano-powder with a particle size of $5-15$ nm from Merck Life Science.

Figure 4.6 presents clusters of nanoparticles with distinct morphologies. Their shape seems to be almost spherical with many small NPs contributing to larger clusters.

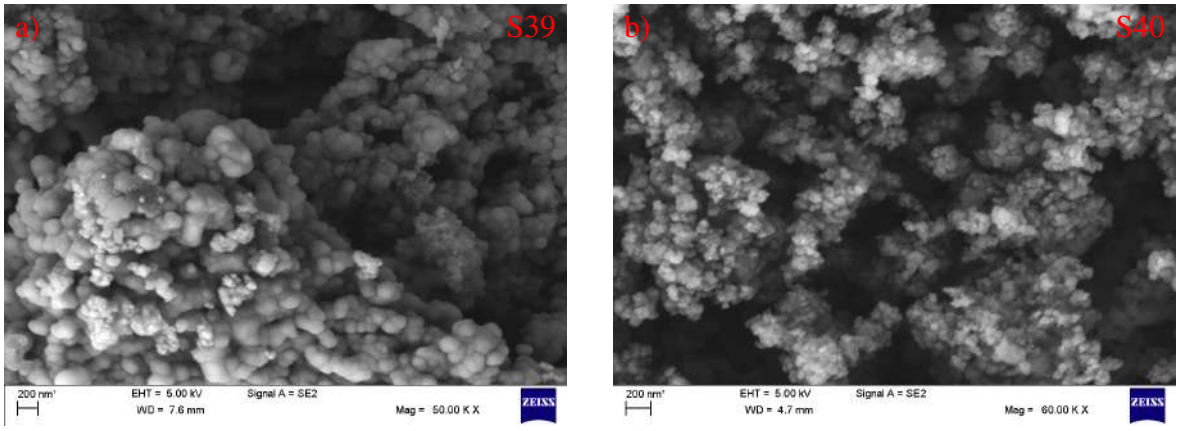

Figure 4.6: *SEM images of the a) IONPs/SiO2 nanostructure and b) Commercial SiO2 NPs*

Figure 4.7 illustrates the X-ray diffraction (XRD) pattern as well as the chemical composition presented by Fourier Transform Infrared Spectroscopy (FTIR). In XRD analysis the peak

marked in blue represents the commercial silica NPs, indicating its crystalline phase which is likely to be quartz or a similar crystalline form. The presence of sharp and well-defined peaks suggests a high degree of crystallinity which is essential for the behaviour of NPs in applications. NPs with small sizes and high crystallinity have higher interfacial energy. Thus, they will readily be adsorbed on the bubble surface [147], making them good candidates for firefighting foam additives as the surface tension of the solution will be decreased. IONPs catalytic activities depend on their size and surface area [185].

The FTIR spectra in Figure 4.7b obtained from SiO_2 (red curve) and IONPs/SiO_2 (blue curve) show clearly the molecular structure of the NPs. The broad peak around 3375 cm^{-1} suggests the presence of Si-OH stretching vibrations, that could be associated with hydroxyl groups attached to silicon atoms. The sharp peak around 1632 cm^{-1} corresponds to the bending vibrations of water molecules. Moreover, the peak around 1056 cm^{-1} is attributed to Si-O-Si stretching vibrations for silica-based materials. Finally, there is a difference between those two samples and that is around the peak at 561 cm^{-1} where it is visible that this is a Fe-O bond confirming the existence of an IONPs/SiO_2 structure.

The chemical composition of the rest NP series was investigated using FTIR spectroscopy. Figure 4.8 presents FTIR spectra obtained from series 3.6, 3.7 and 3.8 from 4000 cm^{-1} to 400 cm^{-1}. The data for the rest of the series 3.3, 3.4, 3.5 are shown in Appendix C. The peaks are mainly ascribed to functional groups (O-H, C=N, C-H, Fe-O) present in the compound. The spectrum in Figure 4.8 a),b) reveals characteristic peaks from the hydrothermal and reflux methods respectively, at 3115 cm^{-1} which shows a medium broad appearance and is connected to the group of O-H stretching. The band at 1556 cm^{-1} and 1636 cm^{-1} belongs to the C=O stretching.

Moreover, FTIR spectra show characteristic absorption bands at 540 cm^{-1} corresponding to the metal-oxygen vibrational band (Fe–O) at the tetrahedral site for series 3.6, 3.7.

Table 4.3 shows the synthesis methods of IONPs (Fe_3O_4) used in the FTIR spectra, distinguishing them between those prepared via hydrothermal (H) and reflux (R) methods, and also lists the IONPs combined with silicon dioxide (IONPs/SiO_2), along with commercial silicon dioxide NPs (SiO_2).

Sample ID	Composition
S26	Fe_3O_4 (H)
S27	Fe_3O_4 (H)
S28	Fe_3O_4 (H)
S34	Fe_3O_4 (R)
S35	Fe_3O_4 (R)
S36	Fe_3O_4 (R)
S37	Fe_3O_4 (R)

Table 4.3: *FTIR samples S26-S37.*

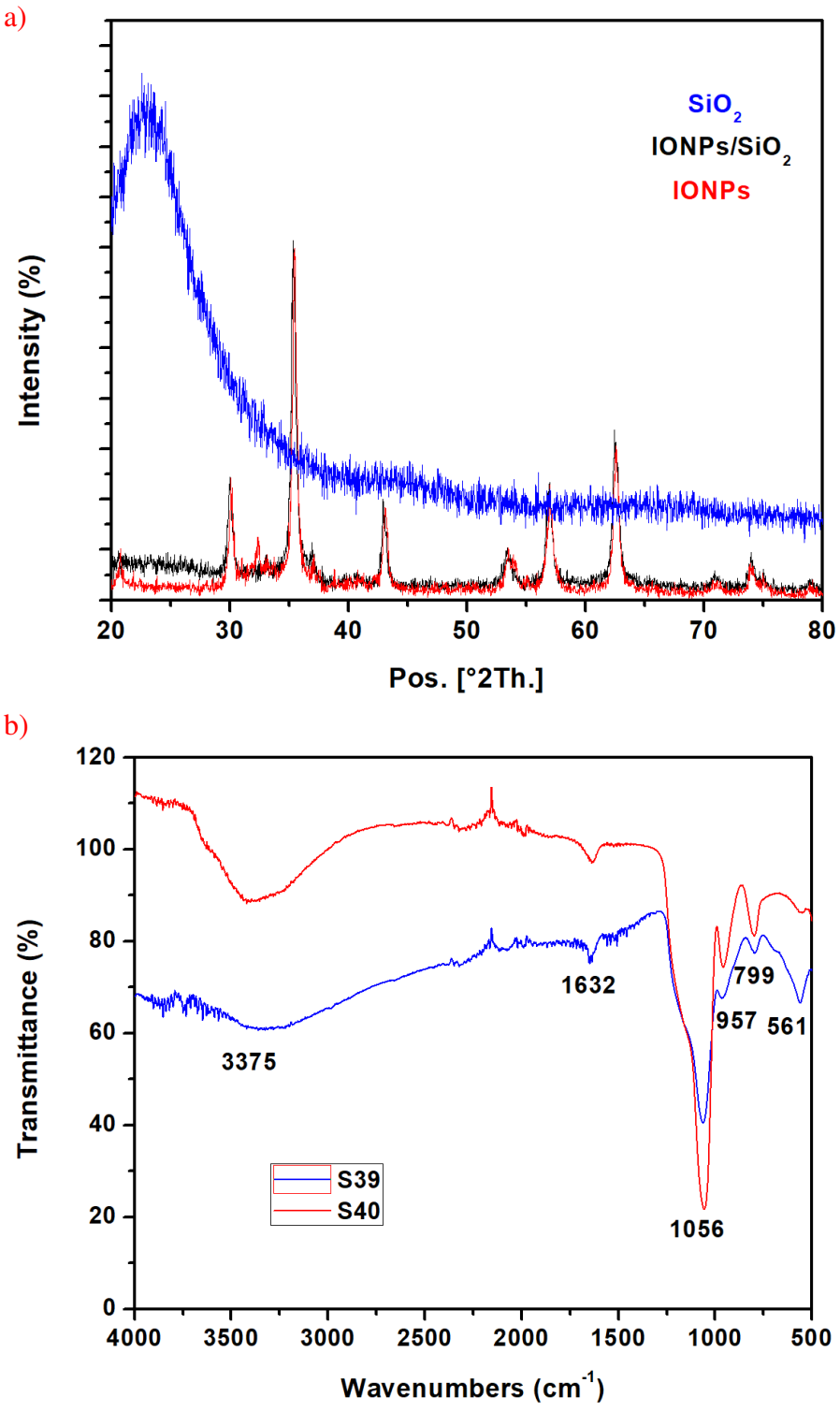

Figure 4.7: *a) XRD analysis of IONPs/SiO_2 (S39), SiO_2 (S40) and synthesised IONPs (S37); b) FTIR spectra of IONPs/SiO_2 (S39) and SiO_2 (S40).*

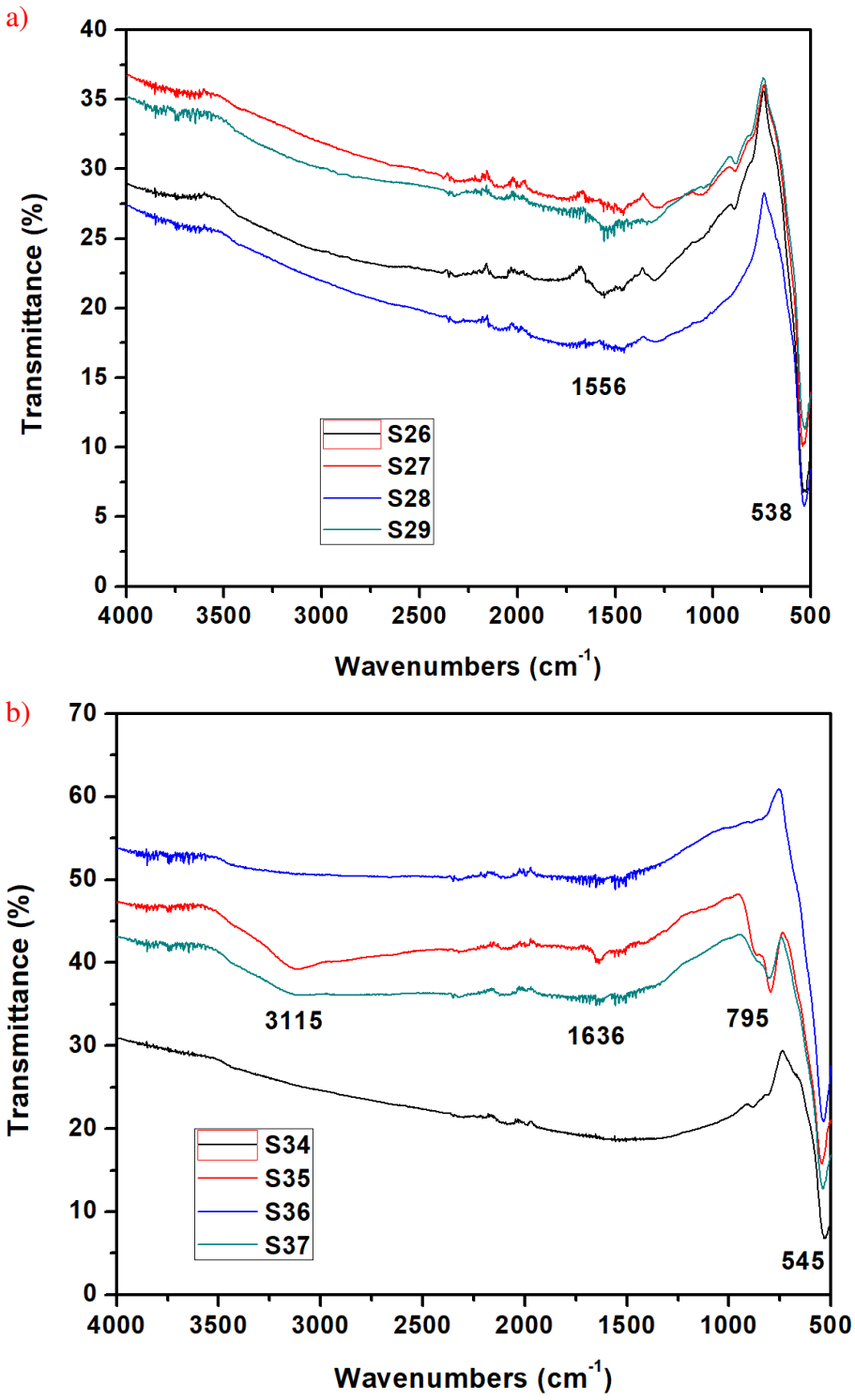

Figure 4.8: *FTIR spectra of synthesised IONPs where a) samples S26-S29; b) samples S34-S37.*

Thermal Stability

Thermogravimetric analysis (TGA) was used to determine the NP thermal stability by monitoring the weight change that occurred while the sample was heated at a constant rate of 20 °C/min to 1000 °C under air. Figure 4.9a) presents the total weight loss as a function of temperature with different slopes. The slopes suggest that samples S27 and S29, both referring to IONPs synthesised by the hydrothermal method, whose weight remained relatively constant, exhibit the best thermal stability among the samples. The fact that the IONPs (H) maintain a higher percentage of their original weight at high temperatures indicated that they decompose much slower and can have a significant effect when added to the foam for fire suppression applications. Similarly, Figure 4.9b) provides the derivative thermogravimetric (DTG) curve which illustrates the rate of weight change of the material as a function of temperature. The samples undergo different thermal events such as the decomposition of organic compounds or dehydration. In the DTG, S27 shows a very slow rate of weight loss as the curve remains close to zero, indicating gradual and minimal weight changes.

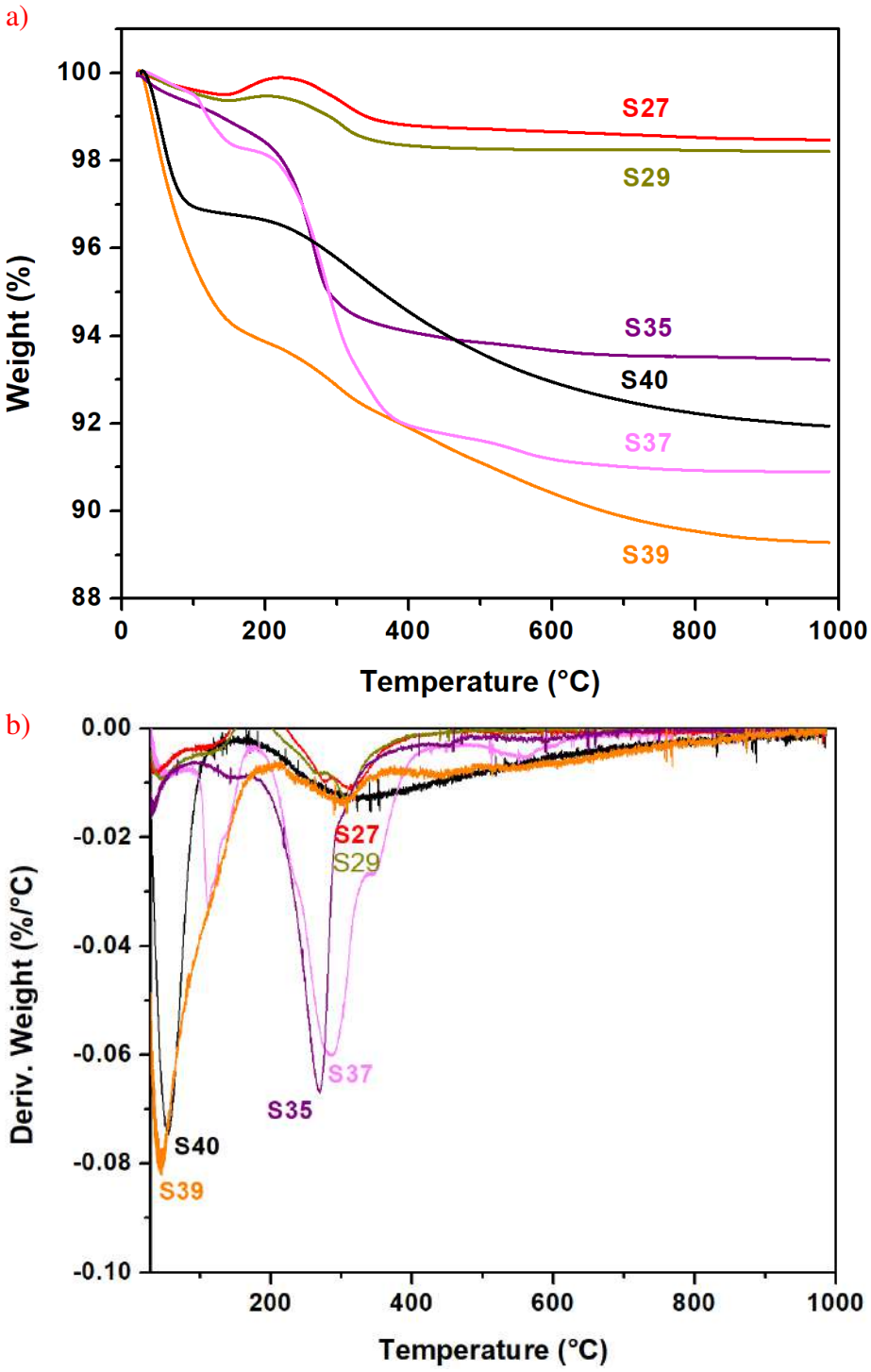

Figure 4.9: *TGA analysis of samples S27-0.1 wt%(IONPs-Hydrothermal), S29-0.1 wt%(IONPs-Hydrothermal), S35-0.1 wt%(IONPs-Reflux), S37-0.1 wt%(IONPs-Reflux), S40-(commercial SiO_2 NPs) and S39-0.1 wt%(IONPs/SiO_2 NPs), illustrating thermal decomposition and overall weight loss from 0 to* 1000 °C.

Figure 4.10 shows the beginning decompose temperature of S27-0.1 wt% is around 220 °C. By around 600 °C the sample weight seems to have levelled off, indicating the loss of most of the volatile components where possibly only the char residue is left. The DTG curve shows the initial decomposition of the sample just before 200 °C due to the moisture loss phase and approximately at 300 °C which may correspond to a major decomposition peak, possibly occurring due to the breakdown of organic components or other volatile substances in the sample.

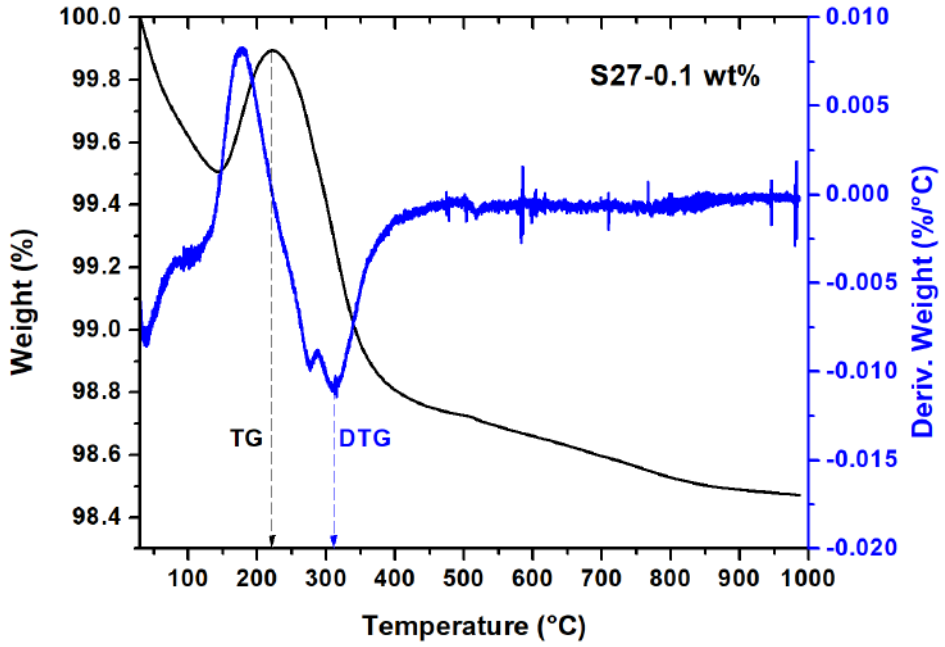

Figure 4.10: *TG and DTG curves for the best-performing sample S27-0.1 wt%.*

This enhanced thermal stability indicates that the IONPs can be beneficial for firefighting purposes as they will remain intact and functional at elevated temperatures, which can lead to more efficient heat absorption and retardation of the flame spread.

4.2.2 Summary and Conclusions

This chapter presents the synthesis of iron oxide nanoparticles (IONPs) from various precursors and in different masses to investigate their impact as additives in Class A foams. The synthesis conditions included various reaction times with different solvents, such as water, triethylamine, and dimethylformamide (DMF), which are widely used in hydrothermal synthesis for the dissolution of precursors and the promotion of particle growth. Scanning electron microscopy (SEM) analysis provided insights into the morphology of the nanoparticles, revealing diversity in particle shapes and sizes. The degree of agglomeration for the nanoparticles is a critical factor in determining which nanoparticles ensure the stability of the firefighting foams by avoiding excess agglomeration. X-ray diffraction (XRD) and

Fourier transform infrared spectroscopy (FTIR) provided details on the crystalline nature and chemical composition of the nanoparticles, indicating a high degree of crystallinity and the presence of functional groups relevant to their use in fire suppression. Thermogravimetric analysis (TGA) and derivative thermogravimetric (DTG) curves highlighted the exceptional thermal stability of IONPs, suggesting they can remain stable at elevated temperatures, thus being effective in fire suppression applications.

Chapter 5

Investigation of the impact of Iron Oxide Nanoparticles on the stability of Class A foam for firefighting purposes

5.1 Introduction

In this chapter, a thorough investigation into the stability of the dry foam, measured by its half-life, was carried out after the addition of the synthesised nanoparticles. The purpose of this evaluation was to determine the impact of the synthesised IONPs on the foam's strength and durability, both of which are vital factors in its effectiveness in suppressing wildfires. To further understand the foam coarsening with time, the morphology of the bubbles was analysed using a digital microscope. The initial assessments indicate potential options for utilising nanoparticles as an effective approach to significantly improve the functionality of Class A firefighting foams.

5.2 Results and Discussions

5.2.1 Foam Drainage

Foam drainage of plain foam was established as a baseline for examining the impact of the synthesized nanoparticles (NPs) on the system. Initially, the foam was subjected to various conditions using an overhead stirrer to determine the most suitable type of stirring for generating sufficient foam structure and to ascertain the optimal rotation speed at which the agitator blade would produce foam. For this purpose, the agitator blade was positioned at three different heights: h1 (1 cm from the bottom), h2 (2 cm from the bottom), and h3 (3 cm from the bottom) of the plastic container, across three distinct rotation speeds of 750 RPM, 1000 RPM, and 1250 RPM. Subsequently, different mixing times were applied to evaluate

the foam drainage and to calculate the average foam height from the three replicates of each experiment. Table 5.1 shows the average foam height repeated from the three replicates for the plain foam. Based on that table there is an increase in foam height with time which suggests that longer times of mixing could be beneficial for achieving greater foam heights. Finally, the increase in foam height from 10 to 15 minutes is less noticeable, suggesting that there is an optimal mixing time beyond which no significant benefits in foam height are gained.

RPM (Blade Height)	**Mixing time (min)**	**Foam Height (Average)**
h1-750-(1cm)	5	3.85
h2-750-(2cm)	10	4.1
h3-750-(3cm)	15	4.16667
h1-1000-(1cm)	5	3.85
h2-1000-(2cm)	10	4.1
h3-1000-(3cm)	15	4.16667
h1-1250-(1cm)	5	3.85
h2-1250-(2cm)	10	4.1
h3-1250-(3cm)	15	4.16667

Table 5.1: *Plain foam drainage for various blade heights (h1, h2, h3), speeds, and time.*

Foam drainage experiments for different agitator blade heights, mixing time and rotation speeds are depicted in Figures 5.1, 5.2.

Based on the plain foam height and foam drainage results in Table 5.1 and Figure 5.2, the 1250 RPM speed was chosen at a 2 cm blade height for a mixing time of 10 minutes because the agitation seemed sufficient to evenly create the foam structure and also distribute the NPs within the foam. The 10-minute duration represents a balanced time to avoid the degradation of foam quality that might occur with prolonged mixing.

Foam stability was then studied for different concentrations of IONPs (see Appendix D). The foam drainage experiments, aimed at evaluating the stability of plain foam compared to foam with higher concentrations of Iron Oxide Nanoparticles (IONPs), namely 0.5 and 1.0 wt%, revealed no significant differences when contrasted with lower concentrations, such as 0.025, 0.05, and 0.1 wt%. Consequently, these lower concentrations were selected for further exploration regarding the potential scaling up of the product for use in extensive fire suppression experiments.

A negative aspect observed for the NPs from Series 5 (see Table3.7), as compared to Series 4 (see Table 3.6), was the reduced foam stability. This was evident in Figure (see Appendix D, Figure D.2), which showed that after 24 hours, the foam structure collapsed due to drainage and coarsening processes. This indicates that this type of NP was detrimental to the foam's lifetime.

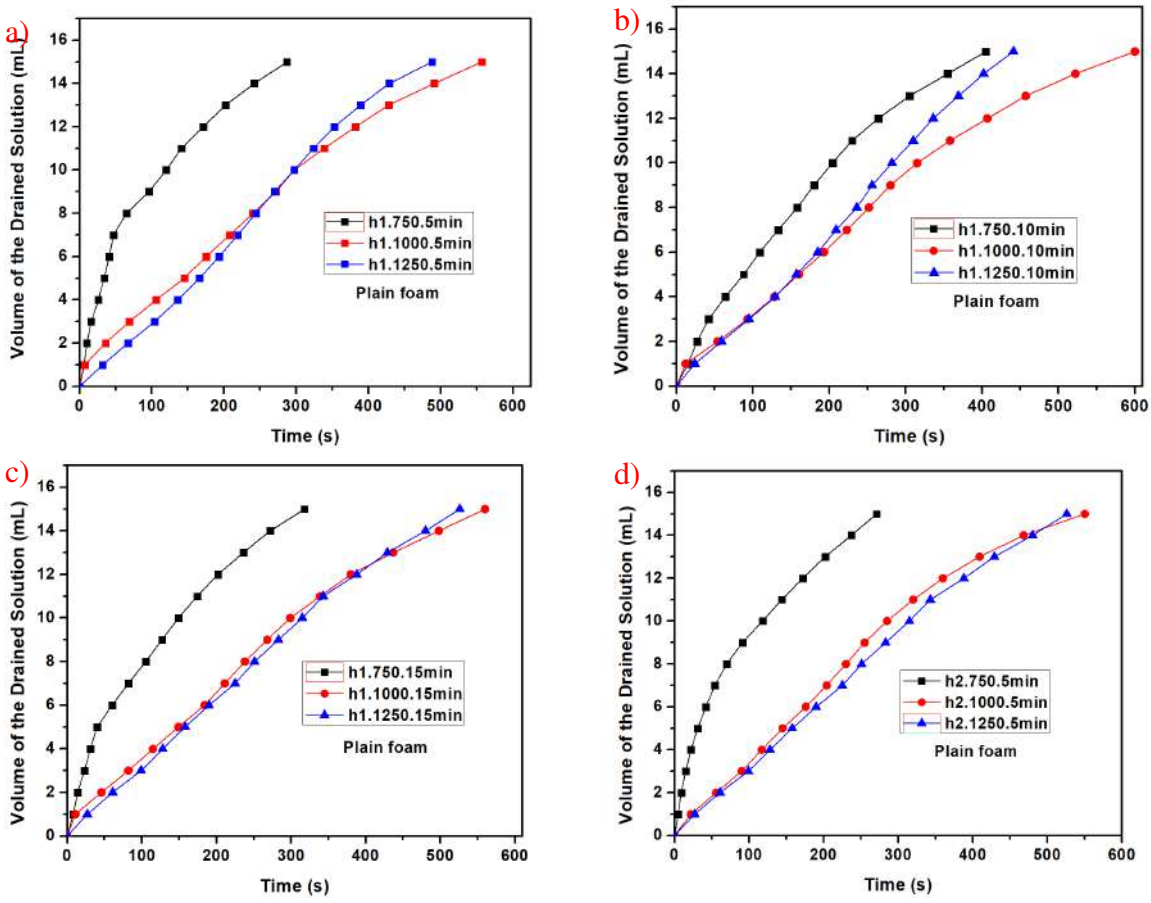

Figure 5.1: *Plain foam drainage for various blade heights (h1, h2, h3), speeds, and time.*

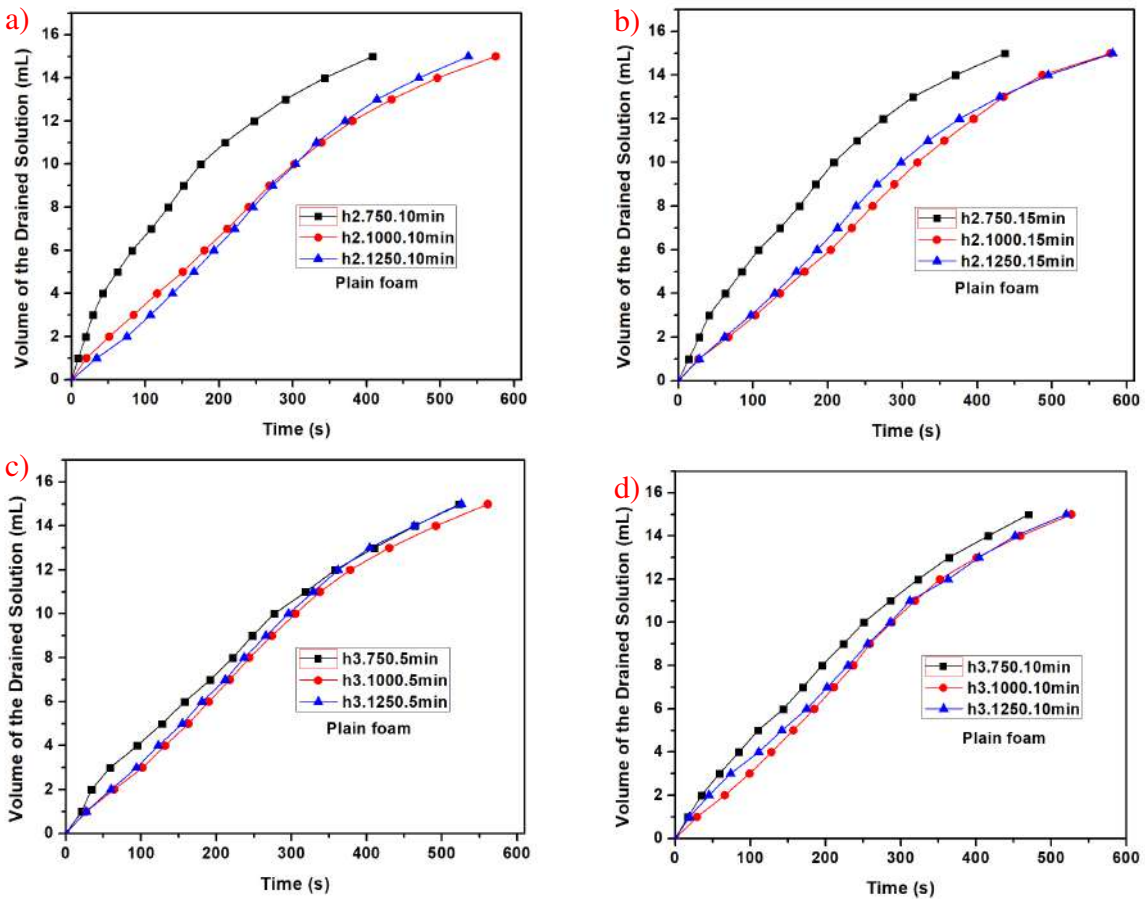

Figure 5.2: *Plain foam drainage for various blade heights (h1, h2, h3), speeds, and time.*

The best-performing samples for S27 and S35 were assigned serial numbers H-0, H-1, H-2, and H-3 for the hydrothermal method, and R-0, R-1, R-2, and R-3 for the reflux method respectively. The new foam solutions were stirred at 1250 revolutions/min for five minutes using an overhead stirrer with a 5 cm paddle, generating a foam solution with entrained liquid. The formulations of the foam dispersions are detailed in Table 5.2.

Sample	Class A Foam Concentrate (%)	Triple Distilled Water (mL)	IONPs (%)
Plain foam	0.6	99.4	0
H-1	0.6	99.4	0.025
H-2	0.6	99.4	0.05
H-3	0.6	99.4	0.1
R-0	0.6	99.4	0
R-1	0.6	99.4	0.025
R-2	0.6	99.4	0.05
R-3	0.6	99.4	0.1

Table 5.2: *Formulations of Class A foam solutions used to generate foam with iron oxide nanoparticles as additives.*

As can be observed in Figures 5.3, 5.4, the drainage time is prolonged for all concentrations, with the effect being more profound at higher concentrations, hence increasing the foam strength and stability. The main mechanism suggested for NPs to improve the foam stability is the adsorption at the gas-liquid interface to make the films more stable [147]. In the absence of the NPs, the liquid is separated from the gas phase faster, indicating higher disproportionation of the bubbles [229]. Typically, the stability of firefighting foams is analysed for 25 % and 50 % drainage [53, 77, 147]. The rate of liquid drainage from the Class A foam was determined for three drainage times; 25%, 50% and 75% of the liquid to drain out of the foam. At 75% drainage time, the foam is still at its highest quality, thus making it necessary to analyse its early performance [7].

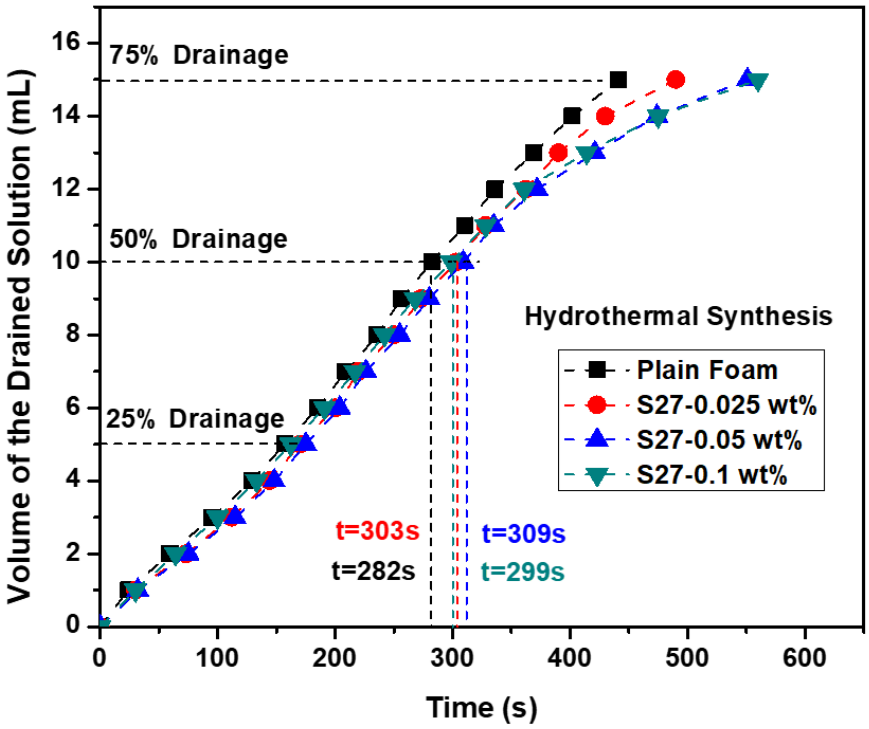

Figure 5.3: *Influence of IONPs synthesised by hydrothermal method on foam drainage.*

In the early stage of drainage (25% drainage time), the concentration with the highest impact in delaying drainage is 0.05wt% IONPs. In the middle stage, which represents foam half-life (50% drainage time), the foam drainage is delayed more for R-Fe_3O_4 than for H-Fe_3O_4 NPs, which indicates higher foam stability. The delay time using R-Fe_3O_4 is 3.2% longer than the one using H-Fe_3O_4. In the late stage of drainage (75% drainage time), when most of the liquid has been drained out of the foam due to gravity, 0.1% concentration seems to stabilise the foam solution in both cases, providing more time to separate the gas and the liquid phase.

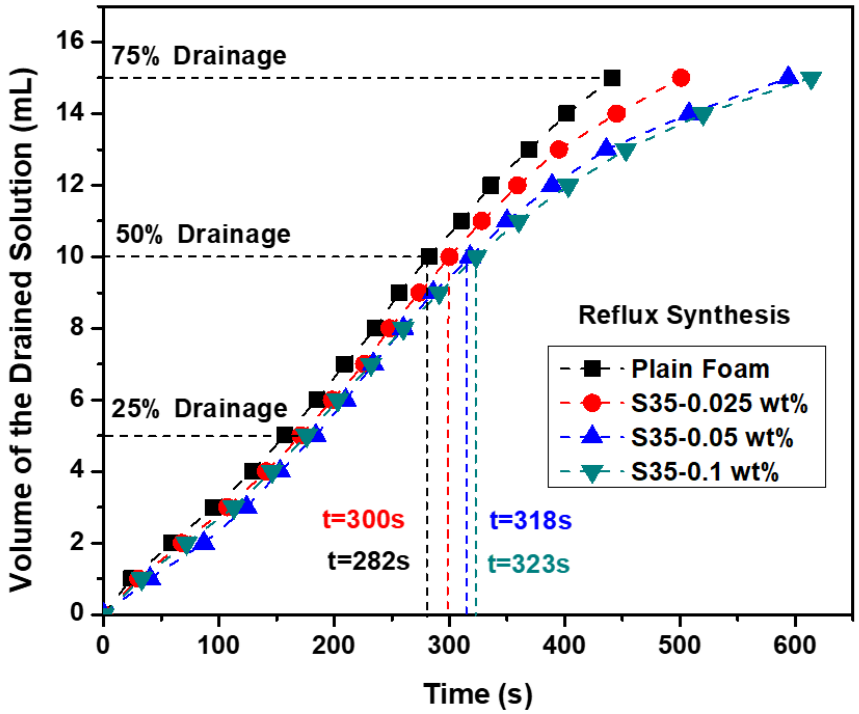

Figure 5.4: *Influence of IONPs synthesised by reflux method on foam drainage.*

Table 5.3 and Table 5.4 present the foam drainage times at different IONPs concentrations for the NPs synthesised via the reflux and the hydrothermal method respectively.

IONPs Conc. Hydro (%)	**Class A Foam (%)**	**Drainage time** $t_{25\%}$ (s)	**Drainage time** $t_{50\%}$ (s)	**Drainage time** $t_{75\%}$ (s)
0	0.6	157 ± 2.00	282 ± 1.53	441 ± 3.00
0.025	0.6	170 ± 2.08	303 ± 2.00	518 ± 2.51
0.5	0.6	175 ± 2.00	309 ± 2.08	551 ± 2.00
0.1	0.6	162 ± 2.05	299 ± 2.00	560 ± 1.63

Table 5.3: *Foam drainage times at different concentrations of synthesised H-Fe_3O_4 into Class A foam solutions.*

This may be attributed to the structure of IONPs at 0.1% being more tightly dispersed on the bubble surface [148]. The dip of the $t_{50\%}$ drainage time at 0.1% concentration is lower for the hydrothermal than for the refulx method. This increased collision probability of IONPs at higher concentrations may lead to a decrease in their dispersity, which may cause some agglomeration [148].

IONPs Conc. Reflux (%)	Class A Foam (%)	Drainage time $t_{25\%}$ (s)	Drainage time $t_{50\%}$ (s)	Drainage time $t_{75\%}$ (s)
0	0.6	157 ± 2.00	282 ± 1.53	441 ± 3.00
0.025	0.6	171 ± 2.05	300 ± 3.3	501 ± 2.49
0.5	0.6	184 ± 2.16	318 ± 3.09	594 ± 3.74
0.1	0.6	176 ± 2.62	323 ± 2.05	614 ± 2.16

Table 5.4: *Foam drainage times at different concentrations of synthesised R-Fe_3O_4 into Class A foam solutions.*

5.2.2 Surface tension

Pendant drop tensiometry (PDT) served as the method to assess the influence of IONPs on the dynamic surface tension of foam solutions [154]. PDT involves the formation of a droplet at the tip of a syringe needle, and the profile of this droplet is analysed to determine the surface tension. In this method, a droplet of the foam solution is slowly extruded from a syringe until it hangs from the needle. The shape and size of the droplet are influenced by the balance of gravitational and surface tension forces. By capturing images of the droplet and applying the Young-Laplace equation 2.28, the surface tension can be calculated.

Figures 5.5 and 5.6 show the different droplets formed from the syringe needle until just before detached from the needle tip. The addition of IONPs reduces the overall mean area of the droplets. The mean area of bubbles decreases with increasing IONPs concentration, indicating smaller droplet sizes with higher concentrations of NPs. This drop can be attributed to the surface activity where the IONPs are adsorbed in the air-liquid interface and tend to modify the surface tension, which leads to the formation of smaller and more stable droplets. Moreover, the mean volume (V) of bubbles decreases with increasing IONPs concentration, consistent with the decrease in mean droplet area. Additionally, electrostatic or steric stabilisation provided by NPs can maintain smaller droplet sizes by preventing droplet coalescence [157].

Figure 5.7 shows the surface tension of foam solutions for various concentrations of H-Fe_3O_4 and R-Fe_3O_4 NPs. The error bars provide an indication of the variability in the measurements. It can be observed that for both reflux and hydrothermal conditions the surface tension (SFT) decreases with the addition of NPs. At 0 % NPs concentration, the SFT is the highest. Despite the variability, the overall trend shows a decrease in SFT with the addition of NPs. This behaviour suggests that the addition of IONPs modifies the air-liquid interfacial properties [230]. The lower surface tension can result in excellent film-forming and spread properties, corresponding to better fire extinguishing capabilities of the foam [155].

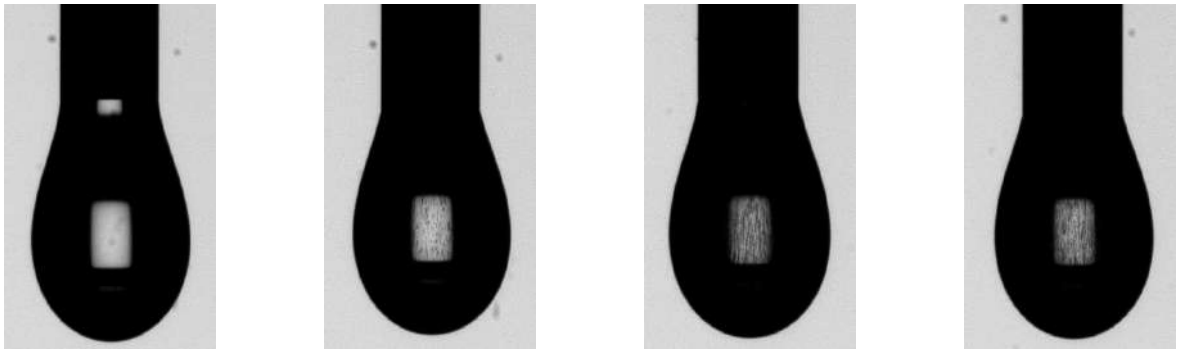

(a) *Plain foam, Area*= $17.2 \pm 0.1\text{mm}^2$, $V = 6.769 \pm 0.034\ \mu L$.

(b) *Foam* + 0.025% *NPs, Area*=$16.05 \pm 0.08\text{mm}^2$, $V = 6.227 \pm 0.051\ \mu L$.

(c) *Foam* + 0.05% *NPs, Area*=$15.96 \pm 0.06\text{mm}^2$, $V = 6.67 \pm 0.043\ \mu L$.

(d) *Foam* + 0.1% *NPs, Area*=$15.78 \pm 0.07\text{mm}^2$, $V = 6.093 \pm 0.046\ \mu L$.

Figure 5.5: *Water droplets analysed by pendant drop method at different concentrations of IONPs (Hydrothermal synthesis).*

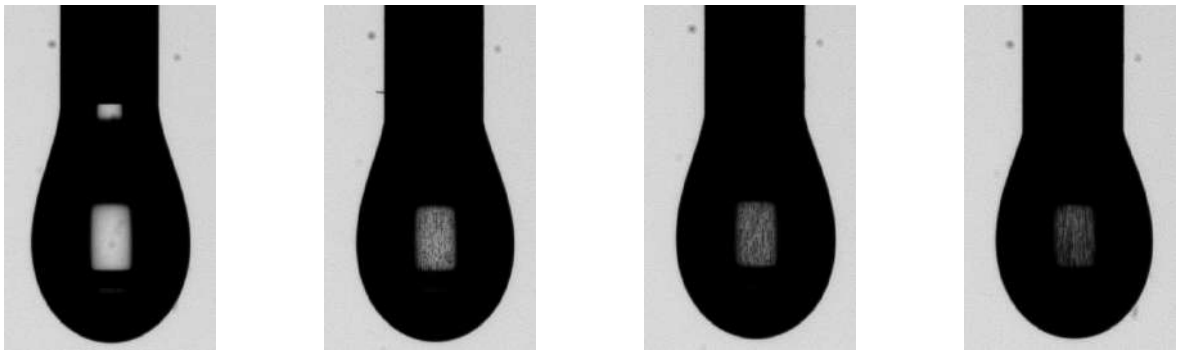

(a) *Plain foam, Area*=$17.2 \pm 0.1\text{mm}^2$, $V = 6.769 \pm 0.034\ \mu L$.

(b) *Foam* + 0.025% *NPs, Area*=$16.7 \pm 0.1\text{mm}^2$, $V = 6.365 \pm 0.101\ \mu L$.

(c) *Foam* + 0.05% *NPs, Area*=$16.25 \pm 0.14\text{mm}^2$, $V = 6.333 \pm 0.096\ \mu L$.

(d) *Foam* + 0.1% *NPs, Area*=$14.86 \pm 0.12\text{mm}^2$, $V = 5.656 \pm 0.07\ \mu L$.

Figure 5.6: *Water droplets analysed by pendant drop method at different concentrations of IONPs (Reflux synthesis).*

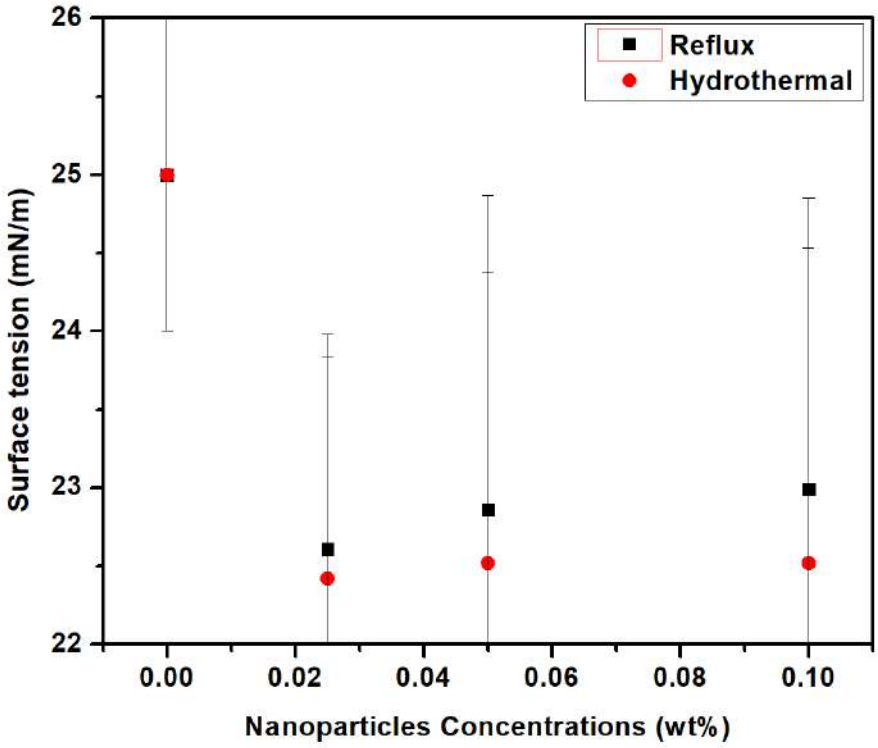

Figure 5.7: *Interfacial surface tension (SFT) for different concentrations of IONPs dispersions in foam solution synthesised using reflux and hydrothermal techniques, with error bars representing standard deviations.*

This behaviour suggests that the addition of the IONPs can modify the air-liquid interfacial properties. A study from Shneider [231] reveals that the surface tensions of a bubble and a droplet respond differently to changes in surface curvature. Specifically, for a bubble, the surface tension decreases as the surface's curvature radius reduces, while for a droplet, the surface tension increases under the same conditions. In our experiment, the surface tension of the droplet was studied and it was found that for higher concentrations with a lower radius, the surface tension was increased. This might also result from the surfactant adsorption on IONPs and depletion at the air-water interface [154].

5.2.3 Zeta Potential

The zeta potential in the foam liquid is closely related to foam stability [77, 232, 233]. Thus, for the in-depth understanding of the effect of the addition of IONPs in class A foams, the relation between the IONPs concentration and the NPs zeta potential in the foam liquid was studied.

Table 5.5 shows the average zeta potential values and particle size of IONPs when added to the foam solution. As can be observed, when increasing the IONPs concentration, the zeta

potential values increase for both foam solutions prepared by the two different techniques. The higher the zeta potential, the more strongly the particles are repelled from each other, and the more stable the dispersion will be [234]. Particles with zeta potentials in the range $\pm 30mV$ are considered to be unstable concerning aggregation. The observed values in Table 5 are within the expected range, hence aggregation of the nanoparticles should be expected [235]. The average hydrodynamic particle size increased as the NP concentrations increased, indicating a higher particle aggregation at higher concentrations.

Table 5.5: *Average zeta potential and particle diameter of IONPs at different concentrations for hydrothermal and reflux methods.*

NPs Concentration (wt%)	Zeta Potential (mV)	Avg Particles Size (nm)
0	0.86 ± 0.19	N/A
H - 1	$\lvert -18.51 \rvert \pm 0.99$	1658
H - 2	$\lvert -17.43 \rvert \pm 0.85$	2564
H - 3	$\lvert -10.20 \rvert \pm 0.92$	3306
R - 1	$\lvert -28.78 \rvert \pm 2.06$	1681
R - 2	$\lvert -14.60 \rvert \pm 0.09$	2096
R - 3	$\lvert -8.80 \rvert \pm 0.60$	2232

The zeta potential absolute value $Zetapotential = |-zetapotential|$, decreased from $18.51mV$ to $10.2mV$ with the addition of IONPs synthesised by the hydrothermal method. In contrast, for the reflux method, the decrease was from $28.78mV$ to $8.8mV$ for increasing IONPs concentration. The decreasing absolute value of the zeta potential indicated that the class A foam surfactant was adsorbed in the surfaces of the NPs [68, 236]. A higher zeta potential indicates a greater degree of electrostatic repulsion between the particles, which makes the dispersion more stable [134, 237]. A corresponding average particle size increase is observed as a result of the presence of the adsorbed NPs. Particle foaming agents are characterised by their strong adsorption energy at the gas-water interface, which means that they have a high adsorption heat [134]. This makes the adsorption at the interface irreversible, meaning that the particles will stay attached to the interface once they are adsorbed. The strongly negative values of zeta potential for lower concentrations indicate the high colloidal stability of the IONPs, which tend to increase as the NPs concentration decreases [238].

5.2.4 Bubble Morphology

Foams that present higher stability can resist the effect of the foam coarsening and bubble coalescence resulting in longer foam half-life. Half-life time of a foam is defined as the time required by a foam to drain 50% of the volume of the initial condition. In the current work, to further understand the foam coarsening with time, the morphology of the bubbles was analysed using a digital microscope. For every sample used, two images were recorded to investigate the coarsening. The first image is recorded immediately after the foam generation, whereas the second image is generated 10 min after the foam generation. The duration

of the coarsening of the foam was chosen at 10 min due to the approximate time of the foam to reach its 75% drainage time.

The destabilisation process of the foam depends on the coalescence (rupture of films between bubbles) and the coarsening (gas diffusion between bubbles due to pressure difference). After 10 min elapsed from the plain foam generation, the bubbles are seen to have formed a polyhedral shape and the average bubble size has increased. By comparing Figure 5.8a) and 5.8b) it can be extracted that the plain foam's bubble distribution changes from circular at the beginning to polyhedral after 10 min, indicating a low liquid volume fraction (ϕ) in the foam [80]. This behaviour can be related to the gas diffused between bubbles of different radii due to differences in the Laplace pressure. The gas is transferred from smaller to bigger bubbles, leading to the disappearance of the former [69]. However, at 0.1 wt% IONPs concentration in Figure 5.8c), bubbles remain approximately spherical even after 10 min elapsed since the foam generation (Figure 5.8d)), demonstrating a delay in foam drainage. This is the result of a higher liquid volume fraction (ϕ) where the bubbles are spherical and move independently (Figure 5.8d-f) [80]. The same trend followed for the 0.1 wt% IONPs (Figure 5.8e,f)) synthesised by the reflux method. This indicated that the NPs were adsorbed fast enough to the bubble surface and stabilized, thus limiting their deterioration. This result can be attributed to the foam solution's improved surface dilational viscoelasticity as a result of NP adsorption and accumulation on the bubble surface and plateau border [7].

When the foam is generated, it is composed of individual bubbles that are separated by thin films of liquid, known as plateau borders [147, 230]. These plateau borders (PBs) are highly unstable and prone to rupture, which can cause the foam to collapse. This behaviour is caused by a combination of various factors, including capillary forces, gravity, and surface tension [155]. Generally, most of the liquid is found in the PBs. When four PBs join together they form junctions or nodes. However, a mechanism to stabilise these plateau borders is the addition of nanomaterials [80]. Figure 5.9 illustrates the main mechanism by which IONPs stabilise the foam lamella and decelerate foam drainage and coarsening.

When nanoparticles are introduced to the foam, they can aggregate at the plateau borders due to their high surface area and surface energy. This aggregation can cause the nanoparticles to form a physical barrier that reinforces the plateau borders and prevents them from rupturing [67]. During this process, the aggregated IONPs delay the flow of the liquid downwards the plateau border, thus providing a steric barrier to film thinning and inter-bubble diffusion [7]. Moreover, the aggregated IONPs can form a layered structure inside the thinning film, thus stabilising it by the so-called oscillatory structural force [149]. The thinning and stability of the aqueous films separating the foam bubbles are crucial for coalescence and foam collapse. Finally, the adsorption of the NPs on the bubble interface is irreversible, which implies that NPs are difficult to detach from the interfaces, thus impeding bubble coalescence and reducing foam drainage. The degradation of the foam was notably accelerated upon contact with water. This phenomenon can be potentially attributed to the aqueous surfactant solution (SDS) that was inherent within the foam, which creates a concentration gradient between the foam lamella and the pure water thus diluting the surfactant solution. As the concentration of

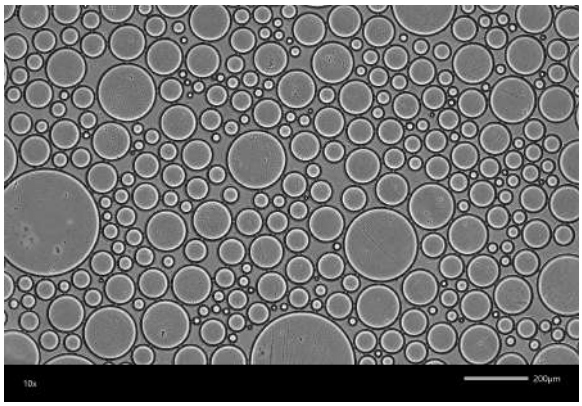

(a) *Plain foam,* $t = 0$ *min.*

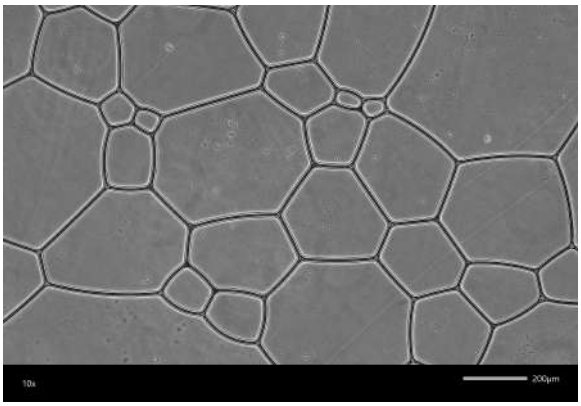

(b) *Plain foam,* $t = 10$ *min.*

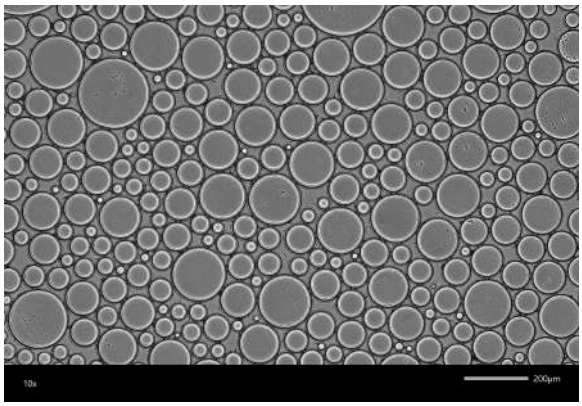

(c) *Enhanced Foam,* $0.1wt\%$ *H-*Fe_3O_4 *NPs,* $t = 0$ *min.*

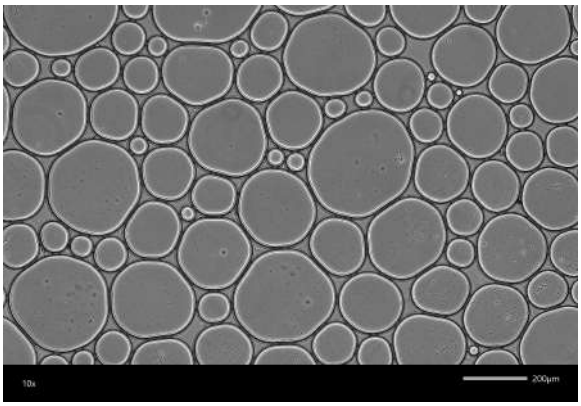

(d) *Enhanced Foam,* $0.1wt\%$ *H-*Fe_3O_4 *NPs,* $t = 10$ *min.*

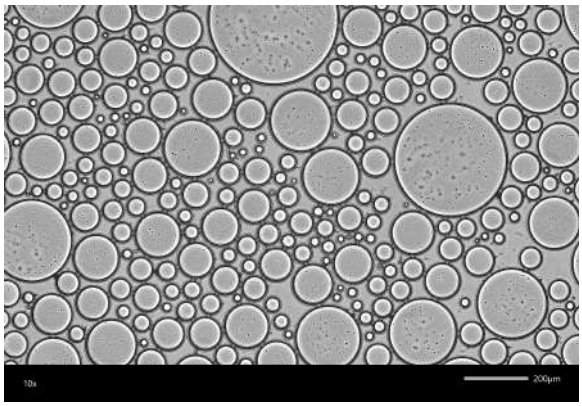

(e) *Enhanced Foam,* $0.1wt\%$ *R-*Fe_3O_4 *NPs,* $t = 0$ *min.*

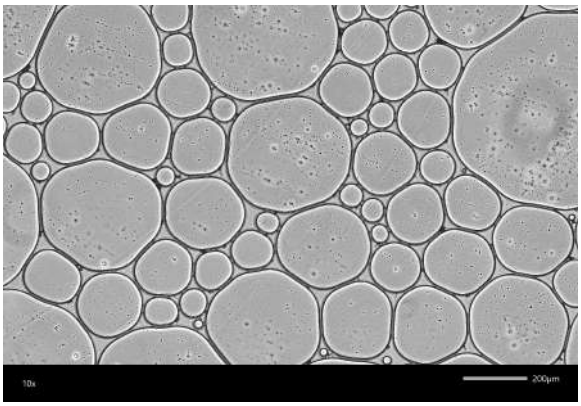

(f) *Enhanced Foam,* $0.1wt\%$ *R-*Fe_3O_4 *NPs,* $t = 10$ *min.*

Figure 5.8: *Foam bubble morphologies (*$10\times$ *magnification) at* $t = 0$ *min (foam generation) and* $t = 10$ *min after foam generation for plain foam, and for foam enhanced with* $0.1wt\%$ Fe_3O_4 *synthesised using the* Hydrothermal *(H) and the* Reflux *(R) methods.*

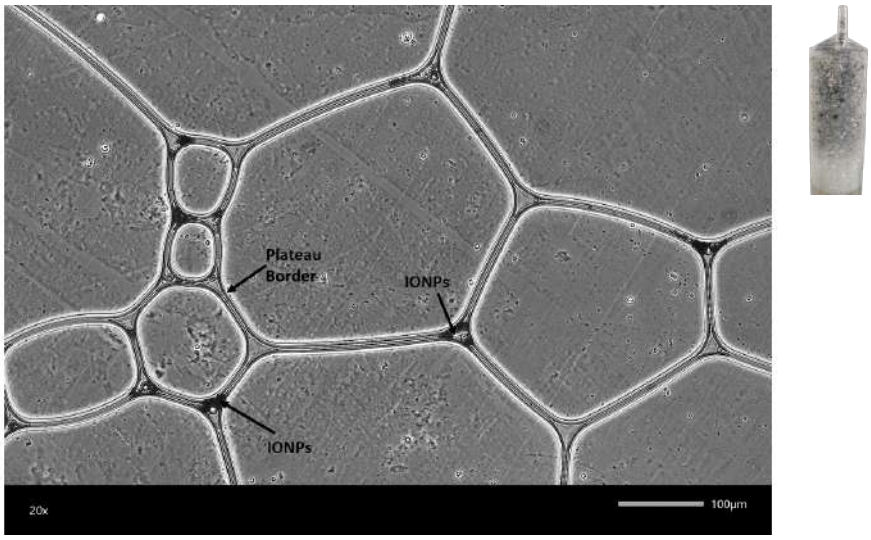

Figure 5.9: *Illustration of the mechanism that IONPs stabilise the foam system. The drainage time of the film may be reduced due to the accumulation of the IONPs within the plateau borders.*

surfactant decreases, the surface tension of the solution increases and the bubbles are more likely to rupture.

5.2.5 Summary and Conclusions

In this chapter, the effect of IONPs synthesised by two different preparation methods, (reflux and hydrothermal), on the stability of a commercial Class A firefighting foam was systematically investigated. Based on the findings, the addition of IONPs at appropriate concentrations into the foam solution improved foam stability. The foam half-life was increased in both cases due to the accumulation of the NPs in the foam network thus providing an interfacial shield to delay the foam drainage.

However, in the absence of NPs, the bubble sizes were larger and fewer thus indicating a high rate of bubble coalescence and coarsening. An analysis of the morphology of the bubbles on the micro-scale suggests that the NPs assemble at the plateau borders and nodes of the bubbles to reduce coarsening and disproportionation. As a result, the foam stability improves due to the adsorption of the NPs on the gas-liquid interface. The results regarding the wetting characteristics of the IONPs show that they decrease the surface tension of the foam solution, indicating that the NPs have changed the air-liquid interfacial properties. The lowest surface tension was achieved at the lowest concentration of IONPs, while higher concentrations resulted in higher surface tension due to surfactant adsorption on IONPs and depletion at the air-water interface. IONPs can aggregate at the PBs of foam bubbles to stabilise them by forming a protective layer that prevents the liquid films from breaking. This mechanism can improve the effectiveness and efficiency of firefighting foam.

Chapter 6

Utilisation of enhanced Class A foam with nanoparticles for the indirect attack of Excelsior fuel

6.1 Introduction

Wildfires present a significant challenge to natural ecosystems and human settlements, frequently leading to catastrophic loss and destruction. Innovative solutions are needed to enhance the efficiency and effectiveness of firefighting technologies, which are critical for mitigating and controlling the spread of wildfires. This chapter involves the use of firefighting foams, specifically Class A foams that are designated for Class A fires, which have demonstrated significant effectiveness in suppressing and mitigating wildfires mixed with synthesised IONPs, combined nanostructures of IONPs/SiO_2 and commercial SiO_2 NPs. The addition of nanoparticles into Class A foams and their comparison to the plain foam performance provides significant advancements in wildfire suppression particularly when addressing the indirect attack of the fire. The formulation and concentration of the foam play a significant role in addressing the fire. An analysis of the foam provides valuable insights into the interaction of nanoparticles at the solution stage, which can consequentially affect the foam's overall performance. Understanding the behaviour of the enhanced foam containing NPs could provide a predictive model for its performance in real-world fire suppression scenarios. Small-scale experiments addressing the combustion of Excelsior fuel and the use of the plain foam against the enhanced one by the NPs are thoroughly discussed in this chapter. Finally, it concludes by exploring key metrics for fire suppression efficiency, such as mass loss, mass loss rate, flame height, flame spread and residual mass to evaluate the performance.

6.2 Results and Discussions

6.2.1 Mass loss

The setup for the fire experiments is detailed in the methodology section (see 3.5). Mass loss profiles of Excelsior treated with water (wet Excelsior) and varying NP concentrations are presented in Figure 6.1, illustrating the critical role between thermal degradation and the effectiveness of NPs in retarding the combustion process. For untreated dry Excelsior (6.1a)), a rapid mass loss rate is observed, with the material diminishing in less than two minutes. Conversely, Excelsior treated with 20 ml of plain water shows a delayed onset of mass loss, likely due to the effect of moisture content. The incorporation of iron oxide nanoparticles/silicon dioxide (IONPs/SiO_2) NPs at concentrations of 0.025 wt% (6.1c)) and 0.1 wt% (6.1d)) significantly affects the mass loss rate and total mass over time. At the lower concentration (0.025 wt%), three peaks are observed, indicating combustion processes starting from the dry part of the Excelsior, used as the ignition source, and moving on to the next two peaks, which represent the combustion processes of Excelsior embedded with wet foam and IONPs/SiO_2 NPs. Conversely, 6.1d) shows a lower mass loss rate, suggesting a prolonged fire-retardant effect from the higher concentration of NPs.

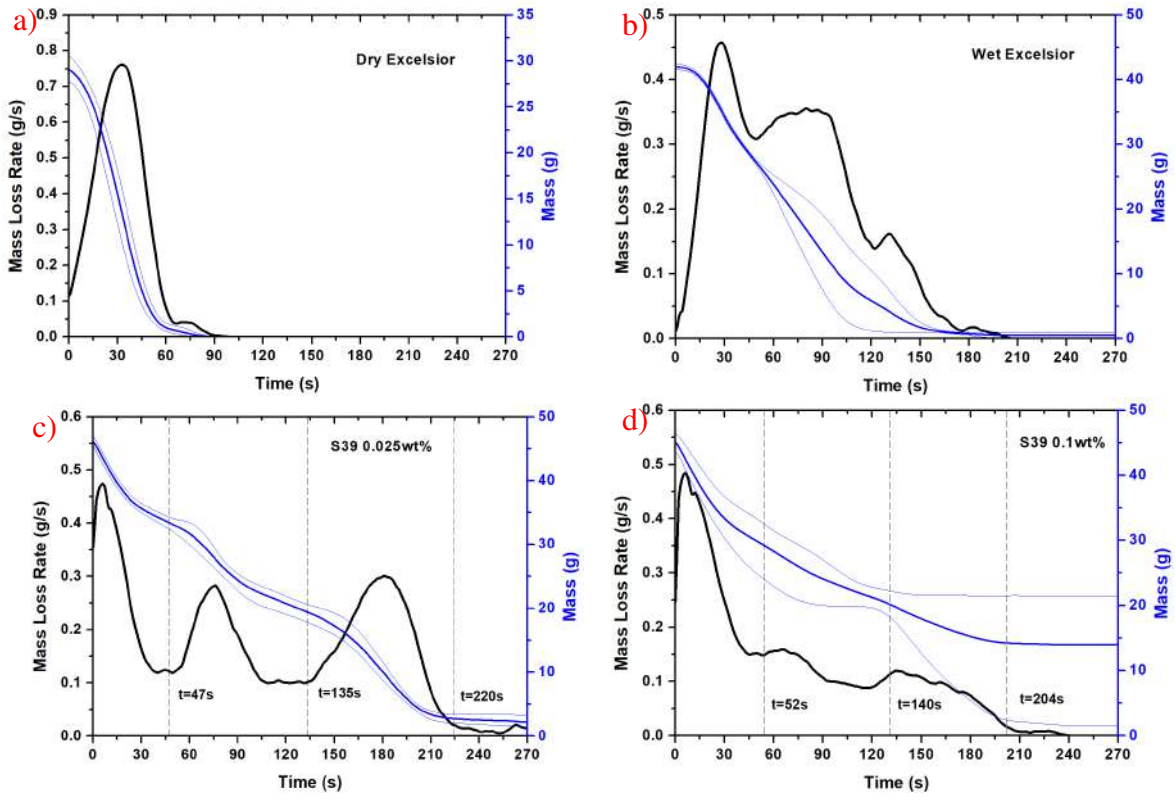

Figure 6.1: *Comparative analysis of mass loss rate and total mass for Excelsior where a) Dry Excelsior, b) Wet Excelsior, c) S39-0.025 wt% d) S39-0.1 wt%.*

The graphs in Figure 6.2 provide a comparative analysis of the mass loss rate and the total mass for Excelsior treated with samples S27 and S35, which are the IONPs synthesised by hydrothermal and reflux synthesis methods, respectively. For S27 at a concentration of 0.025 wt% (6.2a), the mass loss rate profile shows an initial decline at $t = 46$ s, followed by a secondary peak at $t = 95$ s, before a final decline where the Excelsior was completely burnt. Even at a low concentration, the wet foam with IONPs as additives seems to have delayed the combustion process compared to the plain wet foam (Figure 6.3). Remarkably, S27 at 0.1 wt% (Figure 6.2c)) displays a highly effective suppression of the fire at $t = 129$ s. This cessation of fire is consistent across all three experimental replicates and underscores the significance of fire retardancy efficacy at this concentration, the same sample that had high thermal stability from the TGA measurements (see section 4.2.1). This phenomenon is possibly due to the high thermal stability of the IONPs, suggesting that at this concentration, there is a rapid formation of a protective layer on the surface of the Excelsior. This layer absorbs heat, preventing the fire from developing further and eventually slowing it down until it can no longer progress. The S35 wet foam formulations at concentrations of 0.025 wt% (Figure 6.2e)) and 0.1 wt% (Figure 6.2f)) also show moderate mass loss rates, with the 0.1 wt% concentration again appearing more effective.

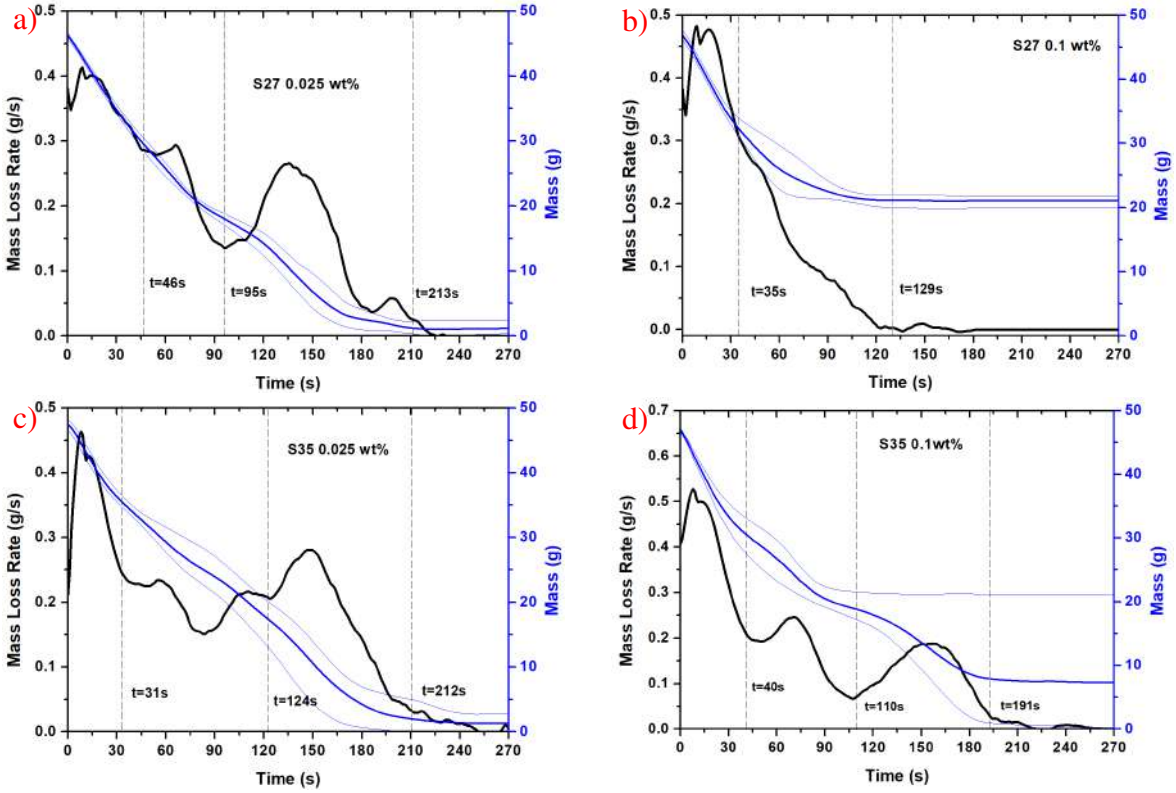

Figure 6.2: *Comparative analysis of mass loss rate and total mass for Excelsior with a) S27-0.025 wt% b) S27-0.1 wt%, c) S35 0.025 wt% and d) S35 0.1 wt%.*

The experimental results provide a clear hierarchy in terms of the average mass loss over

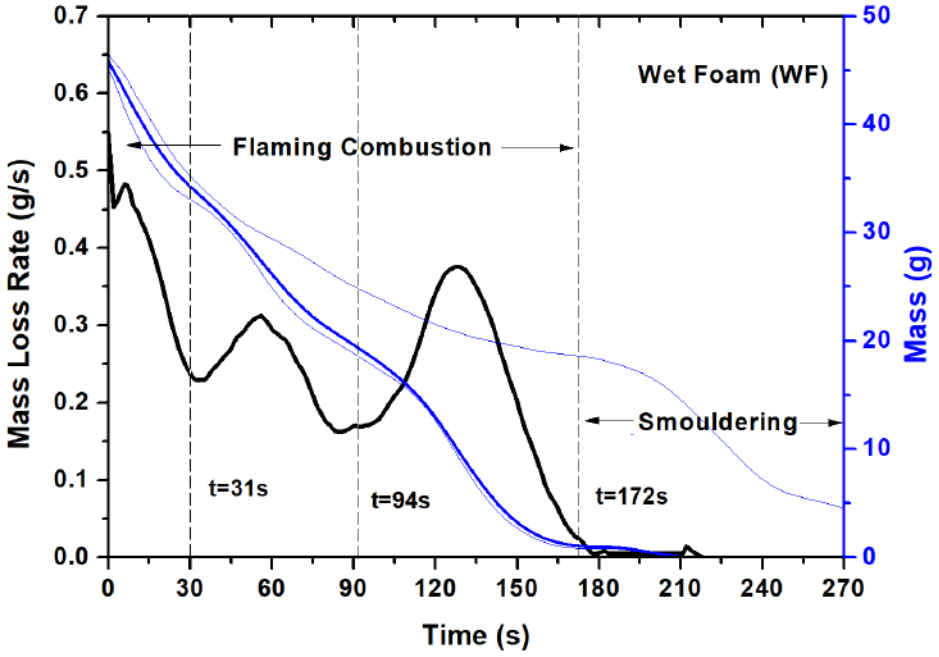

Figure 6.3: *Mass loss rate and total mass loss over time for plain wet foam.*

time of the Excelsior fuel and the effectiveness of various suppressants as shown in Figure 6.4. At the baseline, dry fuel exhibited the highest mass loss rate, with no intervening agents to inhibit the fire. Foam solution achieved some reduction in the mass loss rate, indicating its superior performance over mere water in fire suppression. The peak of fire retardation was attained with the integration of NPs into the dry foam (DF). This combination not only exceeded the abilities of plain foam singularly but also demonstrated the most efficient approach in our investigation for hindering the combustion of the Excelsior fuel.

The experimental data obtained supports our hypothesis. The incorporation of NPs resulted in a noticeable reduction in surface tension within the foam solution. This might have played a pivotal role in modifying the burning of Excelsior. Moreover, higher NP concentration in the fire suppressant solution significantly affects the mass loss rate of the fuel. The mass loss versus time exhibited a decelerated trend, which suggests extended material integrity under fire exposure. On the other hand, the curves demonstrating the mass loss rate over time exhibited an important reduction (see Figure 6.4b)), suggesting a decrease in the rate of material consumption whilst burning.

The baseline (DF-00) containing zero concentration of NPs shows a consistent mass loss rate. This indicates a reduction in the peak mass loss rate compared to the DF-00 when NPs are added, suggesting an improvement in fire retardancy.

It is important to mention that after the initial combustion phase of the dry Excelsior, the dry foam formulations with NPs seem to stabilise and maintain a lower mass loss rate than DF-00 suggesting a potential fire retardant effect. The presence of the peak after 160 s could

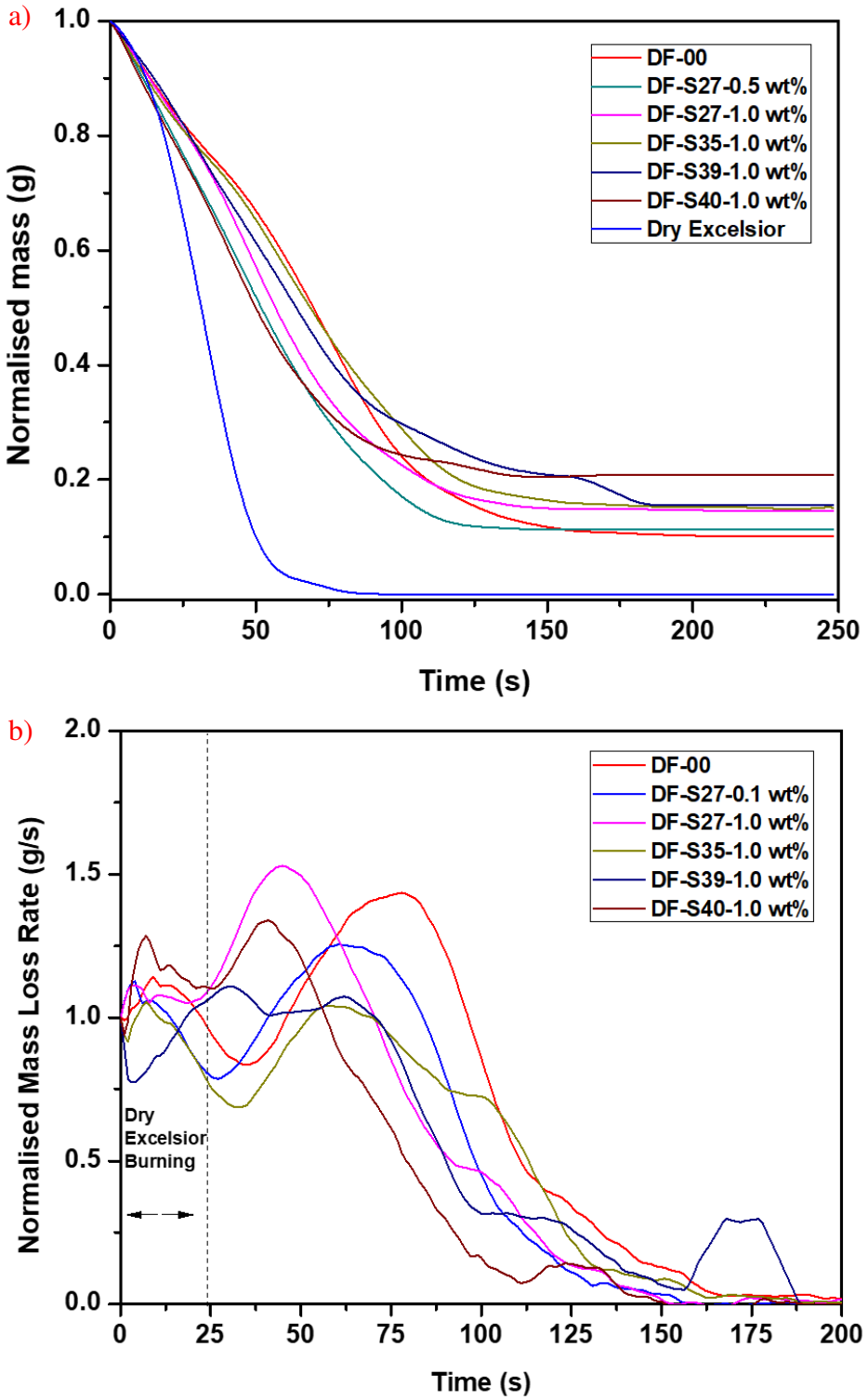

Figure 6.4: *Comparative analysis of a) mass loss over time between dry Excelsior and Excelsior treated with dry foam and NPs, b) variability in degradation speed throughout time for the dry foam with or without NPs.*

indicate secondary combustion or possible inconsistencies in the foam application or the arrangement of the Excelsior itself.

6.2.2 Flame height

Flame height was studied to analyse the impact of various types and concentrations of NPs applied to the Excelsior fuel. ImageJ software [239] was employed to determine the flame heights, and an average was extracted from three measurements for each replicate. This process was repeated for both the leading and trailing edges of the fire at three distinct distances 20 cm, 40 cm, and 60 cm to obtain a singular average flame height for each condition. Figures (6.5, 6.6 depict the flame height for different positions of the fire on the fuel bed, illustrating the leading and trailing edges to collect important information about its behaviour and understand the effect of NPs on the combustion process. The flame height, defined between the fuel bed surface and the top of the flame, increased with fire intensity in the dry section of Excelsior. Under no slope conditions, the fire fronts developed a curvilinear shape (like a U) during spread similar to the study of Morandini and his co-workers [240].

Two main cases are reported: the plain wet foam and the enhanced product with synthesised IONPs, which consistently managed to suppress the fire at a 40 cm distance from the fuel bed in all experimental replicates. This phenomenon is shown in Figure 6.6, where the flame height initially starts very high when burning the dry Excelsior used as the ignition source, then moves on to Figure 6.6b), which shows the trailing edge of the fire sufficiently reduced, indicating that a lot of heat has been dissipated. This is visible in Figure 6.6 c) and d), where we can see that the leading edge of the fire at 40 cm and 60 cm is lowered due to the protective layer formed by the wet foam with IONPs, which have high thermal stability and can withstand high temperatures, stopping the fire at 40 cm and preventing it from moving further while leaving one-third of the residual mass of the fuel unburned.

However, in the case of the commercially available plain wet foam, which only contains foam concentrate and water, all replicates completely burned the whole mass of Excelsior, unable to stop the fire. This is attributed to the poor stability of the foam, which fails to provide a protective layer that can stop the fire and suppress the oxygen from the surface or interact with the chemical or gaseous species produced from the combustion process of Excelsior. In the case of the wet foam, as seen in Figure 6.5, the fire propagates rigorously, although there is a small reduction in flame height. Table 6.2 presents the flame heights for various concentrations of wet foam and NPs, highlighting the notable impact of NPs on flame height reduction. More specifically, sample WF-S27-0.1 wt% demonstrated a significant effect by stopping fire propagation at a 40 cm distance from the fuel bed repeatedly.

As depicted in Figure 6.7, the average height of various wet foam formulations decreases with increasing distance from the spot ignition. Higher concentrations of foam, such as WF-S39-0.1 wt% and WF-S27-0.1 wt%, demonstrate better structural integrity and lower heights compared to lower concentrations or the control formulation (WF-00). This indicates the enhanced performance of higher concentration foams in maintaining coverage and

Figure 6.5: *Flame heights at leading and trailing edges of fire for Excelsior fuel covered with plain wet foam (WF-00) at various positions across the fuel bed: a) leading edge at 20 cm, b) trailing edge at 20 cm, c) leading edge at 40 cm, d) trailing edge at 40 cm, and e) leading edge at 60 cm.*

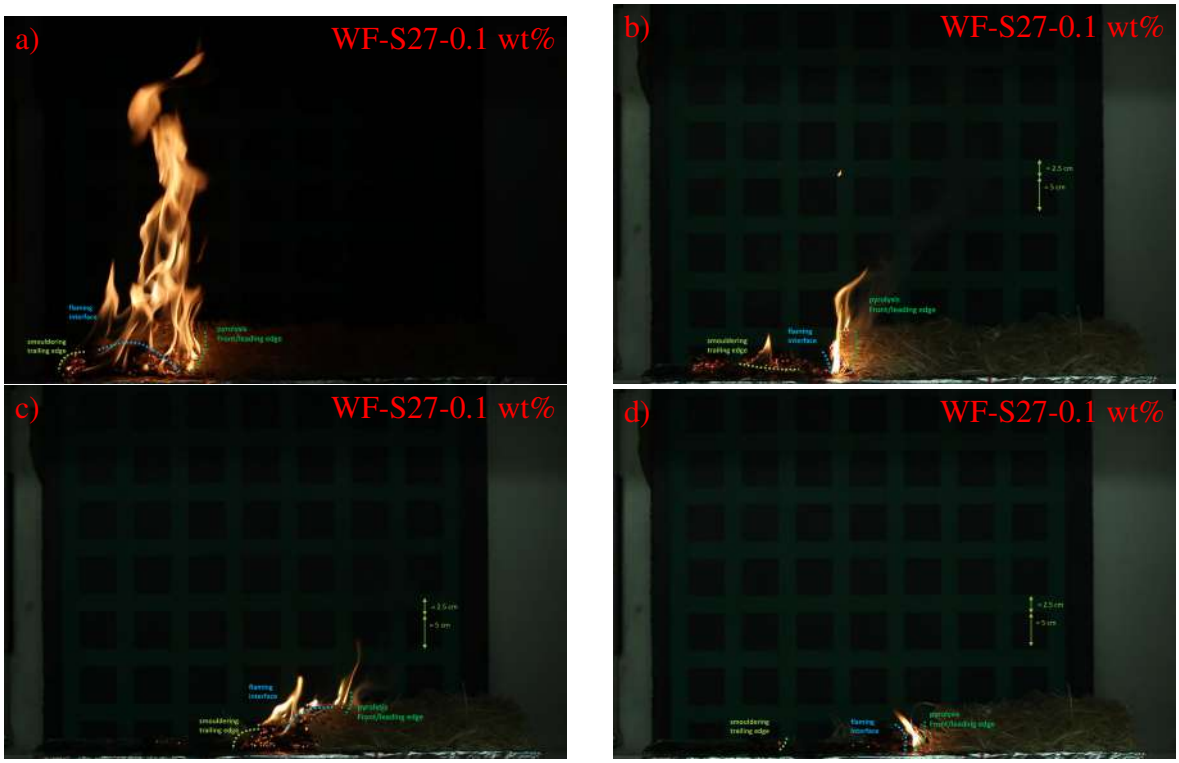

Figure 6.6: *Flame heights at leading and trailing edges of fire for Excelsior fuel covered with wet foam and synthesised IONPs (WF-S27-0.1 wt%) at various positions across the fuel bed: a) leading edge at 20 cm, b) trailing edge at 20 cm, c) leading edge at 40 cm, d) trailing edge at 40 cm.*

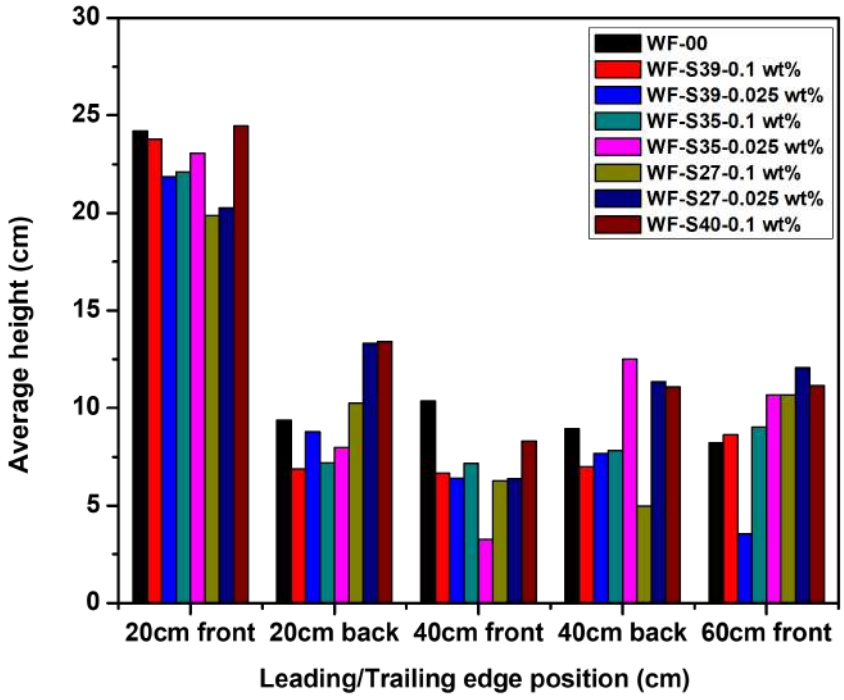

Figure 6.7: *Average height (cm) of wet foam formulations at various leading and trailing edge positions of the fire (20 cm front, 20 cm back, 40 cm front, 40 cm back, 60 cm front).*

effectiveness.

Nano-sized additives can provide excellent fire retardant performance at low concentrations due to their very large specific surface area, resulting in improved interfacial interactions and dispersion [241].

IONPs improve the thermal insulation properties of the foam layer and affect the efficiency of extinguishing and controlling fires [194]. In our experiment, the fire was stopped because the addition of IONPs improved the thermal insulation properties of the foam layer and avoided rapid cracking of the wet foam caused by too high external temperature. Also, another possible explanation for this phenomenon is the capture of radicals discussed in subsection 2.6.3. The flammability of Excelsior depends on the concentration of radicals and by capturing them effectively, eliminates the material's ability to burn.

Beyond their capacity to capture OH radicals in fires, IONPs, when incorporated into water as additives in larger concentrations, change in hydrodynamic size (see Appendix D, Figure D.3). This alteration potentially limits their reactivity with specific chemical or gaseous species in the fire when introduced through the foam.

More specifically the high specific surface area of IONPs at this concentration for the wet foam can absorb a large number of free radicals needed for combustion to quench. Eventually, this interrupts the chain reaction and leads to fire extinguishing. Finally, appropriate dispersion and stability of the foam containing NPs dispersed in other components have a positive effect on the extinguishing efficiency and control of solid fires [113].

Figures 6.9, 6.10, display the flame heights for the dry foam formulation with and without the most effective additive identified in previous experiments with wet foam, using the same concentration of IONPs and water amount to produce the dry foam via the double syringe technique (see Figure 3.4). These figures also reveal the fire intensity, which varies across the fuel bed, primarily spreading through the Excelsior. Figure 6.9, showcasing the plain dry Class A foam, indicates significantly high flame heights, demonstrating the fire's high intensity and its ability to spread more easily across the fuel bed. Conversely, the dry foam with IONPs shows a notable reduction in flame height, nearly halving it when the leading edge of the fire reaches about 20 cm from the fuel bed, as seen in Figure 6.8. This suggests the enhanced foam with IONPs likely influences solid mass transport, slowing the rate at which the fire burns through the fuel, as discussed in the subsection 6.2.3 on the rate of spread.

However, within the combustion zone, areas exist where the drained liquid has not reached, leaving parts of the Excelsior exposed. These dry sections create vulnerabilities, allowing the fire to identify and propagate through the fuel bed, albeit with some resistance. This is evident in Figure 6.10c), where the leading edge of the fire at 40 cm shows the lowest flame height but still manages to propagate underneath and along the sides of the fuel bed. This results in the fire eventually penetrating through but leaving a greater residual mass than what is observed with the plain dry foam as shown in Table 6.6.

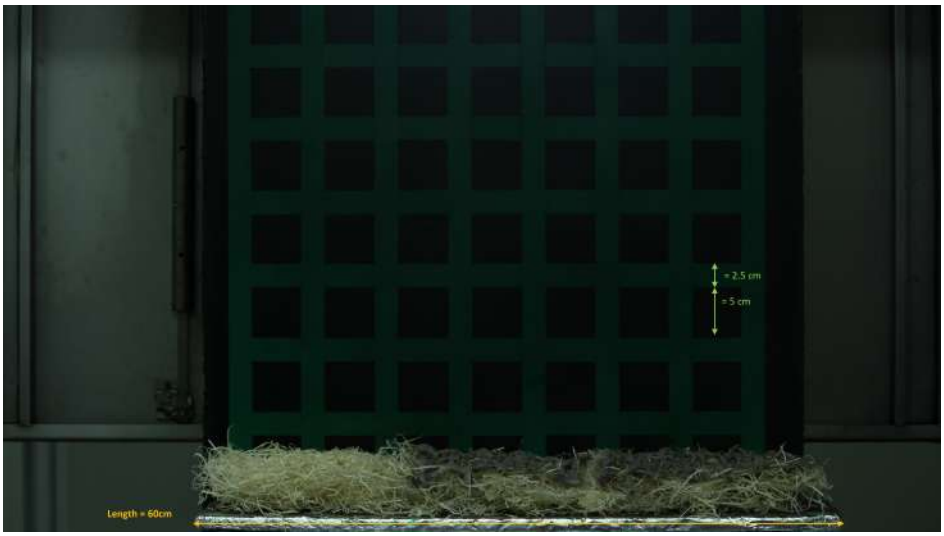

Figure 6.8: *Excelsior fuel covered with Sample DF-S27-0.1 wt%.*

In Appendix E, additional visualisations of flame heights based on the application of both wet and dry foam at varying NP concentrations are presented, showcasing both the leading and trailing edges of the fire at 20 cm, 40 cm, and 60 cm above the fuel bed layered with Excelsior (see methodology 3 Figure 3.8). This comparison aids in understanding the impact of foam type and NP concentration on flame propagation.

As can be seen from Table 6.1, the addition of iron oxide nanoparticles (IONPs) to the foam results in lower average flame heights compared to the commercial foam (DF-00), suggesting that the combustion process is affected by the IONPs. The front flame height of the fire at 20 cm (8.92 cm) from the fuel bed is achieved with the highest concentration (1.0%), indicating an increase in suppression effectiveness.

For the back front of the fire at 20 cm, the lowest average flame height was observed with a 1.0% concentration of IONPs synthesised by the hydrothermal method at 4.97 cm, which is significantly lower than the plain foam's 22.9 cm.

For distances at 40 cm and 60 cm, the flame heights appear to be lower for higher concentrations of IONPs (0.5% and 1.0%). The enhanced stability of the foam, as examined in our previous research [242], contributed to the retention of more liquid over time, thereby serving as a cooling agent and diminishing the flame height. NPs with a reduced size could be adsorbed at the gas-liquid interface [243] to make films more stable thus withstanding higher temperatures. This enhanced performance could also be attributed to the nanoparticles' ability to absorb heat, thus reducing the flame's temperature.

6.2.3 Flame spread

In calculating the fire's rate of spread, the selected measurement range for the distance from the fuel bed was from 20 cm up to 60 cm as shown in Figure 6.11. This decision was

Figure 6.9: *Flame heights at leading and trailing edges of fire for Excelsior fuel covered with plain dry foam (DF-00) at various positions across the fuel bed: a) leading edge at 20 cm, b) trailing edge at 20 cm, c) leading edge at 40 cm, d) trailing edge at 40 cm, and e) leading edge at 60 cm.*

Figure 6.10: *Flame heights at leading and trailing edges of fire for Excelsior fuel covered with dry foam and synthesised IONPs (DF-S27-0.1 wt%) at various positions across the fuel bed: a) leading edge at 20 cm, b) trailing edge at 20 cm, c) leading edge at 40 cm, d) trailing edge at 40 cm, and e) leading edge at 60 cm.*

Foam formulation	Distance(Fuel bed)	Average flame height (cm)
DF-00	20cm front	20.13
	20cm back	22.9
	40cm front	3.55
	40cm back	7.04
	60cm front	5.48
DF-S27-0.1%	20cm front	10.75
	20cm back	7.66
	40cm front	4.16
	40cm back	6.2
	60cm front	5.61
DF-S27-0.5%	20cm front	14.1
	20cm back	7.39
	40cm front	5.62
	40cm back	7.4
	60cm front	3.22
DF-S27-1.0%	20cm front	8.92
	20cm back	4.97
	40cm front	4.67
	40cm back	6.18
	60cm front	3.77
DF-S35-1.0%	20cm front	10.61
	20cm back	4.98
	40cm front	3.88
	40cm back	5.42
	60cm front	3.26
DF-S39-1.0%	20cm front	10.75
	20cm back	3.65
	40cm front	3.30
	40cm back	4.64
	60cm front	4.62
DF-S40-1.0%	20cm front	13.56
	20cm back	5.97
	40cm front	6.34
	40cm back	6.06
	60cm front	6.86

Table 6.1: *Flame heights for dry foam (DF) formulations.*

Foam formulation	Distance(Fuel bed)	Average flame height (cm)
WF-00	20cm front	24.22
	20cm back	9.39
	40cm front	10.36
	40cm back	8.92
	60cm front	8.22
WF-S39-0.1%%	20cm front	23.79
	20cm back	6.88
	40cm front	6.66
	40cm back	7.00
	60cm front	8.63
WF-S39-0.025%	20cm front	21.86
	20cm back	8.78
	40cm front	6.41
	40cm back	7.66
	60cm front	3.55
WF-S35-0.1%	20cm front	22.108
	20cm back	7.188
	40cm front	7.158
	40cm back	7.828
	60cm front	9.022
WF-S35-0.025%	20cm front	23.051
	20cm back	7.974
	40cm front	3.280
	40cm back	12.500
	60cm front	10.662
WF-S27-0.1%	20cm front	19.877
	20cm back	10.253
	40cm front	6.267
	40cm back	4.971
WF-S27-0.025%	20cm front	20.252
	20cm back	13.309
	40cm front	6.386
	40cm back	11.346
	60cm front	12.067
WF-S40-0.1%	20cm front	28.457
	20cm back	13.410
	40cm front	8.323
	40cm back	11.089
	60cm front	11.145

Table 6.2: *Flame heights for wet foam (WF) formulations.*

based on the observation that the initial 0 to 20 cm segment contained only dry Excelsior, whereas, beyond 20 cm, the Excelsior was embedded and covered with either wet or dry foam formulations. This range was selected to specifically assess the impact of synthesised and commercial NPs on reducing the rate of flame spread. Previous experiments [225], have shown that fires were able to attain a quasi-state rate of spread within a distance from the ignition line, thereby enabling a more defined and controlled assessment of each experiment's outcomes.

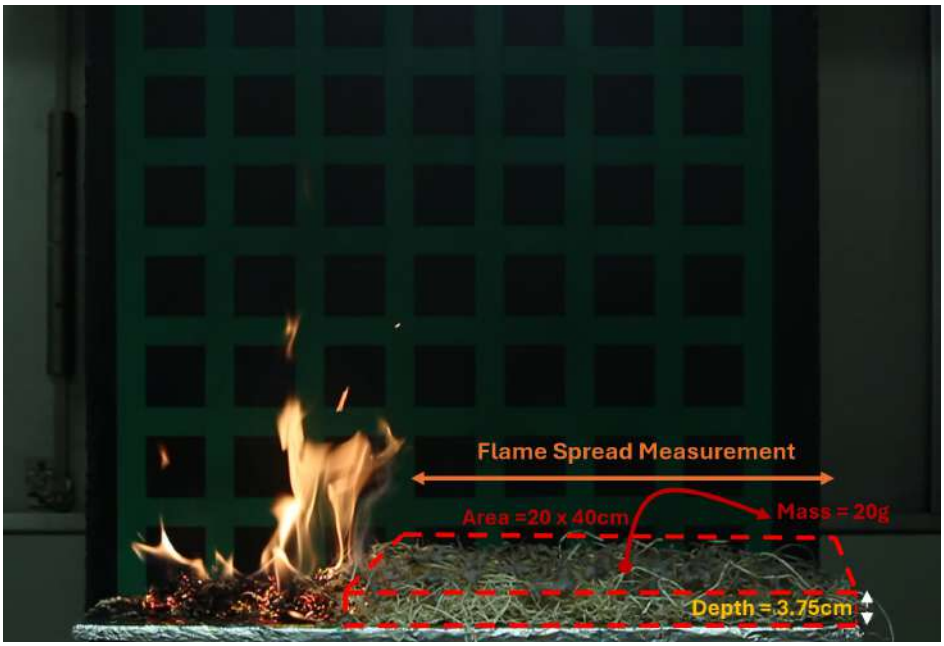

Figure 6.11: *Measurement of flame spread on excelsior treated with foam containing iron oxide nanoparticles as additives.*

Table 6.3 and Table 6.4 list the fire spread rates from all fire experiments. Incorporating NPs into the wet foam formulations decreases the rate of fire spread. In comparing the outcomes of wet foam to dry foam, the initial spread rate for dry foam without additives is 0.752 cm/s. However, the addition of nanoparticles such as DF-S27-0.1% and S27-0.5% results in a modest reduction in spread rates to 0.680 cm/s and 0.707 cm/s, respectively.

Conversely, using S27-1.0% does not decrease but rather increases the spread rate to 1.025 cm/s, suggesting that higher concentrations of this NP type may not be effective in reducing the spread rate. The addition of commercially available silicon dioxide nanoparticles (SiO_2-S40-1.0 wt%), while increasing the residual mass post-burn, does not appear to slow the fire's spread rate, which increases to 1.21 cm/s.

As depicted in Figure 6.12, the average rate of spread (ROS) for various wet foam formulations shows a clear trend where the control formulation (WF-00) has the highest ROS. This indicates its limited effectiveness in slowing fire spread compared to the other formulations. Higher concentration foams, such as WF-S40-0.1 wt% and WF-S39-0.1 wt%, exhibit

significantly lower ROS values, demonstrating their superior performance in reducing fire spread.

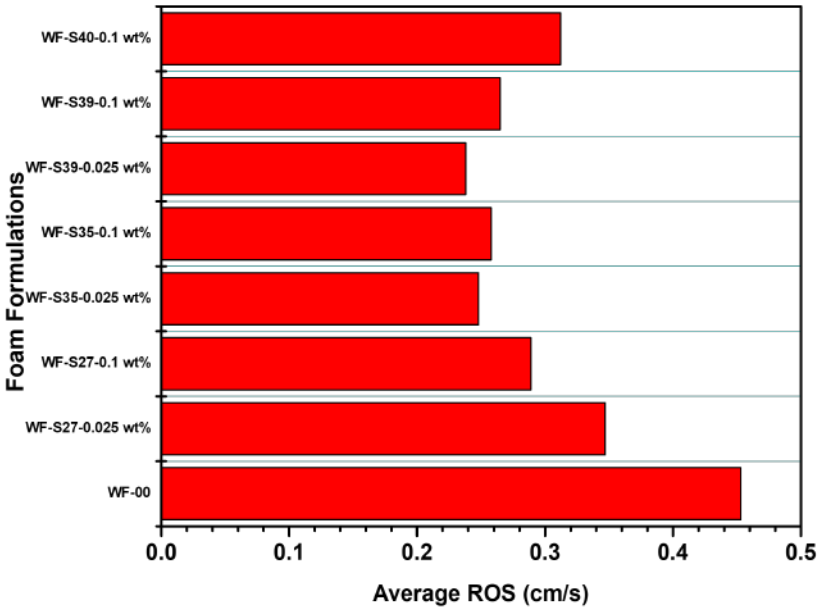

Figure 6.12: *Average rate of spread (ROS) in cm/s for various wet foam formulations.*

Dry Excelsior depicts the highest rate of spread (ROS) with an average of approximately 1.909 cm/s. This shows the clear and rapid combustion of dry Excelsior when not treated with any fire-suppressant additives. The combustion is significantly faster than the other setups where foams, wet or dry (WF, DF) were applied, highlighting the effectiveness of these types of foams in slowing down the fire's spread.

In the case of experiments with wet and dry foams, the average ROS varies depending on the specific NPs formulation with average ROS values of foam as additive being lower than that of dry Excelsior. This variance suggest that NPs can indeed enhance foam's fire suppression properties. The observation that the average rate of spread (ROS) for certain dry foam (DF) formulations is higher than that of the baseline (DF-00) could be related to the distribution and coverage of the foam on the Excelsior.

As shown in Figure 6.13, the average rate of spread (ROS) for various dry foam formulations decreases with increasing foam concentration. The highest ROS is observed for dry excelsior, indicating its rapid fire spread capability. In contrast, the foam formulations, particularly those with higher concentrations such as DF-S40-1.0 wt% and DF-S39-1.0 wt%, exhibit significantly lower ROS values, demonstrating their effectiveness in slowing the fire spread.

Experiment	Distance Traveled (cm)	Time (s)	ROS (cm/s)	Average ROS (cm/s)
WF-00	20 to 40	63	0.317	0.453 ± 0.06
	40 to 60	34	0.588	
WF-S39-0.1%	20 to 40	79.4	0.252	0.265 ± 0.007
	40 to 60	72	0.278	
WF-S39-0.025%	20 to 40	126.3	0.158	0.238 ± 0.04
	40 to 60	63	0.317	
WF-S35-0.1%	20 to 40	65	0.308	0.258 ± 0.027
	40 to 60	96.25	0.208	
WF-S35-0.025%	20 to 40	86	0.233	0.248 ± 0.008
	40 to 60	76	0.263	
WF-S27-0.1%	20 to 40	69.3	0.289	0.289 ± 0.025
	40 to 60	-	-	
WF-S27-0.025%	20 to 40	48.4	0.413	0.347 ± 0.03
	40 to 60	71.3	0.281	
WF-S40-0.1%	20 to 40	66	0.303	0.312 ± 0.005
	40 to 60	62.3	0.321	

Table 6.3: *Rate of spread for fire experiments with wet foam (WF).*

Experiment	Distance Traveled (cm)	Time (s)	ROS (cm/s)	Average ROS (cm/s)
DF-00	20 to 40	23.7	0.844	0.752 ± 0.05
	40 to 60	30.3	0.660	
DF-S27-0.1%	20 to 40	38	0.526	0.680 ± 0.08
	40 to 60	24	0.833	
DF-S27-0.5%	20 to 40	24.0	0.833	0.707 ± 0.07
	40 to 60	34.4	0.581	
DF-S27-1.0%	20 to 40	30.7	0.651	1.025 ± 0.18
	40 to 60	14.3	1.399	
DF-S35-1.0%	20 to 40	40.0	0.500	0.875 ± 0.16
	40 to 60	16.0	1.250	
DF-S39-1.0%	20 to 40	26.4	0.758	0.842 ± 0.04
	40 to 60	21.6	0.926	
DF-S40-1.0%	20 to 40	18.75	1.067	1.248 ± 0.1
	40 to 60	14.0	1.429	

Table 6.4: *Rate of spread for fire experiments with dry foam (DF).*

Experiment	Distance Traveled (cm)	Time (s)	ROS1 (cm/s)	Average ROS (cm/s)
Dry Excelsior	20 to 40	11	1.818	1.909 ± 0.05
	40 to 60	10	2.000	

Table 6.5: *Rate of spread for dry Excelsior without any foam.*

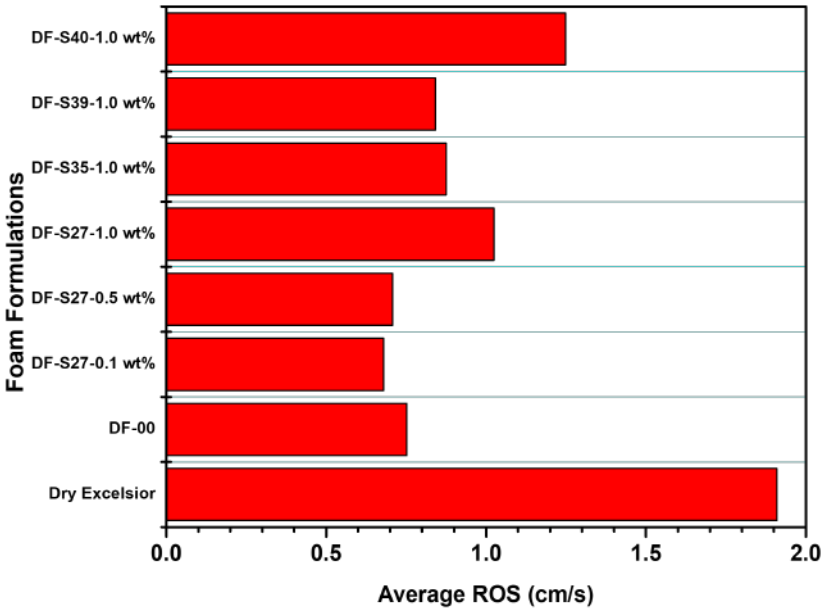

Figure 6.13: *Average rate of spread (ROS) in cm/s for various dry foam formulations and dry excelsior.*

Dry foam is structurally different from wet foam as it has a stiffer and more aerated consistency that might not adhere as uniformly or extensively to the surface of Excelsior as wet foam does. This characteristic could lead to uneven coverage of the Excelsior, leaving some areas less protected and more prone for the fire to be spread.

In contrast, wet foam, with its less structured and more fluid nature, can more easily coat the Excelsior's surface, providing a more uniform and solid barrier against fire. The uniform coverage helps to lower the combustion process across the surface area, effectively reducing the ROS when compared to some dry foam experiments and even suppressing the fire in one of the cases.

This phenomenon highlights the importance of not just the type and concentration of NPs used as fire suppressant additives but also their physical properties and application techniques. For dry foam the challenge relies on optimising the foam's consistency and application method to achieve a more even distribution to enhance its fire suppression capabilities despite its inherent structural limitations.

Between the same quantities of liquid used to generate wet and dry foams, it appears that wet foam offers better distribution due to its structure, leading to lower ROS compared to dry foam. This outcome can be attributed to the fact that the inherent physical properties of wet foam allows it to spread more uniformly over the surface, thus providing a more robust

barrier against fire by filling gaps and covering the material more effectively. Consequently, in fire scenarios where the same volume of liquid is used to produce both types of foam, the wet foam performs better and leads to more effective fire retardancy, as evidenced by lower ROS values. This distinction mainly highlights the critical role of foam structure and distribution in optimising the efficiency enhancement of the Class A Foam.

6.2.4 Residual Mass

The residual mass of Excelsior was analysed as it provides a quantitative measure of the fire's suppression capabilities, indicating the extent of Excelsior consumption during combustion. The resulting mass reflects the combination of either the wet foam's application alongside the original weight of the Excelsior or the integration of the dry foam with the Excelsior. This distinction is crucial for assessing the fire retardant efficacy of various foam formulations enhanced with NPs. For dry Excelsior without any additives, the residual mass was found to be zero, which aligns with the fact that it has a high consumption rate of over 90%.

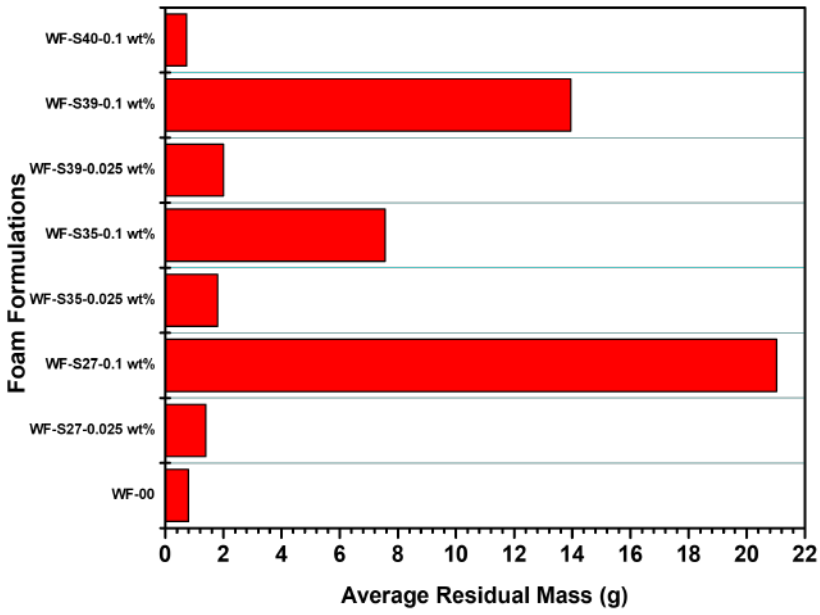

Figure 6.14: *Average residual mass (g) for various wet foam formulations.*

As shown in Figure 6.14, the average residual mass for various wet foam formulations increases with higher foam concentrations. The formulations with the highest concentrations, such as WF-S39-0.1 wt% and WF-S27-0.1 wt%, exhibit the highest residual masses, indicating their effectiveness in leaving substantial residual material. The control formulation (WF-00) has the lowest residual mass, highlighting its limited capability in comparison to the other tested foams.

Tables 6.6 and 6.7 detail how different NP concentrations can refine the efficacy of standard Class A foam, with higher concentrations typically resulting in a greater residual mass, while lower concentrations comparable to the foam alone leave less than two grams, indicating significant Excelsior consumption. However, when adding commercial silica (SiO_2) NPs, the residual mass mirrors that of the standard foam, even at a 0.1% concentration.

Moreover, Table 6.7 presents the average residual mass when the dry foam is applied to the Excelsior surface, covering about 20 grams of the initial 30 grams. The addition of NPs further elevates the residual mass compared to the base dry foam, showcasing enhanced retardant capabilities, notably in samples DF-S27-0.1 wt%, DF-S39-1.0 wt%, and DF-S40-1.0 wt%.

Foam Formulation	**Average Residual Mass (g)**
WF-00	0.8 ± 0.68
WF-S39-0.1%	13.96 ± 3.6
WF-S39-0.025%	2.3 ± 0.79
WF-S35-0.1%	7.56 ± 2.34
WF-S39-0.025%	1.8 ± 0.76
WF-S27-0.1%	21.7 ± 0.79
WF-S27-0.025%	1.4 ± 0.93
WF-S40-0.1%	0.8 ± 0.7

Table 6.6: *Average residual mass for wet foam formulations.*

Foam Formulation	**Average Residual Mass (g)**
DF-00	4.9 ± 1.52
DF-S27-0.1%	9.6 ± 3.34
DF-S27-0.5%	5.5 ± 2.41
DF-S27-1.0%	7.3 ± 1.02
DF-S35-1.0%	7.5 ± 1.6
DF-S39-1.0%	10.4 ± 2.65
DF-S40-1.0%	10.2 ± 1.55

Table 6.7: *Average residual mass for dry foam formulations.*

As shown in Figure 6.15, the average residual mass for various dry foam formulations increases with higher foam concentrations. The formulations with the highest concentrations, such as DF-S40-1.0 wt% and DF-S39-1.0 wt%, exhibit the highest residual masses, indicating their effectiveness in leaving substantial residual material. The control formulation (DF-00) has the lowest residual mass, highlighting its limited capability in comparison to the other tested foams. This trend correlates with the results observed in the wet foam experiments, where higher concentrations also resulted in greater residual mass.

Finally, the structure of the Excelsior, particularly the density and arrangement of its strands,

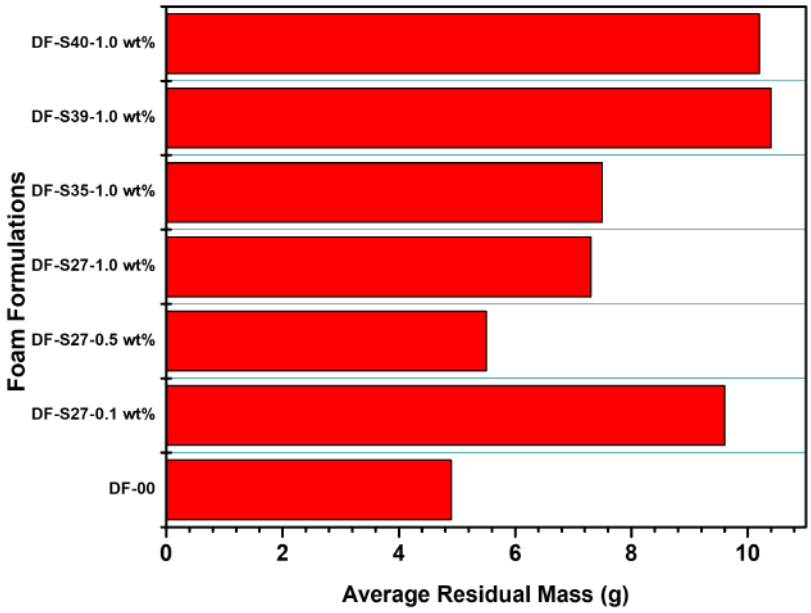

Figure 6.15: *Average residual mass (g) for various dry foam formulations.*

plays a significant and influential role in these experiments. The persistence of the fire beneath the foam and along the edges of the Excelsior, coupled with variables such as the compactness of the strands, adds complexity to the evaluation of the fire spread rate when 20 mL of liquid and 120 mL of foam volume are applied to its surface.

6.2.5 Flame surface area

The average flame surface area of the wet foam, with and without nanoparticles (NPs), was quantified from video recordings, and Python was utilised to analyse the results as listed in Appendix B. This area describes the average area over which the flame spreads over time.

The flame surface area is crucial in studying the combustion processes as it is a quantitative measure of the interface over which the combustion reaction takes place. This metric also depicts the flame propagation over time and the overall efficiency of the combustion. A larger flame surface area indicates a higher rate of fuel consumption. The flame surface area per time is defined as the rate at which the surface area of a flame front changes over time.

Figure 6.16, shows the average flame surface area per time of dry Excelsior, wet foam and the type and concentration of NPs that looked promising as additives in the previous sections. This is significantly higher than that of Excelsior treated with the enhanced foam. This suggests that the new foam with NPs effectively reduces the rate of flame spread and the intensity of the fire by limiting the available surface area for combustion or by interfering

with the combustion process itself.

Comparing the plain wet foam (Figure 6.16b))to the enhanced NPs that managed to suppress fires in all of the replicates (Figure 6.16c)), we can see that the addition of NPs to the foam play a significant role to its fire suppression capabilities. The high average flame surface of the dry Excelsior ($275\,cm^2/s$), as observed in Figure 6.16a), demonstrates its rapid and vigorous combustion in a short period. The application of plain wet foam brings a reduction of the flame surface to $111\,cm^2/s$ which is expected as the Excelsior has more moisture content and the foam prolongs the combustion process over a longer period up to 200 seconds. However, when applying the wet foam with IONPs at 0.1 wt% on the Excelsior, the reduction of the flame surface area to $101\,cm^2/s$ from $111\,cm^2/s$ indicates they can promote better heat absorption, forming a more effective barrier to oxygen or catalysing the breakdown of combustible gases. This three-dimensional grid shows in all cases with NPs, there is a delay in fire spread to the nearest fuel along the x-axis, as observed on the z-axis, while maintaining reduced flame heights indicated by the y-axis. The distinct variation is observed in the fire suppression capabilities presented in Figure 6.16c) where the fire is stopped on an average time of 129 seconds consistently across all replicates as evidenced in Figure 6.2b).

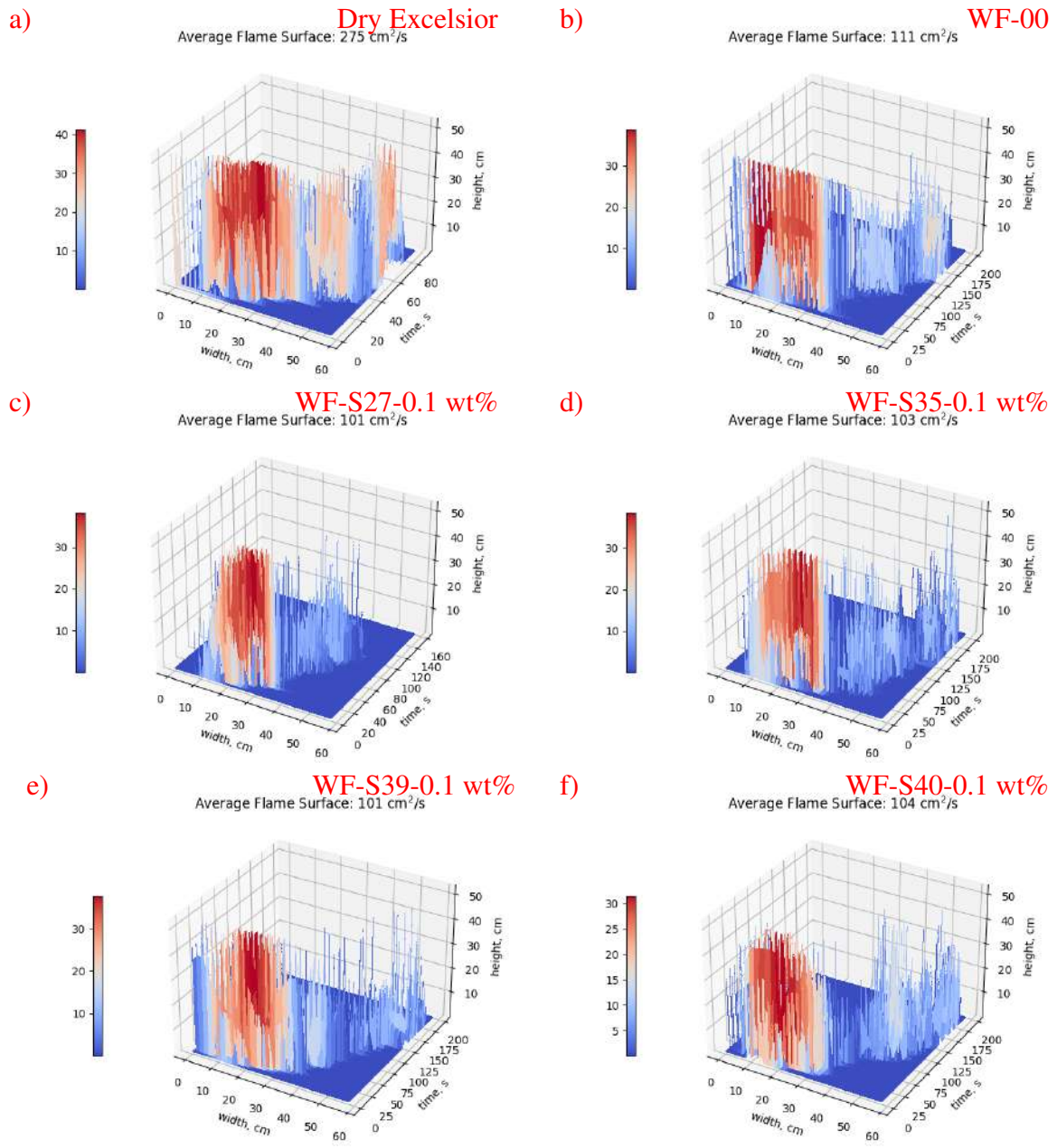

Figure 6.16: *Average flame surface area over time for a) Dry Excelsior, b) Plain wet foam (WF-00), c) WF-S27-0.1 wt%, d) WF-S35-0.1 wt%, e) WF-S39-0.1 wt%, f) WF-S40-0.1 wt%.*

Different materials, such as NPs-enhanced foam, have different molecular structures that influence their combustion behaviour, potentially altering the sooting properties of the flame [244] when applied to Excelsior. This could lead to variations in the effectiveness of fire suppression based on the type and concentration of NPs synthesised and used.

The presence of IONPs as fire retardants, especially in sooting conditions, can lead to significant heat losses. Flame temperature can be lowered due to heat losses from flame radiation, thus lowering the overall reaction rate [245].

6.2.6 Summary and Conclusions

This chapter discussed the impact of NP concentrations on the fire suppression efficiency of Excelsior treated with different foam formulations. Experiments revealed that the untreated Excelsior burns rapidly leaving no mass behind while the introduction of IONPs significantly slows down the combustion process. The analysis of mass loss rates indicated that higher concentrations of NPs enhance the fire-retardant capabilities of the foam possibly due to the formation of a protective layer and the capture of radicals that absorb heat and delay the combustion process. This was further supported by the reduced flame height, flame spread rate and a greater residual mass of Excelsior fuel unburned, highlighting the NPs' potential to enhance the fire retardant performance due to their large specific surface area and thermal stability. The results demonstrated that IONPs significantly influence fire retardancy while in one case consistent flame suppression was achieved.

Moreover, wet foam (WF) does not have a structure and penetrates throughout the depth of the vegetation, contrasting with dry foam which maintains a structural integrity causing it to remain as a blanket on the top of the vegetation. This distinction leads to two different fire suppression strategies. Dry foam (DF), with its blanket application, impedes the flame from radiating to the adjacent fuel on the surface, whereas wet foam acts as a heat sink, which starves the burning front of thermal energy reducing its ability to spread to the adjacent fuel. Although dry foam can prevent flame propagation on the surface of the fuel, smouldering can still take place beneath this protective layer. On the other hand, wet foam allows for flame spread but at a reduced rate due to its moisture in depth.

The quantification of the average flame surface area for the wet foam illustrates a clear advantage of using NP-enhanced foam for fire suppression. The three-dimensional data analysis indicates that IONPs, apart from forming a protective layer, exhibit the potential to capture free radicals and reduce the flame surface area. The enhanced foam's efficiency in extinguishing the fire within an average of 129 seconds supports the hypothesis that IONPs at 0.1 wt% contribute to altering the molecular structure of the combustion surface and affect the sooting properties of the fire thus effectively achieving fire suppression.

Finally, our findings indicate that dry foam leads to a lower but quicker spread of fire, whereas wet foam results in a taller but slower flame spread. The conclusion drawn is that an optimal firefighting foam would incorporate characteristics of both wet and dry foams.

Chapter 7

Conclusions

7.1 Summary of key findings

The research presented in this thesis successfully enhanced the fire suppression performance of Class A foams by incorporating nanoparticles with tailored properties. Each objective set out at the beginning of the study was systematically achieved, and the key findings are summarised below.

The first objective was to synthesise nanoparticles with desirable properties that enhance their effectiveness in fire suppression. Through hydrothermal and reflux methods, various iron oxide nanoparticles (IONPs), along with IONPs/SiO_2 NPs and commercial SiO_2 NPs, were synthesised. These synthesis techniques allowed for precise control over the nanoparticles' characteristics, leading to reduced agglomeration and smaller particle sizes. Characterisation using SEM, XRD, FTIR, and TGA confirmed that the synthesised nanoparticles exhibited high crystallinity, thermal resistance, and uniform morphology, demonstrating their suitability for enhancing fire suppression foams.

The second objective involved identifying the optimal concentration of nanoparticles in the foam solution. It was found that higher concentrations, such as 1.0 wt%, led to increased agglomeration, negatively affecting the foam's properties. In contrast, a concentration of around 0.1 wt% was found to be most effective, significantly improving the foam's stability, structure, and wetting properties by modifying bubble morphology and reducing surface tension.

The third objective focused on producing an enhanced Class A foam with uniformly distributed nanoparticles. This was achieved by carefully adjusting the nanoparticle concentration and mixing speed using an overhead stirrer. The enhanced foams demonstrated superior properties compared to those without nanoparticles, achieving the goal of uniform distribution and improved performance.

The final objective was to test the enhanced Class A foam on real fires and record perfor-

mance metrics. Controlled fire suppression tests were conducted using Excelsior fuel, chosen for its consistent burning properties. The enhanced foam, applied via airbrush and double syringe techniques, showed significant improvements in fire suppression metrics. These included a reduced mass loss rate (MLR), lower flame height and spread, and increased residual mass after burning. The improvements were attributed to the nanoparticles' ability to form protective barriers, alter the molecular structure of the fuel surface, and potentially capture radicals to inhibit fire propagation.

Three-dimensional data analysis further highlighted the positive impact of IONPs on combustion properties, suggesting alterations in the molecular structure of the combustion surface and affecting sooting properties, thus enhancing fire suppression effectiveness.

Comparative analysis of wet and dry foam applications revealed distinct advantages in their fire retardant strategies. This suggests an ideal firefighting foam that combines the benefits of both wet and dry foam to offer more effective fire suppression, indicating a new direction for future research.

In conclusion, this research successfully demonstrated that the addition of tailored nanoparticles significantly enhances the fire suppression performance of Class A foams, achieving the primary aim and objectives set out at the beginning of the study.

7.2 Original contribution to knowledge

- An extensive literature review on the use of Class A foams in forest fire suppression was conducted. This review identified several challenges such as rapid foam degradation due to gravity-induced drainage and bubble collapse as well as various nanoparticles used as fire suppression additives.
- A variety of Iron Oxide Nanoparticles (IONPs) with controllable characteristics were synthesised using hydrothermal and reflux methods. These nanoparticles were tailored to exhibit desirable properties such as reduced agglomeration and smaller particle size.
- Characterization techniques, including Scanning Electron Microscopy (SEM), X-ray Diffraction (XRD), Fourier Transform Infrared Spectroscopy (FTIR), and Thermogravimetric Analysis (TGA), were used to validate the desired properties of the nanoparticles, such as size uniformity, crystallinity, and resistance to degradation at high temperatures.
- The addition of these nanoparticles into Class A foams was investigated by adjusting their concentrations and mixing speed under an overhead stirrer. It was found that nanoparticles at higher concentrations, such as 1.0 wt%, led to higher agglomeration inside the foam solution, while concentrations around 0.1 wt% were most effective, improving the foam's stability, structure, and wetting properties by modifying bubble morphology and reducing surface tension.

- Foam stability was evaluated through tests on drainage, surface tension, particle size distribution, and bubble coalescence over time. The results indicated that liquid loss was delayed when nanoparticles were incorporated, thus keeping the foam wetter for longer, and the morphology of the bubbles remained stable over time.
- Small-scale fire experiments were conducted to test the enhanced foam on shredded wood wool fuel (Excelsior). These experiments demonstrated that the addition of synthesised IONPs significantly enhanced the fire suppression performance of the commercial Class A foam. This was evidenced by a slower mass loss rate, reduced flame height, decreased rate of spread, and increased residual mass post-burning.
- The enhanced fire suppression performance was attributed to the high thermal stability, large surface area, radical capture capabilities, and formation of a protective layer by the nanoparticles, acting as a firebreak.
- Comparative analysis between wet and dry foam applications highlighted unique benefits for enhanced fire control management, suggesting the potential for an ideal firefighting foam that leverages the advantages of both.
- The research demonstrated that incorporating tailored iron oxide nanoparticles into Class A foams significantly improves fire suppression performance, providing a new direction for future research and development in firefighting technology.

7.3 Future Work

Based on the results obtained, we suggest several directions for future work to enhance understanding and validate the findings, despite the repetition and consistency observed in our experimental outcomes.

We recommend future research to assess the ecological impact of Class A firefighting foams containing nanoparticles as additives. Additionally, exploring various foam delivery methods is essential to identify the most effective mechanism for drone incorporation and efficient dispersion over fuel to act as a firebreak. It would also be valuable to compare the effectiveness of different delivery methods designated for direct-fire attacks across both small and large-scale experiments.

Further investigation is necessary to examine how various types and concentrations of NPs influence the properties of the residual layer left after fuel combustion. This would help in understanding their distribution and the patterns of re-ignition.

In this study, we explored only one encapsulation method for IONPs/SiO_2. Future studies should consider alternative nanoparticles with this method to gather more data on enhancing fire suppression efficiency. Moreover, testing other fuels besides Excelsior could provide insights into a wider range of combustible materials, thus evaluating a broader spectrum of potential fire scenarios.

Future work should also focus on optimising the aerial delivery of the new firefighting foam by developing a specialised carrier system. Such a system would ensure the precise and controlled release of the fire suppressants, maximising coverage and efficacy across the forest vegetation. Integrating this technology with drone capabilities would revolutionise rapid response strategies, particularly in restricted areas. The design of this carrier must consider the aerodynamics of flight, the weight constraints of the drones to carry the product, and the importance of quick dispersal to effectively form a firebreak.

Continuing from this advancement, the targeted delivery of the foam product could be further refined by utilising other magnetite IONPs. These NPs possess inherent magnetic properties that could allow for the directional control of the foam, guiding it to specific areas of a fire. The application of an external magnetic field from the drone or a coordinated system could enhance the precision of foam placement on forest fuel, improving the suppression capabilities. Future work should investigate the feasibility of such magnetic guidance systems and assess their integration with drone technology for effective wildfire management.

Bibliography

[1] Wildland Fire Spread and Suppression (U.S. National Park Service).

[2] Use of Low, Medium, High expansion foam in firefighting. BIOEX.

[3] Arnaud Saint-James, Douglas J. Durian, David A. Weitz, and Updated by Staff. Foams. *Kirk-Othmer Encyclopedia of Chemical Technology*, pages 1–24, 2000.

[4] NWCG. Foam vs fire primer, October 1992.

[5] Anne Laure Fameau and Anniina Salonen. Effect of particles and aggregated structures on the foam stability and aging. *Comptes Rendus Physique*, 15:748–760, 10 2014.

[6] Laurier L. Schramm and Fred Wassmuth. Foams: basic principles. ACS Publications, 1994.

[7] Nurudeen Yekeen, Ahmad Kamal Idris, Muhammad A. Manan, Ali Mohamed Samin, Abdul Rahim Risal, and Tan Xin Kun. Bulk and bubble-scale experimental studies of influence of nanoparticles on foam stability. *Chinese Journal of Chemical Engineering*, 25(3):347–357, 2017.

[8] NWCG. Foam vs fire aerial applications, October 1995.

[9] Gregory T. Linteris, Marc D. Rumminger, and Valeri I. Babushok. Catalytic inhibition of laminar flames by transition metal compounds. *Progress in Energy and Combustion Science*, 34(3):288–329, June 2008.

[10] Andrew Burke. FOAM VS FIRE. Class A Foam for Wildland Fires. October 1993 Second Edition PMS NFES 2246.

[11] Frank A. Albini. Wildland Fires: Predicting the behavior of wildland fires—among nature's most potent forces—can save lives, money, and natural resources. *American Scientist*, 72(6):590–597, 1984.

[12] Gavriil Xanthopoulos and Miltiadis Athanasiou. Crown Fire. pages 1–15. Springer International Publishing, Cham, 2019.

[13] Jim Reardon. Ground Fire. pages 557–563. Springer International Publishing, Cham, 2020.

[14] Adam C. Watts and Leda N. Kobziar. Smoldering combustion and ground fires: ecological effects and multi-scale significance. *Fire Ecology*, 9:124–132, 2013.

[15] Claire Belcher, Iain Brown, Gareth Clay, Stefan Doerr, Andy Elliott, Rob Gazzard, Nicholas Kettridge, James Morison, Matthew Perry, Cristina Santin, et al. Uk wildfires and their climate challenges: Expert led report prepared for the third climate change risk assessment. 2021.

[16] Kendra K. McLauchlan, Philip E. Higuera, Jessica Miesel, Brendan M. Rogers, Jennifer Schweitzer, Jacquelyn K. Shuman, Alan J. Tepley, J. Morgan Varner, Thomas T. Veblen, Solny A. Adalsteinsson, et al. Fire as a fundamental ecological process: Research advances and frontiers. *Journal of Ecology*, 108(5):2047–2069, 2020.

[17] Forests Fire. The future: A crisis raging out of control. *World Wide Fund For Nature*, 2020.

[18] Naian Liu, Jiao Lei, Wei Gao, Haixiang Chen, and Xiaodong Xie. Combustion dynamics of large-scale wildfires. *Proceedings of the Combustion Institute*, 38(1):157–198, 2021.

[19] Anil W. Date. *Analytic Combustion: With Thermodynamics, Chemical Kinetics and Mass Transfer*. Cambridge University Press, New York, UNITED STATES, 2011.

[20] Haoran Jiang, Yong Jiang, and Rujia Fan. Extinguishing capability of novel ultrafine dry chemical agents loaded with iron hydroxide oxide. *Fire Safety Journal*, 130:103578, 2022.

[21] Qinghong Kong, Yuan Hu, Lei Song, Yinling Wang, Zuyao Chen, and Weicheng Fan. Influence of Fe-MMT on crosslinking and thermal degradation in silicone rubber/clay nanocomposites. *Polymers for Advanced Technologies*, 17:463–467, 6 2006.

[22] Xiaokun Chen, Tenglong Zhao, Fangming Cheng, Kunlun Lu, Xueqiang Shi, and Wencong Yu. Investigation of the Suppression of Methane Explosions by N2/CO2 Mixtures in Different Proportions. *ACS Omega*, 8(12):10863–10874, March 2023.

[23] V. V. Azatyan. Role of Semenov's Theory of Chain Reactions in the Formation of Modern Concepts on the Processes of Combustion, Explosion, and Detonation of Gases. *Russian Journal of Physical Chemistry B*, 15(2):278–284, 2021.

[24] Bin Su, Zhenmin Luo, Tao Wang, Chao Xie, and Fangming Cheng. Chemical kinetic behaviors at the chain initiation stage of CH4/H2/air mixture. *Journal of Hazardous Materials*, 403:123680, 2021.

[25] Kara Yedinak, Jack Cohen, Jason Forthofer, and Mark Finney. An examination of flame shape related to convection heat transfer in deep-fuel bedsA. *International Journal of Wildland Fire*, 19, January 2010.

[26] Claire M. Belcher, Jonathan M. Yearsley, Rory M. Hadden, Jennifer C. McElwain, and Guillermo Rein. Baseline intrinsic flammability of Earth's ecosystems estimated from paleoatmospheric oxygen over the past 350 million years. *Proceedings of the National Academy of Sciences of the United States of America*, 107(52):22448–22453, December 2010.

[27] Hsiang-Cheng Kung. A mathematical model of wood pyrolysis. *Combustion and Flame*, 18(2):185–195, 1972.

[28] M. I. Asensio and L. Ferragut. On a wildland fire model with radiation. *International Journal for Numerical Methods in Engineering*, 54(1):137–157, May 10, 2002.

[29] Valeriy A. Perminov. Mathematical modelling of wildland fires initiation and spread using a coupled atmosphere-forest fire setting. *Chemical Engineering Transactions*, 70:1747–1752, 2018.

[30] D. Morvan and J. L. Dupuy. Modeling of fire spread through a forest fuel bed using a multiphase formulation. *Combustion and Flame*, 127(1-2):1981–1994, Oct 1, 2001.

[31] B. Porterie, D. Morvan, M. Larini, and J. Loraud. Wildfire propagation: a two-dimensional multiphase approach. *Combustion, Explosion, and Shock Waves*, 34(2):139–150, Mar 1998.

[32] M. Larini, F. Giroud, B. Porterie, and J.-C. Loraud. A multiphase formulation for fire propagation in heterogeneous combustible media. *International Journal of Heat and Mass Transfer*, 41(6-7):881–897, 1998.

[33] A. M. Grishin, A. D. Gruzin, and V. G. Zverev. Study of the structure and limits of propagation of the front of an upstream forest fire. *Combustion, Explosion, and Shock Waves*, 21(1):9–18, Jan 1985.

[34] K. Prasad, C. Li, K. Kailasanath, C. Ndubizu, R. Ananth, and P. A. Tatem. Numerical modeling of water mist suppression of methane-air diffusion flames. *Combustion Science and Technology*, 132(1-6):325–364, Feb 1, 1998.

[35] Seungro Lee, Rosa Padilla, Derek Dunn-Rankin, Trinh Pham, and Oh Chae Kwon. Extinction limits and structure of counterflow nonpremixed h2o-laden ch4/air flames. *Energy*, 93:442–450, 2015.

[36] Jeff Stern and J. Gordon Routley. *Class a foam for structural firefighting*. Federal Emergency Management Agency, US Fire Administration, 1997.

[37] Ashley J. Wilson. *Foams: physics, chemistry and structure*. Springer Science & Business Media, 2013.

[38] Heni Dallagi, Christine Faille, Laurent Bouvier, Maureen Deleplace, Thomas Dubois, Fethi Aloui, and Thierry Benezech. Wet foam flow: A suitable method for improving surface hygiene in the food industry. *Journal of Food Engineering*, 322:110976, 2022.

[39] NFPA:1145. *Use of Class A Foams in Manual Structural Fire Fighting*.

[40] Takayoshi Kawahara, Shuichi Hatae, Takahide Kanyama, Yuki Ishizaki, and Kazuya Uezu. Development of eco-friendly soap-based firefighting foam for forest fire. *Environmental Control in Biology*, 54(1):75–78, 2016.

[41] Robyn Adams, Dianne Simmons, K. Hartskeerl, and M. Koehler. Surviving suppression: no detectable impacts of class a foam on soil invertebrates and some australian native plants. 2004.

[42] Bernard Król, Krystyna Prochaska, and Łukasz Chrzanowski. Biodegradability of firefighting foams. *Fire technology*, 48:173–181, 2012.

[43] Zhi Ming Bao, Xian Zhong Zhang, Xue Cheng Fu, and Ying Nian Hu. Research progress in biodegradation of firefighting foam. *Advanced Materials Research*, 518:817–820, 2012.

[44] M. Koehler, Robyn Adams, and Dianne Simmons. Does application of firefighting foam affect soil invertebrates? 2005.

[45] Ashlea J. Laundess, Mark S. Rayson, Bogdan Z. Dlugogorski, and Eric M. Kennedy. Suppression performance comparison for aspirated, compressed-air and in situ chemically generated class b foams. *Fire technology*, 48:625–640, 2012.

[46] A. Bourgeois, J. Bergendahl, and A. Rangwala. Biodegradability of fluorinated firefighting foams in water. *Chemosphere*, 131:104–109, 2015.

[47] Ivana Tureková and Karol Balog. The environmental impacts of fire-fighting foams. *Research Papers Faculty of Materials Science and Technology Slovak University of Technology*, 18(29):111–120, 2010.

[48] Sameh Abdelghany. *Various Uses of Class A and B High Expansion Foam*. PhD thesis, December 2019.

[49] Diane L. Larson, Wesley E. Newton, Patrick J. Anderson, and Steven J. Stein. Effects of fire retardant chemical and fire suppressant foam on shrub steppe vegetation in northern nevada. *International Journal of Wildland Fire*, 9(2):115–127, 1999.

[50] Tao Chen, Peng Zhang, Dezheng Wang, Yuwei Wang, Cheng Hu, Chenyang Jiang, and Kai Cui. Research on suppression effect of low-expansion afff, afff/ar and fffp foam on hot oil fire for oil-immersed transformers. *Thermal Science and Engineering Progress*, 43:101991, 2023.

[51] Jason R. Kelts. Expansion foam fire suppression. *Professional Safety*, 64(10):59–61, 2019.

[52] Yingchun Liu, Mingju Jing, Rongcen Xu, Xiaoyang Luan, Juncheng Jiang, and Bin Zhang. Study of key properties of expansion foam for process safety incident mitigation using an improved foam generator. *Journal of Loss Prevention in the Process Industries*, 74:104661, 2022.

[53] Joanna Rakowska. Best practices for selection and application of firefighting foam. In *MATEC Web of Conferences*, volume 247, page 00014. EDP Sciences, EDP Sciences, 12 2018.

[54] Paul Stevenson. *Foam Engineering: Fundamentals and Applications*. John Wiley & Sons, Incorporated, Somerset, UNITED KINGDOM, 2012.

[55] National Wildfire Coordinating Group. Wildland fire suppression tactics reference guide, 1996.

[56] SolbergFoam.

[57] A. Chattaway, G. G. Cox, S. R. Preece, and D. J. Spring. The development of a small scale class a fire test. In *Halon Options Technical Working Conference*, volume 5, pages 498–508, 1997.

[58] I. S. Anufriev, S. V. Alekseenko, O. V. Sharypov, and E. P. Kopyev. Diesel fuel combustion in a direct-flow evaporative burner with superheated steam supply. *Fuel*, 254:115723, 2019.

[59] Zhigang Liu, Don Carpenter, and Andrew K. Kim. Cooling characteristics of hot oil pool by water mist during fire suppression. *Fire safety journal*, 43(4):269–281, 2008.

[60] Francisco Cepeda, Alejandro Jerez, Rodrigo Demarco, Fengshan Liu, and Andrés Fuentes. Influence of water-vapor in oxidizer stream on the sooting behavior for laminar coflow ethylene diffusion flames. *Combustion and Flame*, 210:114–125, 2019.

[61] Sean Carter Mitchell. Comparing class a compressed air foam systems (cafs) against plain water suppression in live fire gas cooling experiments for interior structural firefighting. 2013.

[62] Scottish Government. *Fire and rescue service wildfire operational guidance*, page 362. 2013.

[63] Bogdan Z. Dlugogorski and Ted H. Schaefer. Compatibility of aqueous film-forming foams (afff) with sea water. *Fire Safety Journal*, 120:103288, 2021.

[64] National Fire Protection Association and American National Standards Institute. *Standard for Low Expansion Foam*, volume 11. National Fire Protection Association, 1998.

[65] S. A. Magrabi, Bogdan Z. Dlugogorski, and G. J. Jameson. A comparative study of drainage characteristics in afff and fffp compressed-air fire-fighting foams. *Fire Safety Journal*, 37(1):21–52, 2002.

[66] Bernard P. Binks, Mark Kirkland, and Jhonny A. Rodrigues. Origin of stabilisation of aqueous foams in nanoparticle-surfactant mixtures. *Soft matter*, 4(12):2373–2382, Nov 19, 2008.

[67] Robert J. Pugh. *Bubble and foam chemistry*. Cambridge University Press, 2016.

[68] Mingwei Zhao, Ruoyu Wang, Caili Dai, Xuepeng Wu, Youran Wu, Yingjie Dai, and Yining Wu. Adsorption behaviour of surfactant-nanoparticles at the gas-liquid interface: influence of the alkane chain length. *Chemical Engineering Science*, 206:203–211, 2019.

[69] Yang Fei, Kunakorn Pokalai, Ray Johnson, Mary Gonzalez, and Manouchehr Haghighi. Experimental and simulation study of foam stability and the effects on hydraulic fracture proppant placement. *Journal of Natural Gas Science and Engineering*, 46:544–554, 2017.

[70] Youjie Sheng, Menghua Xue, Yubo Wang, Xudong Zhai, Shanwen Zhang, Qiuhong Wang, Li Ma, Xuhan Ding, and Xiangrong Liu. Aggregation behavior and foam properties of the mixture of hydrocarbon and fluorocarbon surfactants with addition of nanoparticles. *Journal of Molecular Liquids*, 323:115070, 2021.

[71] Katherine M. Hinnant, Michael W. Conroy, and Ramagopal Ananth. Influence of fuel on foam degradation for fluorinated and fluorine-free foams. *Colloids and Surfaces A: Physicochemical and Engineering Aspects*, 522:1–17, 2017.

[72] Reinhard Höhler and Sylvie Cohen-Addad. Rheology of liquid foam. *Journal of Physics: Condensed Matter*, 17(41):R1041, 2005.

[73] Denis Weaire. The rheology of foam. *Current Opinion in Colloid & Interface Science*, 13(3):171–176, 2008.

[74] Arnaud Saint-Jalmes. Physical chemistry in foam drainage and coarsening. *Soft Matter*, 2(10):836–849, 2006.

[75] B. S. Gardiner, Bogdan Z. Dlugogorski, and G. J. Jameson. Rheology of fire-fighting foams. *Fire Safety Journal*, 31(1):61–75, 1998.

[76] S. A. Koehler, Howard A. Stone, M. P. Brenner, and J. Eggers. Dynamics of foam drainage. *Physical Review E*, 58(2):2097, 1998.

[77] Rifeng Zhou, Xiaoxiao Dou, Xuqing Lang, Limin He, Jianlin Liu, and Shanjun Mu. Foaming ability and stability of silica nanoparticle-based triple-phase foam for oil fire extinguishing: Experimental. *Soft Materials*, 16(4):327–338, 2018.

[78] Valeriano S. Álvarez Salazar, Leonardo Di G. Sigalotti, Abraham Medina Ovando, Ignacio Carvajal-Mariscal, and Jaime Klapp. Experimental study on the rise of aqueous foams in vertical pipes. *Frontiers in Physics*, 10, 2022.

[79] P. M. Kruglyakov, S. I. Karakashev, A. V. Nguyen, and N. G. Vilkova. Foam drainage. *Current Opinion in Colloid & Interface Science*, 13(3):163–170, June 2008.

[80] Dominique Langevin. Aqueous foams and foam films stabilised by surfactants. Gravity-free studies. *Comptes Rendus Mécanique*, 345:47–55, 1 2017.

[81] Oyindamola Obisesan, Ramadan Ahmed, and Mahmood Amani. The Effect of Salt on Stability of Aqueous Foams. *Energies*, 14(2):279, January 2021.

[82] Dominique Langevin. Coalescence in foams and emulsions: Similarities and differences. *Current Opinion in Colloid & Interface Science*, 44:23–31, 2019.

[83] Gary Kaptay. On the equation of the maximum capillary pressure induced by solid particles to stabilize emulsions and foams and on the emulsion stability diagrams. *Colloids and Surfaces A: Physicochemical and Engineering Aspects*, 282:387–401, 2006.

[84] Eric Vavra, Maura Puerto, Chutian Bai, Kun Ma, Khalid Mateen, Lisa Biswal, and George Hirasaki. Measuring in-situ capillary pressure of a flowing foam system in porous media. *Journal of Colloid and Interface Science*, 621:321–330, 2022.

[85] Ke Qiu, Xiaoyang Yu, Huan Li, and Shouxiang Lu. Tuning rheology and fire-fighting performance of protein-stabilized foam by actively switching the interfacial state of the liquid film. *Journal of Materials Science & Technology*, 178:120–132, 2024.

[86] Isabelle Cantat, Sylvie Cohen-Addad, Florence Elias, François Graner, Reinhard Höhler, Olivier Pitois, Florence Rouyer, and Arnaud Saint-Jalmes. *Foams: structure and dynamics*. OUP Oxford, 2013.

[87] Ping Ping, Bingqing Li, Jian Chen, Xu He, Dongsheng Wang, Jiaqing Zhang, and Depeng Kong. Effect of temperature on stability and film thinning behavior of aqueous film forming foam. *Journal of Molecular Liquids*, 370:120978, 2023.

[88] Youjie Sheng, Yunchuan Peng, Shanwen Zhang, Ying Guo, Li Ma, Qiuhong Wang, and Hanling Zhang. Study on thermal stability of gel foam co-stabilized by hydrophilic silica nanoparticles and surfactants. *Gels*, 8(2):123, 2022.

[89] Laurier L. Schramm. *Emulsions, foams, and suspensions: fundamentals and applications*. John Wiley & Sons, 2006.

[90] R. C. Darton and K.-H. Sun. The effect of surfactant on foam and froth properties. *Chemical Engineering Research and Design*, 77(6):535–542, 1999.

[91] Xiaoyang Yu, Ning Jiang, Xuyang Miao, Fan Li, Jiyun Wang, Ruowen Zong, and Shouxiang Lu. Comparative studies on foam stability, oil-film interaction and fire extinguishing performance for fluorine-free and fluorinated foams. *Process Safety and Environmental Protection*, 133:201–215, 2020.

[92] Olivier Pitois, Elise Lorenceau, Nicolas Louvet, and Florence Rouyer. Specific surface area model for foam permeability. *Langmuir*, 25(1):97–100, 2009.

[93] Paul Grassia and Carlos Torres-Ulloa. A model for foam fractionation with spatially varying bubble size. *Chemical Engineering Science*, 281:119163, 2023.

[94] Tamara Schad, Natalie Preisig, Wiebke Drenckhan, and Cosima Stubenrauch. Foam-based cleaning of surfaces contaminated with mixtures of oil and soot. *Journal of Surfactants and Detergents*, 25(3):377–385, 2022.

[95] S. A. Magrabi, B. Z. Dlugogorski, and G. J. Jameson. Bubble size distribution and coarsening of aqueous foams. *Chemical engineering science*, 54(18):4007–4022, 1999.

[96] Chris G. J. Bisperink, A. D. Ronteltap, and A. Prins. Bubble-size distribution in foams. *Adv. Colloid Interface Sci. 38 (1992) 13-32.*, January 1992.

[97] Nadya Politova, Slavka Tcholakova, Zhulieta Valkova, Konstantin Golemanov, and Nikolai D. Denkov. Self-regulation of foam volume and bubble size during foaming via shear mixing. *Colloids and Surfaces A: Physicochemical and Engineering Aspects*, 539:18–28, 2018.

[98] Ian Sutton. *Process risk and reliability management*. Gulf Professional Publishing, 2014.

[99] Dennis P. Nolan. *Handbook of fire and explosion protection engineering principles: for oil, gas, chemical and related facilities*. William Andrew, 2014.

[100] Brian Fishera, Andrew Awtryb, Ronald S. Sheinson, and James W. Flemingc. The behavior of sub 10 μm water mist drops in propane/air co-flow non-premixed "cup burner" flames. In *Halon Options Technical Working Conference, Albuquerque, New Mexico, May 24*, volume 26, 2005.

[101] J. Gordon Routley Jeff Stern. Technical report series: Class a foam for structural firefighting.

[102] Tony Briggs. Foams for firefighting. *Foams: theory, measurements and applications*, 57:465–509, 1996.

[103] Joshua Feldman, Seth Misenar, and Eric Conrad. *Eleventh hour cissp®: study guide*. Syngress, 2016.

[104] S. J. González-Prieto. Firefighting chemicals. In *Handbook of Fire and the Environment: Impacts and Mitigation*, pages 273–288. Springer, 2022.

[105] Christopher Hill and Julian Eastoe. Foams: From nature to industry. *Advances in colloid and interface science*, 247:496–513, 2017.

[106] Raphael Shadai Oguike. Study of fire fighting foam agent from palm oil for extinguishing of petrol fires. *Science Postprint*, 1(1):e00006, 2013.

[107] Shuai Yuan, Chongye Chang, Shuaishuai Yan, Pan Zhou, Xinming Qian, Mengqi Yuan, and Kai Liu. A review of fire-extinguishing agent on suppressing lithium-ion batteries fire. *Journal of Energy Chemistry*, 62:262–280, 2021.

[108] Charles L. Ford. An overview of halon 1301 systems. 1975.

[109] Ronald S Sheinson, Bradley A Williams, Christian Green, James W Fleming, Robert Anleitner, Scott Ayers, Alexander Maranghides, and Douglas Barylski. The future of aqueous film forming foam (afff): performance parameters and requirements, 2002.

[110] David M. Kempisty, Yun Xing, and LeeAnn Racz. *Perfluoroalkyl substances in the environment: theory, practice, and innovation*. CRC Press, 2018.

[111] Marina Teodora Patrascu, Andrei Dan Busuioc, Cristina Busuioc, Adina Cotarta, Anca Cojocaru, Teodor Visan, and Danut Ionel Vaireanu. Experimental study on the corrosion of carbon steel and aluminum alloy in firefighting protein foam concentrates. *Materials*, 14(23):7259, 2021.

[112] Haidar Ibrahim and Jagannadha Rao Patruni. Experimental investigation on extinguishing performance of a novel nanocomposite for gaseous fires. *Journal of Loss Prevention in the Process Industries*, 65:104143, May 2020.

[113] Anna Rabajczyk, Maria Zielecka, and Justyna Gniazdowska. Application of Nanotechnology in Extinguishing Agents. *Materials*, 15(24):8876, December 2022.

[114] G. W. Song and Y. H. Lu. Handbook of fire resistant textiles. *Sawston: Woodhead*, pages 520–541, 2013.

[115] Shalini Chaturvedi, Pragnesh N. Dave, and Nisha K. Shah. Applications of nanocatalyst in new era. *Journal of Saudi Chemical Society*, 16(3):307–325, 2012.

[116] Norio Taniguchi. On the basic concept of'nano-technology'. In *Proc. Intl. Conf. Prod. Eng. Tokyo, Part II, 1974*. Japan Society of Precision Engineering, 1974.

[117] Naomi Lubick and Kellyn Betts. Silver socks have cloudy lining— court bans widely used flame retardant, 2008.

[118] Alan S. Edelstein and R. C. Cammaratra. *Nanomaterials: synthesis, properties and applications*. CRC press, 1998.

[119] Lu Han, Xuelai Zhang, Jun Ji, and Kunlin Ma. Research progress on the influence of nano-additives on phase change materials. *Journal of Energy Storage*, 55:105807, 2022.

[120] B. Eanest Jebasingh and A. Valan Arasu. A comprehensive review on latent heat and thermal conductivity of nanoparticle dispersed phase change material for low-temperature applications. *Energy Storage Materials*, 24:52–74, 2020.

[121] Rifeng Zhou, Xuqing Lang, Xu Zhang, Bin Tao, and Limin He. Thermal stability and insulation characteristics of three-phase fire-fighting foam exposed to radiant heating. *Process Safety and Environmental Protection*, 146:360–368, February 2021.

[122] I. E. Gerasimov, D. A. Knyazkov, A. G. Shmakov, A. A. Paletsky, V. M. Shvartsberg, T. A. Bolshova, and O. P. Korobeinichev. Inhibition of hydrogen–oxygen flames by iron pentacarbonyl at atmospheric pressure. *Proceedings of the Combustion Institute*, 33(2):2523–2529, January 2011.

[123] C. A. Martins, A. P. Pimenta, J. A. Carvalho Jr., M. A. Ferreira, and A. A. Caldeira-Pires. CH and C2 radicals characterization in natural gas turbulent diffusion flames. *Journal of the Brazilian Society of Mechanical Sciences and Engineering*, 27:110–118, June 2005.

[124] J. Craig Voelkert. Fire and fire extinguishment a brief guide to fire chemistry and extinguishment theory for fire equipment service technicians.

[125] G. T. Linteris, M. D. Rumminger, V. Babushok, and W. Tsang. Flame inhibition by ferrocene and blends of inert and catalytic agents. *Proceedings of the Combustion Institute*, 28(2):2965–2972, January 2000.

[126] Yusuke Koshiba and Masato Sugimoto. Fire-suppression capability of surfactant-free aqueous dispersions of submicron-sized ferrocene particles. *Case Studies in Thermal Engineering*, 28:101459, 12 2021.

[127] Ting Sai, Shiya Ran, Zhenghong Guo, Pingan Song, and Zhengping Fang. Recent advances in fire-retardant carbon-based polymeric nanocomposites through fighting free radicals. *SusMat*, 2(4):411–434, 2022.

[128] Xintai Chen, Yingle Yin, Jie Lu, and Xuhuang Chen. Preparation and properties of iron-based flame-retardant reinforcing agent. *Journal of fire sciences*, 32(2):179–190, 2014.

[129] Xiaomin Ni, Kaiqian Kuang, Donglei Yang, Xiang Jin, and Guangxuan Liao. A new type of fire suppressant powder of NaHCO3/zeolite nanocomposites with core–shell structure. *Fire Safety Journal*, 44(7):968–975, October 2009.

[130] Eric Stauffer, Julia A. Dolan, and Reta Newman. CHAPTER 4 - Chemistry and Physics of Fire and Liquid Fuels. pages 85–129. Academic Press, Burlington, January 2008.

[131] K. Pielichowski and S. Michalowski. 12 - Nanostructured flame retardants: performance, toxicity, and environmental impact. pages 251–277. Woodhead Publishing, January 2014.

[132] Danica Kačíková, Ivan Kubovský, Adriana Eštoková, František Kačík, Elena Kmeťová, Ján Kováč, and Jaroslav Ďurkovič. The Influence of Nanoparticles on Fire Retardancy of Pedunculate Oak Wood. *Nanomaterials*, 11(12):3405, December 2021.

[133] Spencer Umfreville Pickering. CXCVI.—Emulsions. *Journal of the Chemical Society, Transactions*, 91(0):2001–2021, January 1907.

[134] Keliang Wang, Gang Wang, Chunjing Lu, Cuiying Pei, and Ying Wang. Preparation and investigation of foaming amphiphilic fluorinated nanoparticles for enhanced oil recovery. *Materials*, 10(12):1403, 2017.

[135] Bernard P. Binks. Particles as surfactants—similarities and differences. *Current Opinion in Colloid & Interface Science*, 7(1):21–41, March 2002.

[136] Maryam Khajehpour, S.. Reza Etminan, Jon Goldman, Fred Wassmuth, and Steven Bryant. Nanoparticles as Foam Stabilizer for Steam-Foam Process. *SPE Journal*, 23(06):2232–2242, September 2018.

[137] Zuhair AlYousef, Mohammed Almobarky, and David Schechter. Enhancing the Stability of Foam by the Use of Nanoparticles. *Energy & Fuels*, 31(10):10620–10627, October 2017.

[138] David Espinosa, Federico Caldelas, Keith Johnston, Steven L. Bryant, and Chun Huh. Nanoparticle-stabilized supercritical co2 foams for potential mobility control applications. In *SPE Improved Oil Recovery Conference?*, pages SPE–129925. SPE, 2010.

[139] Andrew J. Worthen, Hitesh G. Bagaria, Yunshen Chen, Steven L. Bryant, Chun Huh, and Keith P. Johnston. Nanoparticle stabilized carbon dioxide in water foams for enhanced oil recovery. In *SPE Improved Oil Recovery Symposium*. OnePetro, 2012.

[140] Mengjiao Cao, Yining Wu, Mingwei Zhao, Caili Dai, Ye Yuan, and Zhixue Chen. Modulation of bubble flow resistance and surface fluidity :the effect of nanoparticle packing density at gas–liquid interface. *Journal of Molecular Liquids*, 350:118574, March 2022.

[141] Achinta Bera, T. Kumar, Keka Ojha, and Ajay Mandal. Adsorption of surfactants on sand surface in enhanced oil recovery: Isotherms, kinetics and thermodynamic studies. *Applied Surface Science*, 284:87–99, November 2013.

[142] Laura Anne Lowden and Terence Richard Hull. Flammability behaviour of wood and a review of the methods for its reduction. *Fire Science Reviews*, 2(1):4, September 2013.

[143] Jianping Zhang, Michael A. Delichatsios, and Serge Bourbigot. Experimental and numerical study of the effects of nanoparticles on pyrolysis of a polyamide 6 (PA6) nanocomposite in the cone calorimeter. *Combustion and Flame*, 156(11):2056–2062, November 2009.

[144] Kseniia S. Mosina, Elena A. Nazarova, Aleksandr V. Vinogradov, Vladimir V. Vinogradov, Elena F. Krivoshapkina, and Pavel V. Krivoshapkin. Alumina Nanoparticles for Firefighting and Fire Prevention. *ACS Applied Nano Materials*, 3(5):4386–4393, 2020.

[145] Arturo A. Keller, Hongtao Wang, Dongxu Zhou, Hunter S. Lenihan, Gary Cherr, Bradley J. Cardinale, Robert Miller, and Zhaoxia Ji. Stability and Aggregation of Metal Oxide Nanoparticles in Natural Aqueous Matrices. *Environmental Science & Technology*, 44(6):1962–1967, March 2010.

[146] Wei Wu, Quanguo He, and Changzhong Jiang. Magnetic iron oxide nanoparticles: synthesis and surface functionalization strategies. *Nanoscale research letters*, 3:397–415, 2008.

[147] Baohua Tang, Zhaoliang Wu, and Wei-hong Chen. Effect of nanosilica on foam and thermal stability of a foam extinguishing agent. *Nanomaterials and Energy*, 6(2):67–73, 2017.

[148] Biao Long, Daqiang Wang, Ruixia Niu, Hua Song, Yu Ma, Guangmiao Qu, and Junyao He. In-situ activation of nano-silica and its foam stabilization mechanism. *Journal of Dispersion Science and Technology*, 41(1):72–80, 2020.

[149] Tommy S. Horozov. Foams and foam films stabilised by solid particles. *Current Opinion in Colloid & Interface Science*, 13:134–140, 6 2008.

[150] Urs T. Gonzenbach, André R. Studart, Elena Tervoort, and Ludwig J. Gauckler. Tailoring the microstructure of particle-stabilized wet foams. *(Langmuir)*, 23(3):1025–1032, 2007.

[151] Bernard P. Binks and Ryo Murakami. Phase inversion of particle-stabilized materials from foams to dry water. *Nature materials*, 5(11):865–869, 2006.

[152] Krishna Vijayaraghavan, Alex Nikolov, and Darsh Wasan. Foam formation and mitigation in a three-phase gas–liquid–particulate system. *Advances in colloid and interface science*, 123:49–61, 2006.

[153] Arifur Rahman, Farshid Torabi, and Ezeddin Shirif. Surfactant and nanoparticle synergy: Towards improved foam stability. *Petroleum*, 2023.

[154] Qian Sun, Zhaomin Li, Jiqian Wang, Songyan Li, Binfei Li, Lei Jiang, Hongyu Wang, Qichao Lü, Chao Zhang, and Wei Liu. Aqueous foam stabilized by partially hydrophobic nanoparticles in the presence of surfactant. *Colloids and Surfaces A: Physicochemical and Engineering Aspects*, 471:54–64, 2015.

[155] Youjie Sheng, Yang Li, Canbin Yan, Yunchuan Peng, Li Ma, and Qiuhong Wang. Influence of nanoparticles on the foam thermal stability of mixtures of short-chain fluorocarbon and hydrocarbon surfactants. *Powder Technology*, 403:117420, May 2022.

[156] Tharwat F. Tadros. *Applied surfactants: principles and applications*. John Wiley & Sons, 2006.

[157] Zenaida Briceño-Ahumada, J. F. A. Soltero-Martínez, and Rolando Castillo. Aqueous foams and emulsions stabilized by mixtures of silica nanoparticles and surfactants: A state-of-the-art review. *Chemical Engineering Journal Advances*, 7:100116, 2021.

[158] John Fuchs. Surface Tension and/or Wettability, November 2015.

[159] Dougal Drysdale. *An introduction to fire dynamics*. John wiley & sons, 2011.

[160] J. W. Hastie. Molecular Basis of Flame Inhibition. *Journal of Research of the National Bureau of Standards. Section A, Physics and Chemistry*, 77A(6):733–754, 1973.

[161] Zheng Li, Xinyu Cheng, Yanji Liu, Hao Liu, Yan Jiang, and Na Wang. Intumescent flame retardancy and smoke suppression of Eucommia ulmoides gum/natural rubber blends based on synergistic g-C3N4@Fe3O4 nanocomposites. *RSC Advances*, 12(34):21704–21712.

[162] Leilin Zhang, Yunpeng Bian, and Duolei Kuai. Preparation and flame retardant property of nano-aluminum hydroxide foam for preventing spontaneous coal combustion. *Fuel*, 304:121494, November 2021.

[163] Pradeep Kumar Kushwaha, Vipin Chawla, Anand Nandanwar, B. S. Mamtha, and Narasimha Murhty. Study on the effect of nanoparticles on fire resistance and smoke suppression properties of bamboo strand lumber. *Journal of the Indian Academy of Wood Science*, 18(1):32–38, June 2021.

[164] Gao Jie, Wang Ge, Cheng HaiTao, Shi Qiang, Chen Hong, and Chen FuMing. Effects of in situ deposited calcium carbonate particles on tensile performance of single bamboo fibers. *Journal of Northeast Forestry University*, 40(8):75–95, 2012.

[165] Bhavna Sharma, Ana Gatoo, Maximilian Bock, Helen Mulligan, and Michael Ramage. Engineered bamboo: state of the art. *Proceedings of the Institution of Civil Engineers - Construction Materials*, 168(2):57–67, April 2015.

[166] Bin Fu, Xingong Li, Guangming Yuan, Weimin Chen, and Yage Pan. Preparation and Flame Retardant and Smoke Suppression Properties of Bamboo-Wood Hybrid Scrimber Filled with Calcium and Magnesium Nanoparticles. *Journal of Nanomaterials*, 2014:e959135, July 2014.

[167] Charles D. Litton, Inoka E. Perera, Samuel P. Harteis, Kara A. Teacoach, Maria I. DeRosa, Richard A. Thomas, and Alex C. Smith. Some relevant parameters for assessing fire hazards of combustible mine materials using laboratory scale experiments. *Fuel*, 218:306–315, April 2018.

[168] P. Kiliaris and C. D. Papaspyrides. Polymer/layered silicate (clay) nanocomposites: An overview of flame retardancy. *Progress in Polymer Science*, 35(7):902–958, July 2010.

[169] Michel Le Bras. *Fire Retardancy of Polymers: New Applications of Mineral Fillers*. Royal Society of Chemistry, 2005. Google-Books-ID: dTiL9MSqLgMC.

[170] G. Camino, L. Costa, and M. P. Luda di Cortemiglia. Overview of fire retardant mechanisms. *Polymer Degradation and Stability*, 33(2):131–154, January 1991.

[171] G. A. Skinner. Flame retardancy: the approaches available. Polymer Science and Technology Series, pages 260–267. Springer Netherlands, Dordrecht, 1998.

[172] Philippe Grandjean. Paracelsus Revisited: The Dose Concept in a Complex World. *Basic & clinical pharmacology & toxicology*, 119(2):126–132, August 2016.

[173] Attarad Ali, Muhammad Zia Hira Zafar, Ihsan ul Haq, Abdul Rehman Phull, Joham Sarfraz Ali, and Altaf Hussain. Synthesis, characterization, applications, and challenges of iron oxide nanoparticles. *Nanotechnology, science and applications*, 9:49, 2016.

[174] Latifah Jasmani, Rafeadah Rusli, Tumirah Khadiran, Rafidah Jalil, and Sharmiza Adnan. Application of nanotechnology in wood-based products industry: A review. *Nanoscale Research Letters 2020 15:1*, 15:1–31, 11 2020.

[175] G. Wang, K. L. Wang, and C. J. Lu. Advances of researches on improving the stability of foams by nanoparticles. In *IOP Conference Series: Materials Science and Engineering*, volume 242, page 012020. IOP Publishing, 2017.

[176] Alexander V. Vinogradov, D. S. Kuprin, I. M. Abduragimov, G. N. Kuprin, Evgeniy Serebriyakov, and Vladimir V. Vinogradov. Silica foams for fire prevention and firefighting. *ACS Applied Materials & Interfaces*, 8(1):294–301, 2016.

[177] Tran X. Phuoc and Ruey-Hung Chen. Modeling the effect of particle size on the activation energy and ignition temperature of metallic nanoparticles. *Combustion and Flame*, 159(1):416–419, January 2012.

[178] N. Veronovski, P. Andreozzi, C. La Mesa, and M. Sfiligoj-Smole. Stable tio2 dispersions for nanocoating preparation. *Surface and Coatings Technology*, 204:1445–1451, 1 2010.

[179] Luky Hendraningrat and Ole Torsæter. Metal oxide-based nanoparticles: revealing their potential to enhance oil recovery in different wettability systems. *Applied Nanoscience (Switzerland)*, 5:181–199, 2 2015.

[180] Richard Olawoyin. Nanotechnology: The future of fire safety. *Safety science*, 110:214–221, 2018.

[181] Eric Dickinson, Rammile Ettelaie, Thomas Kostakis, and Brent S. Murray. Factors controlling the formation and stability of air bubbles stabilized by partially hydrophobic silica nanoparticles. *Langmuir*, 20(20):8517–8525, 2004.

[182] Georgios A. Sotiriou, Christa Watson, Kimberly M. Murdaugh, Thomas H. Darrah, Georgios Pyrgiotakis, Alison Elder, Joseph D. Brain, and Philip Demokritou. Engineering safer-by-design silica-coated ZnO nanorods with reduced DNA damage potential. *Environmental Science: Nano*, 1(2):144–153, 2014.

[183] Bernard P. Binks and Tommy S. Horozov. Aqueous foams stabilized solely by silica nanoparticles. *Angewandte Chemie International Edition*, 44(24):3722–3725, 2005.

[184] Muhammad Rukhsar, Zubair Ahmad, Abdur Rauf, Hassan Zeb, Mujeeb Ur-Rehman, and Hassan A. Hemeg. An overview of iron oxide (fe3o4) nanoparticles: from synthetic strategies, characterization to antibacterial and anticancer applications. *Crystals*, 12(12):1809, 2022.

[185] Eunice Aparecida Campos, Denise Villela Barcza Stockler Pinto, José Irineu Sampaio de Oliveira, Elizabeth Da Costa Mattos, and Rita De Cássia Lazzarini Dutra. Synthesis, characterization and applications of iron oxide nanoparticles - a short review. *Journal of Aerospace Technology and Management*, 7(3):267–276, sep 2015.

[186] Evangelos I. Gkanas. In vitro magnetic hyperthermia response of iron oxide MNP's incorporated in DA3, MCF-7 and HeLa cancer cell lines. *Central European Journal of Chemistry*, 11:1042–1054, 2013.

[187] Dipa Dhali. Catalytic Reaction (Catalysis): Definition, Types, & Mechanism, November 2021.

[188] Junling Wang, Yanfang Cao, Zhirong Wang, Haobo Zhou, Yuxin Zhou, Xiaoxi Zheng, Xinrui He, and Chao Wang. Designing hierarchical ternary structure based on NiAl LDH anchored phosphorus-doped g-C3N4 dotted with Fe3O4 nanoparticles towards improving the fire safety of thermoplastic polyurethane. *Applied Surface Science*, 577:151648, 2022.

[189] Aldahir A. Hernández-Hernández, Gabriel Aguirre-Álvarez, Raquel Cariño-Cortés, Luis H. Mendoza-Huizar, and Rubén Jiménez-Alvarado. Iron oxide nanoparticles: synthesis, functionalization, and applications in diagnosis and treatment of cancer. *Chemical Papers*, 74(11):3809–3824, 2020.

[190] Yusuke Koshiba, Yohei Takahashi, and Hideo Ohtani. Flame suppression ability of metallocenes (nickelocene, cobaltcene, ferrocene, manganocene, and chromocene). *Fire Safety Journal*, 51:10–17, July 2012.

[191] Gregory T. Linteris, Vadim D. Knyazev, and Valeri I. Babushok. Inhibition of premixed methane flames by manganese and tin compounds. *Combustion and Flame*, 129(3):221–238, 2002.

[192] V. Babushok, W. Tsang, G. T. Linteris, and D. Reinelt. Chemical limits to flame inhibition. *Combustion and Flame*, 115(4):551–560, December 1998.

[193] W. A. Rosser, S. H. Inami, and H. Wise. The effect of metal salts on premixed hydrocarbon—air flames. *Combustion and Flame*, 7:107–119, January 1963.

[194] S. Youije, Z. Hanling, P. Yunchuan, H. Li, W. Zhenping, L. Yang, and Y. Canbin. Efficient environment-friendly NP-foam extinguishing agent and preparation method thereof., 2022.

[195] Cristina Buzea, Ivan I. Pacheco, and Kevin Robbie. Nanomaterials and nanoparticles: sources and toxicity. *Biointerphases*, 2(4):MR17–MR71, 2007.

[196] Song Ge, Xiangyang Shi, Kai Sun, Changpeng Li, Ctirad Uher, James R. Baker Jr, Mark M. Banaszak Holl, and Bradford G. Orr. Facile hydrothermal synthesis of iron oxide nanoparticles with tunable magnetic properties. *The Journal of Physical Chemistry C*, 113(31):13593–13599, 2009.

[197] Nadir Kiraz, Esin Burunkaya, Ömer Kesmez, Hasan Erdem Çamurlu, Meltem Asiltürk, Zerin Yeşil, and Ertuğrul Arpaç. Preparation of sn doped nanometric tio2 powders by reflux and hydrothermal syntheses and their characterization. *Journal of Sol-Gel Science and Technology*, 59:381–386, 8 2011.

[198] David Perez-Saura, Miguel Fernandez-Cortizas, Rafael Perez-Segui, Pedro Arias-Perez, and Pascual Campoy. Urban firefighting drones: Precise throwing from UAV. *Journal of Intelligent & Robotic Systems*, 108(4):66, 2023.

[199] Akira Yoshida, Yutaka Kaburagi, and Yoshihiro Hishiyama. Chapter 5 - Scanning Electron Microscopy. pages 71–93. Butterworth-Heinemann, January 2016.

[200] M. Abd Mutalib, M. A. Rahman, M. H. D. Othman, A. F. Ismail, and J. Jaafar. Chapter 9 - Scanning Electron Microscopy (SEM) and Energy-Dispersive X-Ray (EDX) Spectroscopy. pages 161–179. Elsevier, January 2017.

[201] L. Marigliano, J. Jimenez-Lamana, Joanna Szpunar, Stephanie Reynaud, and Bruno Grassl. The Challenge of the Analysis of Nanoplastics in the Environment: Current Status and Perspectives. 2022.

[202] Ana P. Ramos. Dynamic light scattering applied to nanoparticle characterization. In *Nanocharacterization techniques*, pages 99–110. Elsevier, 2017.

[203] Alexander Bootz, Vitali Vogel, Dieter Schubert, and Jörg Kreuter. Comparison of scanning electron microscopy, dynamic light scattering and analytical ultracentrifugation for the sizing of poly (butyl cyanoacrylate) nanoparticles. *European journal of pharmaceutics and biopharmaceutics*, 57(2):369–375, 2004.

[204] Jesus Rodriguez-Loya, Maricarmen Lerma, and Jorge L. Gardea-Torresdey. Dynamic light scattering and its application to control nanoparticle aggregation in colloidal systems: A review. *Micromachines*, 15(1):24, 2023.

[205] Dieter Vollath. Agglomerates of nanoparticles. *Beilstein Journal of Nanotechnology*, 11(1):854–857, 2020.

[206] Guozhong Cao. *Nanostructures & nanomaterials: synthesis, properties & applications*. Imperial college press, 2004.

[207] Laurie Donaldson. New foam improves firefighting capabilities. *Materials Today*, 2(19):63, 2016.

[208] Wan Renpu. Chapter 8 - Measures for Putting a Well into Production. pages 417–523. Gulf Professional Publishing, January 2011.

[209] M. Rivai, E. Hambali, A. Suryani, R. Fitria, S. Firmansyah, and G. Pramuhadi. Formulation and performance test of palm-based foaming agent concentrate for fire extinguisher application. In *IOP Conference Series: Earth and Environmental Science*, volume 141, page 012026. IOP Publishing, 2018.

[210] Sameh M. I. Saad, Zdenka Policova, and A. Wilhelm Neumann. Design and accuracy of pendant drop methods for surface tension measurement. *Colloids and Surfaces A: Physicochemical and Engineering Aspects*, 384(1-3):442–452, 2011.

[211] Paul Sennett and J. P. Olivier. Colloidal dispersions, electrokinetic effects, and the concept of zeta potential. *Industrial & Engineering Chemistry*, 57(8):32–50, 1965.

[212] Hema Setia, Ritu Gupta, and R. K. Wanchoo. Stability of nanofluids. In *Materials science forum*, volume 757, pages 139–149. Trans Tech Publ, 2013.

[213] Daniel José Pochapski, Caio Carvalho dos Santos, Gabriel Wosiak Leite, Sandra Helena Pulcinelli, and Celso Valentim Santilli. Zeta potential and colloidal stability predictions for inorganic nanoparticle dispersions: Effects of experimental conditions and electrokinetic models on the interpretation of results. *Langmuir*, 37(45):13379–13389, 2021.

[214] Vandana Gupta and Piyush Trivedi. Chapter 15 - In vitro and in vivo characterization of pharmaceutical topical nanocarriers containing anticancer drugs for skin cancer treatment. pages 563–627. William Andrew Publishing, January 2018.

[215] Wenlong Huo, Xiaoyan Zhang, Ke Gan, Yugu Chen, Jie Xu, and Jinlong Yang. Effect of zeta potential on properties of foamed colloidal suspension. *Journal of the European Ceramic Society*, 39(2-3):574–583, 2019.

[216] Pouria Amani, Reinhard Miller, Aliyar Javadi, and Mahshid Firouzi. Pickering foams and parameters influencing their characteristics. *Advances in Colloid and Interface Science*, 301:102606, 2022.

[217] Bin Huang, Xiaohan Nan, Cheng Fu, and Tianyue Guo. Study of the bubble collapse mechanism and its influencing factors on stability under ultra-low surface tension. *Colloids and Surfaces A: Physicochemical and Engineering Aspects*, 618:126440, 2021.

[218] Forexpan | Angus Fire.

[219] Jingjing Shen, Jianwei Liang, Xinfeng Lin, Hongjian Lin, Jing Yu, and Shifang Wang. The flame-retardant mechanisms and preparation of polymer composites and their potential application in construction engineering. *Polymers*, 14(1):82, 2021.

[220] WR Catchpole, EA Catchpole, BW Butler, RC Rothermel, GA Morris, and DJ Latham. Rate of spread of free-burning fires in woody fuels in a wind tunnel. *Combustion Science and Technology*, 131(1-6):1–37, 1998.

[221] Jeanette Cobian-Iñiguez, AmirHessam Aminfar, Joey Chong, Gloria Burke, Albertina Zuniga, David R Weise, and Marko Princevac. Wind tunnel experiments to study chaparral crown fires. *JoVE (Journal of Visualized Experiments)*, (129):e56591, 2017.

[222] L Terrei, A Lamorlette, and A Ganteaume. Modelling the fire propagation from the fuel bed to the lower canopy of ornamental species used in wildland–urban interfaces. *International journal of wildland fire*, 28(2):113–126, 2019.

[223] Peacock Fibres Ltd.

[224] Mettler-Toledo International Inc all rights reserved. METTLER TOLEDO Balances & Scales for Industry, Lab, Retail.

[225] M. P. Plucinski, A. L. Sullivan, and R. J. Hurley. A methodology for comparing the relative effectiveness of suppressant enhancers designed for the direct attack of wildfires. *Fire Safety Journal*, 87:71–79, 2017.

[226] J.-L. Hazemann, J. F. Bérar, and A. Manceau. Rietveld studies of the aluminium-iron substitution in synthetic goethite. *Materials Science Forum*, 79-82:821–826, 1 1991.

[227] Kazuki Yasuda and Yoshitaka Kitamoto. Fabrication of Fe3O4 nanorods designed for liquid-phase magnetic biosensing. In *AIP Conference Proceedings*, volume 1929. AIP Publishing, 2018.

[228] S. Amala Jayanthi, D. Muthu Gnana Theresa Nathan, J. Jayashainy, and P. Sagayaraj. A novel hydrothermal approach for synthesizing α-Fe2O3, γ-Fe2O3 and Fe3O4 mesoporous magnetic nanoparticles. *Materials Chemistry and Physics*, 162:316–325, 2015.

[229] T. B. J. Blijdenstein, P. W. N. De Groot, and S. D. Stoyanov. On the link between foam coarsening and surface rheology: Why hydrophobins are so different. *Soft Matter*, 6:1799–1808, 2010.

[230] Youjie Sheng, Canbin Yan, Yang Li, Yunchuan Peng, Li Ma, and Qiuhong Wang. Thermal stability of gel foams stabilized by xanthan gum, silica nanoparticles and surfactants. *Gels*, 7(4):179, 2021.

[231] Mikhail N. Shneider and Mikhail Pekker. Surface tension of small bubbles and droplets and the cavitation threshold. *arXiv preprint arXiv:1901.04329*, 2019.

[232] Manas Ranjan Behera, Shailesh Ravi Varade, Pallab Ghosh, Pintu Paul, and Ajay Singh Negi. Foaming in micellar solutions: Effects of surfactant, salt, and oil concentrations. *Industrial & Engineering Chemistry Research*, 53(48):18497–18507, 2014.

[233] Ping Wang, Jidong Wang, Hui Zhang, Yue Dong, and Yongchun Zhang. The role of iron oxides in the preservation of soil organic matter under long-term fertilization. *Journal of Soils and Sediments*, 19:588–598, 2 2019.

[234] Elena Taboada, Elisenda Rodriguez, Anna Roig, Judit Oro, Alain Roch, and Robert N. Muller. New ultrasmall iron-oxide nanoparticles with high magnetisation as potential T1-MRI contrast agents for molecular imaging. *arXiv preprint cond-mat/0611243*, 2006.

[235] Nidhi Raval, Rahul Maheshwari, Dnyaneshwar Kalyane, Susanne R. Youngren-Ortiz, Mahavir B. Chougule, and Rakesh K. Tekade. Importance of physicochemical characterization of nanoparticles in pharmaceutical product development. In *Basic fundamentals of drug delivery*, pages 369–400. Elsevier, 2019.

[236] Hamid Vatanparast, Farshid Shahabi, Alireza Bahramian, Aliyar Javadi, and Reinhard Miller. The role of electrostatic repulsion on increasing surface activity of anionic surfactants in the presence of hydrophilic silica nanoparticles. *Scientific Reports*, 8(1):7251, 2018.

[237] Kandasamy Vinothini and Mariappan Rajan. Mechanism for the nano-based drug delivery system. In *Characterization and biology of nanomaterials for drug delivery*, pages 219–263. Elsevier, 2019.

[238] R. R. Souza, Vera Faustino, J. D. Oliveira, Inês M. Gonçalves, João M. Miranda, Ana S. Moita, A. L. N. Moreira, José C. F. Teixeira, Manuel Bañobre-López, and Rui Lima. A novel and extremely stable nanofluid based on iron oxide nanoparticles: Experimental investigations on the thermal performance. *Thermal Science and Engineering Progress*, 26:101085, 2021.

[239] Caroline A. Schneider, Wayne S. Rasband, and Kevin W. Eliceiri. NIH Image to ImageJ: 25 years of image analysis. *Nature Methods*, 9(7):671–675, July 2012.

[240] Frédéric Morandini, Xavier Silvani, Jean-Luc Dupuy, and Arnaud Susset. Fire spread across a sloping fuel bed: Flame dynamics and heat transfers. *Combustion and flame*, 190:158–170, 2018.

[241] F. Teles, G. Martins, and F. Antunes. Fire retardancy in nanocomposites by using nanomaterial additives. *Journal of Analytical and Applied Pyrolysis*, 163:105466, 2022.

[242] I. Papagiannis, M. S. Innocente, J. D. Davies, J. L. Ryan, and E. I. Gkanas. Investigating the Impact of Iron Oxide Nanoparticles on the Stability of Class A Foam for Wildfire Suppression. Under review in Fire Safety Journal, Elsevier, 2024.

[243] Ioannis Papagiannis, Mauro S. Innocente, and Evangelos I. Gkanas. Synthesis and characterisation of iron oxide nanoparticles with tunable sizes by hydrothermal method. In *Materials Science Forum*, volume 1053, pages 176–181. Trans Tech Publ, 2022.

[244] Robert G. Zalosh. *Appendix A: Flame Radiation Review*. John Wiley & Sons, Ltd, 2003.

[245] Gregory T. Linteris and I. P. Rafferty. Flame size, heat release, and smoke points in materials flammability. *Fire Safety Journal*, 43(6):442–450, 2008.

Appendices

Appendix A

Simulation of combustion process

Before experimental procedures such as synthesis and characterisation of materials, molecular dynamics simulations were conducted. These simulations aimed to predict the behaviour of material interactions, leading to faster product development at lower costs.

Initially, the methane combustion was studied as shown in Figure, where molecules like methane (CH_4) oxygen (O_2), carbon dioxide (CO_2) and water (H_2O) represented with different colored spheres.

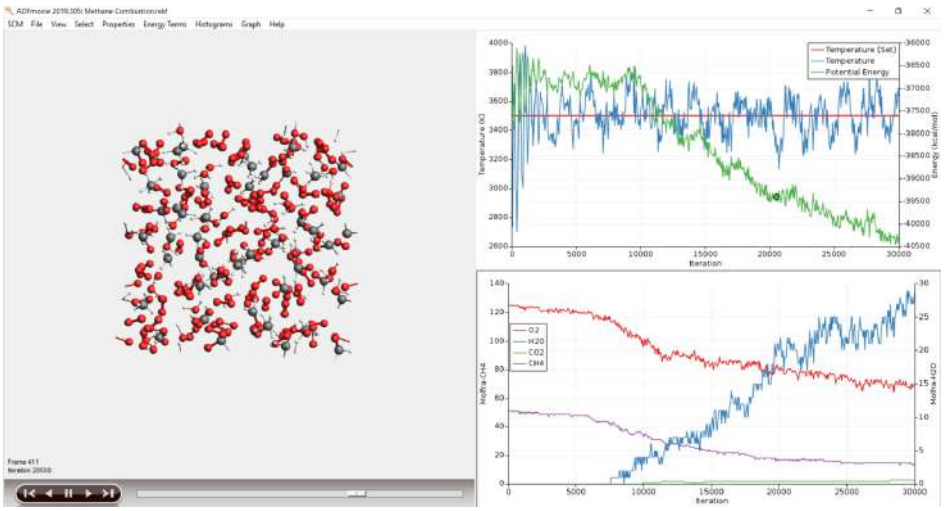

Figure A.1: *ADF Powerful molecular DFT simulations to understand the chemistry of methane combustion.*

Additionally, simulating the interaction of isooctane and diolane (2-Methyl-2,4-pentanediol), structures that are available in foam ingredients are presented in Figure. The aim was to develop reactive simulations to enhance our understanding of the interactions between nanoparticles and plain water. These simulations would provide insight into the mechanistic details,

enabling the tracking and quantification of any decreases in the initiation events of combustion.

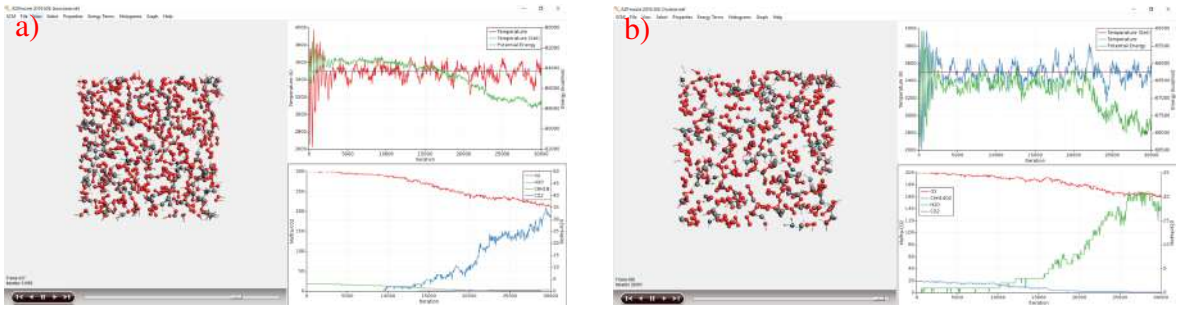

Figure A.2: *ADF Powerful molecular DFT simulations for a) Isooctane b) Diolane.*

However, the simulations were found to be time-intensive and encountered complexities at the molecular scale. Consequently, a reformed plan was structured. This new approach focused on the enhancement of Class A foams by synthesising iron oxide nanoparticles in the laboratory and testing them under small-scale conditions. This change was essential to progress the project effectively and to achieve measurable results within a reasonable time.

Appendix B

Code for calculating the Flame Surface Area

The code in python for the average flame surface area regarding the excelsior sprayed with the wet foam (WF) and the NPs is listed below.

```
import os.path as path
import sys
from typing import Any

import cv2
import matplotlib.pyplot as plt
import numpy as np
import yaml

from parameters import *

"""RUNTIME CONSTANTS"""
gaussian_kernel = np.ones((GAUSSIAN_KERNEL_SIZE, GAUSSIAN_KERNEL_SIZE), np.float32) / (
    GAUSSIAN_KERNEL_SIZE**2
)

def get_area(image: np.ndarray) -> Any:
    # get the red color
    image = image[..., -1]

    # gaussian blur it
    image = cv2.filter2D(image, -1, gaussian_kernel)

    # threshold it
    image = (image > RED_THRESHOLD) * 1.0

    # sum the area, this is a single float where the unit is cm2
    area = np.sum(image) * pixel_area_to_cm_area

    return area
```

```
def process_video(filename: str, start_frame: int, end_frame: int) -> np.ndarray:
    # start video capture
    vidcap = cv2.VideoCapture(path.join('./movs/', filename))

    num_frames = 0
    areas = []
    while True:
        # try read a frame, if fail just break
        success, image = vidcap.read()
        if not success or image is None:
            break

        # only read the frames within the thing
        num_frames += 1
        if num_frames < start_frame:
            continue
        if num_frames > end_frame:
            break

        areas.append(get_area(image))

    # convert to np array
    return np.array(areas)

if __name__ == "__main__":
    # handle names
    mov_path = path.basename(sys.argv[1])
    npy_path = f"{path.join('./npys_area/', mov_path)}.npy"
    csv_path = f"{path.join('./csvs_area/', mov_path)}.csv"
    figs_path = f"{path.join('./figs/', mov_path)}.png"

    # grab the experiment number from the video filepath
    exp_number = int(mov_path[-6:-4])

    with open("./ignition_times.yaml", "r") as f:
        start_frame = yaml.safe_load(f)[exp_number] * FRAME_RATE
        end_frame = start_frame + BURN_DURATION * FRAME_RATE

    # check if we need to process the video if the pixel heights already exists
    if not path.exists(npy_path):
        areas = process_video(mov_path, start_frame, end_frame)
        np.save(npy_path, areas)
    else:
        areas = np.load(npy_path)

    np.savetxt(csv_path, areas, delimiter=",")


from os import path

import matplotlib.patches as patches
import matplotlib.pyplot as plt
import numpy as np
import yaml
from parameters import *
```

```
array_length = FRAME_RATE * BURN_DURATION + 1

def convolve_area(areas):
    # heights is of shape time, range=[0, pixel_area]
    # run a moving average window
    convolve1d = lambda x: np.convolve(
        x, np.ones(AREA_MOVING_AVG_LENGTH) / AREA_MOVING_AVG_LENGTH, mode="valid"
    )
    areas = np.apply_along_axis(convolve1d, axis=0, arr=areas)

    return areas

if __name__ == "__main__":
    # read the groups, and process so that each one is named "Test {num}.MOV"
    # all_sets is a dict of [set_name: [test_name1, test_name2, ...]]
    with open("./groups.yaml", "r") as f:
        all_sets = yaml.safe_load(f)
        for set_name in all_sets:
            for i, element in enumerate(all_sets[set_name]):
                all_sets[set_name][i] = f"Test {element}.MOV"

    # start to process each group into an averaged array
    # the following is a dict of [set_name: np.ndarray]
    mean_areas = dict()
    std_areas = dict()
    for set_name in all_sets:
        individual_areas = []
        for element in all_sets[set_name]:
            npy_filepath = path.join(f"./npys_area/{element}.npy")

            # pad the array to make it 200 seconds long
            padded_array = np.zeros((array_length,), dtype=np.float32)
            loaded_array = np.load(npy_filepath)
            padded_array[: len(loaded_array)] = loaded_array

            # convolve the heights, store the raw data
            # binned_heights here is a list of [time, heights in cm]
            padded_array = convolve_area(padded_array)
            individual_areas.append(padded_array)

        # stack each experiment
        individual_areas = np.stack(individual_areas, axis=0)

        # get mean and var
        mean_areas[set_name] = np.mean(individual_areas, axis=0)
        std_areas[set_name] = np.std(individual_areas, axis=0)

    # 1. flame areas over time
    x_axis = np.arange(mean_areas[list(all_sets.keys())[0]].shape[0]) / FRAME_RATE
    compound_fig, compound_ax = plt.subplots()
    for i, set_name in enumerate(all_sets):
        compound_ax.plot(
            x_axis,
            mean_areas[set_name],
            color=color_palette[i],
            linewidth=linewidths[i],
```

```
        )
        single_fig, single_ax = plt.subplots()
        single_ax.plot(x_axis, mean_areas[set_name])
        single_ax.set_title(f"Flame Area vs Time, {set_name}")
        single_ax.set_xlabel(r"time, s")
        single_ax.set_ylabel(r"flame area, cm$^2$")
        single_fig.tight_layout()
        single_fig.savefig(f"./figs/areas_{set_name}.pdf")
        plt.close(single_fig)

    compound_ax.set_title("Flame Area vs Time")
    compound_ax.set_xlabel(r"time, s")
    compound_ax.set_ylabel(r"flame area, cm$^2$")
    fake_patches = [patches.Patch(color=color, alpha=0.75) for color in color_palette]
    legend = plt.legend(
        fake_patches,
        all_sets.keys(),
        loc="lower right",
        fancybox=True,
        ncol=1,
    )
    plt.tight_layout()
    plt.savefig(f"./figs/all_areas.pdf")
    plt.close()
```

Appendix C

Materials characterisation (additional figures)

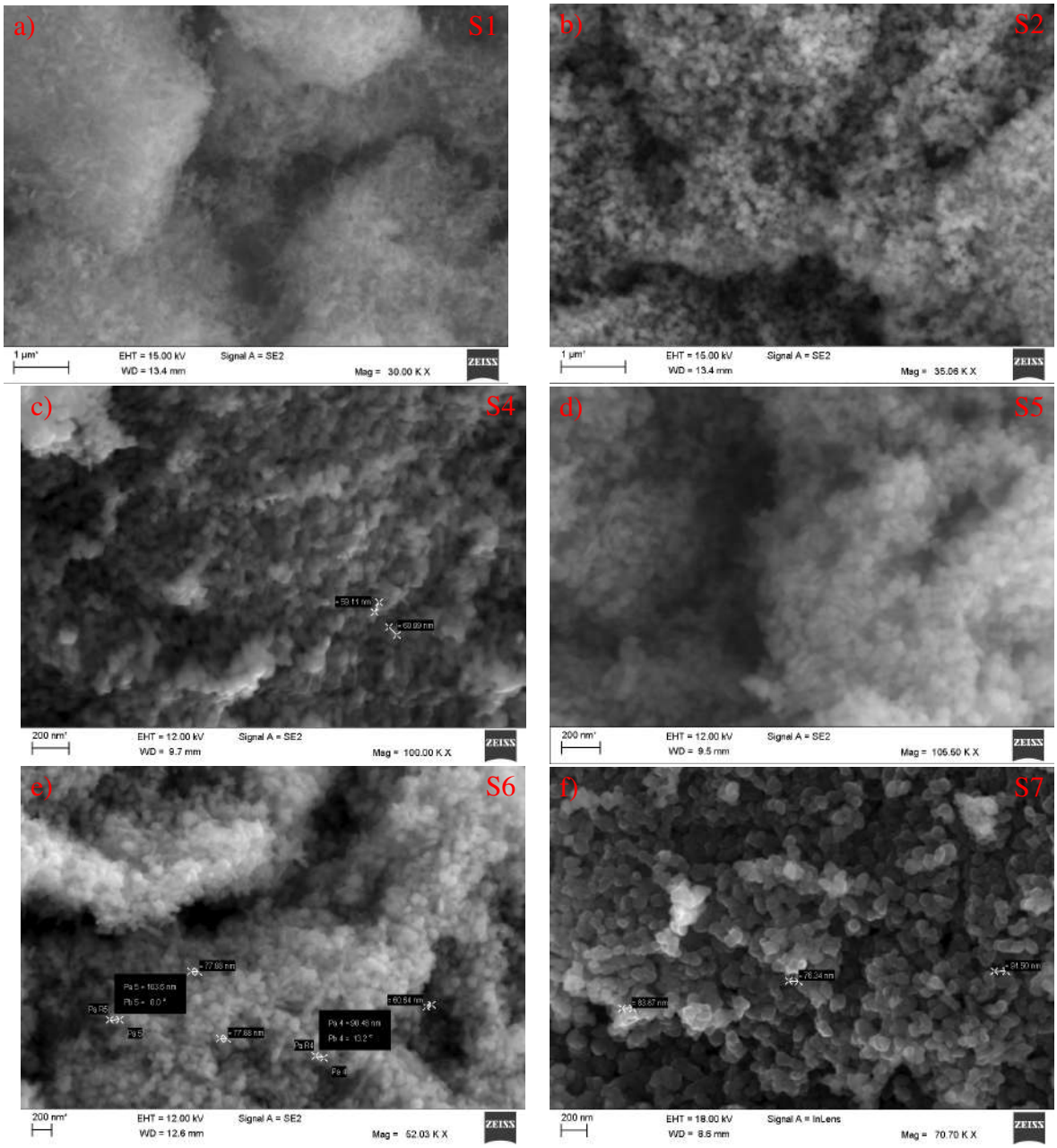

Figure C.1: *SEM Characterisation of NP samples a) Sample S1 with a rod agglomerated structure, b) Sample S2 with aggregated particles mostly circular in shape, c) Sample S4 consisted of clustered particles, d) Sample S5 showing particles consisting of two phases both nearly circular and rod-like structures, e) Sample S6 with different sizes of nearly circular-shaped particles and f) Sample S7 with a clear distribution of nearly spherical particles with some degree of agglomeration.*

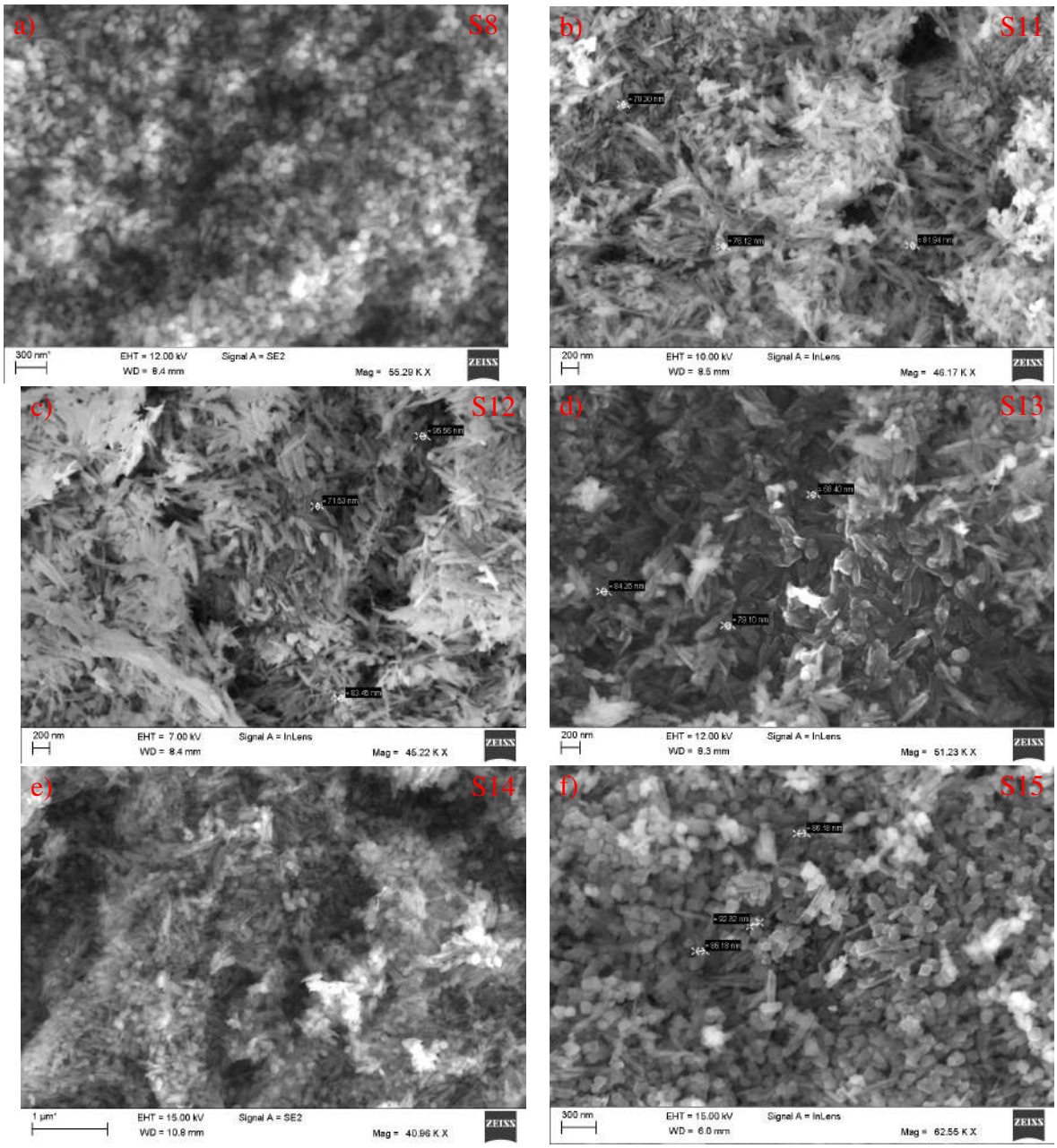

Figure C.2: *SEM Characterisation of NP samples a) Sample S8 exhibits elongated rods and circular structures, b) Sample S14 the rod structure is visible, c) Sample S12 is characterised by dense, rod-like formations, d) Sample S13 displays rod-like structure with some aggregation, e) Sample S14 shows a compact arrangement of both spherical and rod structures and f) Sample S15 presents a better distribution of a heterogeneous composition with both rods and spherical particles.*

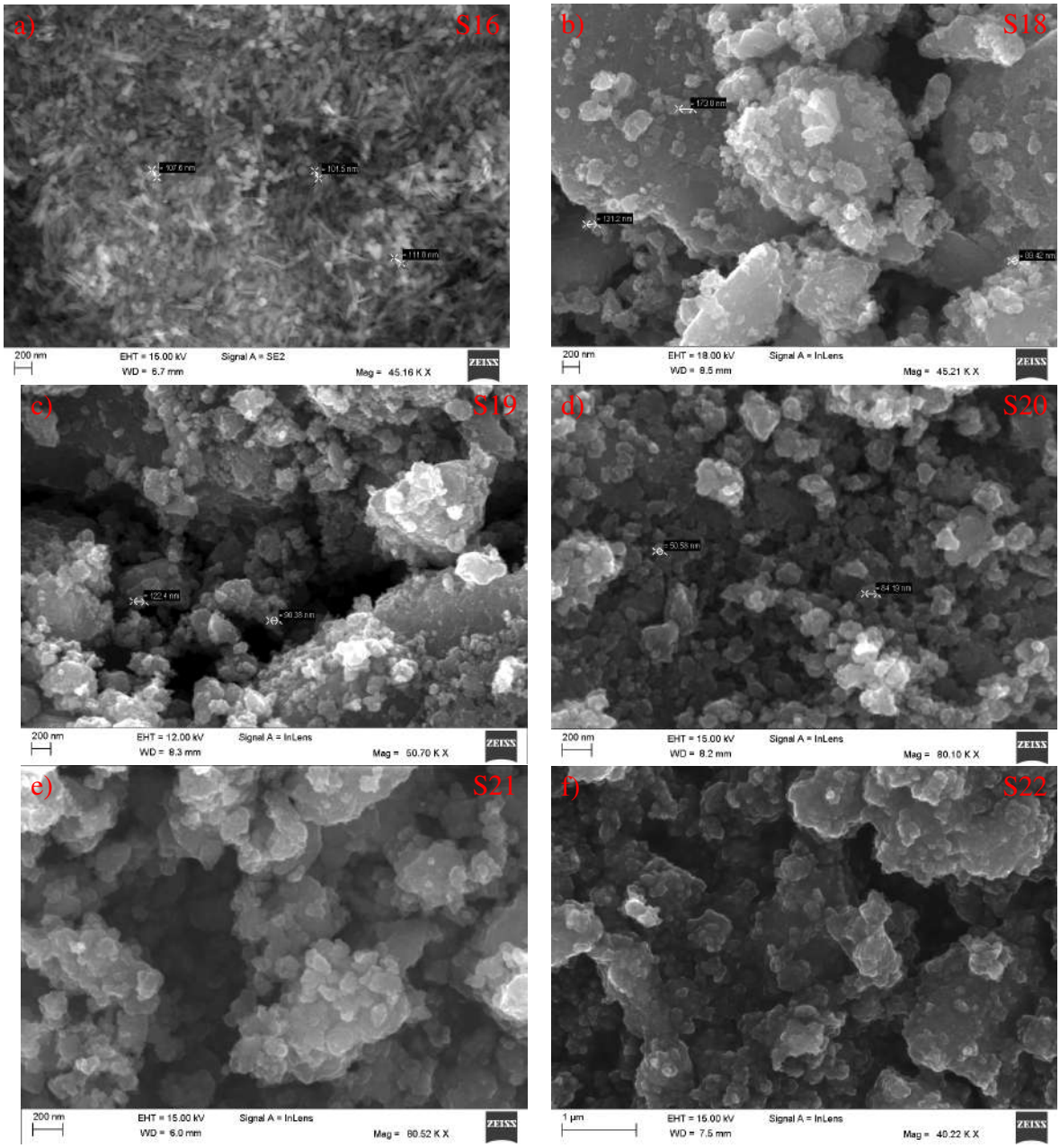

Figure C.3: *SEM Characterisation of NP samples. a) Sample S16 exhibits rod structure with small cubes, b) Sample S18 with variable particle sizes and clustering, c) Sample S19 shows irregular particle aggregation, d) Sample S20 with a more homogeneous distribution, e) Sample S21 depicting agglomerated particles, and f) Sample S22 presenting densely packed particles.*

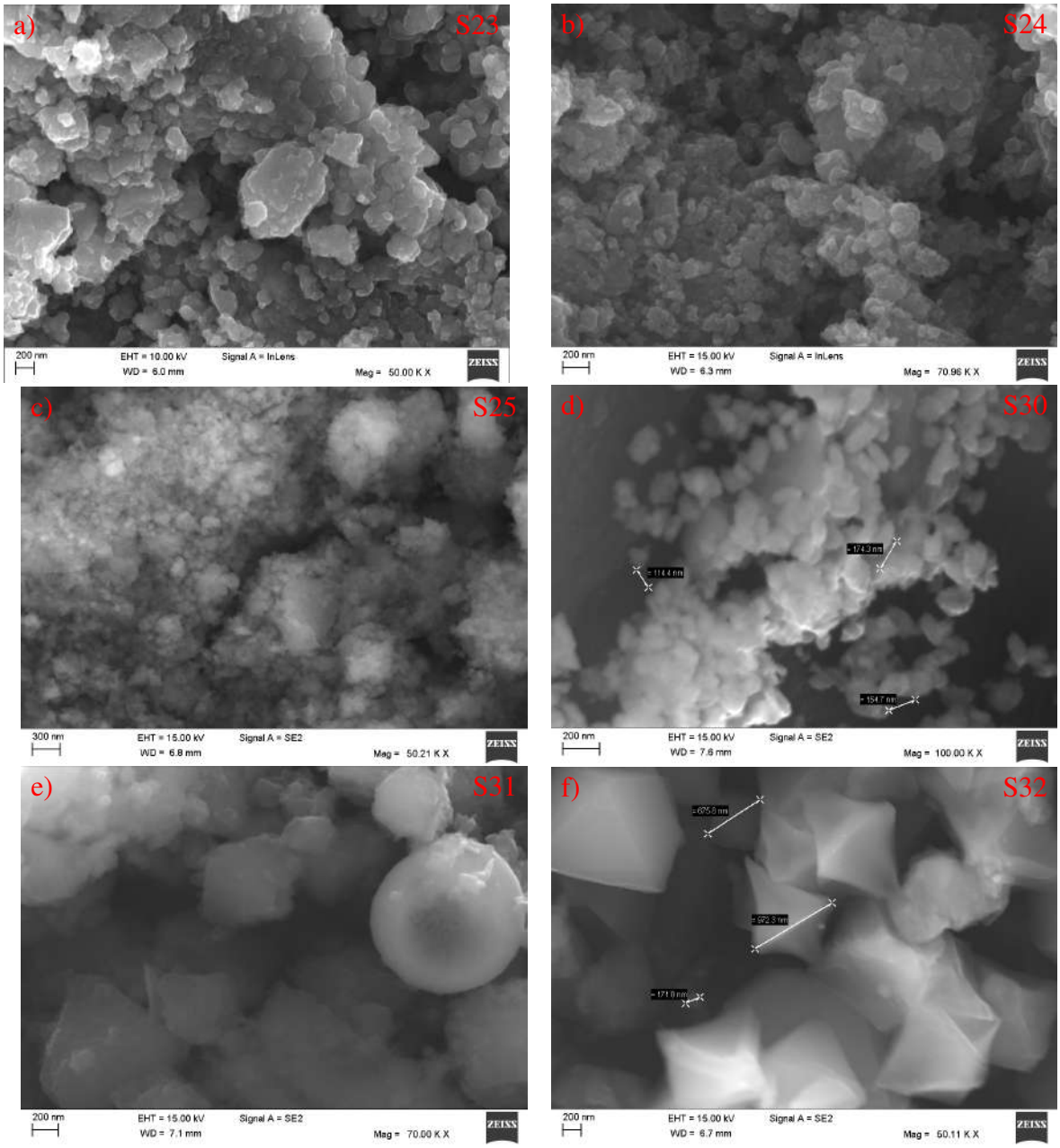

Figure C.4: *SEM Characterisation of NP samples. a) Sample S23 shows clustered NP formations, b) Sample S24 with a densely packed structure, c) Sample S25 presents a more amorphous agglomeration, d) Sample S30 illustrates dispersed NPs with evident individual features, e) Sample S31 reveals spherical rhomboidal NPs with agglomeration, and f) Sample S32 displays rhomboidal NPs with defined edges.*

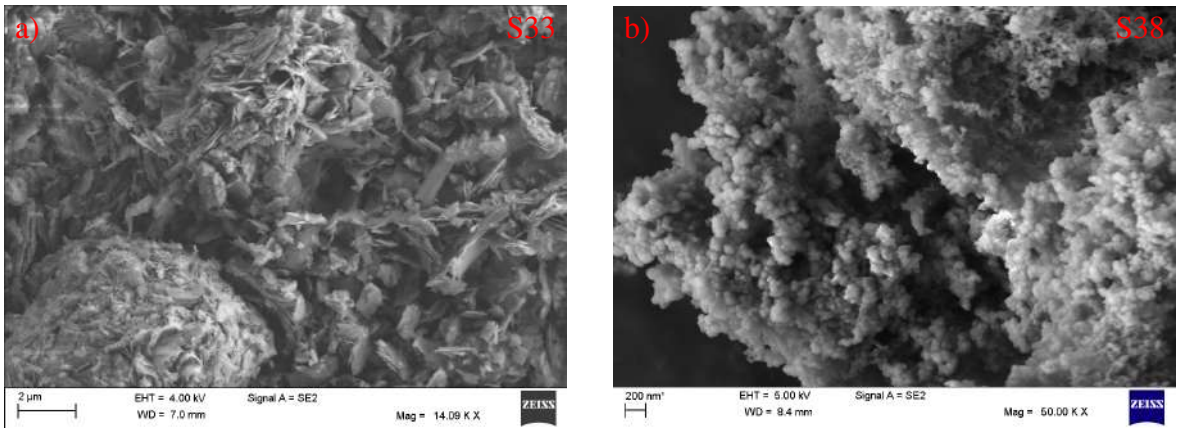

Figure C.5: *SEM Characterisation of NP samples a) Sample S33 displays micro-scale elongated formations b) Sample S38 presents a densely clustered structure with distinct particle size.*

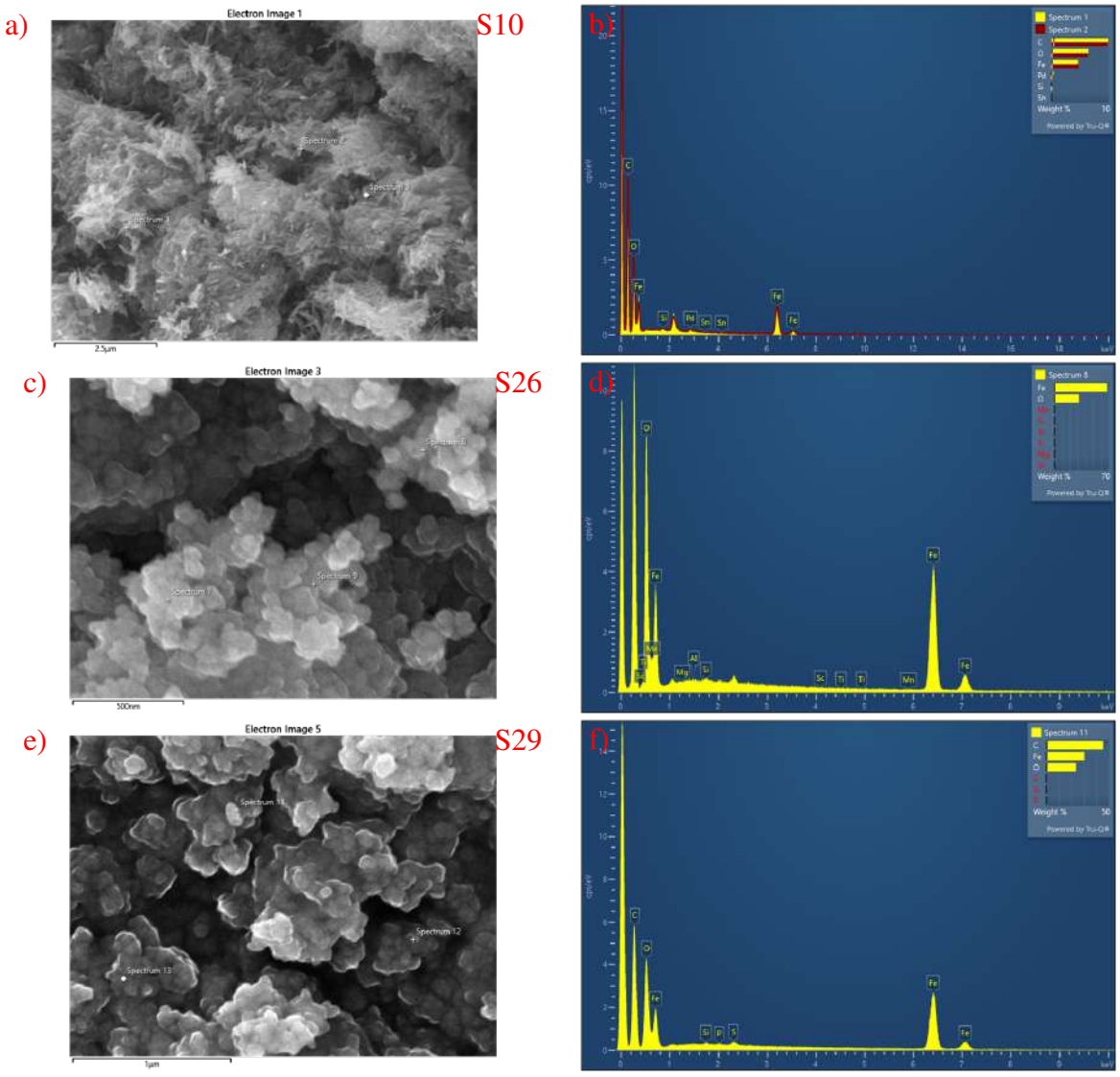

Figure C.6: *a) Scanning Electron Microscopy and Energy-dispersive X-ray spectroscopy analysis for samples a,b) S10, b,c) S26, e,f) S29.*

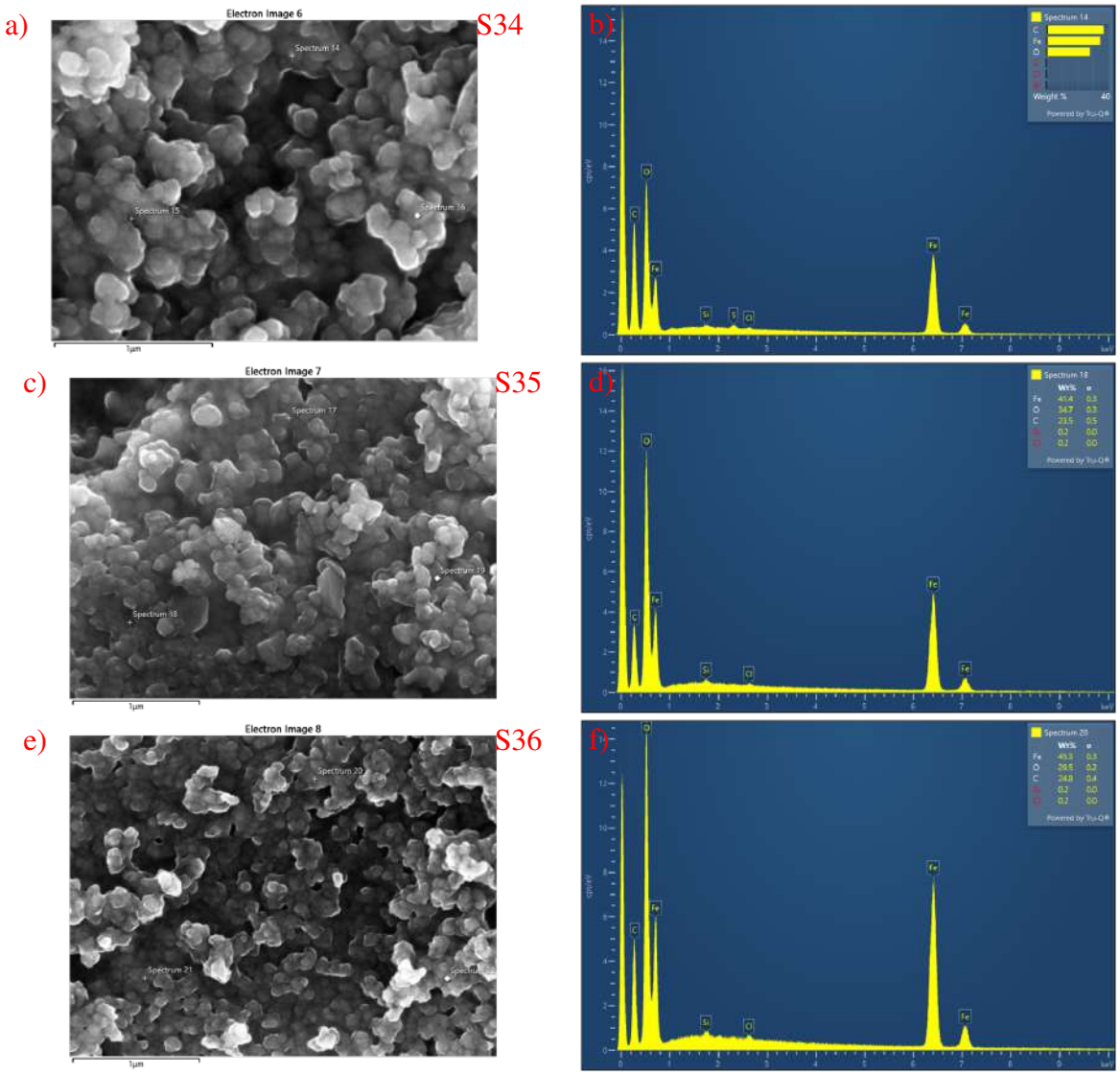

Figure C.7: *a) Scanning Electron Microscopy and Energy-dispersive X-ray spectroscopy analysis for samples a,b) S34, b,c) S35, e,f) S36.*

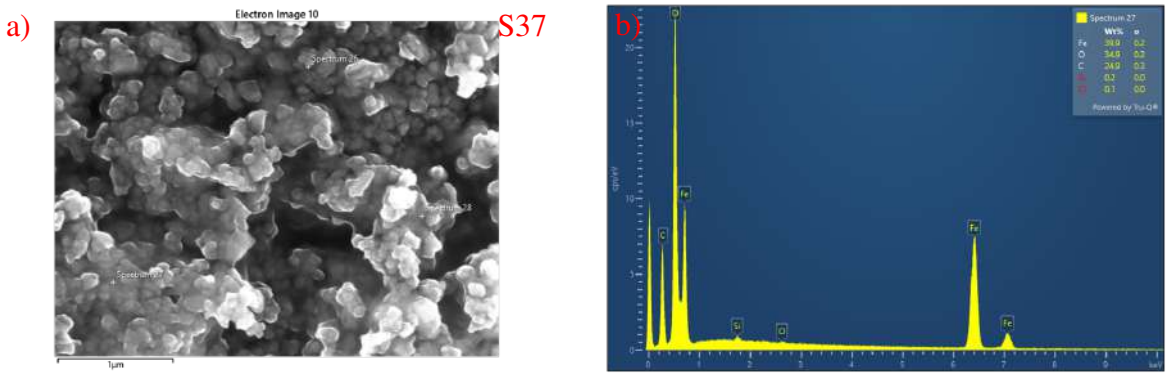

Figure C.8: *a) Scanning Electron Microscopy image of synthesized S37 nanoparticles showing their morphology. b) Energy-dispersive X-ray spectroscopy analysis of S37 NPs confirming elemental composition.*

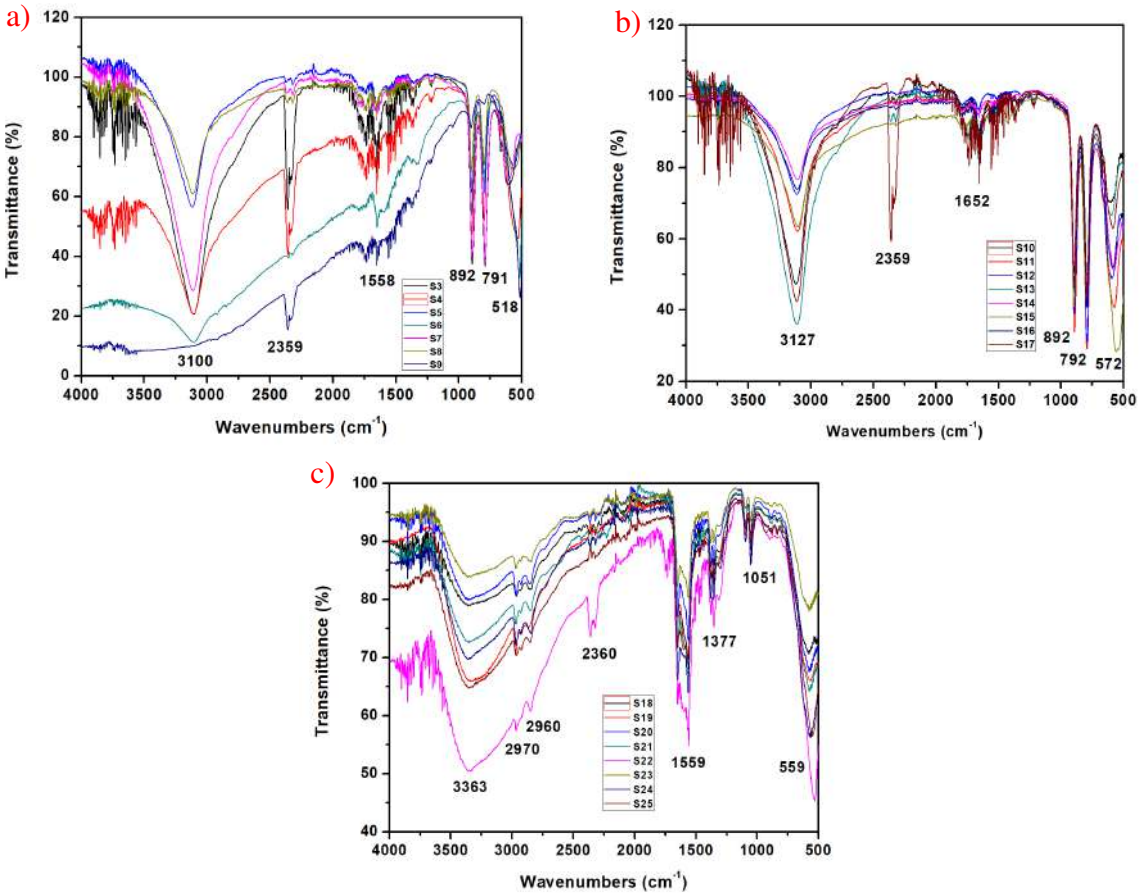

Figure C.9: *FTIR Spectra of synthesised IONPs where a) Samples S3-S9; b) samples S10-S17; c) samples S18-S25*

Appendix D

Foam stability (additional figures)

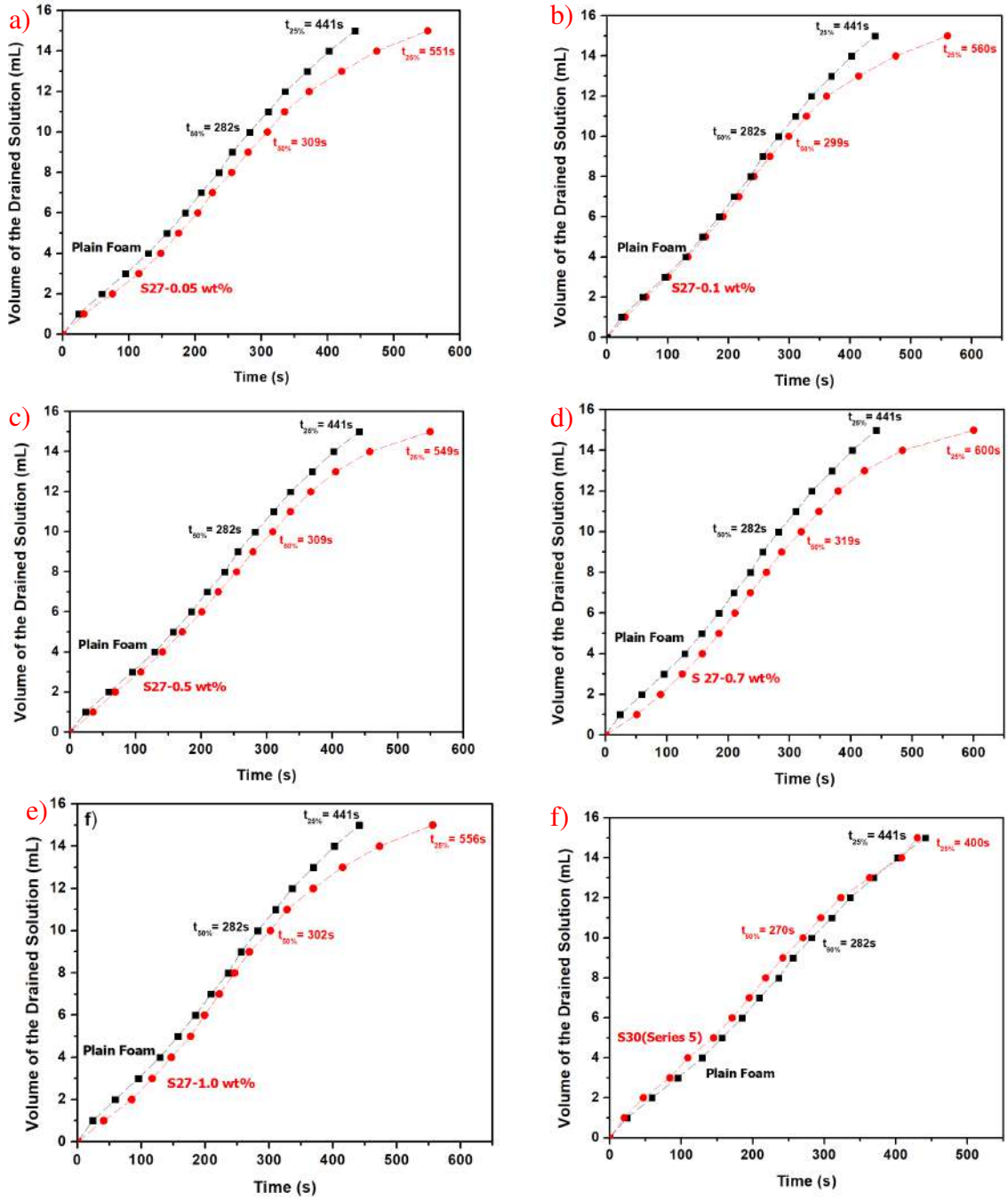

Figure D.1: *Foam drainage experiments for a) Plain foam vs S27-0.05 wt%, b) Plain foam vs S27-0.1 wt%, c) Plain foam vs S27-0.5 wt%, d) Plain foam vs S27-0.7 wt%, e) Plain foam vs S27-1.0 wt%, f) Plain foam vs S30-0.05 wt%.*

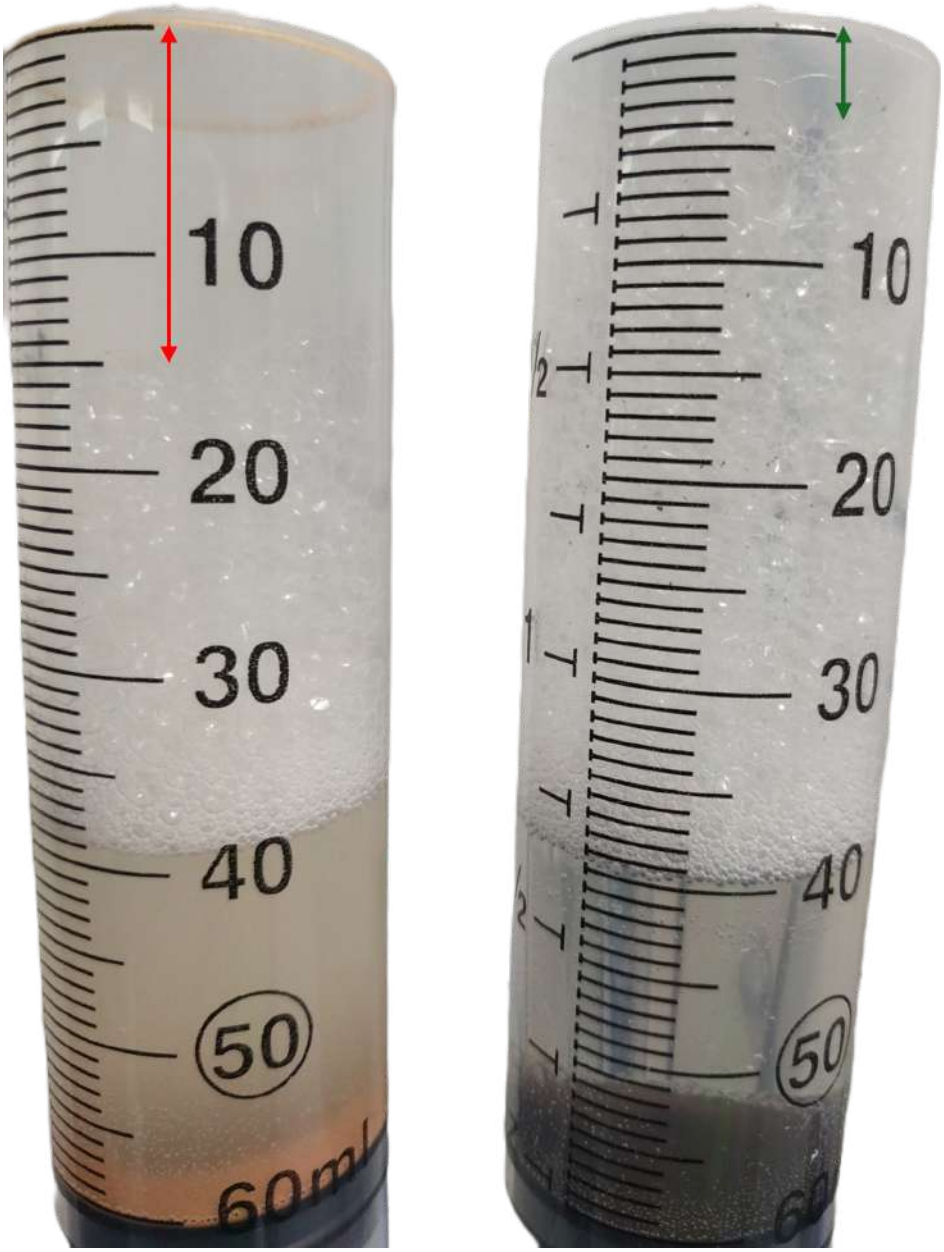

Figure D.2: *Foam structure after 24hr drainage where on the left visualises IONPs from series 5 (Table3.7) and on the right IONPs from series 4(Table 3.6).*

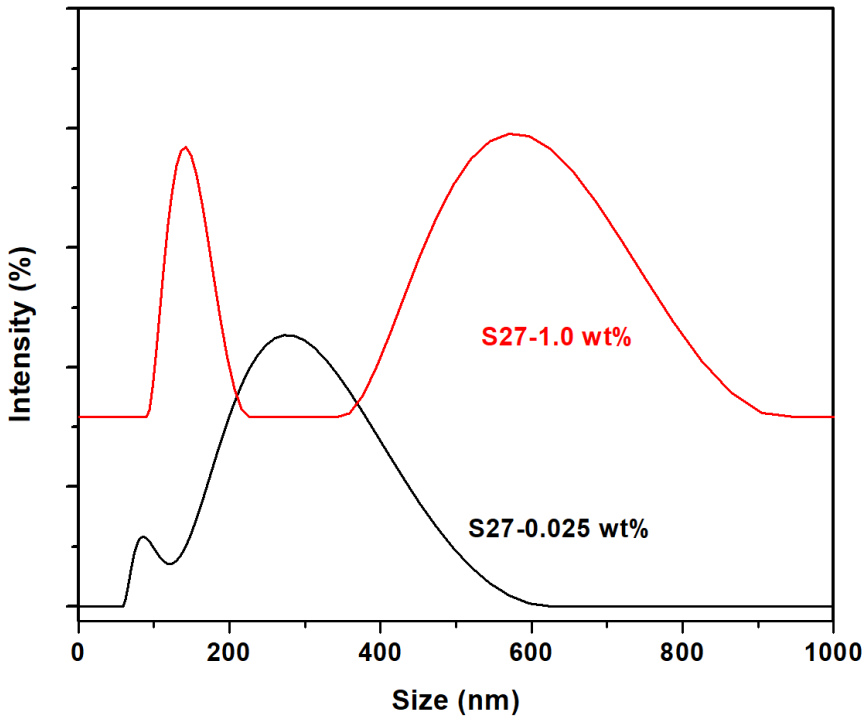

Figure D.3: *Dynamic light scattering (DLS) for different concentrations of sample 27.*

Appendix E

Fire experiments (additional figures)

.

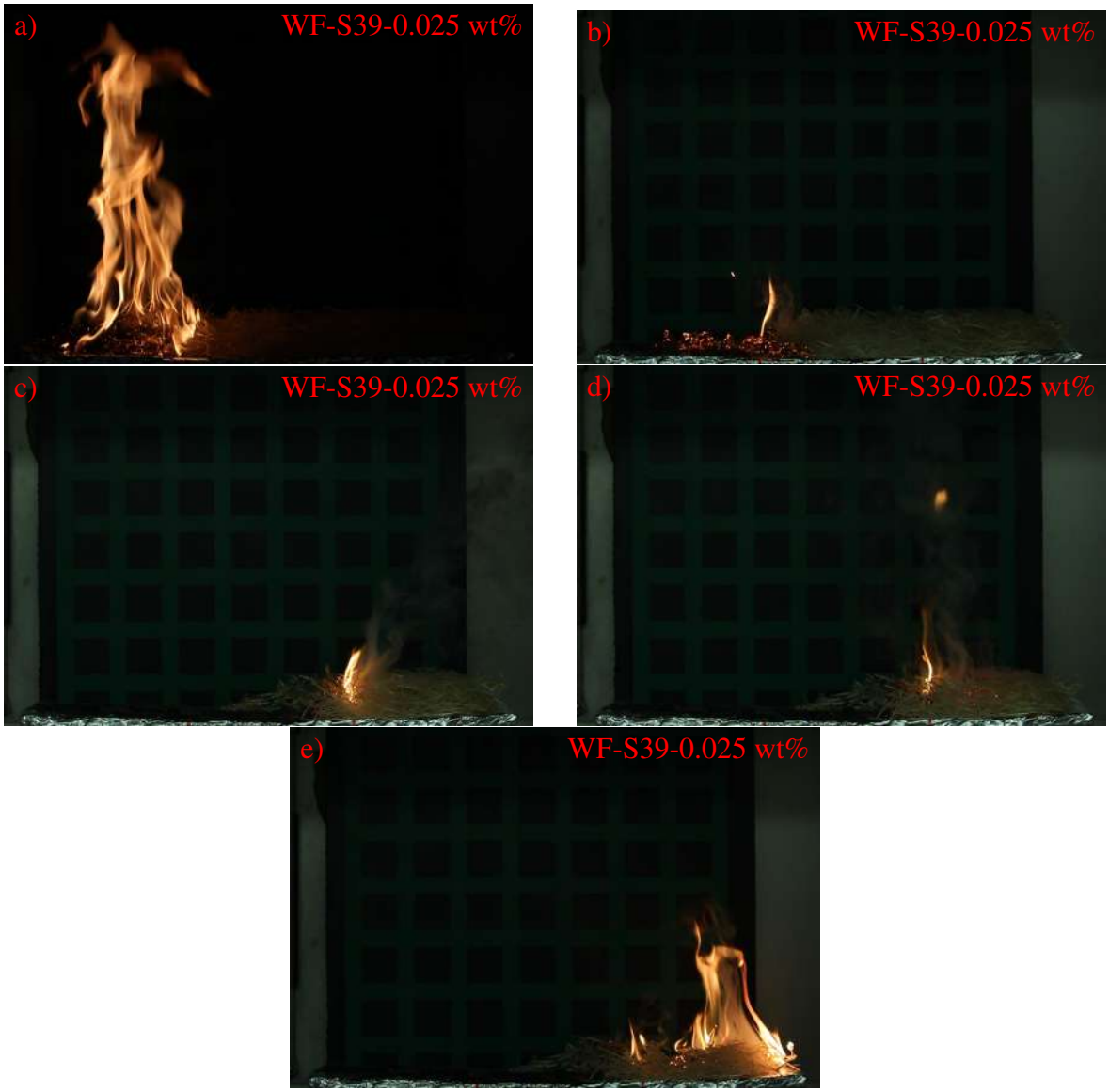

Figure E.1: *Flame heights at leading and trailing edges of fire for excelsior fuel covered with wet foam (WF-S39-0.025 wt%) at various positions across the fuel bed: a) leading edge at 20 cm, b) trailing edge at 20 cm, c) leading edge at 40 cm, and d) leading edge at 60 cm.*

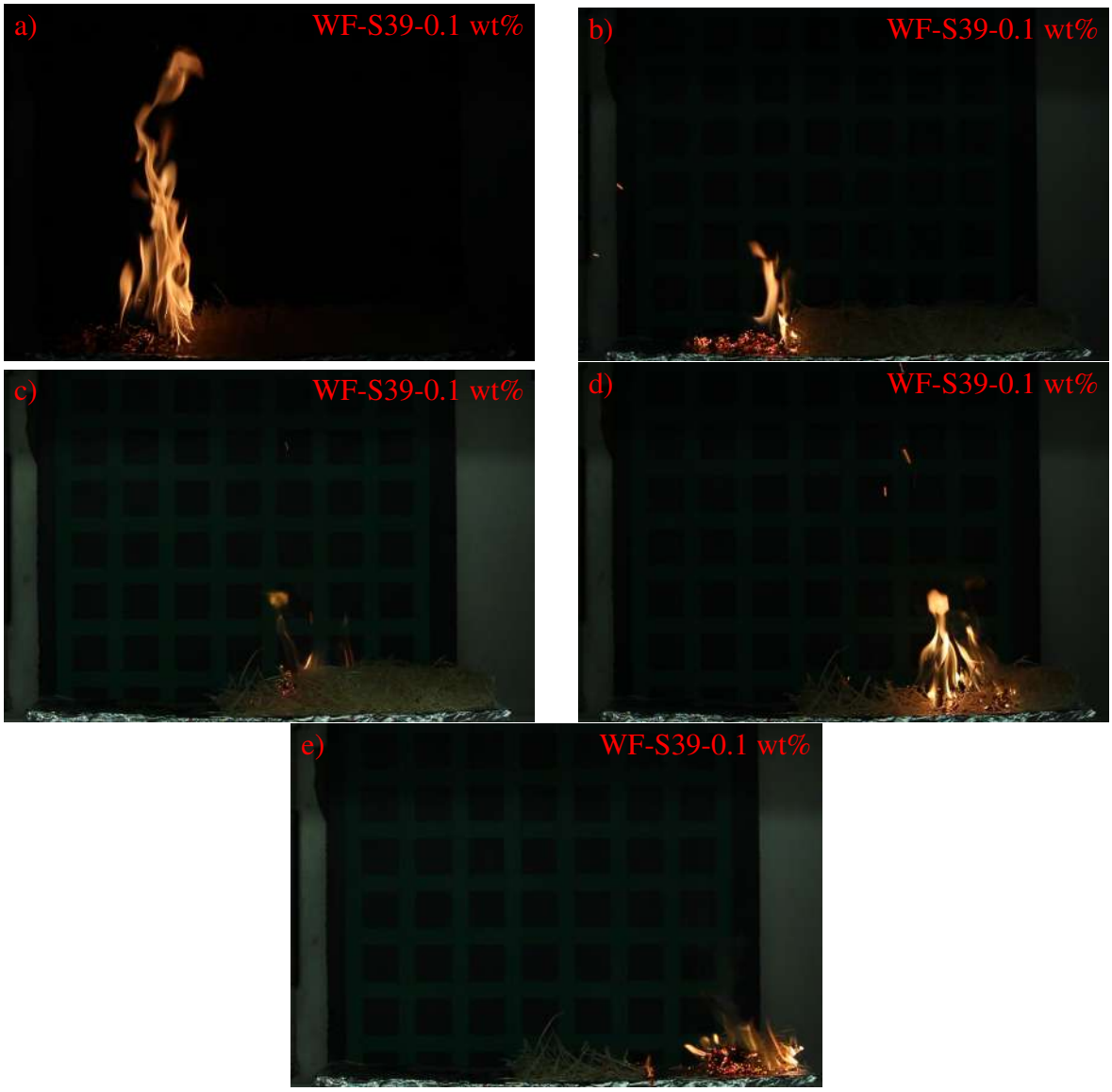

Figure E.2: *Flame heights at leading and trailing edges of fire for excelsior fuel covered with wet foam (WF-S39-0.1 wt%) at various positions across the fuel bed: a) leading edge at 20 cm, b) trailing edge at 20 cm, c) leading edge at 40 cm, and d) leading edge at 60 cm.*

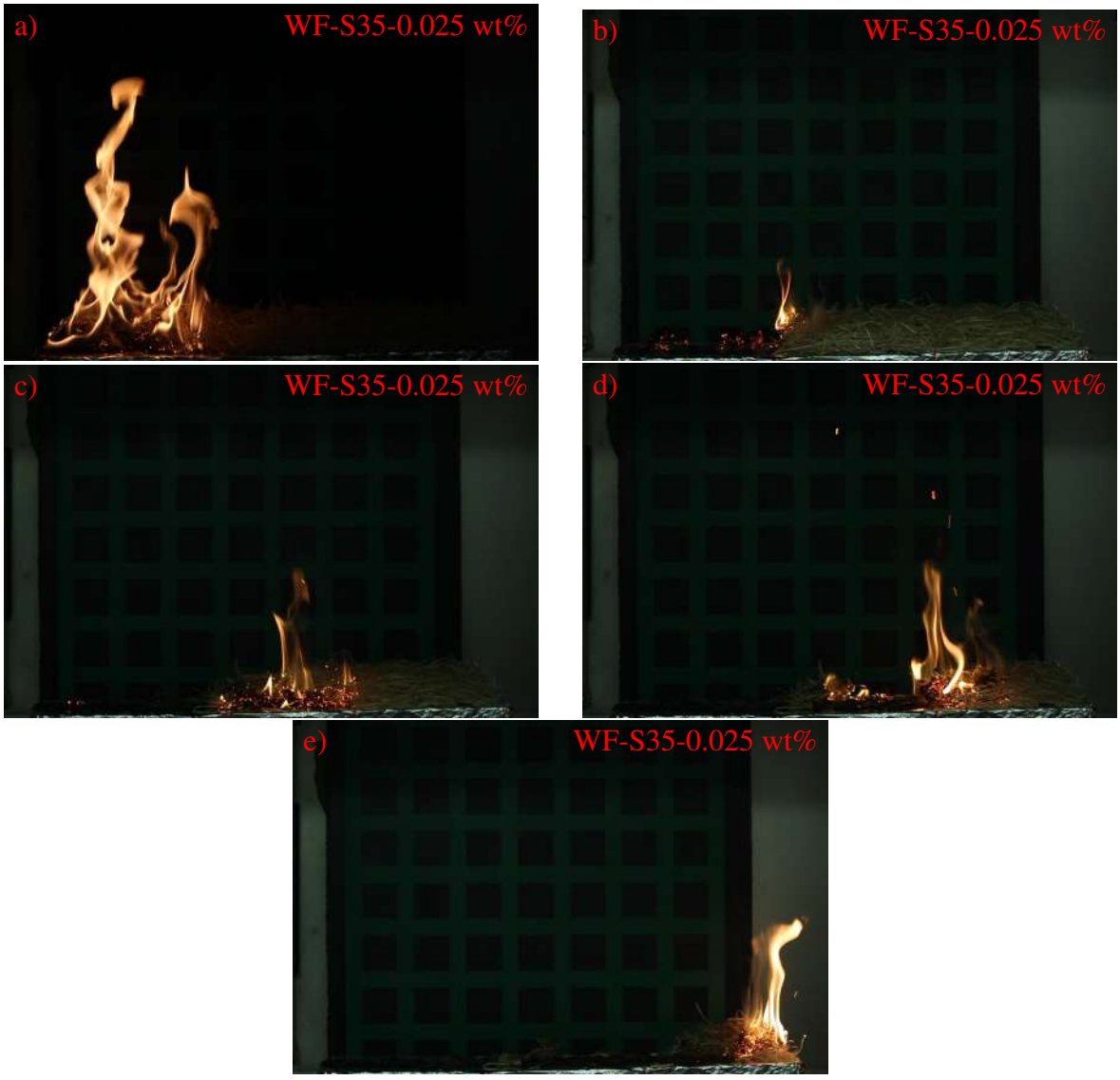

Figure E.3: *Flame heights at leading and trailing edges of fire for excelsior fuel covered with wet foam (WF-S35-0.025 wt%) at various positions across the fuel bed: a) leading edge at 20 cm, b) trailing edge at 20 cm, c) leading edge at 40 cm, and d) leading edge at 60 cm.*

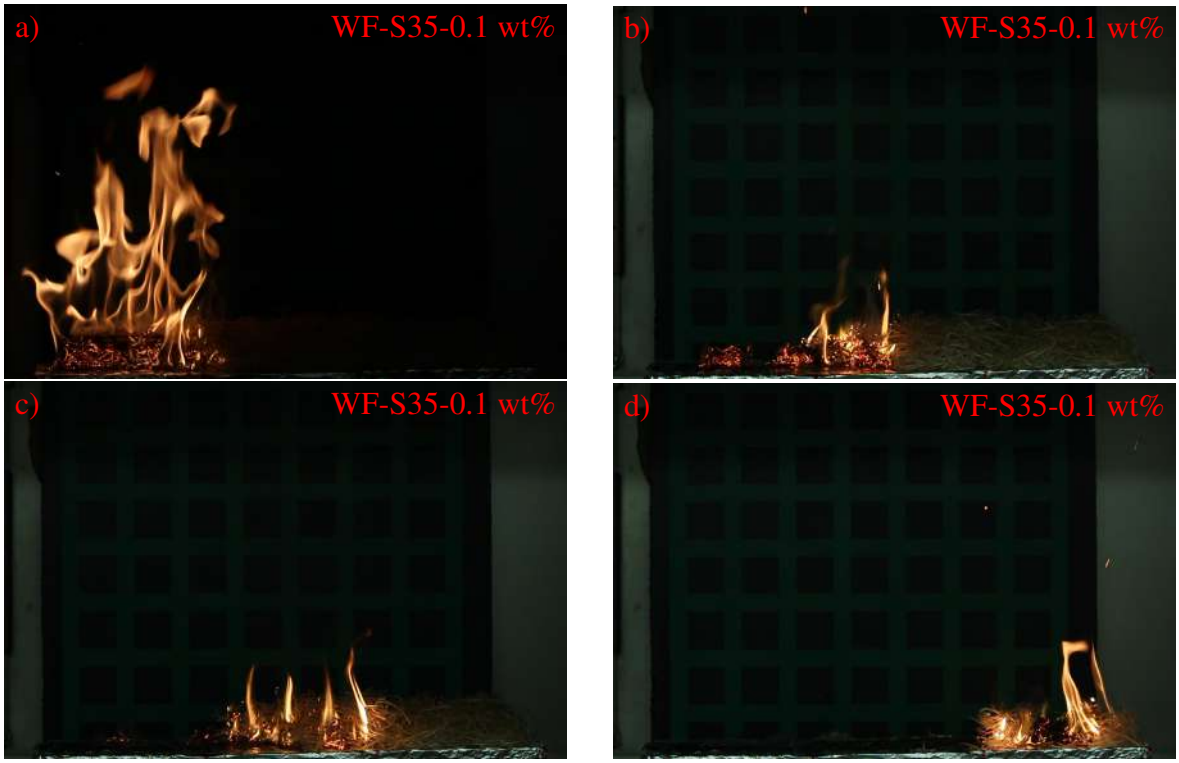

Figure E.4: *Flame heights at leading and trailing edges of fire for excelsior fuel covered with wet foam (WF-S35-0.1 wt%) at various positions across the fuel bed: a) leading edge at 20 cm, b) trailing edge at 20 cm, c) leading edge at 40 cm, and d) leading edge at 60 cm.*

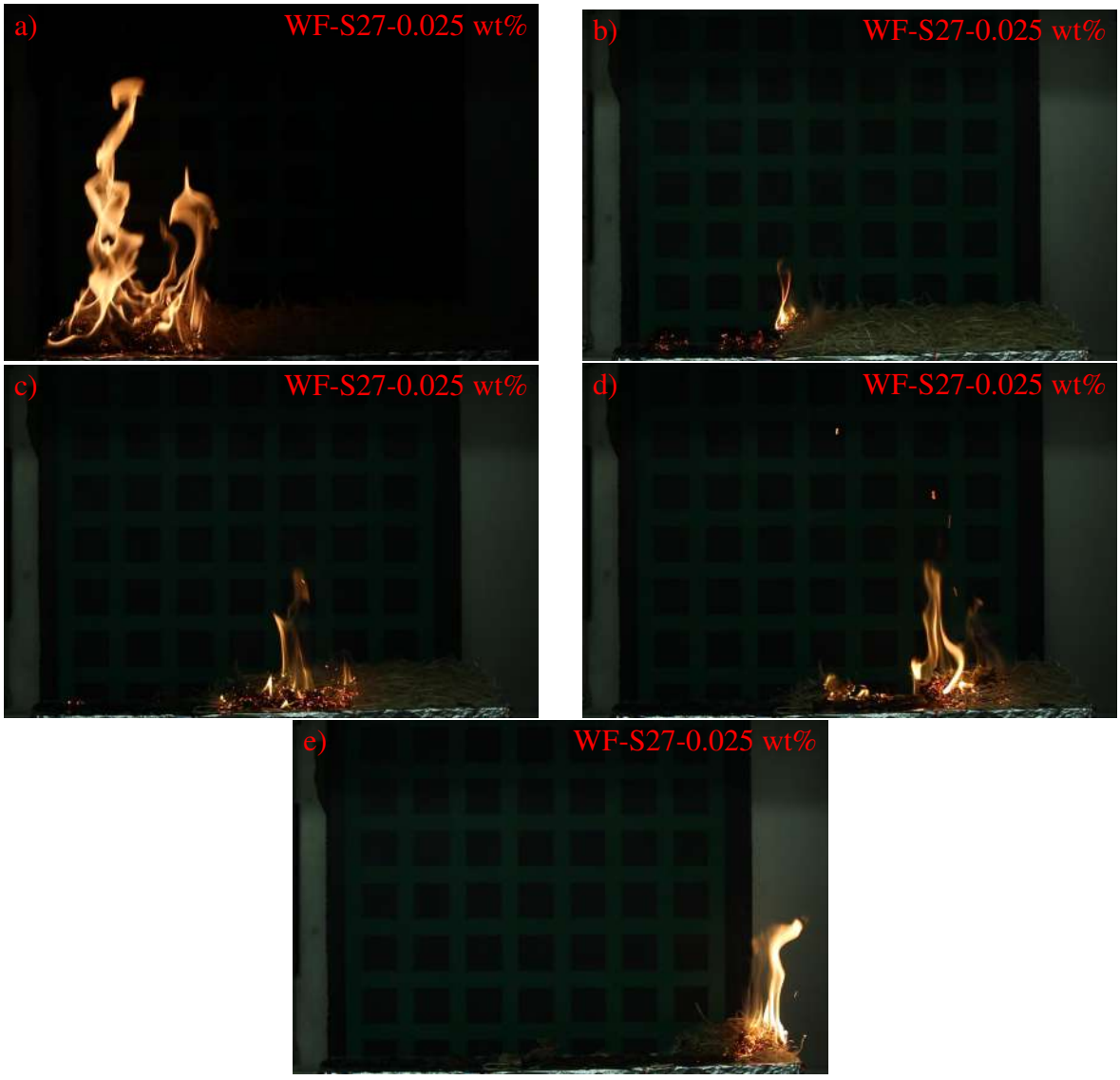

Figure E.5: *Flame heights at leading and trailing edges of fire for excelsior fuel covered with wet foam (WF-S40-0.025 wt%) at various positions across the fuel bed: a) leading edge at 20 cm, b) trailing edge at 20 cm, c) leading edge at 40 cm, d) trailing edge at 40 cm, and e) leading edge at 60 cm.*

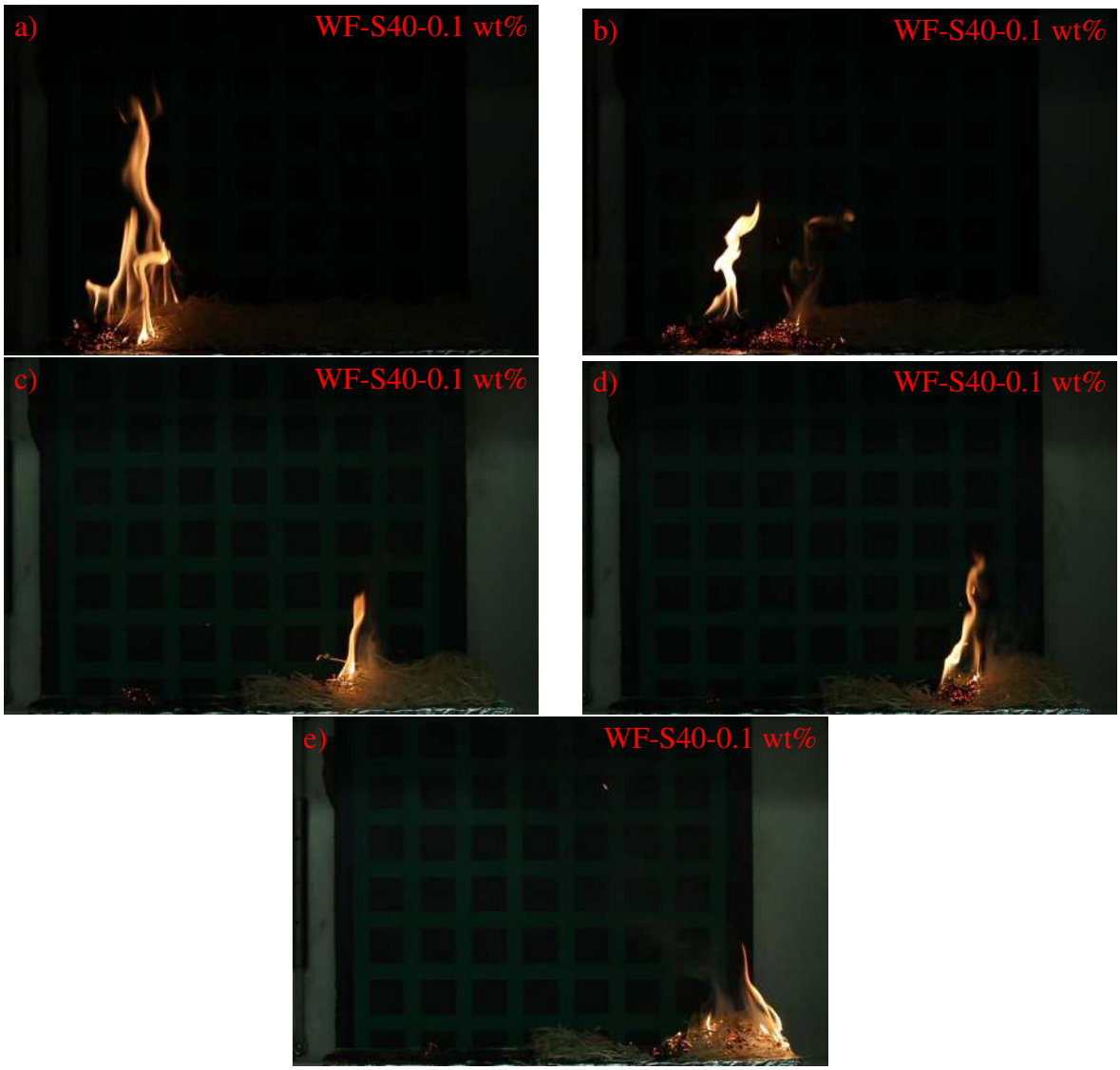

Figure E.6: *Flame heights at leading and trailing edges of fire for excelsior fuel covered with wet foam (WF-S40-0.1 wt%) at various positions across the fuel bed: a) leading edge at 20 cm, b) trailing edge at 20 cm, c) leading edge at 40 cm, d) trailing edge at 40 cm, and e) leading edge at 60 cm.*

Figure E.7: *Flame heights at leading and trailing edges of fire for excelsior fuel covered with dry foam (DF-S27-0.5 wt%) at various positions across the fuel bed: a) leading edge at 20 cm, b) trailing edge at 20 cm, c) leading edge at 40 cm, d) trailing edge at 40 cm, and e) leading edge at 60 cm.*

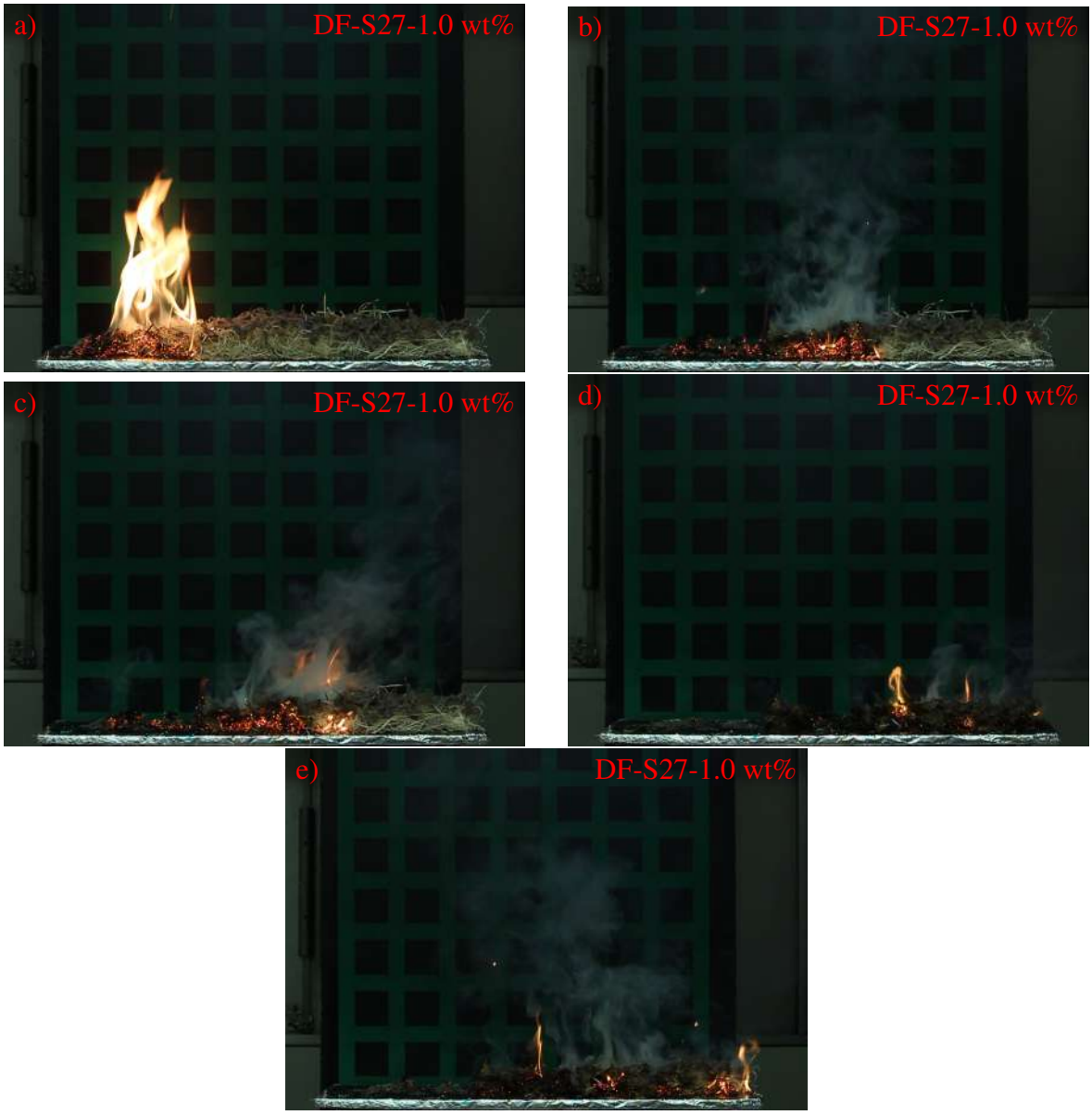

Figure E.8: *Flame heights at leading and trailing edges of fire for excelsior fuel covered with dry foam (DF-S27-1.0 wt%) at various positions across the fuel bed: a) leading edge at 20 cm, b) trailing edge at 20 cm, c) leading edge at 40 cm, d) trailing edge at 40 cm, and e) leading edge at 60 cm.*

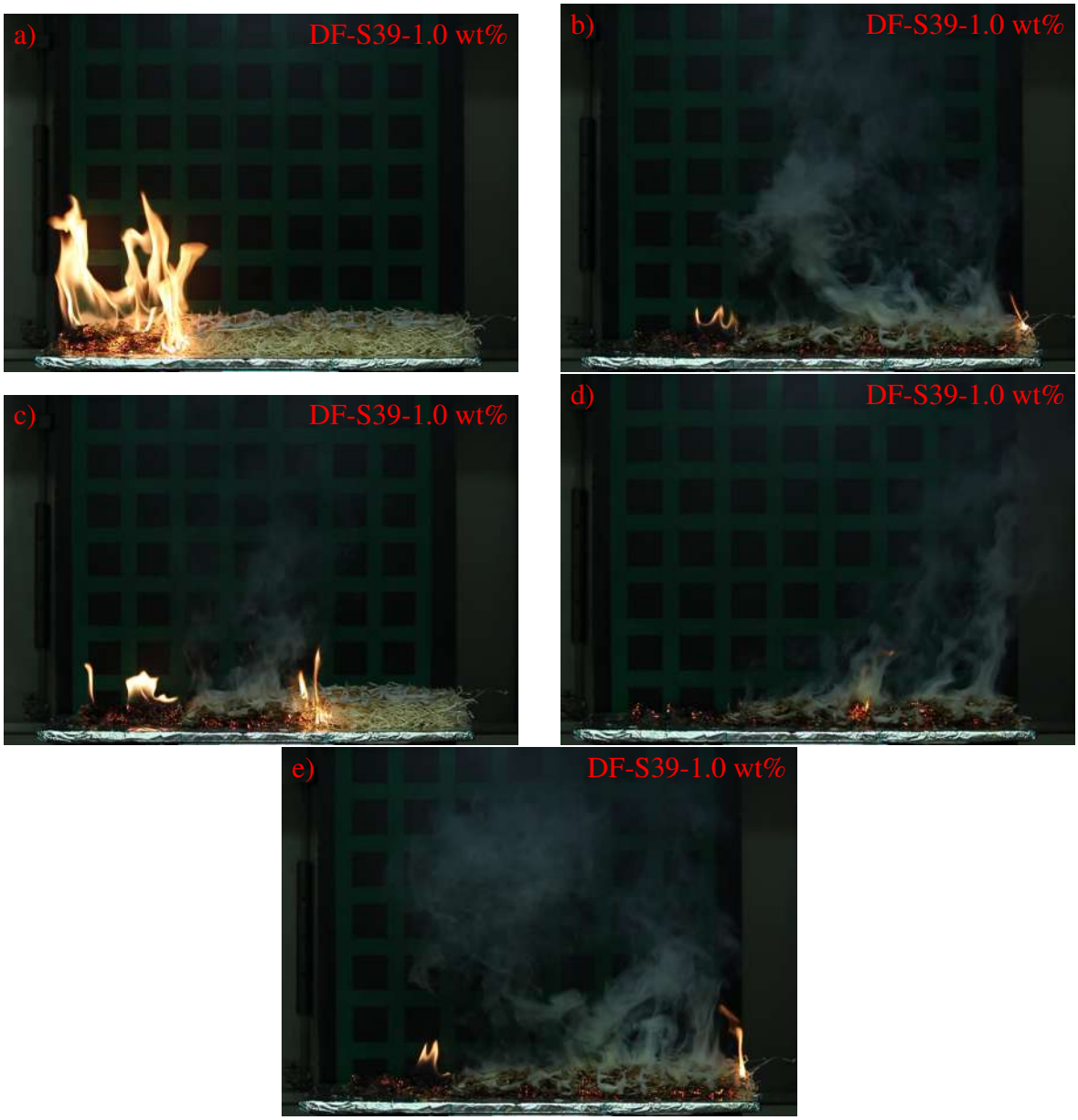

Figure E.9: *Flame heights at leading and trailing edges of fire for excelsior fuel covered with dry foam (DF-S39-1.0 wt%) at various positions across the fuel bed: a) leading edge at 20 cm, b) trailing edge at 20 cm, c) leading edge at 40 cm, d) trailing edge at 40 cm, and e) leading edge at 60 cm.*

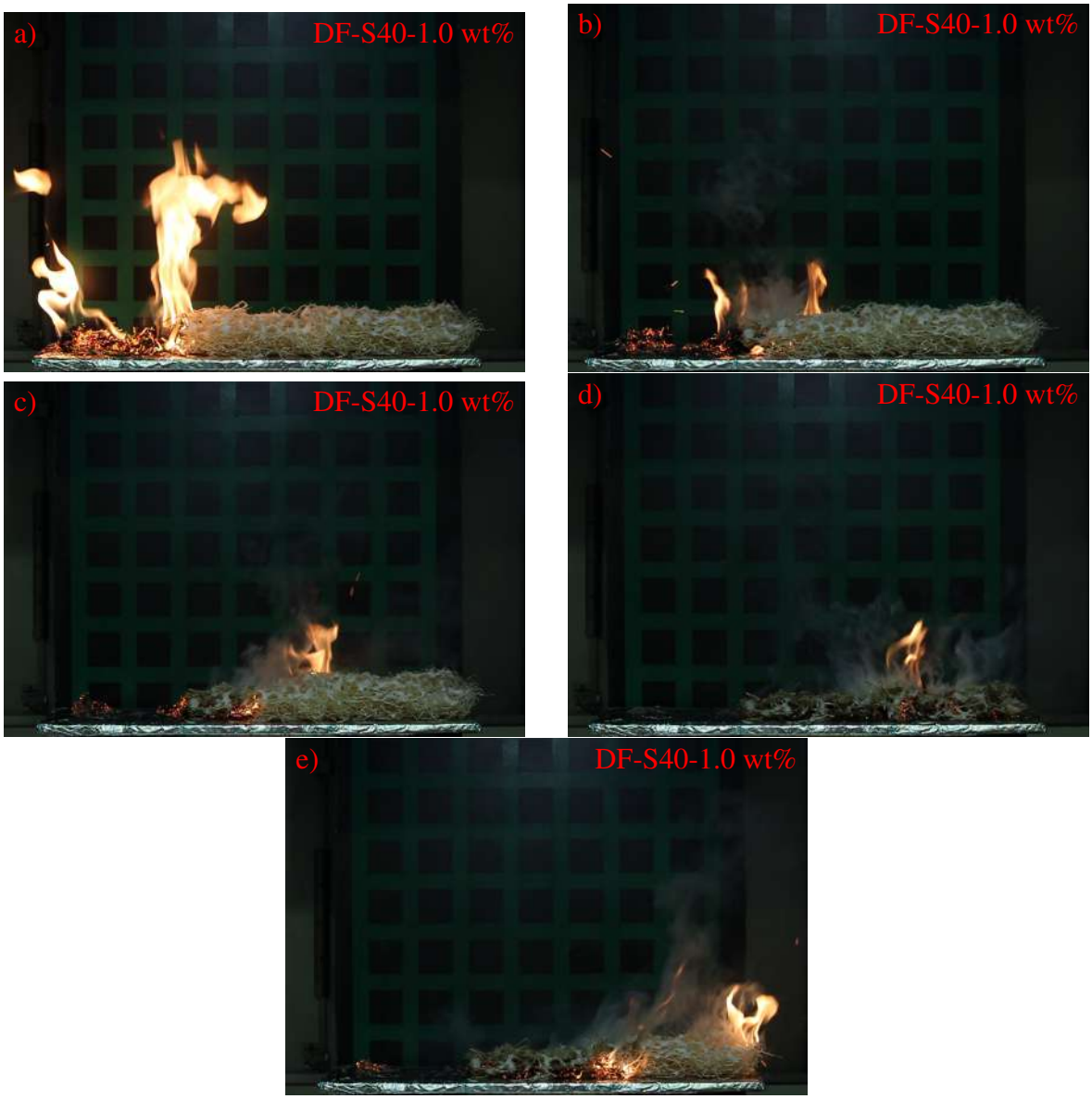

Figure E.10: *Flame heights at leading and trailing edges of fire for excelsior fuel covered with dry foam (DF-S40-1.0 wt%) at various positions across the fuel bed: a) leading edge at 20 cm, b) trailing edge at 20 cm, c) leading edge at 40 cm, d) trailing edge at 40 cm, and e) leading edge at 60 cm.*

Appendix F

List of Derived Publications

- **Papagiannis, I.**, Innocente, M. S., and Gkanas, E. I. (2022, March). Synthesis and Characterisation of Iron Oxide Nanoparticles with Tunable Sizes by Hydrothermal Method. In Materials Science Forum (Vol. 1053, pp. 176-181). Trans Tech Publications Ltd. https://doi.org/10.4028/p-0so8ha
- Sadrabadi, M. T., Innocente, M., Gkanas, E., and **Papagiannis, I.** (2022, December). Comparison of the effect of one-way and two-way fire-wind coupling on the modelling of wildland fire propagation dynamics. In IX International Conference on Forest Fire Research and 17th International Wildland Fire Safety Summit (pp. 115-121). Coimbra University Press. http://doi.org/10.14195/978-989-26-2298-9_18
- **Papagiannis I.**, Innocente, M. S. Davies, J. D., Ryan, J. L. a d Gkanas, E. I. (2024, April). Investigating the Impact of Iron Oxide Nanoparticles on the Stability of Class A Foam for Wildfire Suppression. Under review in Fire Safety Journal, Elsevier, 2024.